Reduction of nitrogen oxides in diesel exhaust using dielectric barrier discharges driven by current-mode power supplies

Vanesa Rueda

THÈSE

En vue de l'obtention du

DOCTORAT DE L'UNIVERSITÉ DE TOULOUSE

Délivré par :

Institut National Polytechnique de Toulouse (Toulouse INP)

Discipline ou spécialité :

COMPOSANTS ET SYSTEMES DE GESTION DE L'ENERGIE

Présentée et soutenue par :

Mme NINI VANESA RUEDA ALGARRA

le mercredi 11 mai 2022

Titre :

Reduction of Nitrogen Oxides in Diesel Exhaust using Dielectric Barrier Discharges driven by current-mode power supplies

---

Ecole doctorale :

Génie Electrique, Electronique, Télécommunications (GEETS)

Unité de recherche :

Laboratoire Plasma et Conversion d'Energie (LAPLACE)

Directeurs de Thèse :

M. HUBERT PIQUET

M. RAFAEL DIEZ MEDINA

Rapporteurs :

M. ALEJANDRO GARCES RUIZ, UT Pereira

M. ROSENDO PENA EGUILUZ, ININ Toluca

Membres du jury :

M. DIEGO PATINO GUEVARA, PONTIFICIA UNIVERSIDAD JAVERIANA BOGOTA, Président

M. HUBERT PIQUET, TOULOUSE INP, Membre

MME FRANÇOISE MASSINES, UNIVERSITE DE PERPIGNAN, Membre

M. RAFAEL DIEZ MEDINA, PONTIFICIA UNIVERSIDAD JAVERIANA BOGOTA, Membre

Contents

List of Figures

List of Tables

Table of Acronyms

DBD	Dielectric Barrier Discharge
NTP	Non-thermal Plasma
PM	Particulate Matter
SCR	Selective Catalytic Reduction
DOC	Diesel Oxidation Catalysts
DPF	Diesel Particulate Filters
EGR	Exhaust Gas Recirculation
LNP	Lean NOx Trap
ED	Energy Density
APGD	Atmospheric Pressure Glow Discharge
ED	Energy Density
SG	Signal Generator
CCM	Continuous Conduction Mode
DCM	Discontinuous Conduction Mode
SRI	Series Resonant Inverter
MFC	Mass Flow Controller
OP	Operating Point
HF	High Frequency
SD	Standard Deviation
CV	Coefficient of variation

Table of Symbols

NO_x	Nitrogen oxides
NO	Nitric oxide
NO_2	Nitrogen dioxide
p	Gas pressure
d_{gap}	Gap distance
V_{br}	Breakdown voltage
A, B	Gas constants
ηNO_x	Nitrogen oxides removal efficiency
ηNO	Nitric oxides removal efficiency
NO_{xE}	Nitrogen oxides energy efficiency
NO_E	Nitric oxides energy efficiency
C_d	DBD Dielectric Capacitance
C_g	DBD Gas Capacitance
C_{eq}	DBD Equivalent Capacitance
V_{th}	DBD Gas Breakdown Voltage
G	DBD Gas Conductance
v_{gas}	DBD gas gap voltage
v_{die}	DBD dielectric voltage
v_{dbd}	DBD voltage
q_{dbd}	DBD charge
i_{gas}	DBD gas current
P_{dbd}	DBD power
E_{dbd}	DBD energy consumed in one cycle
t_{br}	Gas breakdown time instant
d	Duty cycle of the Square Current pulses

J	Amplitude of the Square Current pulses
T_{on}	Time duration of the discharge
T_{br}	Time taken to produce the gas breakdown
T_{pulse}	Time duration of the current pulse
T_s	Period of the Square Current pulses
f_s	Frequency of the Square Current pulses
N	Transformer turn ratio
L_m	Transformer magnetizing inductance
L_{lk}	Transformer leakage inductance
C_p	Transformer stray capacitance
i_{in}	Ideal square current
i_m	Magnetizing inductance current
i_{eq}	Sum of currents flowing through the DBD
C_{off}	Equivalent capacitance of DBD and C_p before breakdown
w_{off}	Resonance frequency before breakdown
C_{on}	Equivalent capacitance of DBD and C_p after breakdown
w_{on}	Resonance frequency after breakdown
k	Iteration number
L	Inductance of CCS
f_{ch}	Frequency of CCS
i_{DC}	DC current of CCS
V_{in}	DC input voltage of CCS
v_{inv}	Inverter input voltage
v_{prim}	DBD voltage reflected in primary winding
v_L	Voltage across L
v_{ch}	Chopper output voltage
I_{ref}	Reference current of the CCS
$f_{L_{ch}}$	Resulting frequency v_L

$T_{L_{ch}}$	Resulting period v_L
d_{ch}	Duty cycle of CCS
$SelectivityNO_2$	NO2 Selectivity
J_{prim}	Amplitude of the Square Current pulses in Primary side of the transformer
f_{burst}	Burst frequency
T_{burst}	Burst period
N_{on}	Number of pulses in burst operation
T_{idle}	Zero Voltage idle time in burst operation
P_{burst}	Average power in the burst period
ξ_n	Energy delivered in each current pulse
G	Total gas flow
μ_{gray}	Mean Gray Level of discharge pictures
SD	Standard Deviation of discharge pictures
CV	Coefficient of Deviation of discharge pictures
C_{dEff}	Effective measurements of Dielectric Capacitance based on Q-V plot
C_{gEff}	Effective measurements of Gas Capacitance
$C_{eq_{Eff}}$	Effective measurements of Equivalent Capacitance
V_{thEff}	Effective measurements of Gas Breakdown Voltage
α	Non-discharging area of partial discharging model
β	Discharging area of partial discharging model

Acknowledgments

The works presented in this doctoral thesis have been developed within the research groups CEPIT of the Pontificia Universidad Javeriana in Bogota, Colombia, and GENESYS of the Laboratoire Plasma et Conversion d'Energie (LAPLACE), unité mixte de recherche CNRS-INPT-UPS nº 5213 in Toulouse, France.

I would like to first thank my supervisors, Professor Rafael Diez, and Professor Hubert Piquet, for their consistent guidance, encouragement, and support throughout this project.

Many thanks also to Eric Bru for his help building the experimentation bench.

I gratefully acknowledge the funding received towards my PhD from the Pontificia Universidad Javeriana PhD fellowship. I am also grateful to the funding received through Eiffel Excellence Scholarship, the French-Colombian cooperation program ECOS Nord (C16P01), the Laplace Laboratory, and the Minciencias project "Prototipo para el tratamiento de material particulado con descargas de barrera dieléctrica" (Contract 294-2016)".

In Javeriana University, my appreciation goes out to my collegues: Arnold, Magin, Miguel V., Sergio, Diego, Eduardo, and Camilo - thanks for your friendship. In Laplace, Kepa, Andallah, Jaime, Najoua, Bernard, and Miguel M., thanks for the warmth you extended to me during my time in Toulouse.

I would also like to say a huge thank you to my Mum, and my whole family for always believing in me. And finally to Juan, who has been on my side every minute of this journey, I dedicate you this work.

Introduction

0.1 Background and Problem Statement

According to the World Health Organization (WHO), air pollution causes almost 4.2 million deaths per year due to stroke, heart disease, lung cancer, and respiratory problems. Furthermore, air pollution affects ecosystems and contributes to climate change. The transportation sector is the most significant source of pollution, and even if this sector has strong emissions regulations, further progress in the efforts to effectively reduce the most dangerous pollutants is urgently needed. Diesel engines are widely used in the transportation and industrial sectors due to their low operating costs, energy efficiency, high durability, and reliability. Despite their advantages, diesel engines produce a high amount of Particulate Matter (PM) and Nitrogen Oxides (NO_x); thus, they have a significant impact on the present air pollution problems. The harmful emissions of Diesel engines are the major weakness of these engines. This thesis will focus on the treatment of NO_x for diesel engines. Nevertheless, it is worth mentioning that when any fossil fuel is burned, several pollutants are released, including NO_x. Therefore, the studies here presented can be used for applications other than diesel engines.

Due to the difficulties of the current NO_x treatment technologies to obtain high removal efficiencies under real-world driving conditions, the use of Non-Thermal Plasma (NTP) has been proposed as an alternative NO_x treatment technology. Two main reasons sustain the use of NTP. First and most important, is that NTP can destroy pollutants in exhaust emissions at low temperatures, where the traditional technologies struggle the most. Second, the treatment does not produce harmful waste. Nonetheless, the process electrical efficiency of NTP treatment is still very low, so improvements in the electrical aspects and reactor design are required to reach practical power consumption levels and market this technology.

Several reactors can generate NTP; among them, the Dielectric Barrier Discharge (DBD) has been successfully employed for gas treatment applications. DBD reactor offers a stable plasma homogeneously distributed over the electrode area, thanks to the presence of at least one dielectric layer. In short, to produce the electric discharge and generate the plasma, the DBD reactor requires a high-voltage power supply with bipolar current waveforms. These supply conditions can be attained using voltage-mode, or current-mode supplies, according to whether the voltage or current is imposed in the DBD. As will be developed in the following chapters, despite that the power supplies operating in voltage-mode are the most popular solution among DBD systems, the current-mode supplies have some exciting advantages unnoticed by many researchers of the area. Particularly on the investigations of NO_x treatment based on NTP, minor attention has been directed to the current-mode supplies.

Some of the current-mode advantages are: it has direct control of the DBD power due to the capacitive behavior of the DBD reactor. The sizing of the current-mode converters is more straightforward than the voltage-mode since all the electric variables can be determined from the design stage of the converters. Moreover, different authors have reported improvements on other DBD applications, such as the ozonizer and UV excimer lamps, with the current imposition. Based on such advantages, this project intents to address the challenge

of enhancing the performance of the NO_x treatment based on NTP, employing current-mode supplies. The focus of this thesis is then the analysis and design of the current-mode power supplies, and the understanding of the interaction between the electrical conditions and the NO_x treatment.

0.2 Objectives

This thesis aims to broaden the knowledge of NO_x treatment based on DBD from the electrical engineering field. The main objective is to identify the operating conditions of the current-mode power supplies that optimize the NO_x removal, and to study the interactions between this type of power supplies and the DBD reactors. For such purposes, the impact of the NO_x removal in terms of a set of electrical degrees of freedom will be thoroughly studied. In order to reach the main objective, the following specific objectives are proposed:

- To develop a current-mode power supply capable of controlling the reactor power and the operating point through several degrees of freedom, and to analyze the working principle of such power supply considering the parasitic elements of the transformer.
- To automate the control of the power supplies and the monitoring and acquisition system, in order to facilitate a parametric scan of the electrical operating conditions.
- To analyze and identify the conditions that enhance the process in terms of $N0_x$ removal efficiency.

The significance of this thesis work rests in the knowledge it provides about the optimal power supply conditions of DBDs for diesel exhaust treatment. Although the results cannot be generalized to any DBD application, the proposed power supplies analysis and design methods can be used to diagnose other DBD processes. Additionally, the potential of the application to improve the air quality and reduce the health and environmental effects caused by diesel engines is of great importance.

0.3 Methodology

The present document is organized into three major parts. Part I presents the state of the art and provides the background information for the development of this work. It is composed of three chapters. Chapter 1 introduces the emissions of diesel engines and treatment methods. In Chapter 2, the NTP technology is presented, taking special attention to the DBDs reactors. Furthermore, a literature review on the NO_x treatment based on NTP is included. Finally, Chapter 3 presents an overview of the power supplies for DBD.

Part II focuses on the methods and materials employed. Chapter 4 presents the experimentation power supply conceived according to the objectives mentioned above. Chapter 5 shows the experimentation bench and DBD reactor design. It also details the methods used to take the measurements and analyze the treatment results.

Finally, part III shows the treatment results. In Chapter 6, the study of the impact of the electrical parameters on the treatment is presented. The results are compared to the

treatment results of the sinusoidal voltage supply, and with the results found in the literature review. Chapter 7 presents the general conclusions.

Part I

State of the Art

Chapter 1

Diesel Exhaust

Contents

1.1 Introduction

Diesel engines are efficient combustion engines used in countless applications such as power generation, transportation and off-road vehicles. However, due to the presence of PM, NO_x, CO_x, and HC, diesel emissions are considered as one of the larger contributors to environmental pollution, as well as responsible for many health problems. These concerns have led to worldwide regulations with more and more stringent standards, especially about PM and NO_x. Although continuous improvements in the engines and exhaust treatment methods have allowed better performances regarding the pollutant emission, the results are not entirely satisfactory yet, and further research is required.

In this chapter, an introduction to the diesel exhaust is presented, taking special attention to the NO_x emissions, subject of study of this thesis. Section 1.2 presents the diesel engines and reviews the exhaust pollutants, their mechanisms of formation, and their health and environmental impact. Each pollutant is explained individually. Additionally, Section 1.3 shows the regulations and standards, and Section 1.4 presents different exhaust treatment methods, including their working principle, applications, advantages, and limitation.

1.2 Diesel Engines

During the 1890s, Rudolf Diesel invented a high-compression non-sparking internal combustion engine [1]. At the time, the new engine produced an unprecedented efficiency as well as exceptional ruggedness and reliability [2]. However, it was not until decades later that diesel engines were fully developed and commercialized. From thereon, diesel engines have significantly contributed to the development of modern history. For instance, in the shipping industry, more powerful, more efficient, more reliable, and more affordable engines led to the increase of traded raw materials and final goods, accelerating the international trade [2]. Cargo ships, cranes, straddle carriers, trucks, and container-carrying trains are all commonly powered by diesel engines and vital to cargo transportation.

At first, due to their weight, diesel engines were only used for heavy vehicles, heavy equipment, and electricity generators. It was not until the end of the 1930s that Mercedes marketed the first passenger car [1]. Currently, the uses of diesel engines extend to almost all industries since diesel engines efficiency still exceeds the performance of other engines. Whereas spark-ignition engines can obtain up to 33 % efficiency at full load, diesel engines can reach between 40 % and 45 % [3]. Additionally, due to the low fuel consumption, diesel engines produce around 15 % less CO_2 than equivalent gasoline engines [4]. Nevertheless, diesel exhaust contains a far higher amount of NO_x and PM, highly harmful to humans and the environment.

1.2.1 Working principle

The working principle of the diesel engine is typically characterized by a four-stroke cycle (Figure 1.1) [5]. In the first stroke, fresh air is taken (Intake). Then, in the second stroke, the air is highly compressed inside the combustion chamber; in the process, the air heats up to temperatures around 1000 $°C$ (Compression). Near the end of the compression stroke, the fuel is injected into the hot compressed air. Then, the fuel/air mixture is self-ignited and burned (Ignition). Due to the expansion of the gas in the combustion chamber, the piston is pushed, and the thermal energy is converted into mechanical energy. Finally, in the last stroke, the burnt mixture is discharged (Exhaust). The complete combustion of fuels would generate CO_2 and H_2O without any other harmful products [6]. However, the ideal thermodynamic equilibrium cannot be achieved, and incomplete combustion occurs, generating a wide range of organic and inorganic components. In the following section, the exhaust gas composition is explained in depth.

1.2.2 Exhaust Composition

Some of the factors that may cause incomplete combustion in diesel engines, and therefore, cause the formation of pollutants in the exhaust are: the air-fuel ratio, the combustion temperature, the ignition timing, and the homogeneity of the air-fuel mixture [7]. All these factors can be tuned and controlled to obtain cleaner emissions; nonetheless, the combustion will never be perfect, and harmful compounds are always produced.

Table 1.1 summarizes the typical composition of the diesel exhaust. Among the compo-

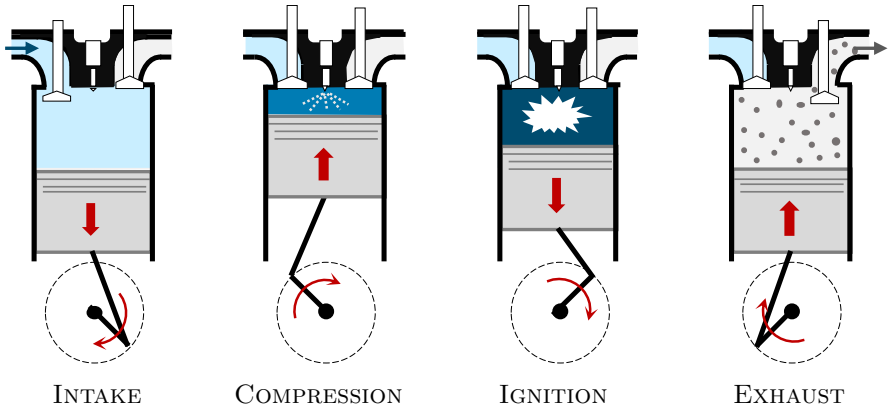

Figure 1.1: Operating Cycle of a four-stroke diesel engine

nents naturally found in the air, the water, oxygen, and nitrogen are unproblematic gases. However, the CO_2 is believed to be the main cause of human-made climate change. The formation of CO_2 depends directly on the fuel consumption of the engine; it means that the higher the hydrocarbons burnt, the higher the CO_2 emission. Given that diesel engines have a better fuel economy, they are well known for producing less CO_2 than gasoline engines. Such an argument has been used to claim that diesel vehicles are more climate-friendly than conventional gasoline vehicles [8], and to encourage a shift from gasoline to diesel vehicles. However, other $non - CO_2$ components, such as PM and NO_x, also play an important role in the climate response [9].

	Component	Concentration
Components naturally found in air	N_2	70 - 75 vol%
	O_2	5 - 15 vol%
	CO_2	2 - 12 vol%
	H_2O	2 - 10 vol%
Regulated harmful Components	CO	100 - 10000 ppm
	HC	50 - 500 ppm
	NO_x	30 - 1000 ppm
	SO_x	Proportional to fuel S content
	PM	20 - 200 mg/m3
Unregulated harmful Components	Ammonia	2 mg/mile
	Cyanide	1 mg/mile
	Benzene	6 mg/mile
	Toluene	2 mg/mile
	PAH	0.3 mg/mile

Table 1.1: Typical diesel exhaust composition [10]

Besides of the effects of diesel exhaust in global warming, many studies concerning the health effects of diesel emissions have been conducted. The presence of PM, HC, NO_x, and CO in diesel exhaust have shown to cause lung damage and many respiratory problems [11–13]. Additionally, there is strong evidence that suggests that diesel emissions can cause lung cancer [14]. Accordingly, in 2012, diesel exhaust was classified as carcinogenic to humans by

the International Agency for Research on Cancer [15]. Furthermore, the pollutants emitted by diesel engines contribute to air pollution, water contamination, and visibility reduction [6].

The effects and characteristics of each emission are outlined below. This description can be used to have a better understanding of the diesel emissions, and to analyze possible by-products of the diesel exhaust treatments.

1.2.2.1 Carbon Monoxide (CO)

The formation of CO is caused by the incomplete oxidation of the fuel carbon atoms [16]. The lack of oxygen in the air/fuel mixture or low combustion temperatures can prevent the conversion of carbon atoms into CO_2, generating CO in the process. CO is a tasteless, odorless, colorless, and non-irritating gas. When inhaled, CO is transmitted into the bloodstream and is bound to hemoglobin. This inhibits oxygen transportation, leading to suffocation, intoxication, slow reflexes, and confusion [7]. CO can be lethal at concentrations over 0.3 $vol\%$, for more than 30 minutes [17].

1.2.2.2 Hydrocarbons (HC)

HC are formed by unburned fuels, as a result of low temperatures, especially near the combustion chamber walls [7]. HC can be emitted as gaseous compounds and as condensed compounds adsorbed on soot particles. There are several species of HC, such as alkanes, alkenes, and aromatics. The toxicity and effects of each specie are different [18]. For instance, the Polynuclear Aromatic Hydrocarbon (PAH) is one of the hydrocarbons forms with severe health effects. PAHs are considered to be carcinogenic and linked to respiratory and cardiovascular diseases [13]. In diesel engines, the fuel is burned almost completely; therefore, the HC and CO emissions are very low in comparison with gasoline engines. However, some exhaust treatment methods, as Exhaust Gas Recirculation (explained in section 1.4.3.1), can increase the HC emissions, leading to the need for after-treatment techniques.

1.2.2.3 Sulfur Oxides (SOx)

The SO_2 is an irritating gas, associated with respiratory and cardiovascular diseases. Furthermore, since the SO_2 transforms into sulfuric acid in contact with water, it is one of the responsible for the acid rain phenomenon. As can be seen in Table 1.1, diesel emissions have an amount of SO_x that depends on the fuel and lubricating oils S content. The SO_x emissions can be easily reduced by high-quality fuels with low S concentrations. Thus, after-treatment techniques are not usually necessary to control the SO_x emissions, and new standards for the fuel levels of S are incorporated worldwide. For instance, in maritime transportation, the maximum content of sulfur in fuel was recently reduced from 3.5 % to 0.5 % [19], which is still high in comparison to the standards of trucks and passenger cars (0.001 %) but have a substantial impact in SOx emissions.

1.2.2.4 Particulate Matter (PM)

PM refers to solid and liquid particles dispersed into the exhaust gases. The diesel PM is mainly composed of carbon, organic compounds, inorganic compounds (*e.g.*, ash), and sulfured compounds [6]. Generally, PM can be categorized according to the particle size, mass, solubility, toxicity, and composition. The categorization, according to particle size, is the most common. By convention, PM_{10} are the particles with diameters less than 10 μm, $PM_{2.5}$ are the fine particles with diameters less than 2.5 μm, and PM_1 are the ultra-fine particles with diameters of 1 μm or less.

By convention, PM_{10} are the particles with diameters between 10 μm and 2.5 μm, $PM_{2.5}$ are the fine particles with diameters between 2.5 μm and 1 μm, and PM_1 are the ultra-fine particles with diameters of 1 μm or less.

The health effects of the PM depend on the toxicity of the particle as well as size. Recent studies have shown that the smaller the particles, the more penetration they achieve in the respiratory system, causing respiratory hazard problems [13, 20]. Additionally, while PM_{10} is rapidly sedimented from the atmosphere, the fine and ultrafine particles ($PM_{2.5}$ - PM_1) remain in the atmosphere for days. Accordingly, PM is considered as a major issue of diesel engines, especially since diesel engines produce between 6 and 10 times more PM than gasoline engines [7].

1.2.2.5 Nitrogen Oxides (NOx)

Nitrogen oxides, NO_x, comprise several gases composed of nitrogen and oxygen. The nitric oxide, NO, and nitrogen dioxide, NO_2, are the most abundant NO_x gases in diesel exhaust. Although the NO and NO_2 are usually treated together, their characteristics are very different. On the one hand, NO is a colorless and odorless gas that represents around 95 % of the NO_x emissions. On the other hand, NO_2 has a reddish-brown color, a pungent odor, and even though it represents less than 5 % of the total NO_x, the NO_2 is more toxic than the NO. Other NO_x forms, such as N_2O, N_2O_5, and N_2O_3, can be found in the diesel exhaust in negligible concentrations; but, some after-treatment techniques might produce them. Among those gases, the nitrous oxide, N_2O, has recently gained much attention due to its global warming potential [18].

The formation of NO_x in diesel engines is mostly explained by a thermal mechanism (Zeldovich mechanism), that only occurs at temperatures above 1000 $°C$. According to Zeldovich, due to the high temperatures reached in the combustion chamber, the oxygen and nitrogen react to generate NO. The NO is the first NO_x product, then, oxidation at lower temperatures forms NO_2. The conversion of NO into NO_2 continues after the exhaust gas is released into the air.

The health and environmental issues related to NO_x are some of the biggest concerns for diesel emissions. Both, NO and NO_2, are irritant gases that, as well as the CO, penetrate the airways and bound to hemoglobin, causing asphyxia and lung irritation, even at low concentrations. At temperatures above 21 $°C$, the NO and NO_2 react with O_2 in the presence of sunlight, generating ozone, O_3, another toxic and harmful gas [21]. The ozone is a very

reactive form of the oxygen that protects the earth from the ultraviolet rays. However, ground-level ozone contributes to global warming and has significant effects on human health. Moreover, the NO_x, together with the SO_2, are the main precursors of the acid rain formation, affecting bodies of water, soils, and ecosystems. Some other consequences of NO_x are the greenhouse effect, smog formation, and pollutant haze.

1.3 NOx Sources and Regulations

Figure 1.2 shows the primary sources of NO_x emission. As reported by the European Environment Agency (EEA) [22], the largest source of NO_x in the EU is the road transport, which includes light-duty vehicles (passenger cars), and heavy-duty vehicles (tractors, trucks, and buses). Therefore, since more than half of the vehicles fleet in Europe is diesel-powered, the excess of NO_x in the atmosphere has been attributed to diesel vehicles. It is important to highlight that although the vehicle fleet is mostly composed of passenger cars, the emissions contribution of heavy-duty vehicles is much higher. Additionally, diesel engines are the power source of heavy-duty vehicles and non-road vehicles (such as cranes, backhoes, bulldozers, and mining equipment), the latter, non-road vehicles, with a contribution of 8 % to the total NO_x emission.

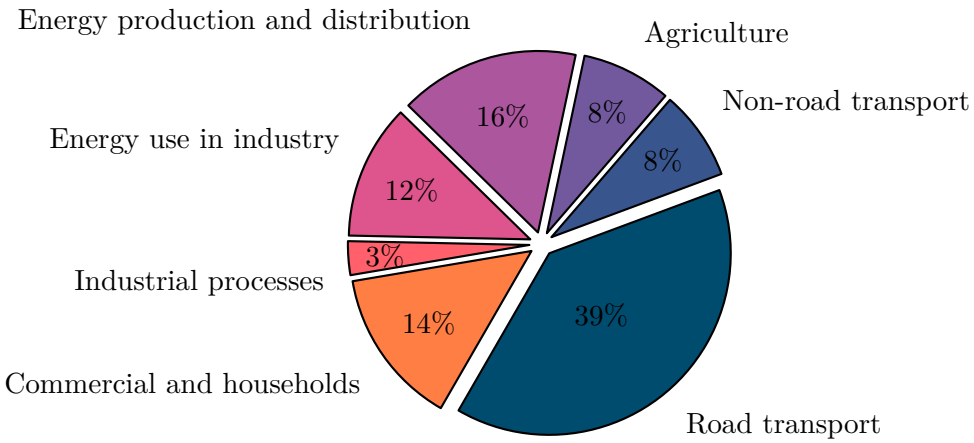

Figure 1.2: NO_x amount in the atmosphere emitted by source in EU. [22]

To control the emission of pollutants and to prevent the damage of the environment and human health, governments have implemented stringent standards for diesel engines. Different standards apply for light-duty vehicles, heavy-duty vehicles, non-road engines, locomotives, marine engines, and stationary engines. Figure 1.3 presents the European standards (Euro) of heavy and light-duty vehicles for NO_x emissions. These standards are used by many countries outside Europe and follow the trends of regulations in the United States (EPA and Tier). As shown in Figure 1.3, the regulatory development of NO_x in Europe has been gradually tightening. From Euro V to Euro VI, a reduction of of 80% in the NO_x limits was introduced. In the same way, PM, HC, and CO regulations have toughened.

The evolution of the emission standards has forced the vehicle manufacturers and researchers to work on the emissions treatment. Currently, the NO_x reduction is one of the

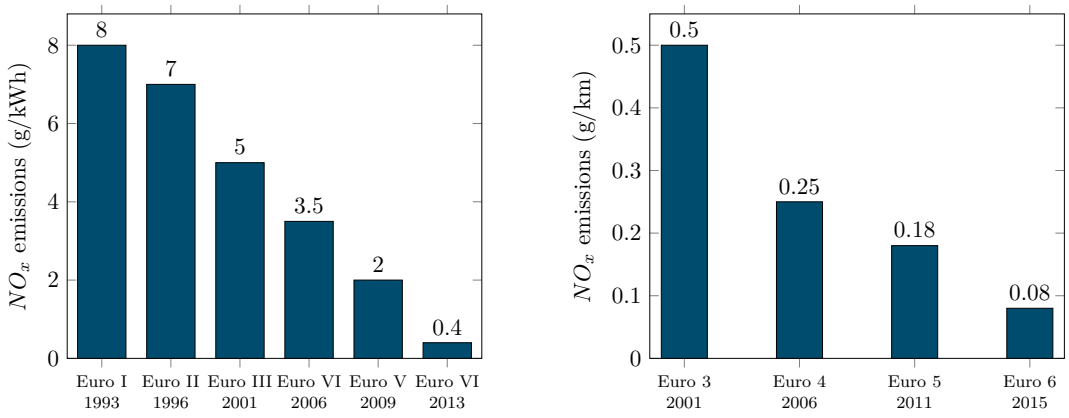

(a) Heavy-duty vehicles (b) Ligth-duty vehicles

Figure 1.3: Euro standards of NO_x emission

most urgent challenges for the transportation sector. After the Volkswagen scandal was revealed in 2015, the differences between the vehicles emission certifications and the real on-road NO_x emissions, have been exposed [8]. Real-world driving conditions produce an excess of NO_x that is not detected during laboratory testings. Consequently, significant improvements in the emissions control techniques, as well as changes in the certification protocols are required, especially at the most challenging driving conditions (low exhaust temperatures).

1.4 Treatment methods

Exhaust treatment methods can be classified into two types: internal engine modifications and after-treatment methods. The fuel injection, air management, supercharged engines, fuel additives, and exhaust gas recirculation, are some of the possible engine modifications that improve the pollutant emissions. However, it is impossible to fulfill the current regulations using only engine modifications, and the use of after-treatment methods is mandatory. The after-treatment technologies can be used to control the majority of diesel engine emissions. Usually, engine modifications and several treatment methods are used together in order to create a fully integrated system. In this section, a description of the most common technologies is presented, paying particular attention to the NO_x control techniques.

1.4.1 Treatment of CO and HC

The Diesel oxidation catalysts (DOC) is a passive device, installed on the exhaust flow that converts unburned hydrocarbons (HC) and carbon monoxide (CO) into carbon dioxide (CO_2) and water vapor [23]. DOC has a honeycomb structure coated by a catalytic layer of rare metals which react with CO and HC. The DOC requires high-temperature conditions in order to oxidize those compounds; usually, it can be attained with the naturally high temperature of the exhaust. Under optimal conditions, DOC can reduce around 80 - 90 % of HC and CO [23]. Furthermore, as 10-30 % of PM is attributed to HC, DOC can oxidize the compounds condensed on the soot, and reduce the PM mass in about 20 % [6].

1.4.2 Treatment of PM

Diesel Particulate Filters (DPF) are used to remove PM from the exhaust gas. The PM filter contains membranes with small pores, which remove the PM by filtration. Once the filter is saturated, a regeneration process is required to remove the excessive soot. Otherwise, it would block the filter, resulting in a rise of the back-pressure, a fuel penalty, and engine degradation. During the regeneration, the accumulated soot is oxidized into gaseous products at high temperatures; therefore, an additional heating system is usually required. After the soot ignition, only incombustible substances remain in the filter. These substances decline the filter capacity and decrease the lifetime of the filter. According to the literature, conventional particulate filters have filtration efficiency between 85 to 95% of the PM mass [24].

1.4.3 Treatment of NOx

There are several NO_x reduction methods, or $DeNO_x$ methods, some of them are already employed by diesel vehicles, and others are still in a research stage. None of the methods already implemented on diesel engines can eliminate the NO_x emissions in the whole operating conditions of the engine. Thus, the techniques are usually combined. Three of the most common NO_x abatement methods are here presented: Exhaust Gas Recirculation (EGR), Lean NOx Trap (LNP), and Selective Catalytic Reduction (SCR); followed by a table comparing them.

1.4.3.1 Exhaust Gas Recirculation (EGR)

The EGR is a $DeNO_x$ method that falls into the category of internal engine modifications. As was previously presented, the generation of NO_x emissions is strongly related to the high temperature in the combustion chamber. Therefore, to reduce the temperature, the EGR method seeks to decrease the amount of oxygen in the chamber. The working principle of the EGR is fairly simple; basically, a portion of the exhaust gas is cooled down and then added to the fresh combustion air. Since the exhaust gas contains CO_2 and water vapor, the oxygen in the combustion chamber is decreased. Unfortunately, some side effects of the lack of oxygen are the decrease of the engine efficiency, and the increase of PM, since the soot oxidation becomes harder to get. Despite of its disadvantages, EGR can obtain an NO_x reduction of up to 50 % [25].

1.4.3.2 Lean NOx Trap (LNT)

LNT is another NO_x abatement technology. The working principle of LNP is based on three operating phases: First, NO is oxidized into NO_2 by a catalyst. Then, the NO_2 is adsorbed and captured by some specific materials. And finally, when the maximum storage capacity of the LNP is reached, a reducing agent is injected, and the NO_2 is reduced to N_2. One of the significant problems of LNP is the adsorption of SO_x instead of NO_x in the storage phase. In order to remove the absorbed SO_x, a desulphurization phase is required. Considering the aging effect due to the high desulphurization temperatures, the removal efficiency of LNT is between 60-70%. There is a significant decrease in the efficiency at high exhaust temperatures.

1.4.3.3 Selective Catalytic Reduction (SCR)

The SCR is established as the $DeNO_x$ method for heavy-duty applications [23]. The SCR is used to convert NO_x into N_2, and water, with the aid of a catalyst agent. The ammonia (NH_3) is an excellent catalyst agent towards NOx, but its transportation is very dangerous and not advisable. Therefore, different agents, such as urea, are used. The urea is injected into the exhaust gas and then decomposed to ammonia and CO_2. The produced ammonia is adsorbed by the porous walls of the SCR catalyst, where the NO_x is reduced. The removal efficiency of the SCR is very sensitive to temperature changes. The effective temperature window is from 200 $°C$ to 450 $°C$. Outside this range, the urea is not completely activated, and the efficiency is affected. If the required conditions are satisfied, the NO_x removal efficiency can achieve 95%. Besides the thermal limitations, the SCR has some problems, such as the possibility of ammonia leakage, catalyst poisoning, and the need for urea tanks.

Table 1.2 summarizes the three $DeNO_x$ technologies previously exposed. In brief, their strongest disadvantages are the sensitivity of the $DeNO_x$ efficiency toward the exhaust temperature or engine load, the need for additional reducing agents, and their respective tanks. Due to these disadvantages, the need for new treatment methods has been highlighted.

1.4.3.4 Non-thermal Plasma (NTP)

Non-thermal plasma (NTP) has become a rising technology for the emissions control since it induces the formation of free radicals, molecular dissociation, and different reactions capable of destroying pollutants in the exhaust gas at low temperatures. Effective removal of pollutants such as NO_x, SO_2, CO_2, HC, and PM have been reported [26, 27], and different NTP treatment methods and reactors have been proposed. Concerning the $DeNO_x$ methods, some authors have used NTP as an intermediate step to perform the oxidation of NO to NO_2, and employ a catalyst afterward for the NO_2 removal [28]. Other authors propose to use the NTP to produce ozone and then inject it into the exhaust gas, as an indirect NTP treatment [29]; And the direct plasma treatment has been proposed as well [26]. The following chapter presents in detail the state of the art of NTP and NO_x treatment based on it.

	Exhaust Gas Recirculation (EGR)	Lean NO_x Trap (LNP)	Selective Catalytic Reduction (SCR)
Working Principle	It recirculates a fraction of exhaust gas into the combustion chamber to decrease the combustion temperature.	The NO_x is absorbed in a catalyst. Once the it is saturated, the NO_x is released and converted into nitrogen.	Through the use of ammonia or urea as a catalyst agent, the SCR reduces NO_x to nitrogen and water.
Advantages	Simple engine modification. No additional reducing agent nor reducing tank is required.	Good efficiency at low loads (60-70 %). No need for reducing agent.	Very high efficiency (up to 95 %).
Disadvantages	Lower efficiency at high loads. Trade-off between NO_x reduction, the PM formation and the engine efficiency. Real-world driving conditions increase the NO_x emissions.	Limited NO_x storage. Storage depends on the LNP size. Big engines require more frequent regeneration processes. SO_x adsorbed instead of NO_x. Expensive costs of the needed noble metals.	Require additional urea tank and heating system. Lower NO_x removal at low loads. NO_x removal efficiency sensitive to the exhaust temperature.
Applications	Widespread applications. It is usually used together with other NO_x techniques.	Mostly used in light-duty applications.	Light and heavy-duty applications. LNT can be used together to improve the efficiency at low loads.

Table 1.2: Comparison of the main technologies for the NO_x abatement

1.5 Conclusions

Due to the harmful effects of diesel emissions, the need for better treatment methods has been stated in this chapter. Different emissions control techniques were here explained, and although the research is advancing rapidly in the subject, and the industry is adapting to the new regulations, better removal performances are still required. For the NO_x emissions control, after-treatments have to be improved to work under real-world driving conditions, and in the whole temperature range of the exhaust gas. As an alternative to the traditional NO_x treatment methods, the NTP technology was introduced.

Bibliography

[1] K.-H. Dietsche, "History of the diesel engine," in *Fundamentals of Automotive and Engine Technology*. Wiesbaden: Springer Fachmedien Wiesbaden, 2014, pp. 8–17. doi: https://doi.org/10.1007/978-3-658-03972-1_2

[2] V. Smil, "The two prime movers of globalization: History and impact of diesel engines and gas turbines," *Journal of Global History*, vol. 2, no. 3, pp. 373–394, 2007. doi: https://doi.org/10.1017/S1740022807002331

[3] R. Frank, "Diesel-powered cars electronic systems Similarities and Differences," *Auto Electronics Magazine*, no. April 2006, pp. 12–18, 2006.

[4] R. Backhaus, "We Still Need Diesel Engines," *MTZ worldwide*, vol. 80, no. 3, pp. 6–7, 2019. doi: https://doi.org/10.1007/s38313-019-0008-1

[5] H. Grieshaber and T. Raatz, "Basic principles of the diesel engine," in *Fundamentals of Automotive and Engine Technology*. Wiesbaden: Springer Fachmedien Wiesbaden, 2014, pp. 22–39. doi: https://doi.org/10.1007/978-3-658-03972-1_4

[6] R. Prasad and V. R. Bella, "A review on diesel soot emission, its effect and control," *Bulletin of Chemical Reaction Engineering and Catalysis*, vol. 5, no. 2, pp. 69–86, 2010. doi: https://doi.org/10.9767/bcrec.5.2.794.69-86

[7] I. A. Resitoglu, K. Altinisik, and A. Keskin, "The pollutant emissions from diesel-engine vehicles and exhaust aftertreatment systems," *Clean Technologies and Environmental Policy*, vol. 17, no. 1, pp. 15–27, 1 2015. doi: https://doi.org/10.1007/s10098-014-0793-9

[8] K. Tanaka, M. T. Lund, B. Aamaas, and T. Berntsen, "Climate effects of non-compliant Volkswagen diesel cars," *Environmental Research Letters*, vol. 13, no. 4, p. 044020, 4 2018. doi: https://doi.org/10.1088/1748-9326/aab18c

[9] K. Tanaka, T. Berntsen, J. S. Fuglestvedt, and K. Rypdal, "Climate Effects of Emission Standards: The Case for Gasoline and Diesel Cars," *Environmental Science & Technology*, vol. 46, no. 9, pp. 5205–5213, 5 2012. doi: https://doi.org/10.1021/es204190w

[10] S. J. Jelles, "Development of catalytic systems for diesel particulate oxidation." Ph.D. dissertation, Delft University of Technology, 1999.

[11] J. Lelieveld, J. S. Evans, M. Fnais, D. Giannadaki, and A. Pozzer, "The contribution of outdoor air pollution sources to premature mortality on a global scale," *Nature*, vol. 525, no. 7569, pp. 367–371, 9 2015. doi: https://doi.org/10.1038/nature15371

[12] N. M. Liu and J. Grigg, "Diesel, children and respiratory disease," *BMJ Paediatrics Open*, vol. 2, no. 1, 2018. doi: https://doi.org/10.1136/bmjpo-2017-000210

[13] D. Diaz-Sanchez, "The role of diesel exhaust particles and their associated polyaromatic hydrocarbons in the induction of allergic airway disease," *Allergy*, vol. 52, no. 3, pp. 52–56, 10 1997. doi: https://doi.org/10.1111/j.1398-9995.1997.tb04871.x

[14] D. T. Silverman, "Diesel Exhaust and Lung Cancer—Aftermath of Becoming an IARC Group 1 Carcinogen," *American Journal of Epidemiology*, vol. 187, no. 6, pp. 1149–1152, 6 2018. doi: https://doi.org/10.1093/aje/kwy036

[15] International Agency for Research on Cancer, *Diesel and Gasoline Engine Exhausts and Some Nitroarenes. Iarc Monographs on the Evaluation of Carcinogenic Risks To Humans*, 2014, vol. 105. [Online]. Available: https://www.ncbi.nlm.nih.gov/books/NBK294269/

[16] C. W. Wu, R. H. Chen, J. Y. Pu, and T. H. Lin, "The influence of air-fuel ratio on engine performance and pollutant emission of an SI engine using ethanol-gasoline-blended fuels," *Atmospheric Environment*, vol. 38, no. 40 SPEC.ISS., pp. 7093–7100, 2004. doi: https://doi.org/10.1016/j.atmosenv.2004.01.058

[17] K.-H. Reif, Konrad ; Dietsche, *Automotive handbook*, 9th ed. Robert Bosch GmbH, 2014.

[18] H. Yamada, K. Misawa, D. Suzuki, K. Tanaka, J. Matsumoto, M. Fujii, and K. Tanaka, "Detailed analysis of diesel vehicle exhaust emissions: Nitrogen oxides, hydrocarbons and particulate size distributions," *Proceedings of the Combustion Institute*, vol. 33, no. 2, pp. 2895–2902, 1 2011. doi: https://doi.org/10.1016/j.proci.2010.07.001

[19] European Comission, "Cleaner Air for All - Environment." [Online]. Available: https://ec.europa.eu/environment/air/cleaner_air/

[20] D. Brown, M. Wilson, W. MacNee, V. Stone, and K. Donaldson, "Size-Dependent Proinflammatory Effects of Ultrafine Polystyrene Particles: A Role for Surface Area and Oxidative Stress in the Enhanced Activity of Ultrafines," *Toxicology and Applied Pharmacology*, vol. 175, no. 3, pp. 191–199, 9 2001. doi: https://doi.org/10.1006/taap.2001.9240

[21] F. C. Barbosa, "Heavy Duty Emission Standards Assessment - An Engine and Aftertreatment Technological Approach," in *SAE Technical Papers*, vol. Part F1270, no. October, 10 2016. doi: https://doi.org/10.4271/2016-36-0167

[22] EEA, "European Union emission inventory report 1990-2017," Tech. Rep. 6, 2019. [Online]. Available: https://www.eea.europa.eu/publications/european-union-emission-inventory-report-1

[23] Z. Liu, "Overview of heavy-duty diesel engines," in *Advanced Direct Injection Combustion Engine Technologies and Development*. Elsevier, 2010, pp. 269–288. doi: https://doi.org/10.1533/9781845697457.2.269

[24] P. Eastwood, "Exhaust gas aftertreatment for light-duty diesel engines," in *Advanced Direct Injection Combustion Engine Technologies and Development*. Elsevier, 2010, pp. 562–594. doi: https://doi.org/10.1533/9781845697457.3.562

[25] I. Aslan Resitoglu, "NO x Pollutants from Diesel Vehicles and Trends in the Control Technologies," in *Diesel and Gasoline Engines*. IntechOpen, 2 2018, vol. i, p. 13. doi: https://doi.org/10.5772/intechopen.81112

[26] P. Talebizadeh, M. Babaie, R. Brown, H. Rahimzadeh, Z. Ristovski, and M. Arai, "The role of non-thermal plasma technique in NOx treatment: A review," *Renewable and Sustainable Energy Reviews*, vol. 40, no. x, pp. 886–901, 12 2014. doi: https://doi.org/10.1016/j.rser.2014.07.194

[27] C.-L. Song, F. Bin, Z.-M. Tao, F.-C. Li, and Q.-F. Huang, "Simultaneous removals of NOx, HC and PM from diesel exhaust emissions by dielectric barrier discharges," *Journal of Hazardous Materials*, vol. 166, no. 1, pp. 523–530, 7 2009. doi: https://doi.org/10.1016/j.jhazmat.2008.11.068

[28] M. Apeksha and B. S. Rajanikanth, "Plasma/adsorbent system for NOx treatment in diesel exhaust: a case study on solid industrial wastes," *International Journal of Environmental Science and Technology*, vol. 16, no. 7, pp. 2973–2988, 7 2019. doi: https://doi.org/10.1007/s13762-018-1776-x

[29] H.-J. Kim, B. Han, C. G. Woo, and Y.-J. Kim, "NOx Removal Performance of a Wet Reduction Scrubber Combined With Oxidation by an Indirect DBD Plasma for Semiconductor Manufacturing Industries," *IEEE Transactions on Industry Applications*, vol. 54, no. 6, pp. 6401–6407, 11 2018. doi: https://doi.org/10.1109/TIA.2018.2853113

Chapter 2

NOx Treatment based on Non-Thermal Plasma

Contents

2.1 Introduction

In the preceding chapter, the impact of the NO_x emissions and different exhaust treatment technologies were presented. Although the described $DeNO_x$ technologies can satisfy the current regulations, several limitations and difficulties were exposed. Due to those limitations, and particularly to the fact that the exhaust gas temperature and real-driving conditions affect the $DeNO_x$ treatments efficiency, the necessity for more suitable solutions was stated.

This chapter introduces general aspects of the NTP, a technology that has been proposed as an alternative $DeNO_x$ solution. In order to generate NTP, gases are submitted to electric discharges; thus, Section 2.2 provides an overview of the gases breakdown and electric discharge regimes. Then, a review of the NTP reactors (Section 2.3), typical configurations, and applications is presented. Finally, Section 2.4 summarizes the literature review of the NO_x treatment based on NTP.

2.2 Plasma Technology

Plasma, also known as the fourth state of matter, is an ionized gas composed of ions, electrons, radicals, photons, atoms, and molecules. It is estimated that plasma constitutes 99% of the universe matter. Some examples of natural plasmas are the earth's ionosphere, the sun, lightning, polar auroras, and the interior of the stars. Plasma can also be artificially generated in laboratories or for industrial applications. In order to do so, neutral gases can be energized by employing thermal energy, the injection of charged particles, or applying an external electric or magnetic field. Fluorescent lamps and plasma displays are some common artificial plasma examples.

Plasma can be classified as thermal or non thermal plasmas (NTP), depending on the average kinetic energy of the particles, referred to as temperature [1]. In thermal plasma, the gas is strongly ionized, and all plasma species (ions, electrons, and neutrals) are in thermal equilibrium, which means that the temperature of charged and uncharged particles is similar. Due to the high temperature of thermal plasmas, they are used in processes such as welding, plasma cutting, and treatment of waste materials [2]. However, there are many applications where the high temperature is not desired and even prohibited. In contrast, in NTP, the gas is weakly ionized, and the temperature of the electrons is much higher than the rest of the species. Therefore, the ions and neutrals remain almost at room temperature, and consequently, it is possible to employ NTP for low-temperature applications. Some typical applications that benefit from NTP are the processing of gases (including diesel exhaust) [3, 4], ozone generation [5], surface treatment [6], film deposition [7], photo-chemistry [8], light and UV production [9, 10], and in biology and medicine [11, 12].

Several chemical reactions are constantly occurring in plasma. Most of them are the result of collisions between the electrons and heavy species (ions, neutrals, and radicals). The collisions can be either elastic or inelastic. In the case of elastic collisions, the total kinetic energy remains the same, and the particles maintain their structure. On the contrary, in inelastic collisions, the kinetic energy is not conserved, and the energy difference can cause particles excitation, ionization, dissociation, among others. In addition to the reactions caused by electrons, there are also reactions caused by energetic photons and collisions between heavy species. The plasma chemistry is very complex and involves several processes that are not a matter of study in this thesis. Consequently, it is not going to be examined in depth. Table 2.1 lists some elementary NTP reactions in order to have later a better understanding of the NO_x reduction mechanisms.

2.2.1 Electric Breakdown

NTP is usually produced by submitting the gases to an external electric field. In this way, free electrons are accelerated, gaining enough energy to ionize the neutral molecules and atoms in a chain reaction. Under normal conditions, without any external field, gases have a dielectric behavior; it means that they do not carry charges. However, the generation of electrons in a chain reaction can turn into an electron avalanche; as a result, the gas loses its insulating properties and starts carrying charges.

In the 1900s, John Townsend proposed the classic Townsend theory for electric break-

Name	Reaction	Description
Excitation	$e + A_2 \rightarrow A_2^* + e$	Electron collision produces molecules and atoms electronically excited.
Ionization	$e + A_2 \rightarrow A_2^+ + 2e$	Neutral species are converted into electrically charged particles.
Dissociation	$e + AB \rightarrow A + B + e$	Electrons impacts cause molecules dissociation.
Dissociative ionization	$e + AB \rightarrow A^+ + B$ + 2e	Ions produced by dissociation of molecules.
Dissociative attachment	$e + A_2 \rightarrow A^- + A$	Ions produced when free electrons attach to neutral species.
De-excitation	$e + A_2^* \rightarrow A_2 + e + hv$	Returning to ground state, excited species emit their energy as a photon.
Penning ionization and dissociation	$M^* + A_2 \rightarrow A_2^+ + M + e$ $M^* + A_2 \rightarrow 2A + M$	Metastable species transfer their energy and ionize or dissociate species.
Recombination of : Ions or Electron - Ions	$A^- + B^+ \rightarrow AB$ $e + A^+ + B^+ \rightarrow AB$	Ions and electrons collide to recombine as a molecule.

Table 2.1: Elementary NTP reactions. A and B represent atoms and M represents a metastable specie [1]

downs. This theory describes the flow of charges in a gas submitted to a static and uniform electric field, a good starting point for understanding electric discharges. In an early stage of his research, Townsend studied the electron avalanches. According to his theory [13], there are three processes involved in the generation of charged particles. The first process is the electrons ionization. Electrons, accelerated by the electric field, move toward the anode and collide with neutral gas particles, generating a large number of electrons and positive ions. The second process is the positive ions ionization. In this case, positive ions moving toward the cathode collide with the gas particles and generate electrons and positive ions. And the third process is the electrode surface ionization. When charged particles strike the electrodes, secondary electrons are emitted. Each of those processes is related to a Townsend coefficient (α, β, γ), which have to be experimentally determined. Equation 2.1 presents the gas breakdown current, I_{br}, as a function of the distance between electrodes, d. In this formula, the second Townsend coefficient, β, is not taken into account since the ionization caused by the ions is considered neglected, in comparison to the electrons and electrodes ionization.

$$I_{br} = I_0 \left(\frac{e^{\alpha d}}{1 - \gamma(e^{\alpha d} - 1)} \right) \tag{2.1}$$

where: I_0 is the initial current, α and γ are the Townsend coefficients, and d is the gas gap.

From this theory, it is possible to deduce the limit voltage between an electron avalanche and a self-sustained discharge, also known as the breakdown voltage. However, regardless of the theoretical value of Townsend theory, scientists and researchers usually rely on Paschen's law to determine the breakdown voltage.

The Paschen's law, empirically discovered by Friedric Paschen in 1889, describes the breakdown voltage, V_{br}, as a function of the product pd_{gap}, where p is the gas pressure, and d_{gap} is the distance between the electrodes. In Paschen's formula (Equation 2.2), γ is the third Townsend coefficient, and A and B are constants specific to each gas. Based on this equation, Paschen curves are available for several gases at constant temperatures. Those curves can be used to estimate the breakdown voltage of the reactors employed in this work. Nevertheless, it is important to mention that Townsend theory and Paschen's law are not accurate at high pressures and long gaps, as well as in the case of nonuniform electric fields. In those cases, more complex theories and approaches have been proposed, such as the streamers theory [14].

$$V_{br} = \frac{Bpd_{gap}}{\ln\left(\frac{Apd_{gap}}{\ln(1+1/\gamma)}\right)} \tag{2.2}$$

2.2.2 Low pressure Discharge Regimens

Figure 2.1 shows the typical current-voltage characteristics of low pressure discharges. This curve is obtained by applying a DC voltage across two parallel electrodes, which are separated by a gas gap. Different discharge modes can be distinguished based on the applied voltage: dark discharge, glow discharge, and arc discharge. Dashed lines represent the transitions between discharge modes. Additionally, as can be seen in Figure 2.1, each discharge mode has different regimes explained bellow [15, 16].

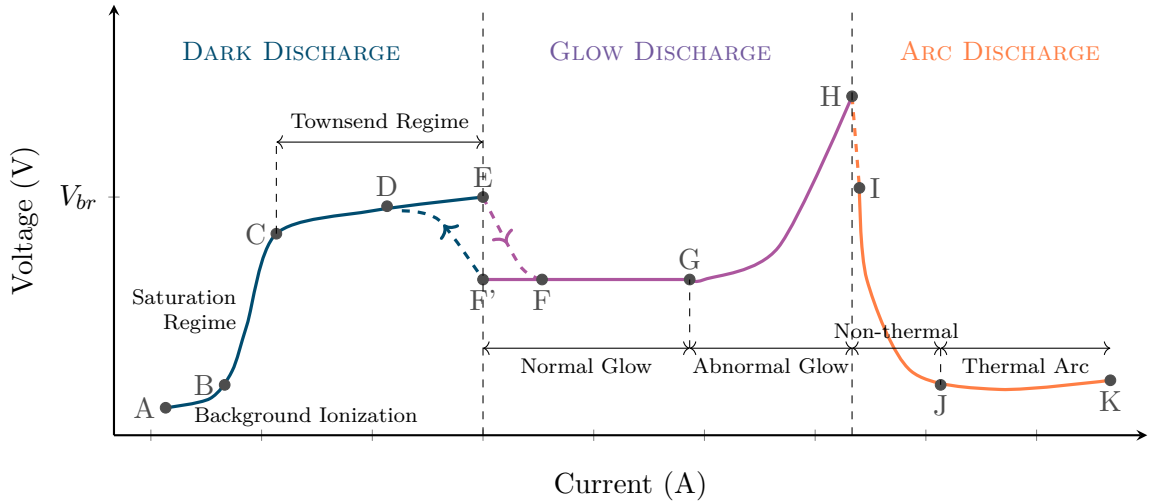

Figure 2.1: Typical current-voltage characteristics of a low pressure electric discharge.

2.2.2.1 Dark Discharge

The dark discharge, as its name suggests, is characterized by the absents of a luminous phenomena. The following three regimes can be here identified:

Background Ionization (A-B): Gases usually carry free charges created by the ionization from the background radiation. In the presence of a small electric field, the free electrons flow toward the anode; consequently, a weak current is produced. As the voltage increases, the current increases until the saturation regimen begins.

Saturation Regime (B-C): Once the electric field has accelerated all free electrons, the current is saturated. In this regime, despite the increase of the voltage, the current remains constant. This is caused because the kinetic energy of the electrons is not enough to ionize new neutral particles.

Townsend Regime (C-E): When the kinetic energy of the electrons can ionize neutral particles, the Townsend regime takes place. The mechanisms of ionization of the Townsend regime were already explained in the previous section. Accordingly, in this regime, the current increases exponentially with the voltage, due to the electron avalanche.

2.2.2.2 Glow Discharge

At point E, the electrical breakdown occurs, and a luminous and homogeneous discharge is produced. After this point, the ionization is sufficiently strong to generate a self-sustained discharge (plasma). Due to the large number of electrons generated by the breakdown, the current increases rapidly, whereas the voltage drops and remains constant at a value lower than the breakdown voltage. As mentioned before, the breakdown voltage can be determined by the Townsend theory or Paschen curves. The glow discharge has two regimes explained below.

Normal Glow (F-G): After the electric breakdown, the plasma is produced and it starts to spread over the surface of the electrodes with a constant current density. Therefore, as the current increases, the area of the electrodes covered by plasma increases as well. In this regime, the voltage does not change significantly with the increment of the current. At the point G, the whole area of the electrodes is covered.

Abnormal Glow (G-H): Once the plasma has covered the whole area of the electrodes, the current density has to be increased in order to increase the current. As a consequence, the voltage starts rising to point H.

2.2.2.3 Arc Discharge

In the arc discharge, the current density continues rising and heats the electrodes. Due to electrodes warming, additional electrons are emitted, and the kinetic energy of the particles is increased. According to the plasma temperature, arc discharges can work under a non-thermal or thermal regime.

Non thermal Arc (H-J): The non-thermal arc visually appears as a glow discharge; however, it is characterized by high current densities caused by the thermal ionization.

Thermal Arc (J-K): At the point I, the thermal equilibrium of the plasma is achieved. It means that the temperature of the electrons and heavy species is the same; in this way, thermal plasma is produced. In general, the thermal arc discharge seems more intense than the glow discharge and covers a small area the electrodes.

2.3 NTP Reactors

This section presents a review of several NTP reactors. For each reactor, the working principle and typical configurations are provided. This information will be used in the next section to analyze different $DeNO_x$ methods. As this thesis uses a DBD reactor, special attention will be given to this technology.

2.3.1 Electron Beam

The electron beam, also called e-beam, is an alternative method for producing NTP without an electric discharge. In principle, the e-beam requires a separate generator of electrons high vacuum, which accelerates the electrons using a high electrical potential. Then, the beam of energetic electrons is injected into the gas chamber. The electrons collide with the gas molecules producing their ionization, dissociation, and/or excitation. As the electrons usually contain way much energy than the one required to produce the ionization and other reactions, the energy cost of this method is higher than the electric discharges. Additionally, the e-beam has the inconvenience of requiring an electron generator separated from the plasma chamber.

2.3.2 Corona Discharge

In the previous section, the glow discharge was presented as an NTP regime working at low pressure ($< 10\ mbar$). Nevertheless, since there are not many applications working under such conditions, high-pressure discharges are needed. As the pressure increases, the electric field required to produce the breakdown increases, and the characteristics of the discharge change [17]. At atmospheric pressures ($1\ bar$), the discharge becomes more unstable, and the transition to an arc discharge is much easier. Therefore, in order to stabilize the discharge, non-uniform electric fields are used, usually produced by asymmetrical electrodes geometries, such as pointed electrodes, thin wires, and coaxial geometries [18]. However, even with the non-uniform electric field, the discharge may tend to an electric arc. This type of non-uniform discharge is known as corona discharge. Figure 2.2 shows different geometries of corona reactors.

The corona discharge can be generated using a positive or negative polarity. In the positive corona, the electrons flow from the flat electrode toward the highly curved or sharped electrode. Whereas in the negative corona, electrons flow in the opposite direction. The physics of the discharge change with the polarity, reason why its effects are commonly studied. Furthermore, as corona discharges do not require an insulating layer, they can be supplied

using a DC, AC, or pulsed voltage.

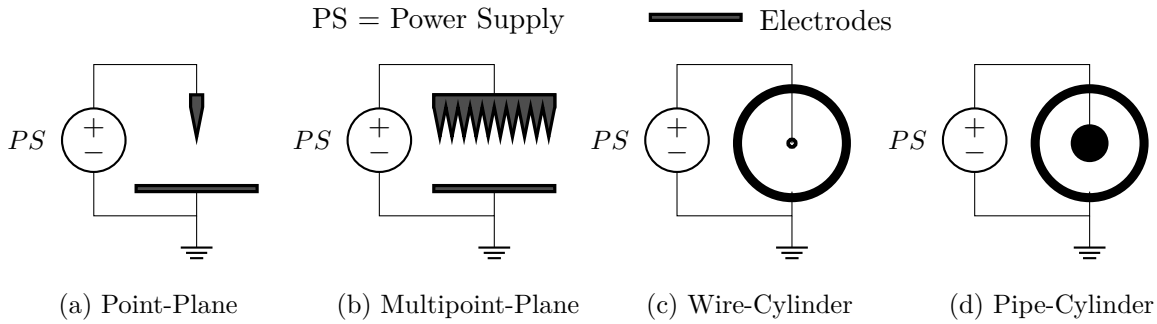

(a) Point-Plane (b) Multipoint-Plane (c) Wire-Cylinder (d) Pipe-Cylinder

Figure 2.2: Different geometries of corona reactors

2.3.3 Dielectric Barrier Discharge (DBD)

DBD is another type of efficient atmospheric NTP source characterized by the presence of at least one dielectric barrier between the electrodes and the gas. This insulating layer limits the current and prohibits the evolution of the discharge to arc regime when the voltage is increased [19]. Figure 2.3 presents typical configurations of DBDs. Compared with the corona reactor, DBD produces a stable discharge, although the voltage required to produce it is higher due to the dielectric barrier. Additionally, since the dielectrics protect the electrodes from corrosive gases, the lifetime of DBD is higher [20]. This advantage is only valid when the dielectric fully covers both electrodes (Figure 2.3 a - d).

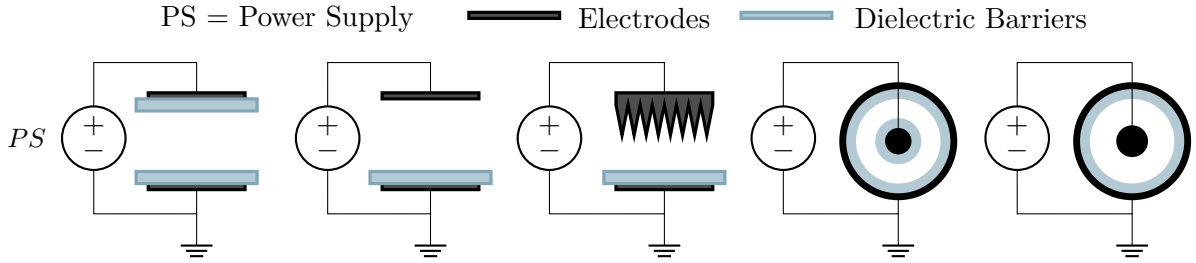

(a) Plane-Plane 2 dielectric [21] (b) Plane-Plane 1 dielectric [22] (c) Multipoint-Plane [23] (d) Coaxial 2 dielectrics [24, 25] (e) Coaxial 1 dielectric [26, 27]

Figure 2.3: Different geometries of DBD reactors

The discharge process in DBD begins similarly to the Townsend theory. The electrons, initially available in the gas, are accelerated due to the applied electric field, gaining enough energy to ionize the neutral gas molecules and produce the electric discharge. However, in the DBD, the electrons cannot pass through the dielectric barrier, so they accumulate on their surface. The accumulation of charges on the dielectric surface forms a local electric field opposite to the field externally applied. In consequence, the total field in the plasma

decreases, causing the self-extinction of the discharge. In order to restart the discharge, the voltage polarity has to be inverted. In this way, the voltage inversion causes a new electron avalanche in the opposite direction, and the whole process starts again. Due to the necessary polarization change, it is impossible to use DC power sources; instead, DBDs are commonly supplied by AC or pulsed voltage sources, guaranteeing an average null current. In the next chapter, the supply conditions of DBD are studied in depth.

DBDs can operate in two modes: filamentary or homogeneous. Experimental conditions such as the reactor geometry, materials, gas mixture, pressure, and electrical supply waveforms influence the discharge mode [28]. At atmospheric pressure, DBD generally operates in filamentary mode. The filamentary discharge consists of channels with a high current density, also called streamers or micro-discharges, distributed over the area of the electrodes. The streamers have a short time duration (tens of ns), their diameter is around 100 μs, and the current density is up to 100 A/cm^2 [19]. Moreover, the number of streamers increases as the DBD current increases.

On the other hand, in the homogeneous discharge, the plasma is uniform and diffuse, similar to the low-pressure glow discharge. Accordingly, the homogeneous discharge operated at atmospheric pressure is called Atmospheric Pressure Glow Discharge (APGD). The conditions that lead to homogeneous discharges have been investigated for several gas compositions and gas volumes, particularly to control the transition to filamentary discharge that tends to disrupt discharge operation [29–32]. Moreover, the homogeneous plasma has proven to improve several DBD processes. For instance, some surface treatments require homogeneous discharges to obtain a uniform treatment and prevent local damage on the treated surface [33]. Contrary to the ozone generation, which benefits from the filamentary mode.

2.3.4 Packed bed DBD

Figure 2.4 shows the typical configuration of a packed bed DBD. As can be seen, the packed bed reactor has the same structure of the DBD reactors, except that the gas gap contains dielectric pellets. Thus, the plasma is generated in the void between pellets.

When an external electric field is applied to the packed bed reactor, the pellets are spontaneously polarized, and the total electric field is enhanced. In particular, an intense electric field is produced near the contact points of the pellets. In consequence, the field enhancement reduces the breakdown voltage over large separation of electrodes. Additionally, pellets can have a catalytic material. In this way, the plasma improves the catalyst selectivity and performance. Such a combination is known as a plasma/catalyst process. Another advantage of packed bed reactors is the increment of the gas residence time, which has proven to be an essential parameter in the gas treatment [34]. However, the pellets wear out over time and generate a high back-pressure, undesired for the gas treatment applications, and particularly bad for the engines.

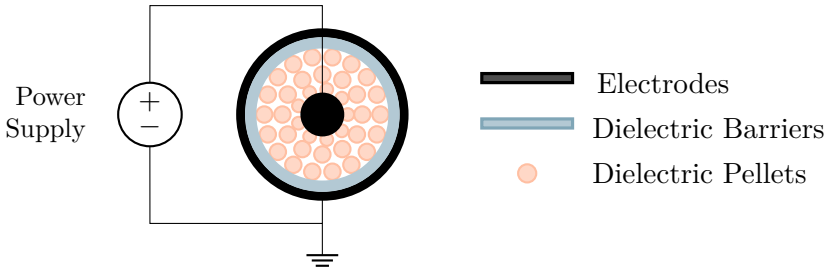

Figure 2.4: Typical Packed bed DBD reactor

2.4 NOx treatment based on Plasma

2.4.1 NOx removal mechanisms

As indicated in the previous chapter, the diesel exhaust is mainly composed by N_2 ($\approx 75\%$) and O_2 ($\approx 15\%$). Considering only those two elements, Figure 2.5 shows the dominant reaction pathways in the NO_x plasma treatment. In this diagram, each curved line represents a reaction, and the circles are the main products. For example, the reactions $NO+N = N_2+O$ is represented by the line connecting the NO and N_2 circles. In this case, reading in the direction of the lines arrows, the reaction's reactants are NO, and N and the product are O and N_2.

The reaction pathways are generally divided into two groups [35, 36]. The first group involves NO reduction reactions (solid blue lines). In these reactions the NO is reduced to form N_2 and O_2. Whereas in the second group, the oxidation reactions produce higher oxides of nitrogen, such as NO_2, NO_3, and N_2O_5 (dashed purple lines).

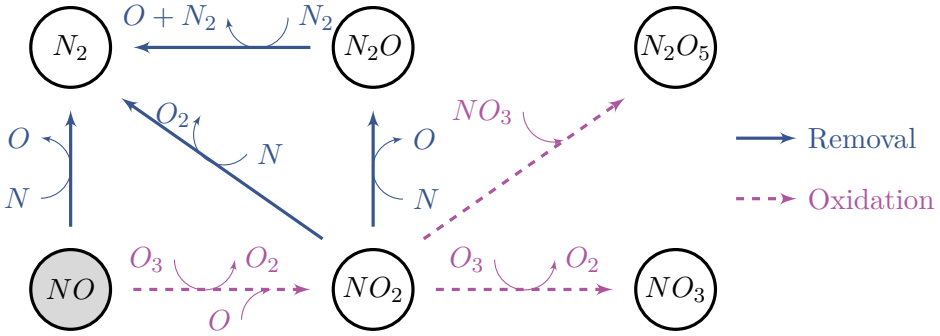

Figure 2.5: $DeNO_x$ dominant reaction pathways

The group of reactions, which dominates the $DeNO_x$ treatment, depends on the gas composition and plasma conditions. Although the reduction pathway is very attractive since its products (N_2 and O_2) can be released directly to the atmosphere, high oxygen concentration inhibits this route. According to [37], O_2 has smaller dissociation and ionization energies than N_2; consequently, the formation of oxygen radicals and O_3 is much easier, and the oxidation pathway is favored. At low O_2 concentrations, high NO removal efficiencies can be obtained as a result of the reduction mechanisms. However, when the O_2 concentration increases, the

oxidation pathway starts dominating the treatment. In this case, a reducing agent can be injected, or the NTP can be used to oxidize NO to NO_2, and then use a catalyst to remove the NO_2. It is worth mentioning that successive oxidation can generate unwanted byproducts of the treatment, and even increase the NO concentration. In consequence, the challenge for the NPT $DeNO_x$ is to control the plasma conditions either to remove the NO or to convert it into NO_2 without producing harmful byproducts, and with a low energy cost.

When other compounds of the diesel exhaust are included in the gas mixture, the reaction pathways change significantly. The HC have shown to increase the oxidation of NO to NO_2, as well as decrease the electric cost of the process [4, 38, 39]. The H_2O reinforces the NO removal, but generates nitric acids [37]. The carbonaceous soot enhances the NO_x removal, since it reacts directly with the produced NO_2 [36]. Whereas the CO_2 has almost no effect in the NO_x treatment [40].

2.4.2 Review on NTP based DeNOx treatment methods

Various approaches have been proposed for the $DeNO_x$ based on NTP. Overall, two treatment methods can be identified. In the first method, called direct plasma, the gas flows through the discharge zone. In this way, the plasma is produced in the gas stream, allowing the NO_x reduction or oxidation. The second method is indirect plasma; this method uses the discharge to produce ozone in an external reactor. Then, the ozonized air is injected into the gas stream, producing the NO oxidation. Either additives, catalysts, or adsorbent can enhance direct or indirect plasma treatment. For the review here presented, we will focus only on the direct plasma treatment. Some interesting results about the indirect plasma $DeNO_x$ can be found in [41–44].

Concerning the NTP reactors for $DeNO_x$, DBDs are usually preferred by the researchers due to the discharge stability and homogeneity [19, 26, 27, 45, 46]. Corona discharges are also commonly used [47–51], and recently, the use of packed-bed reactors with catalyst pellets is gaining importance [52–56]. Different kinds of power sources are employed to supply the NTP reactors. The traditional AC and pulsed voltage sources are the most popular solutions with a typical frequency range between 1 kHz and 100 kHz. The power and voltage ratings depend on the volume of the reactor and gas flow.

Furthermore, different gas conditions can be found in the literature. Some authors use simulated gases with various compounds mixtures and temperatures, which intend to imitate the diesel exhaust composition. This strategy allows the researchers to examine the effect of each parameter in treatment. In contrast, the experiments with diesel engines show the applicability of the treatment under real conditions. The relevant publications of each treatment method are summarized below, showing the experimentation conditions and results. But first, it is necessary to introduce some definitions to be able to analyze and compare those research results.

The NO_x and NO removal are defined as:

$$\eta NO_x = \frac{NO_{xi} - NO_{xf}}{NO_{xi}} * 100 \tag{2.3}$$

$$\eta NO = \frac{NO_i - NO_f}{NO_i} * 100 \tag{2.4}$$

where NO_{xi} is the concentration in ppm of $(NO + NO_2)$ before treatment, and NO_{xf} is the concentration after treatment. In the parameter ηNO, only the NO amount is considered. Note that when the oxidation dominates the reaction pathways, a high ηNO can be achieved, however, as the NO oxidizes into NO_2 the ηNO_x may not follow the same trend. On the contrary, when the reduction dominates the reactions, both ηNO and ηNO_x increase.

The Energy Density (ED) is defined as the relation between the discharge power and the gas flow rate. In the literature, the ED has also been referred to as specific energy, specific energy density or specific input energy. All these terms describe the amount of input energy applied to one liter of gas.

$$ED = \frac{P\ [W] * 60\ [s/min]}{G\ [l/min]}\ [J/l] \tag{2.5}$$

where P is the electric discharge power, and G is the gas flow rate.

Finally, the last parameter is the energy efficiency of the NO removal (NO_E). This parameter measures the energy consumed for the removal of one mole of NO [57]. In the same way, the NO_x removal efficiency can be defined, NO_{xE}.

$$NO_E = \frac{\frac{G\ [l/min]}{22.4\ [l/mole]} * (NO_i - NO_f) * 60\ [min/h] * 10^{-3}}{P\ [W]}\ [mole/kWh] \tag{2.6}$$

$$NO_{xE} = \frac{\frac{G\ [l/min]}{22.4\ [l/mole]} * (NO_{xi} - NO_{xf}) * 60\ [min/h] * 10^{-3}}{P\ [W]}\ [mole/kWh] \tag{2.7}$$

where 22.4 is the volume of one mole of gas ($[l/mole]$).

2.4.2.1 Direct Plasma

Figure 2.6 shows the schematic of different solutions for the direct plasma treatment, which are going to be discussed below.

Only Plasma For the only plasma solution, as its name suggests, just the plasma acts on the NO_x abatement. In this thesis, only the plasma effect will be studied for the NO_x treatment. Therefore, to be able to compare this thesis results with the literature, a detailed review of the publications using only plasma is presented in Table 2.2.

Some of the most simplified experiments use a simulated gas of NO diluted in N_2. In such a way, a reduced number of chemical reactions take place in gas, and it is much easier to determine the NO_x removal mechanisms. In an early stage of the $DeNO_x$ research,

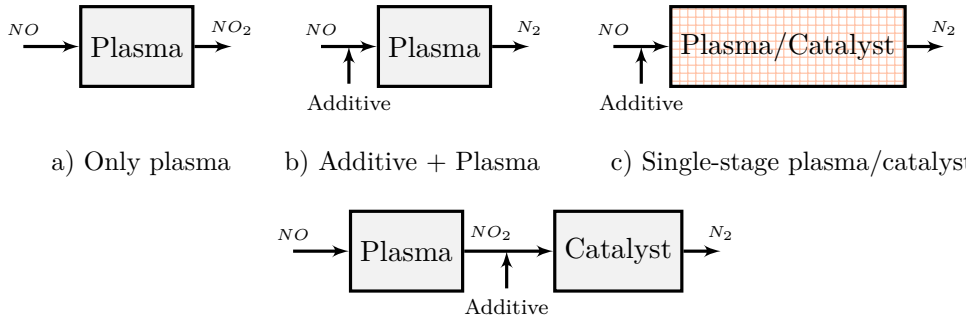

Figure 2.6: Schematic of direct plasma solutions

Penetrante et al. compared the energy consumption of a pulsed corona, a DBD , and a packed bed DBD in a NO/N_2 mixture [50]. According to their results, all the discharges have similar energy consumption as long as the ED and gas conditions are the same. Additionally, McLarnon and Penetrante presented the effect of the DBD reactor design in the $DeNO_x$. The conclusion was that packaging material and electrodes diameter have little influence on the energy consumption [25, 58]. However, more recent publications have shown that the reactor design does have an impact on energy consumption, even in a simple NO/N_2 mixture. Moreover, the power supply conditions have also proven to play an important role in the plasma treatment.

In 2012, Wang et al. carried out a study on the effect of the reactor structure on the NO removal in a NO/N_2 gas mixture [26]. A coaxial DBD supplied by an AC voltage source was employed. The study results showed that smaller discharge gaps produce a lower breakdown voltage and better removal efficiency (ηNO_x). This finding is in agreement with other authors who affirm as well that small gas gaps are preferred for the $DeNOx$ treatment [27, 59]. Furthermore, different electrodes and dielectric materials were compared in [26].

In 2015, Anaghizi et al. examined the use of an inner screw electrode compared with a rod electrode in a coaxial DBD [27]. This comparison was made in a NO/N_2 gas mixture with a pulsed voltage source and showed that the ηNO_x was higher with the screw electrode than with the rod electrode. The reason for this is that the screw electrode generates a large number of micro discharges with a small energy deposition per micro discharge. Moreover, the residence time is higher with the screw electrode. Experiments with screw electrodes were also carried out in [26], resulting in the same conclusion. Later, this group presented an experimental optimization of the reactor and the pulsed power supply for NO_x removal efficiency [59], and the effect of the residence time in the removal efficiency [34].

To have more realistic results of the NO_x treatment, several authors include O_2, H_2O and HC in the simulated gases. In 2004, Arai et al. studied the role of the O_2 on the NO_x removal using a corona discharge [48]. It was shown that in the presence of oxygen, the NO is oxidized into NO_2 and N_2O_5 due to the ozone and O_2 radicals. Other authors have studied the O_2 effect on the NO_x abatement, resulting in similar conclusions [37, 39, 40, 45].

In [45, 60], Vinh et al. included simulated PM into the gas mixture of NO, N_2 and O_2.

Its purpose was to study the effect of the PM on the NO_x removal for a DBD with a needle to cylinder geometry. According to their results, the PM promoted the $DeNO_x$ with and without O_2. This behavior is attributed to the reduction effect of the PM on the NO_2. In such a way, the PM works as an additive agent. Rajanikanth et al. studied as well the effect of the PM [36]. However, they used a diesel engine instead of simulated gases and included a catalyst and absorbent stage. The NO_x removal was also increased by the PM.

In addition to the experiments using simulated gases, some authors have tested the $DeNOx$ treatment using only the plasma effect with real diesel exhaust gases. Song et al. studied the simultaneous removal of NO_x, HC, and PM from a real diesel engine, using a coaxial DBD supplied by an AC voltage source [24]. Several aspects, such as the peak voltage, frequency, and engine load, were considered in the analysis. According to their results, the PM and HC removal increases with the applied voltage. On the contrary, after the maximum NO_x removal is obtained, if the applied voltage continues rising, the NO_x removal decreases. The maximum PM, HC, and NO_x removal were 80%, 75%, and 65% respectively. Du et al. used also a real diesel exhaust with a coaxial DBD and an AC voltage source [61]. As well as in [24], the NO_x removal increases with the AC voltage, but after certain level, it shows a decreasing tendency.

In 2015, Mohapatro and Rajanikanth compared a cross-flow and axial-flow DBD supplied by a pulsed voltage [46]. This type of DBD reactor obtained a high NO_x removal efficiency compared to other experiments using real diesel engine exhaust without any catalysts/adsorbents. A ηNO_x of 70% was obtained with both reactors (axial and cross-flow). Additionally, in 2017, Mohapatro et al. exceeded the NO_x removal efficiency of [46], using as well just plasma [62]. In this case, a comparison of a coaxial DBD using three types of inner electrodes, one square, and two cylinders, was presented. Additionally, two pulsed power supplies were compared. One of them has a rise time of less than $12ns$ and a low input voltage, which is suitable for mobile applications. The best results were obtained by the square electrode and the mentioned power supply. A maximum ηNO_x of 85% was obtained with a low ED.

Details of the presented publications are in Table 2.2. In order to compare all the results using the same parameters, some calculations were done based on the information found in the papers. The gray font represents the values that were manually calculated because they were not explicit in the papers. In general, for this solution, the experiments with real engines have reported NO_x efficiencies between 45% and 85%. As stated in the removal mechanisms section, the NTP cannot effectively reduce the NO_x in the presence of high oxygen concentrations; consequently, those removal efficiencies are mostly obtained at a high energy cost. Although the treatment only based on plasma technology is not practical yet because of the low energy efficiency, it is required in order to understand and optimize the treatment, even for a plasma/catalyst solution.

Plasma + Additive In order to improve the plasma performance, a possible solution is to inject additives into the gas mixture (Figure 2.6-b). The ammonia (NH_3) and hydrazine (N_2H_4) are some additives that can enhance the NO_x removal based on reduction pathways, without the need of an additional catalyst stage [37, 63].

Plasma + Catalyst or Adsorbent Another alternative to increase the $DeNO_x$ efficiency is to use plasma/catalyst processes. The plasma/catalyst solution can be classified as a single-stage or two-stage process. In the single-stage process (Figure 2.6-c), the catalyst is placed inside the plasma, as in a packed bed reactor [53, 56, 64–67]. Therefore, the plasma activates the catalyst pellets, and the reduction reactions occur in both the gas and catalyst surface. Some typical catalyst materials employed in the packed bed pellets are $BaTiO_3$, Al_2O_3, and TiO_2.

On the other hand, in the two-stage process, the catalyst or absorbent is separated from the plasma reactor and located downstream of the plasma (Figure 2.6-d). The purpose of the plasma reactor is to convert the NO into NO_2, and then the catalyst or adsorbent reduces the NO_2. In comparison with the typical SCR, the two-stage plasma/catalyst process improves the treatment performance at low temperatures, where the SCR is limited [66, 68–70]. Additionally, both plasma/catalyst processes may include additives to promote the NO_x reduction or to enhance the NO oxidation. Table 2.3 presents the review of Plasma + Catalyst or Adsorbent results.

2.5 Conclusions

Overall, this chapter has introduced general aspects of plasma technology in order to understand the NTP NO_x treatment. Some key points presented in the chapter are:

NOx removal mechanisms: The gas composition significantly affects the treatment, and their compounds have to be considered in order to analyze whether a reduction or oxidation mechanism causes the $DeNO$.

Reactors: As can be seen in the literature revision of Tables 2.2 and 2.3, DBD are commonly used reactors due to their stability, homogeneity, effectiveness and scalability.

Direct Plasma Treatment: Different $DeNO_x$ solutions have been proposed with the direct plasma; however, the energy consumption using just plasma is still very high to have a practical use. Therefore, the plasma has been combined with additives and catalysts to improve the efficiency. Nevertheless, if energy consumption is reduced to practical levels, a preferred solution would be only to use the plasma effect. The improvement of the $DeNO_x$ energy cost is one of the main challenges of the treatment. Moreover, as seen in Tables 2.2 and 2.3, only AC and pulsed voltage sources supply the DBD reactors. Nobody has studied the effect of a current source instead of a voltage source. Therefore, a research opportunity is there stated. The next chapter will present this opportunity in depth.

Author Year	Reactor Type	Gas Mixture	Flow [lpm]	NO_{xi} [ppm]	Power Supply	Voltage [kV]	Frequency	Power [W]	Best Performance
1998 [25] McLarnon and Penetrante	DBD Coaxial 2 dielectrics, Packed DBD with glass-wool	NO/N_2	–	250	AC	0 - 30	60 - 1000 Hz	–	ηNO = 100% at ED = 300 J/l. Similar results for both DBD and packed bed DBD reactors.
2012 [26] Wang et al.	DBD Coaxial 1 dielectric	NO/N_2	10	500	AC	0 - 13	10 kHz	0-120	ηNO = 90% at ED = 675 J/l and NO_E = 0.11 mole/kWh with a screw electrode and small gap (Figure 13 in [26]).
2015 [27] Anaghizi et al.	DBD Coaxial 1 dielectric	NO/N_2	8	720	Pulsed	0 - 20	10 - 30 kHz	0-160	ηNO_x =100% at ED = 1260 J/l and NO_{xE} = 0.09 mole/kWh with a 1mm thread electrode (Figure 17 in [27]) .
2004 [48] Arai et al.	Corona Coaxial	$NO/N_2/O_2$ (O_2 0-20%)	1	100	DC	0 - 15	–	0-25	ηNO =100%, ηNO_x =88% at ED = 500 J/l and NO_{xE} = 0.03 mole/kWh with O_2 =10% (Figure 5 in [48]) .
2012 [45, 60] Vinh et al.	DBD Reactor	$NO/N_2/O_2/PM$ (O_2 0-20%)	0.5, 1, 2	100	AC	0 - 15	50 Hz	0-3	ηNO =60%, ηNO_x =35% at ED = 194 J/l and NO_{xE} = 0.09 mole/kWh with G =1 lpm, O_2 =10%, PM = 100 mg (Figure 9 in [45]) .
2007 [47] Vinogradov et al.	Corona Needle - plane	Diesel Engine	8	–	DC	50	–	0-120	ηNO_2 = 55 % at 60 J/l
2009 [24] Song et al.	DBD Coaxial 2 dielectrics	Diesel Engine	5	476.3	AC	0 - 14	10 - 27 kHz	0-60	ηNO_x =67.3% at ED = 178 J/l and NO_{xE} = 0.29 mole/kWh (Figure 4 in [24]) .
2015 [46] Mohapatro and Rajanikanth	DBD Duct Type	Diesel Engine	2, 5, 10	310	Pulsed	0 - 25	74 pps	0-7	ηNO_x =71.2% at ED = 183 J/l and NO_{xE} = 0.19 mole/kWh with G = 2 lpm and axial flow .
2017 [62] Mohapatro et al.	DBD Coaxial 1 dielectric	Diesel Engine	4	388	Pulsed	0 - 30	80 pps	0-17	ηNO_x =85% at ED = 55 J/l and NO_{xE} = 0.96 mole/kWh with square inner electrode and nanosecond pulsed supply.

Table 2.2: Publications review of $DeNO_x$ based only on the NTP effect.

Author Year	Reactor Type	Gas Mixture	Catalyst - Adsorbent - or Additives	Flow [lpm]	NO_{xi} [ppm]	Power Supply	Voltage [kV]	Frequency	Power [W]	Best Performance
2019 [37] Wang et al.	Coaxial DBD	$NO/N_2/O_2/H_2O/CO_2$	Plasma + Additives: NH_3	2	500 - 1000	AC - Burst	0 - 12	6 - 8 kHz	0-7	ηNO_x =80% at ED = 2250 J/l and NO_{xE} = 0.06 mole/kWh at O_2 = 1% and ηNO_x =25% at ED = 2250 J/l and NO_{xE} = 0.02 mole/kWh at O_2 = 10% (Figure 12 in [37])
2001 [64] Yamamoto et al.	Packed DBD Packed Corona	NO/Air	Pellets: $BaTiO_3$ + Chemical reactor: Na_2SO_3	2	200	AC	0 - 15	60 Hz	0-2.5	ηNO_x =96% at ED = 55 J/l and NO_{xE} = 0.56 mole/kWh with the packed DBD.
2003 [65] Ravi et al.	Packed DBD Glass beads	$NO_x/N_2/O_2$ (100-200 °C)	Catalyst: $V_2O_5 - WO_3/TiO_2$ Additive: Ethynel and NH_3	2	300	AC	4 - 14	60 Hz	0-3.3	ηNO_x =88% at ED = 30 J/l and NO_{xE} = 1.41 mole/kWh with O_2=10%, HC=750 ppm, NH_3=300 ppm and T=100 °C
2007 [68] Rajanikanth and Srinivasan	DBD Coaxial 1 dielectric	Diesel Engine (25-300 °C)	Adsorbent: MS-13 or Catalyst: γAl_2O_3	4	220	Pulsed	0 - 25	130 pps	0-7	ηNO_x =75% at ED = 60 J/l and NO_{xE} = 0.44 mole/kWh with the catalyst. And ηNO_x =75% at ED = 85 J/l and NO_{xE} = 0.41 mole/kWh with the adsorbent.
2017 [53] Okubo et al.	Packed DBD	$NO/N_2/Air$ (120 °C)	Pellets: γAl_2O_3 or $Ag/\gamma Al_2O_3$	1	2000	Pulsed	0 - 30	105 - 525 pps	9.4	ηNO_x =30% at ED = 564 J/l and NO_{xE} = 0.17 mole/kWh with the $Ag/\gamma Al_2O_3$ pellets.
2018 [69] Banu and Rajanikanth	DBD Duct type	Diesel Engine	Adsorbent: lignite flyash	8	346.9	Pulsed	0 - 25	94.34 Hz	0-5.2	ηNO_x =75.5% at ED = 39.41 J/l and NO_{xE} = 1.07 mole/kWh.
2019 [56] Nguyen et al.	Packed DBD	$NO/N_2/O_2$ (150-350 °C)	Pellets: $Ag/\gamma Al_2O_3$ + Additives: HC	2	300	AC	0 - 11	400 Hz	0-7	ηNO_x =90% at ED = 30 J/l and NO_{xE} = 1.07 mole/kWh at 350 °C with 3.7% H_2O, 10% O_2 and additives: 48 ppm naphthalene, 265 ppm n-heptane. (Figure 3 in [56])

Table 2.3: Publications review of $DeNO_x$ based on hybrid plasma/ catalyst process.

Bibliography

[1] V. Nehra, A. Kumar, and H. K. Dwivedi, "Atmospheric Non-Thermal Plasma Sources," *International Journal of Engineering*, vol. 2, no. 1, pp. 53–68, 2008.

[2] E. Gomez, D. A. Rani, C. Cheeseman, D. Deegan, M. Wise, and A. Boccaccini, "Thermal plasma technology for the treatment of wastes: A critical review," *Journal of Hazardous Materials*, vol. 161, no. 2-3, pp. 614–626, 1 2009. doi: https://doi.org/10.1016/j.jhazmat.2008.04.017

[3] H.-H. Kim, "Nonthermal Plasma Processing for Air-Pollution Control: A Historical Review, Current Issues, and Future Prospects," *Plasma Processes and Polymers*, vol. 1, no. 2, pp. 91–110, 9 2004. doi: https://doi.org/10.1002/ppap.200400028

[4] J. O. Chae, "Non-thermal plasma for diesel exhaust treatment," *Journal of Electrostatics*, vol. 57, no. 3-4, pp. 251–262, 2003. doi: https://doi.org/10.1016/S0304-3886(02)00165-1

[5] S. Pekarek, "Non-Thermal Plasma Ozone Generation," *Acta Polytechnica*, vol. 43, no. 6, pp. 47–51, 1 2003. doi: https://doi.org/10.14311/498

[6] L. J. W. Seidelmann, "Atmospheric Pressure Dielectric Barrier Discharges for the Surface Modification of Polypropylene," Ph.D. dissertation, Manchester Metropolitan University, 2015.

[7] F. Massines, C. Sarra-Bournet, F. Fanelli, N. Naudé, and N. Gherardi, "Atmospheric pressure low temperature direct plasma technology: Status and challenges for thin film deposition," *Plasma Processes and Polymers*, vol. 9, no. 11-12, pp. 1041–1073, 2012. doi: https://doi.org/10.1002/ppap.201200029

[8] E. A. Sosnin, T. Oppenländer, and V. F. Tarasenko, "Applications of capacitive and barrier discharge excilamps in photoscience," *Journal of Photochemistry and Photobiology C: Photochemistry Reviews*, vol. 7, no. 4, pp. 145–163, 12 2006. doi: https://doi.org/10.1016/j.jphotochemrev.2006.12.002

[9] M. Lomaev, E. Sosnin, and V. Tarasenko, "Excilamps and their applications," *Progress in Quantum Electronics*, vol. 36, no. 1, pp. 51–97, 1 2012. doi: https://doi.org/10.1016/j.pquantelec.2012.03.003

[10] M. I. Lomaev, E. A. Sosnin, V. F. Tarasenko, D. V. Shits, V. S. Skakun, M. V. Erofeev, and A. A. Lisenko, "Capacitive and barrier discharge excilamps and their applications (Review)," *Instruments and Experimental Techniques*, vol. 49, no. 5, pp. 595–616, 2006. doi: https://doi.org/10.1134/S0020441206050010

[11] G. Fridman, G. Friedman, A. Gutsol, A. B. Shekhter, V. N. Vasilets, and A. Fridman, "Applied Plasma Medicine," *Plasma Processes and Polymers*, vol. 5, no. 6, pp. 503–533, 8 2008. doi: https://doi.org/10.1002/ppap.200700154

[12] M. Laroussi, "Low Temperature Plasma-Based Sterilization: Overview and State-of-the-Art," *Plasma Processes and Polymers*, vol. 2, no. 5, pp. 391–400, 6 2005. doi: https://doi.org/10.1002/ppap.200400078

[13] D. Xiao, "Fundamental Theory of Townsend Discharge," in *Gas Discharge and Gas Insulation. Energy and Environment Research in China.* Springer, Berlin, Heidelberg, 2016, pp. 47–88. doi: https://doi.org/10.1007/978-3-662-48041-0_3

[14] L. B. . Loeb and J. M. Meek, "The Mechanism of Spark Discharge in Air at Atmospheric Pressure. I," *Journal of Applied Physics*, vol. 11, no. 6, pp. 438–447, 1940. doi: https://doi.org/10.1063/1.1712792

[15] M. Keidar and I. I. Beilis, "Electrical Discharges," in *Plasma Engineering.* Elsevier, 2013, pp. 103–126. doi: https://doi.org/10.1016/B978-0-12-385977-8.00003-2

[16] J. Reece Roth, *Industrial Plasma Engineering.* CRC Press, 1 1995. doi: https://doi.org/10.1201/9780367802615

[17] B. Eliasson and U. Kogelschatz, "Nonequilibrium volume plasma chemical processing," *IEEE Transactions on Plasma Science*, vol. 19, no. 6, pp. 1063–1077, 1991. doi: https://doi.org/10.1109/27.125031

[18] J.-S. Chang, P. Lawless, and T. Yamamoto, "Corona discharge processes," *IEEE Transactions on Plasma Science*, vol. 19, no. 6, pp. 1152–1166, 1991. doi: https://doi.org/10.1109/27.125038

[19] U. Kogelschatz, "Dielectric-barrier Discharges: Their History, Discharge Physics, and Industrial Applications," *Plasma Chemistry and Plasma Processing*, vol. 23, pp. 1–43, 2003. doi: https://doi.org/10.1023/A:1022470901385

[20] R. Brandenburg, "Dielectric barrier discharges: Progress on plasma sources and on the understanding of regimes and single filaments," *Plasma Sources Science and Technology*, vol. 26, no. 5, 2017. doi: https://doi.org/10.1088/1361-6595/aa6426

[21] M. J. Kirkpatrick, W. C. Finney, and B. R. Locke, "Plasma-catalyst interactions in the treatment of volatile organic compounds and NOx with pulsed corona discharge and reticulated vitreous carbon Pt/Rh-coated electrodes," *Catalysis Today*, vol. 89, no. 1-2, pp. 117–126, 2004. doi: https://doi.org/10.1016/j.cattod.2003.11.017

[22] M. A. Jani, K. Toda, K. Takaki, and T. Fujiwara, "Experimental comparison between electrode shapes for NOx treatment using a dielectric barrier discharge," *Journal of Physics D: Applied Physics*, vol. 33, no. 23, pp. 3078–3082, 2000. doi: https://doi.org/10.1088/0022-3727/33/23/311

[23] M. A. Jani, K. Takaki, and T. Fujiwara, "Streamer polarity dependence of NOx removal by dielectric barrier discharge with a multipoint-to-plane geometry," *Journal of Physics D: Applied Physics*, vol. 32, no. 19, pp. 2560–2567, 1999. doi: https://doi.org/10.1088/0022-3727/32/19/313

[24] C.-L. Song, F. Bin, Z.-M. Tao, F.-C. Li, and Q.-F. Huang, "Simultaneous removals of NOx, HC and PM from diesel exhaust emissions by dielectric barrier discharges," *Journal of Hazardous Materials*, vol. 166, no. 1, pp. 523–530, 7 2009. doi: https://doi.org/10.1016/j.jhazmat.2008.11.068

[25] C. R. McLarnon and B. M. Penetrante, "Effect of Reactor Design on the Plasma Treatment of NOx," in *International Fall Fuels and Lubricants Meeting and Exposition*. SAE International, 10 1998. doi: https://doi.org/10.4271/982434

[26] T. Wang, B. M. Sun, H. P. Xiao, J. Y. Zeng, E. P. Duan, J. Xin, and C. Li, "Effect of reactor structure in DBD for nonthermal plasma processing of NO in N2 at ambient temperature," *Plasma Chemistry and Plasma Processing*, vol. 32, no. 6, pp. 1189–1201, 2012. doi: https://doi.org/10.1007/s11090-012-9399-3

[27] S. J. Anaghizi, P. Talebizadeh, H. Rahimzadeh, and H. Ghomi, "The Configuration Effects of Electrode on the Performance of Dielectric Barrier Discharge Reactor for NOx Removal," *IEEE Transactions on Plasma Science*, vol. 43, no. 6, pp. 1944–1953, 2015. doi: https://doi.org/10.1109/TPS.2015.2422779

[28] U. Kogelschatz, "Filamentary, patterned, and diffuse barrier discharges," *IEEE Transactions on Plasma Science*, vol. 30, no. 4, pp. 1400–1408, 8 2002. doi: https://doi.org/10.1109/TPS.2002.804201

[29] Z. Fang, Y. Qiu, C. Zhang, and E. Kuffel, "Factors influencing the existence of the homogeneous dielectric barrier discharge in air at atmospheric pressure," *Journal of Physics D: Applied Physics*, vol. 40, no. 5, pp. 1401–1407, 2007. doi: https://doi.org/10.1088/0022-3727/40/5/013

[30] E. E. Kunhardt, "Generation of large-volume, atmospheric-pressure, nonequilibrium plasmas," *IEEE Transactions on Plasma Science*, vol. 28, no. 1, pp. 189–200, 2000. doi: https://doi.org/10.1109/27.842901

[31] N. Gherardi and F. Massines, "Mechanisms controlling the transition from glow silent discharge to streamer discharge in nitrogen," *IEEE Transactions on Plasma Science*, vol. 29, no. 3, pp. 536–544, 2001. doi: https://doi.org/10.1109/27.928953

[32] N. Naudé, J.-P. Cambronne, N. Gherardi, and F. Massines, "Electrical model and analysis of the transition from an atmospheric pressure Townsend discharge to a filamentary discharge," *Journal of Physics D: Applied Physics*, vol. 38, no. 4, pp. 530–538, 2 2005. doi: https://doi.org/10.1088/0022-3727/38/4/004

[33] H.-E. Wagner, R. Brandenburg, K. Kozlov, A. Sonnenfeld, P. Michel, and J. Behnke, "The barrier discharge: basic properties and applications to surface treatment," *Vacuum*, vol. 71, no. 3, pp. 417–436, 5 2003. doi: https://doi.org/10.1016/S0042-207X(02)00765-0

[34] P. Talebizadeh, H. Rahimzadeh, M. Babaie, S. J. Anaghizi, H. Ghomi, G. Ahmadi, and R. Brown, "Evaluation of residence time on nitrogen oxides removal in non-thermal plasma reactor," *PLoS ONE*, vol. 10, no. 10, 2015. doi: https://doi.org/10.1371/journal.pone.0140897

[35] A. C. Gentile and M. J. Kushner, "Reaction chemistry and optimization of plasma remediation of N xOy from gas streams," *Journal of Applied Physics*, vol. 78, no. 3, pp. 2074–2085, 1995. doi: https://doi.org/10.1063/1.360185

[36] B. S. Rajanikanth, A. D. Srinivasan, and V. Ravi, "Discharge plasma treatment for NOx reduction from diesel engine exhaust: A laboratory investigation," *IEEE Transactions on Dielectrics and Electrical Insulation*, vol. 12, no. 1, pp. 72–79, 2005. doi: https://doi.org/10.1109/TDEI.2005.1394017

[37] Z. Wang, H. Kuang, J. Zhang, L. Chu, and Y. Ji, "Nitrogen oxide removal by non-thermal plasma for marine diesel engines," *RSC Advances*, vol. 9, no. 10, pp. 5402–5416, 2019. doi: https://doi.org/10.1039/c8ra09217f

[38] B. M. Penetrante, M. Pitz, W. J.Hsiao, B. Merritt, and G. Vogtlin, "Effect of hydrocarbons on plasma treatment of NO_x," *Proceedings of the 1997 diesel engine emissions reduction workshop*, vol. 298, pp. 1–5, 1997.

[39] A. Khacef, J. M. Cormier, and J. M. Pouvesle, "NOx remediation in oxygen-rich exhaust gas using atmospheric pressure non-thermal plasma generated by a pulsed nanosecond dielectric barrier discharge," *Journal of Physics D: Applied Physics*, vol. 35, no. 13, pp. 1491–1498, 2002. doi: https://doi.org/10.1088/0022-3727/35/13/307

[40] C. R. McLarnon and B. M. Penetrante, "Effect of Gas Composition on the NOx Conversion Chemistry in a Plasma," in *International Fall Fuels and Lubricants Meeting and Exposition*. SAE International, 1998. doi: https://doi.org/10.4271/982433

[41] I. Jõgi, E. Stamate, C. Irimiea, M. Schmidt, R. Brandenburg, M. Hołub, M. Bonisławski, T. Jakubowski, M.-L. Kääriäinen, and D. C. Cameron, "Comparison of direct and indirect plasma oxidation of NO combined with oxidation by catalyst," *Fuel*, vol. 144, no. January, pp. 137–144, 3 2015. doi: https://doi.org/10.1016/j.fuel.2014.12.025

[42] H.-J. Kim, B. Han, C. G. Woo, and Y.-J. Kim, "NOx Removal Performance of a Wet Reduction Scrubber Combined With Oxidation by an Indirect DBD Plasma for Semiconductor Manufacturing Industries," *IEEE Transactions on Industry Applications*, vol. 54, no. 6, pp. 6401–6407, 11 2018. doi: https://doi.org/10.1109/TIA.2018.2853113

[43] T. Yamamoto, H. Fujishima, M. Okubo, and T. Kuroki, "Pilot-scale NOx and SOx removal from boiler emission using indirect-plasma and chemical hybrid process," *IEEE Transactions on Industry Applications*, vol. 46, no. 1, pp. 29–37, 2010. doi: https://doi.org/10.1109/TIA.2009.2036669

[44] M. Apeksha and B. S. Rajanikanth, "Plasma/adsorbent system for NOx treatment in diesel exhaust: a case study on solid industrial wastes," *International Journal of Environmental Science and Technology*, vol. 16, no. 7, pp. 2973–2988, 7 2019. doi: https://doi.org/10.1007/s13762-018-1776-x

[45] T. Q. Vinh, S. Watanabe, T. Furuhata, and M. Arai, "Fundamental study of NO x removal from diesel exhaust gas by dielectric barrier discharge reactor," *Journal of Mechanical Science and Technology*, vol. 26, no. 6, pp. 1921–1928, 2012. doi: https://doi.org/10.1007/s12206-012-0402-y

[46] S. Mohapatro and B. S. Rajanikanth, "Studies on NOX Removal from Diesel Engine Exhaust Using Duct-Type DBD Reactor," *IEEE Transactions on Industry Applications*, vol. 51, no. 3, pp. 2489–2496, 2015. doi: https://doi.org/10.1109/TIA.2014.2365049

[47] J. Vinogradov, B. Rivin, and E. Sher, "NOx reduction from compression ignition engines with DC corona discharge—An experimental study," *Energy*, vol. 32, no. 3, pp. 174–186, 3 2007. doi: https://doi.org/10.1016/j.energy.2006.04.011

[48] M. Arai, M. Saito, and S. Yoshinaga, "Effect of oxygen on NOX removal in corona discharge field: NOX behavior without a reducing agent," *Combustion Science and Technology*, vol. 176, no. 10, pp. 1653–1665, 2004. doi: https://doi.org/10.1080/00102200490487535

[49] B. R. Locke, A. Ichihashi, H. H. Kim, and A. Mizuno, "Diesel engine exhaust treatment with a pulsed streamer corona reactor equipped with reticulated vitreous carbon electrodes," *IEEE Transactions on Industry Applications*, vol. 37, no. 3, pp. 715–723, 2001. doi: https://doi.org/10.1109/28.924750

[50] B. Penetrante, M. Hsiao, B. Merritt, G. Vogtlin, and P. Wallman, "Comparison of electrical discharge techniques for nonthermal plasma processing of NO in N/sub 2/," *IEEE Transactions on Plasma Science*, vol. 23, no. 4, pp. 679–687, 1995. doi: https://doi.org/10.1109/27.467990

[51] R. . V. E. Tas, Marnix ; Hardeveld, "Reactions of NO in a Positive Streamer Corona Plasma," *Plasma Chemistry and Plasma Processing*, vol. 17, pp. 371–391, 1997. doi: https://doi.org/10.1023/A:1021818313047

[52] H. H. Kim, S. M. Oh, A. Ogata, and S. Futamura, "Decomposition of benzene using Ag/TiO 2 packed plasma-driven catalyst reactor: Influence of electrode configuration and Ag-loading amount," *Catalysis Letters*, vol. 96, no. 3-4, pp. 189–194, 2004. doi: https://doi.org/10.1023/B:CATL.0000030119.69922.07

[53] M. Okubo, H. Yamada, K. Yoshida, and T. Kuroki, "Simultaneous Reduction of Diesel Particulate and NOx Using a Catalysis-Combined Nonthermal Plasma Reactor," *IEEE Transactions on Industry Applications*, vol. 53, no. 6, pp. 5875–5882, 2017. doi: https://doi.org/10.1109/TIA.2017.2748925

[54] M. Okubo, M. Inoue, T. Kuroki, and T. Yamamoto, "NOx reduction aftertreatment system using nitrogen nonthermal plasma desorption," *IEEE Transactions on Industry Applications*, vol. 41, no. 4, pp. 891–899, 2005. doi: https://doi.org/10.1109/TIA.2005.851565

[55] B. S. Rajanikanth and V. Ravi, "Pulsed electrical discharges assisted by dielectric pellets/catalysts for diesel engine exhaust treatment," *IEEE Transactions on Dielectrics and Electrical Insulation*, vol. 9, no. 4, pp. 616–626, 2002. doi: https://doi.org/10.1109/TDEI.2002.1024440

[56] V. T. Nguyen, D. B. Nguyen, I. Heo, and Y. S. Mok, "Plasma-Assisted Selective Catalytic Reduction for Low-Temperature Removal of NO x and Soot Simulant," no. x, 2019.

[57] T. Matsumoto, D. Wang, T. Namihira, and H. Akiyama, "Energy efficiency improvement of nitric oxide treatment using nanosecond pulsed discharge," *IEEE Transactions on Plasma Science*, vol. 38, no. 10 PART 1, pp. 2639–2643, 2010. doi: https://doi.org/10.1109/TPS.2010.2045903

[58] B. M. Penetrante, M. C. Hsiao, B. T. Merritt, G. E. Vogtlin, P. H. Wallman, M. Neiger, O. Wolf, T. Hammer, and S. Broer, "Pulsed corona and dielectric-barrier discharge processing of NO in N2," *Applied Physics Letters*, vol. 68, no. 26, pp. 3719–3721, 1996. doi: https://doi.org/10.1063/1.115984

[59] P. Talebizadeh, H. Rahimzadeh, S. J. Anaghizi, H. Ghomi, M. Babaie, and R. Brown, "Experimental study on the optimization of dielectric barrier discharge reactor for NOx treatment," *IEEE Transactions on Dielectrics and Electrical Insulation*, vol. 23, no. 6, pp. 3283–3293, 12 2016. doi: https://doi.org/10.1109/TDEI.2016.005690

[60] T. Q. Vinh, S. Watanabe, T. Furuhata, and M. Arai, "Effects of particulate matter on NOx removal in dielectric barrier discharges," *Journal of the Energy Institute*, vol. 85, no. 3, pp. 163–169, 2012. doi: https://doi.org/10.1179/1743967112Z.00000000015

[61] B. X. Du, H. J. Liu, X. H. Wang, and K. F. Wang, "Application of dielectric barrier discharge in the removal of NO x from diesel exhaust," *Annual Report - Conference on Electrical Insulation and Dielectric Phenomena, CEIDP*, pp. 617–620, 2009. doi: https://doi.org/10.1109/CEIDP.2009.5377724

[62] S. Mohapatro, S. Allamsetty, A. Madhukar, and N. K. Sharma, "Nanosecond pulse discharge based nitrogen oxides treatment using different electrode configurations," *High Voltage*, vol. 2, no. 2, pp. 60–68, 2017. doi: https://doi.org/10.1049/hve.2017.0011

[63] Z. Guan, J. Ren, D. Chen, L. Hong, F. Li, D. Wang, Y. Ouyang, and Y. Gao, "NOx removal by non-thermal plasma at low temperatures with amino groups additives," *Korean Journal of Chemical Engineering*, 2016. doi: https://doi.org/10.1007/s11814-016-0179-2

[64] T. Yamamoto, M. Okubo, K. Hayakawa, and K. Kitaura, "Towards ideal NO x control technology using a plasma-chemical hybrid process," *IEEE Transactions on Industry Applications*, vol. 37, no. 5, pp. 1492–1498, 2001. doi: https://doi.org/10.1109/28.952526

[65] V. Ravi, Y. S. Mok, B. S. Rajanikanth, and H.-c. Kang, "Studies on Nitrogen Oxides Removal Using Plasma Assisted Catalytic Reactor," *Plasma Science and Technology*, vol. 5, no. 6, pp. 2057–2062, 12 2003. doi: https://doi.org/10.1088/1009-0630/5/6/007

[66] H. H. Kim, K. Takashima, S. Katsura, and A. Mizuno, "Low-temperature NO x reduction processes using combined systems of pulsed corona discharge and catalysts," *Journal of Physics D: Applied Physics*, vol. 34, no. 4, pp. 604–613, 2 2001. doi: https://doi.org/10.1088/0022-3727/34/4/322

[67] B. J. Lee, H. C. Kang, J. O. Jo, and Y. S. Mok, "Consideration of the role of plasma in a plasma-coupled selective catalytic reduction of nitrogen oxides with a hydrocarbon reducing agent," *Catalysts*, vol. 7, no. 11, 2017. doi: https://doi.org/10.3390/catal7110325

[68] B. S. Rajanikanth and A. D. Srinivasan, "Pulsed plasma promoted adsorption/catalysis for NOx removal from stationary diesel engine exhaust," *IEEE Transactions on Dielectrics and Electrical Insulation*, vol. 14, no. 2, pp. 302–311, 2007. doi: https://doi.org/10.1109/TDEI.2007.344608

[69] R. A. Banu and B. S. Rajanikanth, "Nox removal from petro-diesel exhaust using duct type DBD plasma coupled with industry waste adsorbent," *Proceedings of 2017 IEEE International Conference on Technological Advancements in Power and Energy: Exploring Energy Solutions for an Intelligent Power Grid, TAP Energy 2017*, 2018. doi: https://doi.org/10.1109/TAPENERGY.2017.8397362

[70] A. D. Srinivasan, M. Ieee, B. S. Rajanikanth, and S. M. Ieee, "A Laboratory Analysis of Plasma Based Hybrid Techniques for Treating Engine Exhaust," *2010 IEEE Industry Applications Society Annual Meeting*, pp. 1–6, 2010. doi: https://doi.org/10.1109/IAS.2010.5615403

Chapter 3

Power Supplies for DBD

Contents

3.1 Introduction

The gas composition, supply waveforms, and reactor design are some of the DBD operating conditions that alter the plasma properties, affecting the $DeNO_x$ performance. In order to optimize the NOx treatment, the impact of several of those conditions has been studied in the literature. Regarding the electrical supply conditions, sinusoidal and pulsed voltage waveforms in a wide frequency and voltage range have been studied, showing a preference for pulsed voltages with short rising time. Unfortunately, even with pulsed voltage waveforms, the energy consumption of the treatment using only plasma is still very high to market the technology. As an alternative supply method, in this thesis, the imposition of current instead of voltage waveforms is examined, focusing on the design and control of the power supply and its interaction with the DBD reactor.

Accordingly, this chapter presents a review of the DBD supply waveforms and their respective power supplies. Due to the emphasis of this thesis on the design of the power supplies, the chapter starts by presenting the DBD electrical models and their parameters identification. At the end of Section 3.2, the model selected for the analysis and design of the power supplies is presented. Then, an explanation of the differences between the current and voltage supply modes is given in Section 3.3.1. Finally, a survey of the voltage and current sources is presented in Section 3.3.2.

3.2 DBD Modeling

The objective of the DBD modeling is to obtain a mathematical model to approximate the DBD behavior. The model structure and parameters identification can be obtained using different approaches. The physics-based approach uses plasma physics to describe the spatial and temporal evolution of the particles inside the plasma reactor. This approach provides a microscopic model based on Maxwell and Lorentz equations. With this set of partial differential equations, the electromagnetic forces acting on the plasma particles and their trajectories can be precisely determined. However, solving those equations requires advanced numerical methods and high computational resources. Another modeling approach is the statistical-based one. In this approach, the Boltzmann equation is used to describe the statistical behavior of the plasma species. Although the solution of the statistical-based models usually requires less computational resources than the physics-based models, the numerical solution of the Boltzmann equation is still a very complex problem.

The models obtained with the physics and statistical-based approaches are fundamental for understanding and optimizing physical phenomena inside the plasma. Nonetheless, due to their complexity, and to the emphasis of this thesis on power supplies, a circuit-based model describing only the reactor electrical characteristics will be used.

3.2.1 Electric Models

The circuit-based modeling is essential to the analysis, design, dimension, and control of the power supplies. Simple electrical models allow scientists to analyze and simulate the interaction between the DBD reactors and power converters quickly and accurately. Moreover, some internal electric variables of the reactor, that cannot be experimentally measured, can be calculated through the electric model. For example, based on the model, the voltage across the gas gap, dielectrics voltage, and the gas conduction current can be deduced.

Figure 3.1 shows different DBD electric models. In general, the circuit models describe the capacitive nature of the DBD and the electric discharge process. Accordingly, the DBD dielectric layers are represented by a capacitance, C_d, in series with the gas. The gas modeling changes between models, but overall, the gas behaves as a capacitance, C_g, in parallel to the discharge model. The value of the capacitances C_d and C_g can be calculated from the DBD geometry.

3.2.1.1 Variable Conductance Model

In the circuit of Figure 3.1-a, the DBD model using a variable conductance is presented. In this type of model, the gas is represented by a capacitance, C_g, in parallel to the gas conductance, G. The latter can be described using a nonlinear differential equation, which terms are related to the discharge physics processes. Some of the variable conductance models are briefly explained below.

In [1], Bhosle et al. propose a variable conductance, whose equation has two terms. The first term relates to the ionization process at the gas breakdown and depends on the voltage drop in the gas gap, v_{gas}. Whereas the second term relates to the recombination process after

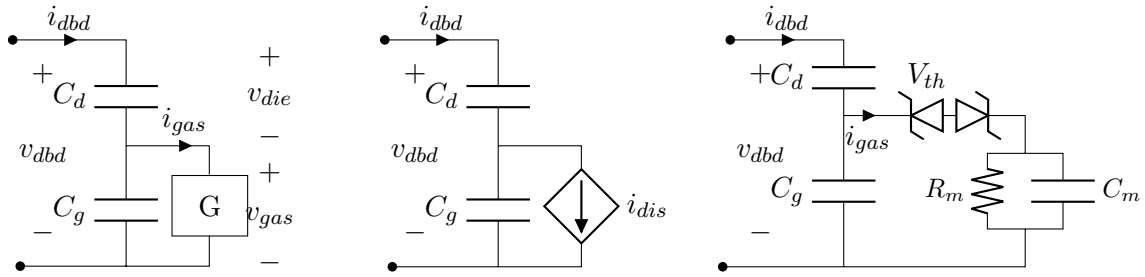

(a) Variable Conductance (b) Dependant Current Source (c) Zener Diodes

Figure 3.1: DBD Electrical Models in the literature

the gas breakdown. Based on this approach, another conductance model was proposed by Díez et al. [2]. In this model, besides of the ionization and recombination terms, a third term is introduced. The new term establishes a proportional relation between the conductance and the gas current, i_{gas}. Furthermore, Lopez et al. [3] improved the previous model. In [3], the third term is replaced by a series of polynomial terms, which relate the conductance with different powers of the gas conduction current. In order to illustrate the conductance equation of one of these models, Equation 3.1 presents the conductance proposed in [2].

$$\frac{dG}{dt} = K_1 u(V_{th} - |v_{gas}|) - K_2 G + K_3 |i_{gas}| \tag{3.1}$$

Where K_1 is the ionization coefficient, $u(.)$ is the Heaviside function, V_{th} is the breakdown voltage of the gas, K_2 is the recombination coefficient, and K_3 is the proportional coefficient.

3.2.1.2 Dependant Current Source Model

Another type of DBD electric model employs dependant current sources to describe the discharge current. Liu and Neiger [4] model a homogeneous discharge in a plane-plane configuration using the circuit shown in Figure 3.1-b. The authors present the theoretical analysis of the model using a voltage-controlled current source. This analysis was later applied to a filamentary coaxial DBD in [5, 6]. In these papers, besides the current source, an additional impedance parallel to the gas capacitance, which represents the filamentary impedance of the micro discharges, is included. Moreover, the gas capacitance, C_g, is defined as a variable capacitance, since the degree of ionization changes the relative permittivity of the gas.

Zhiyu Chen [7] develops another current source model. In this model, two voltage-controlled current sources simulate the discharge current as an exponential function of the gas voltage. Each of the current sources generates the discharge current in one-half of the supply waveform cycle. Flores-Fuentes et al. [8] use a similar model with the current as an exponential function of the gas voltage. To exemplify the equation that governs one of the dependant current source models, the discharge current proposed by [8] is presented.

$$i_{dis} = \begin{cases} 0 & v_{gas} < V_{th}, \\ i_0 (v_{gas}/V_{th})^{\alpha} & v_{gas} \geq V_{th} \end{cases} \tag{3.2}$$

Where i_0 is the initial current related to the electron emission, and the coefficient α ranges from 1 to 12.

3.2.1.3 Zener Diodes Model

Naudé et al. [9] introduce an electric model of the discharge made out of Zener diodes, as shown in Figure 3.1-c. In this model, the avalanche of the semiconductors is related to the gas avalanche. Accordingly, the Zener voltage is associated with the gas breakdown voltage, V_{th}. Another feature of the model proposed by Naudé et al. is the use of a $R_m C_m$ circuit to describe the memory effect. The memory effect explains that the voltage required to obtain the gas breakdown decreases once the first breakdown has occurred. This phenomenon is caused because the gas remains excited after the discharge. The time constant of the $R_m C_m$ circuit represents the duration of the effect.

Besides these models, a variable resistance is also commonly employed to model the discharge [10]. Additionally, a full diode bridge connected to a constant voltage source has been used to represent the discharge in [11]. And a model that describes the variation of the capacitances due to partial discharges has been proposed in [12].

3.2.1.4 Simplified Model

The models previously presented have been successfully employed to describe the nonlinear electrical behavior of the DBD devices. However, for this dissertation, a much simple electrical model will be used (Figure 3.2). In this model, the discharge is represented by a bipole component with a current-voltage characteristic shown inside the component symbol. This model is equivalent to the model of the full diode bridge connected to a DC voltage source [10], or to the Zener diodes model [9], without taking into account the $R_m C_m$ circuit.

According to the gas discharge characteristics, when the gas voltage is not high enough to produce the gas breakdown ($|v_{gas}| < V_{th}$), the conductance of the discharge is assumed null. It means the current only flows throw the capacitances. In other words, when the plasma is not ignited, the equivalent circuit is purely capacitive, and it consists of the capacitances C_d and C_g connected in series. The equivalent capacitance in this state is :

$$C_{eq} = (C_g C_d)/(C_g + C_d) \tag{3.3}$$

The gas discharge is obtained when the gas voltage reaches the breakdown voltage, V_{th}. At this point, the voltage drop on the gas remains almost constant and equal to V_{th}. Therefore, the DBD is modeled by the series connection of C_d, and a constant voltage source of $\pm V_{th}$ value (the sign depends on the current direction). On this basis, using the current laws and Kirchhoff's voltages, the model voltages can be determined as follows

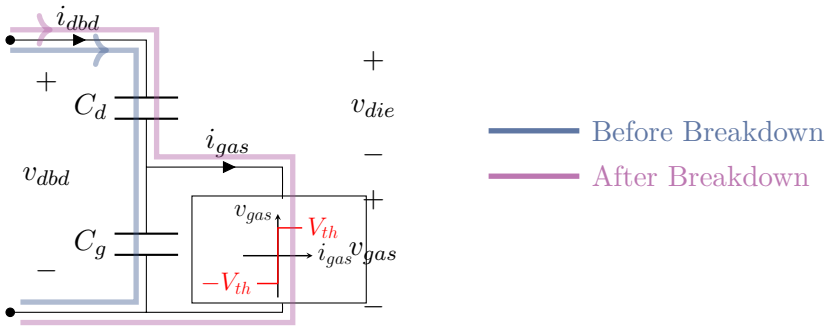

Figure 3.2: Simplified DBD Electrical Model

$$v_{gas}(t) = \begin{cases} \dfrac{1}{C_g}\displaystyle\int_0^t i_{dbd}(\tau)d\tau + v_{gas}(0) & \text{before breakdown,} \\ \pm V_{th} & \text{after breakdown} \end{cases} \tag{3.4}$$

$$v_{die}(t) = \frac{1}{C_d}\int_0^t i_{dbd}(\tau)d\tau + v_{die}(0) \tag{3.5}$$

$$v_{dbd}(t) = v_{gas}(t) + v_{die}(t) \tag{3.6}$$

3.2.2 Charge-Voltage diagrams

The Charge-Voltage diagram (Q-V plot), originally introduced by Manley [13], is a useful tool in the characterization and analysis of DBD. Figure 3.3 shows the ideal Q-V plot of a DBD device, where, V_{dbd} is the voltage across the DBD device, and Q_{dbd} is the electric charge, which can be obtained as the integral of the DBD current waveform, i_{dbd}. Based on this plot, it is possible to experimentally estimate the parameters of the electric model of Figure 3.2 (C_g, C_d, V_{th}).

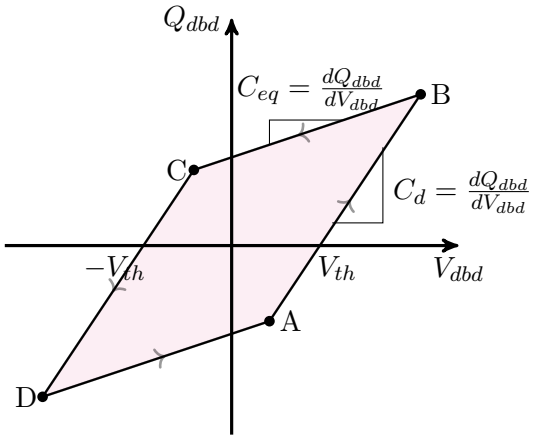

Figure 3.3: Charge-voltage (Q-V) diagram of DBD

When the plasma is ignited, the Q-V plot forms a parallelogram. Each corner of the paral-

lelogram, represent a change of gas state during one operation cycle of the supply waveforms, T. The segments AB and CD are obtained when the discharge is ignited, and its slope is equivalent to the dielectric capacitance C_d. On the other hand, the segments BC and DA are obtained without discharge, and the slope is related to the DBD equivalent capacitance, C_{eq}. The intersections of the V_{dbd}-axis with the segments AB and CD give the value of the gas breakdown voltage, V_{th}.

Furthermore, the total energy consumed in one operation cycle, E_{dbd}, is equivalent to the area enclosed by the parallelogram. Therefore, the total power delivered to the DBD can be determined by $P_{dbd} = E_{dbd}/T$. In the following chapters, this tool will be used for the experimental identification of the DBD parameters and the analysis of electrical quantities of the reactor operation.

3.3 DBD Power Supplies

3.3.1 Voltage vs Current supply modes

Most of the power supplies employed for DBD applications are based on the voltage imposition due to their simplicity, low cost, and traditional use. However, because of the capacitive nature of DBD devices, different authors have proposed to impose the DBD current rather than the voltage [14–18]. In order to justify the use of the current supply mode, this section compares both excitation methods.

Figure 3.4 shows the typical DBD waveforms using a square voltage source and a square current source. These two waveforms are used to illustrate the differences between the supply modes. For the first case, as a voltage source drives the DBD, the output current is determined by the imposed voltage and the load characteristics. Given that the DBD has a capacitive behavior, when the pulsed voltage is imposed, the DBD resists the voltage variations, resulting in current spikes at the voltage edges. This response can be deduced from the derivative equation of DBD current, Equation (3.7). Furthermore, note that the duration and amplitude of the current spikes cannot be easily controlled since they depend on the rising and falling slopes of the voltage waveform, as well as the parasitic components of the power supplies. Therefore, the design of the voltage mode power supplies is complicated, generally resulting in the use of over-sized devices or damages on the components.

$$i_{dbd}(t) = \begin{cases} (C_d + C_g)\dfrac{d}{dt}v_{dbd}(t) & \text{before breakdown,} \\ C_d\dfrac{d}{dt}(v_{dbd}(t) - V_{th}) & \text{after breakdown} \end{cases} \tag{3.7}$$

On the other hand, when the current is imposed, there is no opposition to the current flow, and the voltage can be deduced as Equation (3.8). Hence, it is possible to calculate all the electrical variables of the converter from a design stage, ensuring the correct sizing of the converter components.

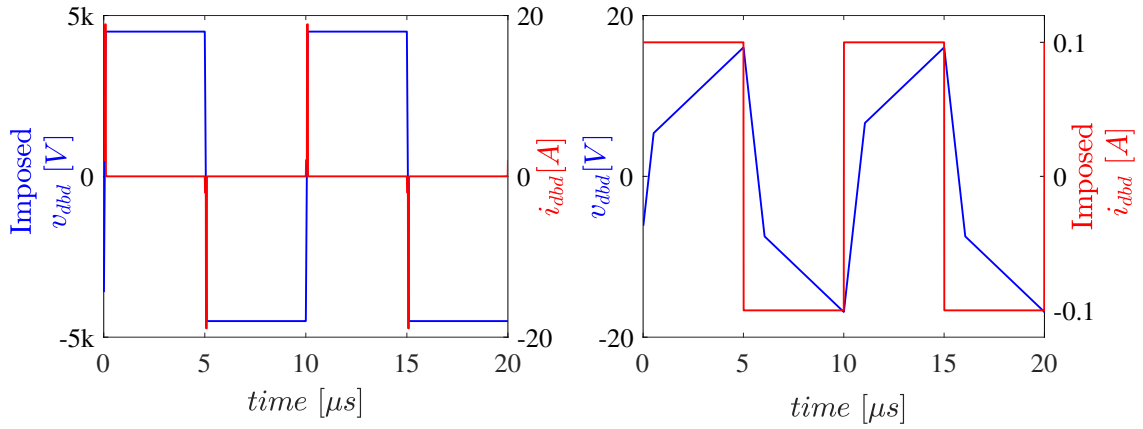

a) Square Voltage Source b) Square Current Source

Figure 3.4: Voltage vs Current supply modes: DBD Ideal Waveforms

$$v_{dbd}(t) = \begin{cases} \dfrac{1}{C_{eq}} \displaystyle\int i_{dbd}(t)dt & \text{before breakdown,} \\ V_{th} + \dfrac{1}{C_d} \displaystyle\int i_{dbd}(t)dt & \text{after breakdown} \end{cases} \tag{3.8}$$

Another advantage of the current supply mode is related to the control of the power consumed by DBD. Compared with the voltage mode, the current mode has a more natural control of the DBD power, as will be here demonstrated. In the simplified electrical model of the DBD device (Figure 3.2), it can be seen that the only dissipative element is the gas conductance, G. It means that the average power of the DBD, P_{dbd}, is equal to the gas average power, P_{gas}. Since after the gas breakdown, all the current injected into the DBD flows throw the gas conductance and considering that during the discharge the gas voltage remains constant at V_{th}, P_{dbd} can be calculated as:

$$P_{dbd} = \frac{1}{T}\int_0^T v_{gas}(t) * i_{gas}(t)dt = \frac{2}{T}V_{th}\int_{t_{br}}^{T/2} i_{dbd}(t)dt \tag{3.9}$$

where t_{br} is the instant when the gas voltage, v_{gas}, reaches the breakdown voltage, V_{th}, and the electric discharge is produced. Note that the equation has a factor 2 since each operation cycle of the current waveform has two symmetric semi-cycles (positive and negative). From Equation (3.9), a direct relationship between the DBD power and the current injected into the DBD can be observed. Thus, one can deduce that the current supply mode has a more explicit control over the DBD power.

For the specific application of the NO_x treatment based on DBDs, minor attention has been directed to the current supply mode. Nonetheless, in other DBD applications such

as excimer lamps and ozonizers, interesting results have been attained using current mode converter. For instance, in the DBD excimer lamps, a strong relationship between the UV emission and the gas current has been reported [15]; therefore, the use of current sources seems preferable. Moreover, excellent ozone production characteristics have been achieved in ozonizers supplied with current sources [14, 16].

3.3.2 Survey of Power Supply Topologies

Several topologies of power supplies and electrical waveforms are available to drive DBD devices. This section presents a review of the power supplies working in voltage and current mode. All these topologies are characterized by two crucial conditions for the correct performance of the DBD. Firstly, they must be able to generate a high output voltage. Secondly, the injected current must be bidirectional with zero average. Otherwise, the magnitude of the voltage will grow uncontrollably until the converter breaks down.

3.3.2.1 Sinusoidal Voltage Source

The sinusoidal voltage source with several kilo-volts amplitudes and frequencies in the kilohertz range is the most common DBD supply solution. For experimentation purposes, the configuration shown in Figure 3.5-a is typically used. It is composed of a signal generator (SG), an audio amplifier, and a step-up transformer. The signal generator produces a low voltage sinusoidal signal and controls its amplitude and frequency. As the signal generator cannot deliver the DBD power and voltage, an amplification stage is required. For such purposes, an audio amplifier that feeds a step-up transformer is employed. In order to limit the amplifier current, a series resistance needs to be included. Figure 3.5-b presents the characteristic DBD waveforms of the sinusoidal voltage supply. As can be seen in the waveforms, the discharge ignition occurs when the gas voltage reaches V_{th}, and the discharge extinction occurs at the DBD peak voltage, where $dV_{dbd}/dt = 0$.

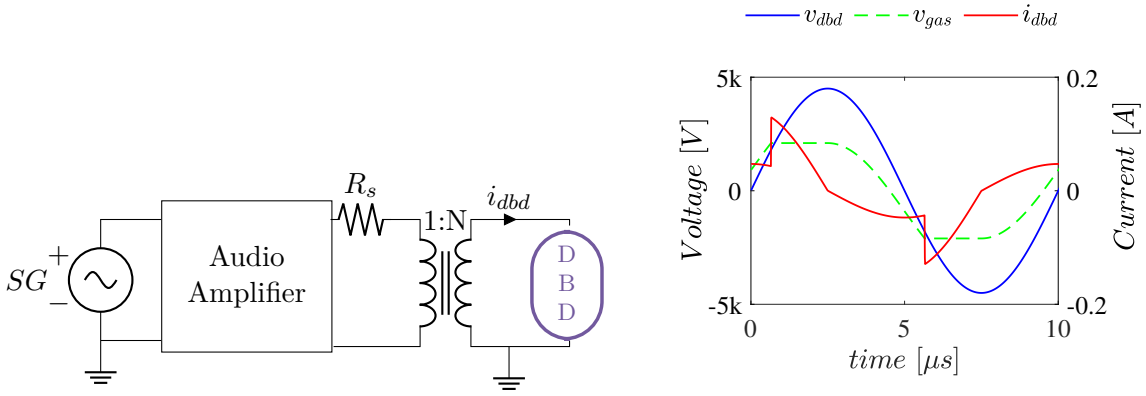

(a) Supply configuration (b) Typical DBD waveforms

Figure 3.5: Sinusoidal Voltage Source

Due to the high losses of the audio amplifier and series resistance, this power supply is

not practical for final products, so it is only used in experimentation environments. Resonant converters, working at a fixed frequency, can attain better electrical performances generating sinusoidal waveforms. Despite the low electrical efficiency of this configuration, we will later use it to compare the NO_x treatment performance of the sinusoidal voltage source with the current sources proposed in this work.

3.3.2.2 Pulsed voltage source

It has been demonstrated that for many DBD applications, pulsed voltage waveforms are more efficient and suitable than sinusoidal ones. The NO_x treatment is one of those applications which benefits from pulsed sources. In theory, the pulsed operation produces more diffuse and homogeneous discharges, since the rapid application of the electric field increases the energy of the electrons [19]. Therefore, waveforms with high dV/dt are preferred to supply DBDs. In order to achieve this voltage characteristic, the implementation of pulsed power supplies relies on rotary spark gaps devices or fast switching solid-state components. However, as rotary spark gaps have a short lifetime, and a limited number of switching cycles [20], we will only consider solid-state power supplies.

Different types of pulsed waveforms have been found in the literature. These include unipolar pulses [21], bipolar pulses [22, 23] , pulses with low rising/falling times [24, 25], and pulses separated by idle times [20, 26, 27]. Figure 3.6 illustrates two generalized pulsed waveforms (bipolar and unipolar pulses). For these waveforms, the frequency, voltage amplitude, and the duty cycle can be controlled. Furthermore, in the case of the bipolar voltage, some authors include an idle time between pulses.

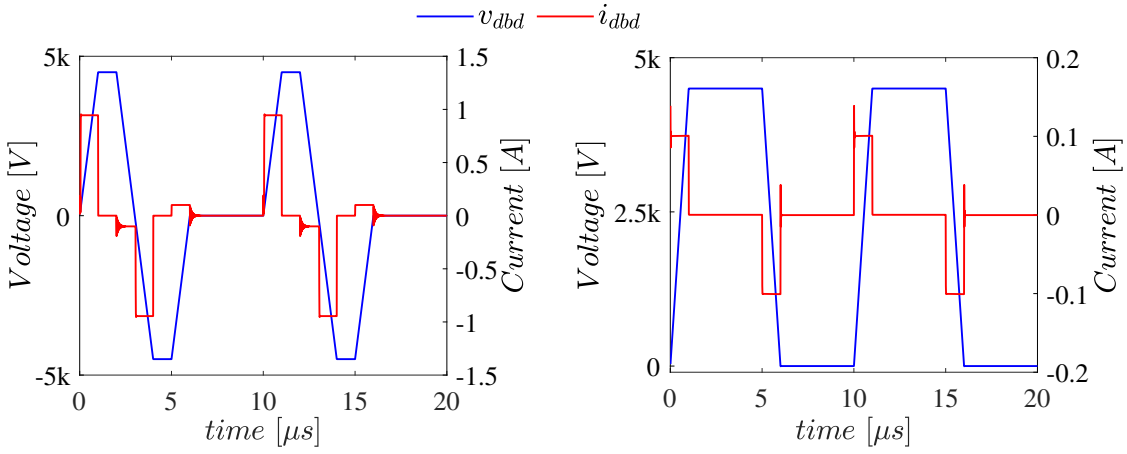

a) Bipolar Pulsed Waveform

b) Unipolar Pulsed Waveform

Figure 3.6: Pulsed Voltage Waveforms

In order to generate the pulsed waveforms, several topologies can be used [21]. Figure 3.7 presents four of them. The first topology is based on the Push-Pull inverter [26]. This converter generates high voltage pulses of altering polarity, similar to the bipolar waveforms shown in Figure 3.6-a. The Push-Pull converter has two switches with complementary con-

trol signals, and a central-tapped transformer, which boosts the voltage, provides galvanic insulation and generates the bipolar voltage waveform. Due to the magnetizing inductance of the transformer, the ideal square voltage cannot be achieved experimentally. Conversely, the transformer inductance resonates with the capacitive DBD load and generates pulses with a semi-sinusoidal shape. The higher the inductance, the more square is the pulsed voltage.

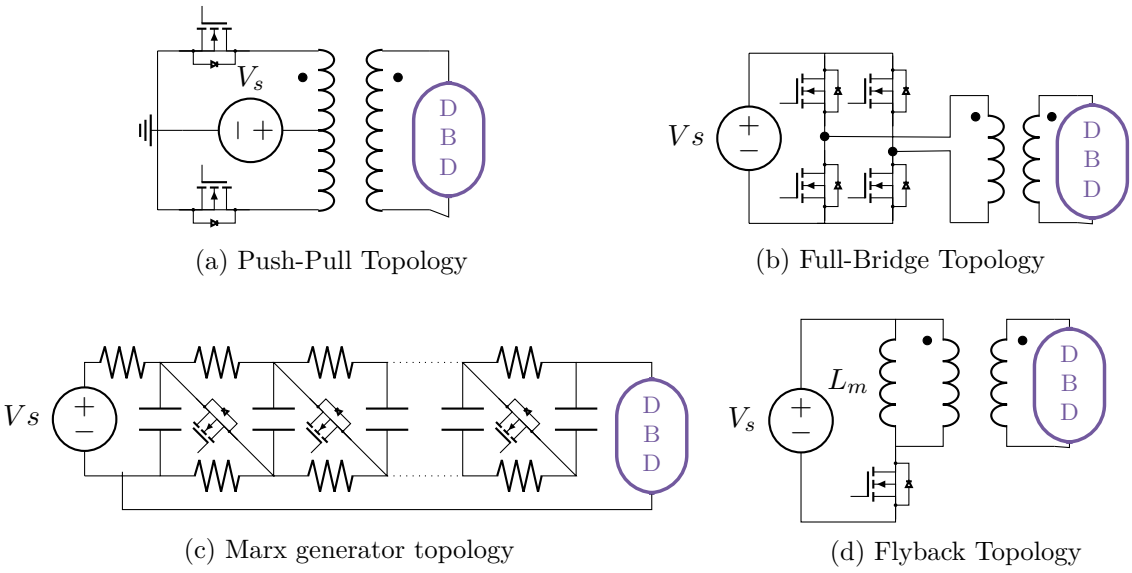

(a) Push-Pull Topology

(b) Full-Bridge Topology

(c) Marx generator topology

(d) Flyback Topology

Figure 3.7: Topologies of Pulsed Voltage Sources

Another simple alternative to produce bipolar pulses is the full-bridge inverter (Figure 3.7-b) [20, 28, 29]. In this topology, the voltage pulses may also acquire a sinusoidal shape due to the leakage inductance of the transformer, which forms a series resonant circuit with the DBD.

The Marx generator is a topology that can produce either bipolar or unipolar pulses [30, 31]. This converter, depicted in Figure 3.7-c, has M stages in cascade. In each stage, a capacitor stores the energy which will be delivered to the DBD. Accordingly, the Marx generator has two switching intervals. First, the capacitors are charged in a parallel connection. And then, they are discharged in a series connection though the DBD. The series connection allows a high output voltage, equal to the number of stages times the input voltage. Therefore, no transformer is required, and the waveforms are very sharp.

Finally, the flyback converter, presented in Figure 3.7-d, can generate unipolar pulses with positive or negative polarity [32, 33]. This converter has two switching intervals. During the first interval, the magnetizing inductance of the transformer is charged (switch closed). Then, in the second interval, the switch is opened, and a parallel resonance between the transformer inductance and the DBD is formed. Consequently, the generated voltage pulse has a sinusoidal shape.

Note that the first three topologies are classified as voltage-mode sources. Therefore, as was previously explained, the semiconductors and energy-storage elements must carry high currents, which are difficult to control. Whereas, the fourth topology (Flyback converter),

operates as a current-mode source. In this converter, the voltage pulse is produced using the current stored in the magnetizing inductance. Thus, the current amplitude is fully controlled. In this sense, it is worth highlighting that the current-mode sources can control the dV/dt through the applied current intensity [34]. In this way, a fast variation of the electric field can be produced by keeping controlled the current.

3.3.2.3 Pulsed current source

The analogous power supply of the pulsed voltage source is the pulsed current source. Figure 3.8 shows the topology of the square current source proposed by [35] and its output waveforms. This power supply consists of a DC current source, connected in cascade with a full-bridge current inverter. [34] proposed another pulsed current source. In this novel approach, two current sources are connected in parallel at the output, and no transformer is employed.

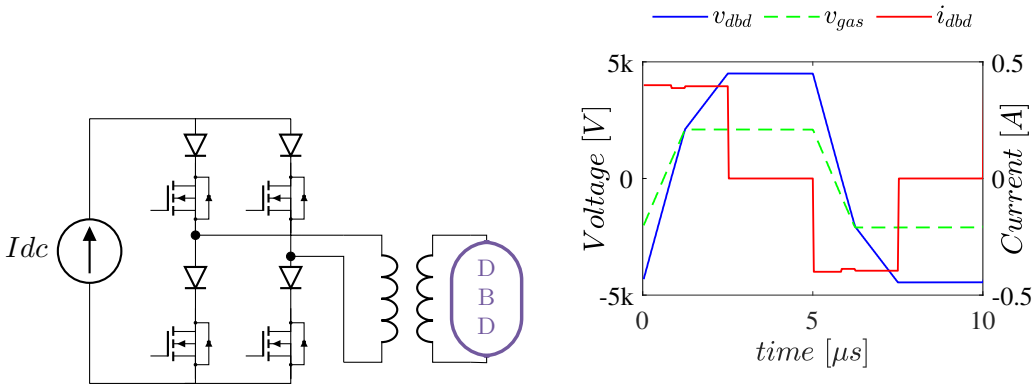

(a) Topology (b) DBD waveforms

Figure 3.8: Pulsed Current Source

With this type of source, the current amplitude, frequency, and duration of the pulses can be controlled. Therefore, the power injected into the DBD is regulated by means of several degrees of freedom. The flexibility of this supply makes it suitable for experimentation purposes. Indeed, [36] employed it to study the effects of the three degrees of freedom on the excimer lamps efficiency. Due to the required hard switching, the electrical efficiency of this power supply is very low.

In accordance with this thesis objectives, the pulsed current source will be used to perform a parametric study of the impact of the operating conditions over the NO_x removal. Additionally, a contribution to the converter analysis, taking into account the parasitic transformer elements, will be presented.

3.3.2.4 Resonant Topologies

Resonant converters are another alternative for designing DBD power supplies. These converters use the capacitive nature of the DBD to create a resonant circuit with at least one additional inductance. Due to their low switching loss, low cost, robust performance, less EMI, and a low number of switching devices, resonant converters are becoming a frequent solution among the DBD systems [37, 38]. In general, resonant converters can be classified based on the resonant tank configuration, or conduction mode. According to the resonant tank configuration, three possible topologies can be distinguished: series, parallel, and mixed. In the series topologies, as the inductance is in series with the DBD, it opposes DBD current changes. Consequently, the inductance acts as a current limiter. DBD sources working with series resonant topologies are proposed in [39–42]. Parallel topologies have quite different characteristics from those of the series resonant converters. For instance, in some parallel topologies, the inductance can be pre-charged, this allows the converter to transfer to the DBD a specific amount of energy previously-stored [27, 33, 43]. The Flyback topology presented above (Figure 3.7-d) is a typical example of a parallel resonant converter with a pre-charged inductance. The buck–boost-based converter shares the same feature. Finally, mixed topologies have characteristics combined from the parallel and series topologies [27].

According to the conduction mode, there are two types of operating modes: continuous and discontinuous. In the converters operating with continuous conduction mode (CCM), the current flows continuously through the DBD, so they usually work at the resonance frequency, or near it. Consequently, the output waveforms have a sinusoidal shape. The series resonant inverter (SRI), presented in Figure 3.9, is widely used in the CCM [37, 41]. Nonetheless, some parallel topologies have also been employed in the CCM operation of DBD [17, 43, 44]. On the other hand, in the discontinuous conduction mode (DCM), the inductance current remains at zero for a portion of the switching cycle [42, 45, 46]. Note that Figure 3.9 uses generic switches to represent the switching devices because the synthesis of the switching cells depends on the conduction mode. Figure 3.10 shows the DBD waveforms of the series resonant inverter working in a continuous and discontinuous mode. Compared with a CCM, the DCM has some advantages: as the time-domain analysis is easier and more accurate in the DCM, the converter design procedure is simpler [42]. Moreover, the zero-current switching can be naturally achieved, reducing the switching losses, and the working frequency is not limited to the resonance frequency.

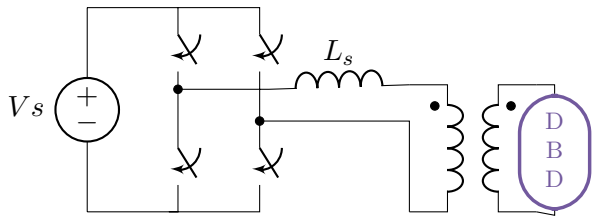

Figure 3.9: Series Resonant Inverter. Full-bridge Topology

In [47], a review of 4 different current-mode topologies is presented; three of them resonant inverters operated in DCM. According to that research, the buck–boost-based resonant converter is the best choice for accurate control of the injected power and stability (parallel

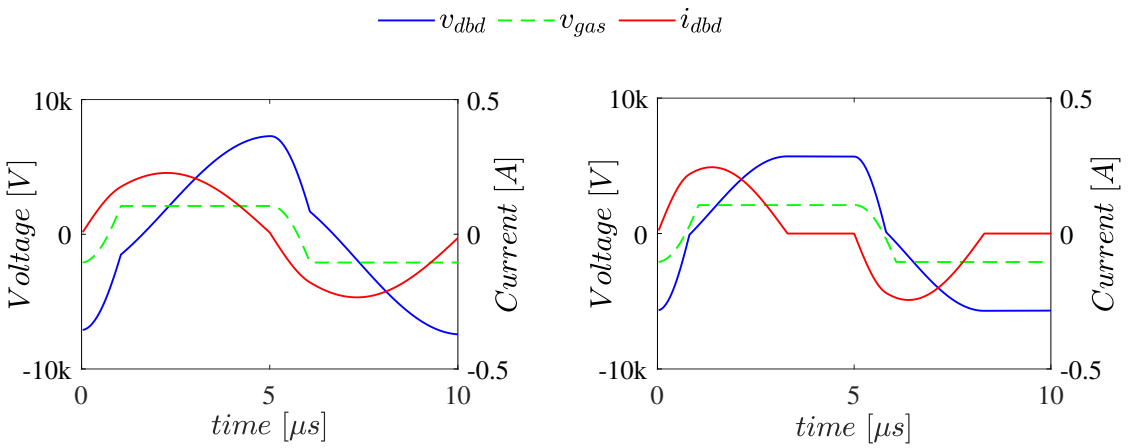

a) Continuous Conduction Mode

b) Discontinous Conduction Mode

Figure 3.10: Series Resonant Inverter Waveforms

topology). In contrast, the boost-based converter requires the lowest input voltage, and the SRI achieves the highest electrical efficiency. Based on this study, SRI working in DCM was one of the converters studied in this project. Therefore, some improvements in this topology were proposed as part of this work [48]. Nonetheless, they were experimentally validated only in a DBD excimer lamp, thus it is out of the NO_x treatment scope.

3.3.2.5 Transformer-less Power Supplies

To provide the high DBD voltage (tens of kV), most of the converters for DBDs require a step-up transformer. However, the parasitic transformer elements significantly affect system behavior [49]. One of the most relevant effects is produced by transformer equivalent capacitance. Due to this element, a significant portion of the DBD current is lost in the transformer and does not flow through the plasma. This may even prevent the discharge ignition. Other effects are produce by the leakage and magnetizing inductance of the transformer, which may create unexpected resonances.

Based on the presented difficulties of converters with transformers, some research has been conducted on designing high-voltage transformers to reduce the parasitic capacitive effects [50]. Although improvements in winding arrangements result in better operation of the power supplies, transformer design is challenging. Therefore, a different approach involves eliminating the step-up transformer [20, 22, 34, 51, 52]. However, even when the transformers' parasitic effects are avoided in a transformer-less power supply, the capacitance of the switches and other components may also affect converter operation. Due to these issues, most of the contributions of this work are in the design of power supplies including the effects of the parasitic elements [48, 53–55].

3.4 Conclusions

In this chapter, the importance of the DBD electrical model for the design and analysis of the power supply has been highlighted. Different models available in the literature were compared to select a simple one that accurately represents the capacitive and non-linear behavior of the DBD load. Furthermore, some characterization techniques, such as the Manley diagram, were introduced.

Based on the DBD electrical model, the comparison of the voltage and current supply modes was carried out. Accordingly, the current supply mode is preferable for driving DBD devices. Two aspects were used to come up with such conclusion. Firstly, the current mode ensures the correct sizing of the converter, since all the electrical waveforms can be easily deduced from the current imposition. Secondly, the current mode has more direct control of the DBD power.

Finally, several power supply topologies for DBD devices were presented. Among these power supplies, three topologies were selected for analysis in this work. The square current source was chosen to perform the study of the injected current parameter on the NO_x treatment. The Series Resonant Inverter, working in DCM, was picked up for the implementation of a highly efficient power supply. The sinusoidal voltage source will be used to compare the results of the current mode supplies with a voltage mode supply. Moreover, the need for including the parasitic elements into the analysis of the converters was stated.

Bibliography

[1] S. Bhosle, G. Zissis, J. J. Damelincourt, A. Capdevila, K. Gupta, F. P. Dawson, and V. F. Tarasenko, "Electrical modeling of an homogeneous Dielectric Barrier Discharge (DBD)," *Conference Record - IAS Annual Meeting (IEEE Industry Applications Society)*, vol. 4, pp. 2315–2319, 2005. doi: https://doi.org/10.1109/IAS.2005.1518783

[2] R. Díez, J.-P. Salanne, H. Piquet, S. Bhosle, and G. Zissis, "Predictive model of a DBD lamp for power supply design and method for the automatic identification of its parameters," *The European Physical Journal Applied Physics*, vol. 37, no. 3, pp. 307–313, 3 2007. doi: https://doi.org/10.1051/epjap:2007017

[3] A. M. Lopez, H. Piquet, D. Patino, R. Diez, and X. Bonnin, "Parameters identification and gas behavior characterization of DBD systems," *IEEE Transactions on Plasma Science*, vol. 41, no. 8, pp. 2335–2342, 2013. doi: https://doi.org/10.1109/TPS.2013.2273462

[4] S. Liu and M. Neiger, "Electrical modelling of homogeneous dielectric barrier discharges under an arbitrary excitation voltage," *Journal of Physics D: Applied Physics*, vol. 36, no. 24, pp. 3144–3150, 12 2003. doi: https://doi.org/10.1088/0022-3727/36/24/009

[5] R. Valdivia-Barrientos, J. Pacheco-Sotelo, M. Pacheco-Pacheco, J. S. Benítez-Read, and R. López-Callejas, "Analysis and electrical modelling of a cylindrical DBD configuration at different operating frequencies," *Plasma Sources Science and Technology*, vol. 15, no. 2, pp. 237–245, 5 2006. doi: https://doi.org/10.1088/0963-0252/15/2/008

[6] U. N. Pal, M. Kumar, M. S. Tyagi, B. L. Meena, H. Khatun, and A. K. Sharma, "Discharge analysis and electrical modeling for the development of efficient dielectric barrier discharge," *Journal of Physics: Conference Series*, vol. 208, p. 012142, 2 2010. doi: https://doi.org/10.1088/1742-6596/208/1/012142

[7] Zhiyu Chen, "PSpice simulation of one atmosphere uniform glow discharge plasma (OAUGDP) reactor systems," *IEEE Transactions on Plasma Science*, vol. 31, no. 4, pp. 511–520, 8 2003. doi: https://doi.org/10.1109/TPS.2003.815241

[8] A. Flores-Fuentes, R. Peña-Eguiluz, R. López-Callejas, A. Mercado-Cabrera, R. Valencia-Alvarado, S. Barocio-Delgado, and A. de la Piedad-Beneitez, "Electrical model of an atmospheric pressure dielectric barrier discharge cell," *IEEE Transactions on Plasma Science*, vol. 37, no. 1, pp. 128–134, 2009. doi: https://doi.org/10.1109/TPS.2008.2006844

[9] N. Naudé, J.-P. Cambronne, N. Gherardi, and F. Massines, "Electrical model and analysis of the transition from an atmospheric pressure Townsend discharge to a filamentary discharge," *Journal of Physics D: Applied Physics*, vol. 38, no. 4, pp. 530–538, 2 2005. doi: https://doi.org/10.1088/0022-3727/38/4/004

[10] U. Kogelschatz, "Dielectric-barrier Discharges: Their History, Discharge Physics, and Industrial Applications," *Plasma Chemistry and Plasma Processing*, vol. 23, pp. 1–43, 2003. doi: https://doi.org/10.1023/A:1022470901385

[11] O. Koudriavtsev, Shengpei Wang, Y. Konishi, and M. Nakaoka, "A novel pulse-density-modulated high-frequency inverter for silent-discharge-type ozonizer," *IEEE Transactions on Industry Applications*, vol. 38, no. 2, pp. 369–378, 2002. doi: https://doi.org/10.1109/28.993158

[12] F. Peeters, "The Electrical Dynamics of Dielectric Barrier Discharges," Ph.D. dissertation, Technische Universiteit Eindhoven, 2015.

[13] T. C. Manley, "The Electric Characteristics of the Ozonator Discharge," *Transactions of The Electrochemical Society*, vol. 84, no. 1, p. 83, 1943. doi: https://doi.org/10.1149/1.3071556

[14] M. Ponce-Silva, J. A. Aqui, V. H. Olivares-Peregrino, and M. A. Oliver-Salazar, "Assessment of the Current-Source, Full-Bridge Inverter as Power Supply for Ozone Generators with High Power Factor in a Single Stage," *IEEE Transactions on Power Electronics*, 2016. doi: https://doi.org/10.1109/TPEL.2016.2520925

[15] R. Díez, H. Piquet, S. Bhosle, and J. M. Blaquière, "Current mode converter for dielectric barrier discharge lamp," *PESC Record - IEEE Annual Power Electronics Specialists Conference*, pp. 2485–2491, 2008. doi: https://doi.org/10.1109/PESC.2008.4592314

[16] L. Wang, X. Tang, S. Luan, and S. Chen, "Comparison and analysis of DBD-ozonizers powered by current-and voltage-mode power supplies," *2015 6th International Conference on Power Electronics Systems and Applications: Electric Transportation - Automotive, Vessel and Aircraft, PESA 2015*, pp. 4–8, 2016. doi: https://doi.org/10.1109/PESA.2015.7398919

[17] Y. Wang, Y. Feng, O. Koudriavtsev, S. Moisseev, Y. Konishi, and M. Nakaoka, "Pulse density modulated soft switching high frequency parallel load resonant current-source inverter with a single auxiliary active resonant snubber," in *4th IEEE International Conference on Power Electronics and Drive Systems. IEEE PEDS 2001 - Indonesia. Proceedings (Cat. No.01TH8594)*, vol. 2, no. June. IEEE, 2010, pp. 657–662. doi: https://doi.org/10.1109/PEDS.2001.975397

[18] S. Hao, C. Zhang, T. Guo, X. Liu, S. Hu, J. Liu, and X. He, "A current-fed asymmetric LLCC resonant converter for DBD applications," *Conference Proceedings - IEEE Applied Power Electronics Conference and Exposition - APEC*, pp. 873–878, 2014. doi: https://doi.org/10.1109/APEC.2014.6803410

[19] A. A. El-deib, "Modeling of and Driver Design for a Dielectric Barrier Discharge Lamp," Ph.D. dissertation, University of Toronto, 2010. [Online]. Available: http://hdl.handle.net/1807/24745

[20] D. Tastekin, Q. K. Nguyen, A. Lunk, and J. Roth-Stielow, "Pulsed voltage converter with bipolar output voltages up to 10 kV for Dielectric Barrier Discharge," *8th International Conference on Power Electronics - ECCE Asia: "Green World with Power Electronics", ICPE 2011-ECCE Asia*, pp. 1558–1565, 2011. doi: https://doi.org/10.1109/ICPE.2011.5944531

[21] T. Shao, D. Zhang, Y. Yu, C. Zhang, J. Wang, P. Yan, and Y. Zhou, "A compact repetitive unipolar nanosecond-pulse gnerator for dielectric barrier discharge application," *IEEE Transactions on Plasma Science*, vol. 38, no. 7, pp. 1651–1655, 2010. doi: https://doi.org/10.1109/TPS.2010.2048724

[22] M. Meißer, R. Kling, and W. Heering, "Transformerless High Voltage Pulse Generators for Bipolar Drive of Dielectric Barrier Discharges," in *Proceedings of the International Exhibition and Conference for Power Electronics, Intelligent Motion and Power Quality 2011 (PCIM Europe 2011)*, vol. 1, no. May, 2011, pp. 243–248.

[23] Y. Mi, J. Wan, C. Bian, Y. Zhang, C. Yao, and C. Li, "A High-Repetition-Rate Bipolar Nanosecond Pulse Generator for Dielectric Barrier Discharge Based on a Magnetic Pulse Compression System," *IEEE Transactions on Plasma Science*, vol. 46, no. 7, pp. 2582–2590, 2018. doi: https://doi.org/10.1109/TPS.2018.2841651

[24] S. Mohapatro, S. Allamsetty, A. Madhukar, and N. K. Sharma, "Nanosecond pulse discharge based nitrogen oxides treatment using different electrode configurations," *High Voltage*, vol. 2, no. 2, pp. 60–68, 2017. doi: https://doi.org/10.1049/hve.2017.0011

[25] A. Zouaghi, A. Mekhaldi, R. Gouri, and N. Zouzou, "Analysis of nanosecond pulsed and square AC dielectric barrier discharges in planar configuration: Application to electrostatic precipitation," *IEEE Transactions on Dielectrics and Electrical Insulation*, 2017. doi: https://doi.org/10.1109/TDEI.2017.006505

[26] P. Davari, F. Zare, and A. Ghosh, "Analysing DBD plasma lamp intensity versus power consumption using a push-pull pulsed power supply," *2013 15th European Conference on Power Electronics and Applications, EPE 2013*, pp. 1–8, 2013. doi: https://doi.org/10.1109/EPE.2013.6634416

[27] M. Meisser, R. Kling, and W. Heering, "Universal resonant topology for high frequency pulsed operation of dielectric barrier discharge light sources," *Conference Proceedings - IEEE Applied Power Electronics Conference and Exposition - APEC*, pp. 1180–1187, 2011. doi: https://doi.org/10.1109/APEC.2011.5744743

[28] J. Kolek, T. Jakubowski, and M. Balcerak, "Impact of voltage shape on efficiency of ozone generation," in *2017 19th European Conference on Power Electronics and Applications (EPE'17 ECCE Europe)*. IEEE, 9 2017, pp. P.1–P.10. doi: https://doi.org/10.23919/EPE17ECCEEurope.2017.8099087

[29] S. Y. Lee, J. S. Gho, B. H. Kang, and J. S. Cho, "Analysis of pulse power converter for plasma application," *IECON Proceedings (Industrial Electronics Conference)*, pp. 556–560, 2008. doi: https://doi.org/10.1109/IECON.2008.4758014

[30] Y. Wang, L. Tong, Q. Han, and K. Liu, "Repetitive High-Voltage All-solid-state Marx Generator for Excimer DBD UV Sources," *IEEE Transactions on Plasma Science*, vol. 44, no. 10, pp. 1933–1940, 2016. doi: https://doi.org/10.1109/TPS.2016.2558519

[31] Y. Achour, J. Starzynski, and A. Lasica, "New Marx Generator Architecture with a Controllable Output Based on IGBTs," *IEEE Transactions on Plasma Science*, vol. 45, no. 12, pp. 3271–3278, 2017. doi: https://doi.org/10.1109/TPS.2017.2766879

[32] Z. Liu, W. J. Wang, H. C. Wei, and C. L. Liu, "A novel ZVS double switch flyback inverter and pulse controlled dimming methods for flat DBD lamp," *IEEE Transactions on Consumer Electronics*, vol. 57, no. 3, pp. 995–1002, 2011. doi: https://doi.org/10.1109/TCE.2011.6018847

[33] V. J. Law, V. Milosavljević, N. O'Connor, J. F. Lalor, and S. Daniels, "Handheld Flyback driven coaxial dielectric barrier discharge: Development and characterization," *Review of Scientific Instruments*, vol. 79, no. 9, pp. 0–11, 2008. doi: https://doi.org/10.1063/1.2988833

[34] B. Chae, J. Min, Y. Suh, H. Kim, and H. Kim, "Pulse Current Generator with Improved Waveform Fidelity for High Voltage Capacitively-Coupled Plasma System," *2018 IEEE Energy Conversion Congress and Exposition, ECCE 2018*, pp. 7179–7185, 2018. doi: https://doi.org/10.1109/ECCE.2018.8558425

[35] D. Florez, R. Diez, H. Piquet, and A. K. Hay Harb, "Square-Shape Current-Mode Supply for Parametric Control of the DBD Excilamp Power," *IEEE Transactions on Industrial Electronics*, vol. 62, no. 3, pp. 1451–1460, 3 2015. doi: https://doi.org/10.1109/TIE.2014.2361601

[36] D. M. Flórez Rubio, "Power Supplies for the Study and Efficient use of DBD Excimer UV Lamps," Ph.D. dissertation, Institut National Polytechnique de Toulouse and Pontificia Universidad Javeriana, 2014.

[37] L. Chang, T. Guo, J. Liu, C. Zhang, Y. Deng, and X. He, "Analysis and design of a current-source CLCC resonant converter for DBD applications," *IEEE Transactions on Power Electronics*, vol. 29, no. 4, pp. 1610–1621, 2014. doi: https://doi.org/10.1109/TPEL.2013.2266376

[38] J. Kolek, S. Kalisiak, and M. Holub, "Resonant, high voltage power supply for non-thermal plasma reactors," *2018 14th Selected Issues of Electrical Engineering and Electronics, WZEE 2018*, pp. 1–6, 2018. doi: https://doi.org/10.1109/WZEE.2018.8748959

[39] S. Kalisiak, M. Hołub, and T. Jakubowski, "Resonant inverter with output voltage pulse-phase-shift control for DBD plasma reactor supply," in *2009 13th European Conference on Power Electronics and Applications, EPE '09*, 2009, pp. 1–9.

[40] M. Meißer, "Resonant behaviour of pulse generators for the efficient drive of optical radiation sources based on dielectric barrier discharges," Ph.D. dissertation, Karlsruher Institut für Technologie (KIT), 2013.

[41] X. Tang, Z. Li, and M. Zhang, "A wide-range frequency model for dielectric barrier discharge type ozone generators powered by series resonant inverters," *IEEE Access*, vol. 7, pp. 124 309–124 314, 2019. doi: https://doi.org/10.1109/ACCESS.2019.2901718

[42] T. Guo, S. Hao, C. Zhang, J. Liu, Y. Deng, and X. He, "Analysis and design of pulse frequency modulation discontinuous-current-mode dielectric barrier corona discharge with constant applied electrode voltage," *IET Power Electronics*, vol. 7, no. 11, pp. 2857–2869, 2014. doi: https://doi.org/10.1049/iet-pel.2013.0840

[43] Y. L. Feng, Y. Konishi, S. P. Wang, Y. X. Wang, E. H. Chu, O. Koudriavtsev, and M. Nakaoka, "Next generation current-Source soft-Switched pdm and ppvm hybrid mode inverter for silent discharge ozone generating tube drive," *Proceedings - IPEMC 2000: 3rd International Power Electronics and Motion Control Conference*, vol. 1, pp. 312–317, 2000. doi: https://doi.org/10.1109/IPEMC.2000.885421

[44] S. Hao, X. Liu, W. Li, Y. Deng, and X. He, "Energy Compression of Dielectric Barrier Discharge with Third Harmonic Circulating Current in Current-Fed Parallel-Series Resonant Converter," *IEEE Transactions on Power Electronics*, vol. 31, no. 12, pp. 8528–8540, 2016. doi: https://doi.org/10.1109/TPEL.2016.2520953

[45] D. Florez, R. Diez, and H. Piquet, "DCM-operated series-resonant inverter for the supply of DBD excimer lamps," *IEEE Transactions on Industry Applications*, vol. 50, no. 1, pp. 86–93, 2014. doi: https://doi.org/10.1109/TIA.2013.2271216

[46] X. Tang, Y. lü, M. Zhang, and Y. Zhu, "Analysis and Experimentation of a New Half-Bridge High-Frequency Resonant Inverter for DBD Type Ozonizer," *Ozone: Science and Engineering*, vol. 41, no. 4, pp. 332–338, 2019. doi: https://doi.org/10.1080/01919512.2018.1535888

[47] R. Diez, H. Piquet, D. Florez, and X. Bonnin, "Current-mode approach in power supplies for DBD excilamps: Review of 4 topologies," *IEEE Transactions on Plasma Science*, vol. 43, no. 1, pp. 452–460, 2015. doi: https://doi.org/10.1109/TPS.2014.2370796

[48] V. Rueda, A. Diop, R. Diez, and H. Piquet, "Series Resonant Inverter Efficiency Improvement with Valley Switching for Dielectric Barrier Discharges," *Proceedings of the International Conference on Power Electronics and Drive Systems*, vol. 2019-July, no. July, 2019. doi: https://doi.org/10.1109/PEDS44367.2019.8998891

[49] D. Florez, X. Bonnin, R. Diez, and H. Piquet, "Impact of the transformer in the current mode supply of dielectric barrier discharge excimer lamps," in *2013 Brazilian Power Electronics Conference*. IEEE, 10 2013, pp. 1171–1176. doi: https://doi.org/10.1109/COBEP.2013.6785263

[50] X. Bonnin, H. Piquet, R. Diez, and D. Florez, "Designing the high voltage transformer of power supplies for DBD: Windings arrangment to reduce the parasitic capacitive effects," in *2013 15th European Conference on Power Electronics and Applications (EPE)*. IEEE, 9 2013, pp. 1–9. doi: https://doi.org/10.1109/EPE.2013.6631928

[51] M. A. Diop, A. Belinger, and H. Piquet, "DBD tranformerless power supplies: impact of the parasitic capacitances on the power transfer." *Journal of Physics: Conference Series*, vol. 825, p. 012004, 4 2017. doi: https://doi.org/10.1088/1742-6596/825/1/012004

[52] A. El-Deib, F. Dawson, and G. Zissis, "Transformer-less current controlled driver for a dielectric barrier discharge lamp using HV silicon carbide (SiC) switching devices," *IEEE Energy Conversion Congress and Exposition: Energy Conversion Innovation for a Clean Energy Future, ECCE 2011, Proceedings*, pp. 1124–1131, 2011. doi: https://doi.org/10.1109/ECCE.2011.6063901

[53] V. Rueda, R. Diez, and H. Piquet, "Optimum transformer turns ratio for the power supply of dielectric barrier discharge lamps," *IET Power Electronics*, vol. 11, no. 1, pp. 62–67, 2018. doi: https://doi.org/10.1049/iet-pel.2016.0497

[54] V. Rueda, A. Wiesner, R. Diez, and H. Piquet, "Enhancement of the DBD power for current-mode converters using the step-up transformer elements," *2018 IEEE Industry Applications Society Annual Meeting, IAS 2018*, pp. 1–8, 2018. doi: https://doi.org/10.1109/IAS.2018.8544496

[55] ——, "Power Estimation of a Current Supplied DBD Considering the Transformer Parasitic Elements," *IEEE Transactions on Industry Applications*, vol. 55, no. 6, pp. 6567–6575, 11 2019. doi: https://doi.org/10.1109/TIA.2019.2933519

Part II

Methodology

Chapter 4

Experimentation Power Supply

Contents

4.1 Introduction

There are three essential aspects to consider in the design of power supplies for any DBD application. The first aspect is the coupled interaction between the power supply waveforms and the application performance. The plasma processes in DBDs are strongly affected by the supply waveforms and operating conditions. Therefore, to find the optimum setting of the current mode excitation, an experimentation power supply is proposed in this chapter. The power supply delivers square current pulses, which control the DBD power through several degrees of freedom. Although this sort of power supplies was initially introduced in [1] for the study of DBD excimer UV lamps, improvements in the implementation and analysis of the converter will be developed.

The second aspect to consider is the DBD electrical model. The previous chapter addressed this point, where a simple electrical model is chosen to analyze the converters. The accuracy of the electrical quantities and waveforms estimation depends on both the model and the converter analysis. Hence their importance for the power supplies design.

Finally, the last aspect for a correct analysis and design of DBD power supplies concerns the effects of the parasitic elements. Due to the capacitive nature of the DBD, elements such as the capacitances of the transformer, switches, and even measurement instruments can strongly alter the supplied waveforms. Additionally, undesirable resonances can be produced by the transformer magnetizing inductance, L_m, and leakage inductance, L_{lk}. The impact of those elements in the supply waveforms also influences the plasma processes. Consequently, this chapter presents and validates the expressions and methods to predict the DBD electrical behavior under the excitation of square current waveforms considering parasitic effects.

The chapter is organized as follows: First, the ideal operation of the DBD excited by square current pulses is presented. Then, the operation under the effects of the parasitic elements of the transformer is introduced. The second section presents the implementation of the power supply and its limitations. Next, some experimental results are shown using the continuous injection of pulses into two different DBD loads: the NO_x treatment reactor and a DBD excimer lamp. Lastly, the implementation of a different supply mode called "burst mode" is introduced. In this mode, a train of current pulses is injected into the DBD, followed by a zero voltage idle time.

4.2 Square Current: Ideal Operation

Figure 4.1 shows the ideal DBD waveforms when a square current is imposed. Due to the capacitive behavior of the DBD, the voltage of the gas, v_{gas}, and dielectric, v_{die}, can be deduced using the injected current and the DBD model of Figure 3.2. The total DBD voltage is calculated as: $v_{dbd} = v_{gas} + v_{die}$. Before the gas breakdown, the injected DBD current only flows through the series capacitance, C_d, and C_g; therefore, the gas current, i_{gas}, is null, and no power is dissipated into the DBD. Once the gas voltage is inverted from $-V_{th}$ to V_{th}, at the time t_{br}, the DBD current starts flowing through the gas conductance until the current pulse extinction at $dT_s/2$. It means that only during the T_{on} time interval, the DBD has an active power consumption, that can be calculated as :

$$P_{dbd} = \frac{2}{T_s}\int_{t_{br}}^{dT_s/2} V_{th} J dt = JdV_{th} - 4f_s C_g V_{th}^2 \tag{4.1}$$

The duration of the discharge, T_{on}, is calculated in Equation 4.2, as the current pulse duration, T_{pulse}, minus the time it takes to produce the gas breakdown, T_{br}. Those time intervals can be derived from the voltage slopes in Figure 4.1. Moreover, the DBD peak voltage, also deduced from Figure 4.1, is computed in Equation 4.3.

$$T_{on} = T_{pulse} - T_{br} \text{ where: } T_{pulse} = \frac{dT_s}{2} \text{ and } T_{br} = \frac{2V_{th}C_g}{J} \tag{4.2}$$

$$\hat{V_{dbd}} = V_{th} + \frac{JdT_s}{4C_d} \tag{4.3}$$

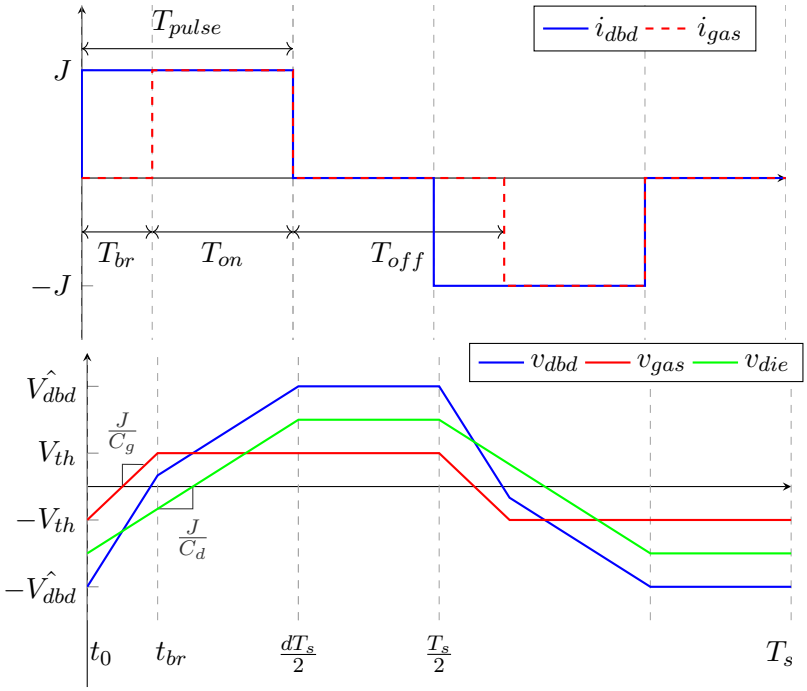

Figure 4.1: Ideal Square Current Source waveforms

4.3 Operation with parasitic Elements

If we consider an ideal transformer and assume that the power supply provides perfect square current pulses, the DBD waveforms and electrical ratings, such as DBD power and peak voltage, can be easily deduced. Nonetheless, both the transformer and the power supply are far from an ideal operation. Therefore, this section studies the operation of the DBD when the square current is injected into a non-ideal transformer.

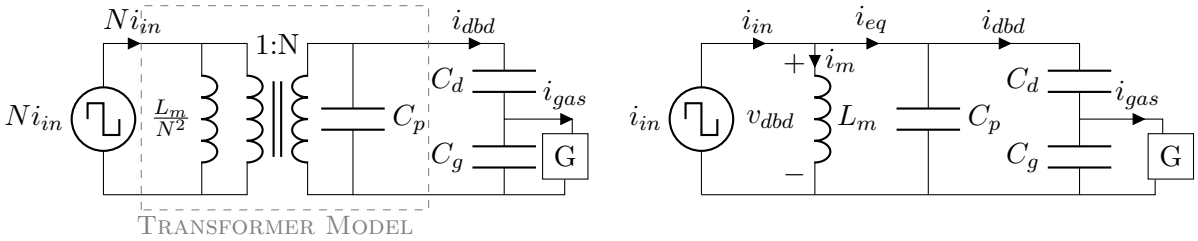

(a) Square Current Source with non-ideal transformer (b) Equivalent circuit seen in secondary winding

Figure 4.2: Equivalent circuit with non-ideal transformer

Figure 4.2-a shows the schematic of the square current source connected to the DBD through a non-ideal transformer. The transformer model includes the magnetizing inductance, which is placed parallel to the primary winding, and the stray capacitance, C_p, which is placed parallel to the secondary winding. At this point, the leakage inductance is neglected; however, its effects will be discussed later. In Figure 4.2-b, all the circuit elements are reflected in the

secondary winding following the transformer turns ratio relation. Observe that i_{eq} represents the sum of currents flowing through the DBD and C_p. Additionally, the current i_{eq} is equal to the input current (ideal square current), i_{in}, minus the magnetizing current i_m.

The DBD waveforms, considering the parasitic elements, are shown in Figure 4.3. In this figure, the red current waveform corresponds to the ideal square current injected into the transformer, i_{in}. The green current waveform is the current flowing through the magnetizing inductance, and the blue current is the DBD current. As can be seen, the DBD current differs from the ideal square current due to L_m, and C_p effects.

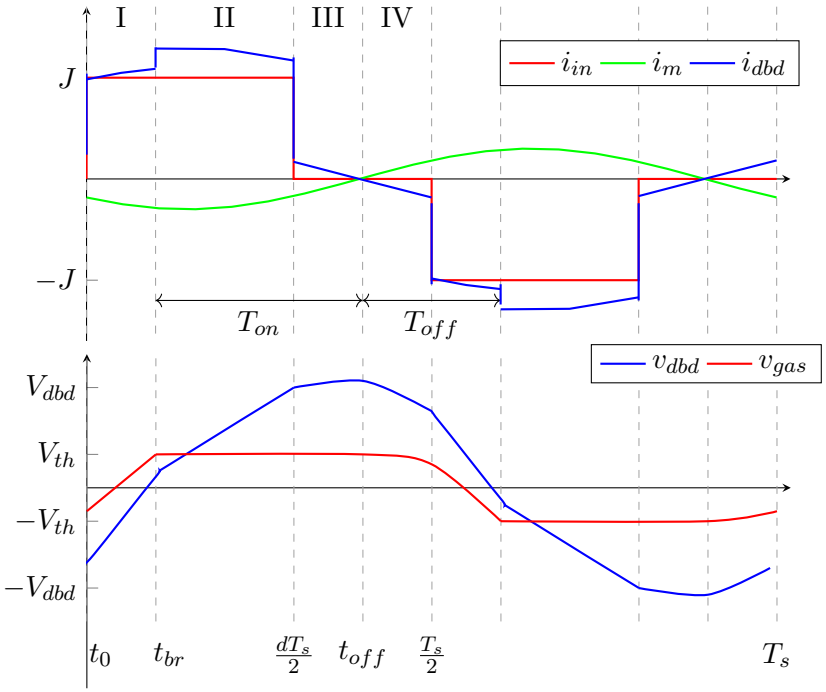

Figure 4.3: Non-ideal square current waveforms

In Figure 4.3, four switching modes can be distinguished for the positive half-cycle (Mode I, II, III, and VI) and the complementary switching modes for the negative half-cycle. The equivalent circuits of the positive switching modes are illustrated in Figure 4.4, and a description of their operation is given below:

- **Mode I** At the time $t = t_0$, the current pulse is injected, however, the DBD remains off until the gas breakdown at $t = t_{br}$. As shown in the voltage waveform of Figure 4.3, v_{gas} is completely inverted from $-V_{th}$ to V_{th} to produce the discharge.

  The equivalent circuit of this switching mode is shown in Figure 4.4-a. As the DBD is off, it can be modeled as a capacitance of C_{eq} value (Equation 3.3), parallel to the transformer stray capacitance C_p. This parallel connection is simplified by $C_{off} = C_p + C_{eq}$, and the resonance frequency is given by $w_{off} = \frac{1}{\sqrt{L_m C_{off}}}$. The current

divider defined by C_p and C_{eq} determines the DBD current.

$$i_{dbd} = \frac{C_{eq}}{C_{eq} + C_p} i_{eq}, \text{ before Breakdown} \tag{4.4}$$

- **Mode II** Once the DBD is ignited, the equivalent DBD model changes. After the breakdown, the DBD is modeled by the dielectric capacitance, C_d, in series with a V_{th} voltage source. As the DBD is in parallel to C_p, the circuit can be reduced to its Thevenin equivalent circuit as shown in Figure 4.4-b, where V_{eq} and C_{on} are:

$$V_{eq} = V_{th} \frac{C_d}{C_d + C_p} \text{ and } C_{on} = C_d + C_p \tag{4.5}$$

  Due to the change of the equivalent DBD capacitance, the resonance frequency must be redefined as $w_{on} = 1/\sqrt{L_m C_{on}}$. And the current divider is redefined as:

$$i_{dbd} = \frac{C_d}{C_d + C_p} i_{eq}, \text{ after Breakdown} \tag{4.6}$$

- **Mode III:** At the time $dT_s/2$ the current pulse ends. In the ideal operation, the discharge extinguishes at this point, and the DBD reaches the peak value. However, due to the parallel branch of the magnetizing inductance, $-i_m$ keeps flowing even though the input current, i_{in}, is null. In consequence, the discharge remains ignited until the cross through zero of the DBD current. In this switching mode, due to the magnetizing current, the DBD voltage continues increasing. The DBD peak voltage is obtained when the magnetizing current is equal to zero at the time $t = t_{off}$. The equivalent circuit of this switching mode is shown in Figure 4.4-c. As the discharge is ignited in both modes II and III, the circuit operates with the same resonance frequency specified above.

- **Mode IV** When the DBD current passes through zero, at t_{off} the DBD is turned off; its voltage reaches the peak value of $\hat{V_{dbd}}$ and starts to decrease according to the magnetizing inductance current. The equivalent circuit of this switching mode is shown in Figure 4.4-d.

4.3.1 Method for the DBD Waveforms Estimation

Due to the complex nonlinear relationships between the duration of the switching modes and the resonant behavior, it is not possible to obtain a closed-form equation to describe the DBD operation with an non-ideal transformer. Accordingly, numerical analysis is proposed to find the solution of the output waveforms under the effects of the parasitic elements. An iterative method to find successively better approximations of the DBD waveforms is proposed [2]. This method starts with the ideal DBD voltage waveform (without the transformer effects), v_{dbd}, to calculate the magnetizing current of the first iteration, following the equation:

$$i_{m,k} = \frac{1}{L} \int v_{dbd,k-1} dt \tag{4.7}$$

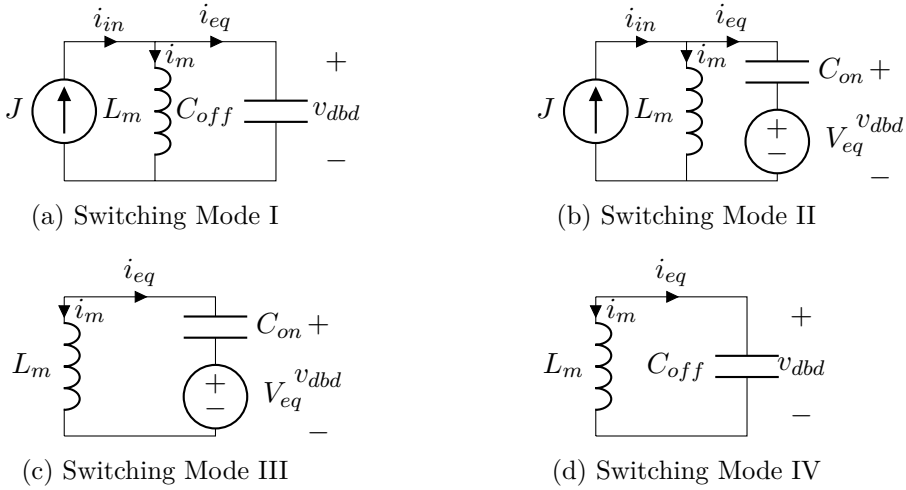

(a) Switching Mode I (b) Switching Mode II

(c) Switching Mode III (d) Switching Mode IV

Figure 4.4: Equivalent circuits of switching modes

where k is the iteration number.

Once the magnetizing current has been calculated, the DBD current can be deduced using the current divider formed between the parasitic capacitance and the DBD :

$$i_{dbd,k} = \begin{cases} \dfrac{(i_{in} - i_{m,k})C_{eq}}{C_{eq} + C_p} & \text{before breakdown,} \\ \dfrac{(i_{in} - i_{m,k})C_d}{C_d + C_p} & \text{after breakdown} \end{cases} \tag{4.8}$$

Then, $i_{dbd,k}$ is used to solve the equations of the DBD model (Equations 4.10-4.11), and thus, to find the DBD voltage and DBD power.

$$v_{gas,k} = \begin{cases} \dfrac{1}{C_g} \displaystyle\int i_{dbd,k} dt & \text{before breakdown,} \\ \pm V_{th} & \text{after breakdown} \end{cases} \tag{4.9}$$

$$v_{die,k} = \frac{1}{C_d} \int i_{dbd,k} dt \tag{4.10}$$

$$v_{dbd,k} = v_{gas,k} + v_{die,k} \tag{4.11}$$

These operations are recursively executed until the calculation of the DBD power converges. The numerical analysis is implemented in Matlab® to achieve a fast estimation of the converter behavior. In order to exemplify the functioning of the method, Figure 4.5 shows the DBD waveforms obtained by the four first iterations for a given operating point. In the DBD voltage plot, the black trace shows the ideal DBD voltage, $v_{dbd,0}$, which is employed for the calculation of $i_{m,1}$, $i_{dbd,1}$, and $v_{dbd,1}$, represented by the blue traces. As can be seen, the waveforms require few iterations to converge, since, after the second iteration, the waveforms

start to overlap. In section 4.5, the method results are compared with experimental data.

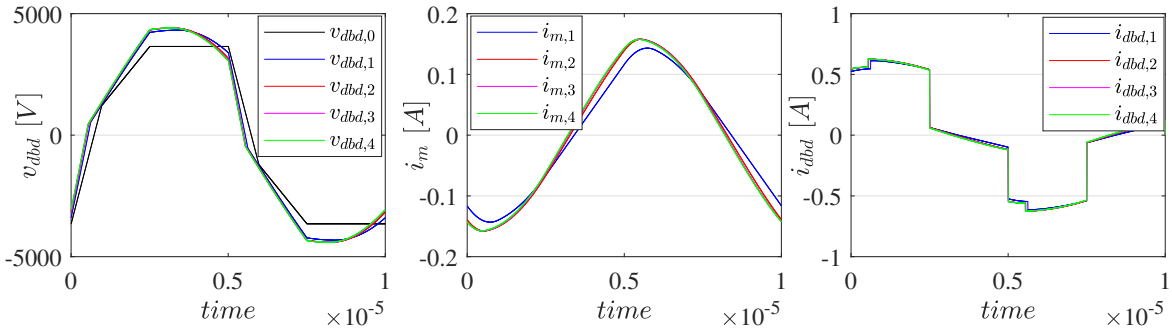

Figure 4.5: Waveforms of the Interactive Estimation of the DBD operation

4.3.2 Effects of the magnetizing inductance

In order to understand how the transformer elements affects the DBD operation, the iterative method is employed to simulate several conditions. First, only the effects of L_m are studied; therefore a negligible stray capacitance is used. On this basis, the DBD power is computed for three different duty cycles of the square current pulses, d, at a fixed current intensity, J, and frequency, f_s, considering a large range of L_m values. Figure 4.6 shows the results, the dotted lines show the ideal DBD power (Equation 4.1). If the magnetizing inductance is large enough, the output power is close to the ideal case, and its effects can be neglected. As the inductance decreases, the resonance frequency gets higher and closer to the switching frequency, f_s, increasing the magnetizing current and output power.

As the magnetizing current charges the gas capacitance during the relaxation time, if this current is high enough, it could cause the discharge ignition even before the current pulse injection. Thus, the discharge time, T_{on} would be mostly controlled by the magnetizing current and not by the input current, i_{in}. Figure 4.7 presents the DBD waveforms of an example operating point for different values of L_m. In these waveforms, it can be seen that the smaller L_m, the higher the current injected to the DBD, and consequently, the higher voltage and power.

4.3.3 Effects of the parasitic capacitance

Figure 4.8 shows the effects of C_p in the output power for a fixed operating point and a high magnetizing inductance. As was previously explained, the parasitic capacitance draws part of the current i_{eq}, decreasing the injected current and power to the DBD. When C_p is comparable to the lamp equivalent capacitance, their effects are stronger, even inhibiting the ignition of the discharge. In order to have the maximum power injected into the DBD, the minimization of the parasitic capacitance of the transformer, and other parasitic capacitances such as the ones from switches or voltages probes, is necessary. Three different values of C_p are used in Figure 4.9 to exemplify the effects of C_p at a given operating point.

In general, to maintain the converter close to the ideal operation, the transformer design should maximize the magnetizing inductance while the stray capacitance is minimized.

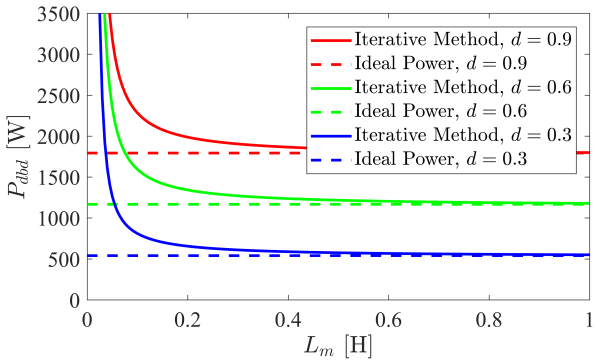

Figure 4.6: Impact of L_m in the DBD Power. Example Conditions: $C_p = 1\ pF$, $N = 10$, $C_d = 299\ pF$, $C_g = 119\ pF$, $V_{th} = 1740\ V$, $J = 1.2\ A$, $f_s = 60\ kHz$

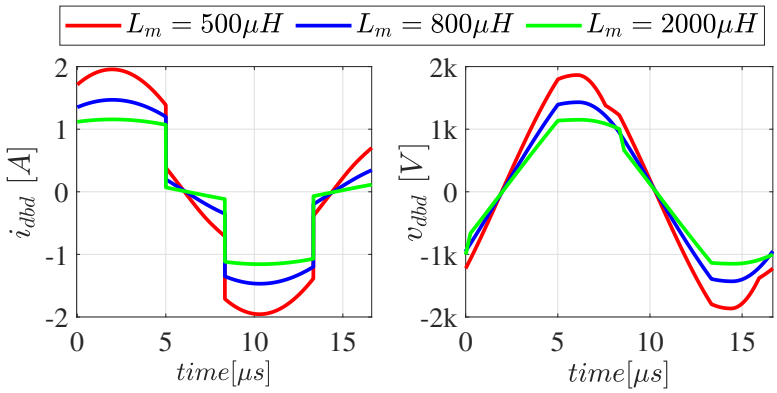

Figure 4.7: Impact of L_m in the DBD Waveforms. Example Conditions: $C_p = 1\ pF$, $N = 10$, $C_d = 299\ pF$, $C_g = 119\ pF$, $V_{th} = 1740\ V$, $J = 1.2\ A$, $f_s = 60\ kHz$

Nonetheless, it is very challenging to design a high voltage transformer following such requirements. As an alternative, with this analysis, a smaller magnetizing inductance can be employed, leading to a smaller transformer. This will enhance the DBD power and simplify the transformer design since the parasitic capacitance can be minimized more easily with a smaller transformer.

4.4 Implementation of the Square Current Source

In order to provide square current pulses, controlled in frequency, f_s, amplitude, J, and pulse duration, T_{pulse}, the converter presented in Figure 4.10 is suggested. The power supply consists of a Constant Current Source (CCS), connected in cascade with a full-bridge current inverter, a step-up transformer, and the DBD load. With this topology, the current amplitude, J, is controlled by the DC current source. Whereas, the frequency, f_s, and pulse duration, T_{pulse}, are controlled by the current inverter.

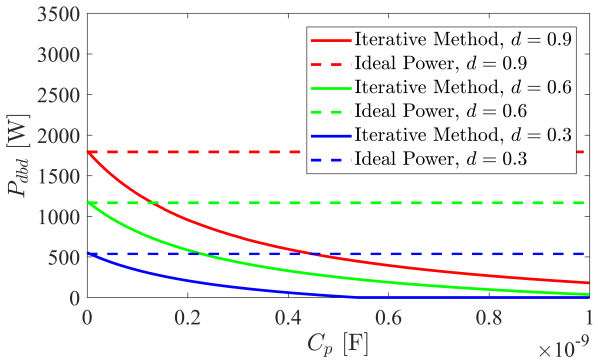

Figure 4.8: Impact of C_p in the DBD Power. Example Conditions: Example Conditions: $L_m = 1\ H$, $N = 10$, $C_d = 299\ pF$, $C_g = 119\ pF$, $V_{th} = 1740\ V$, $J = 1.2\ A$, $f_s = 60\ kHz$

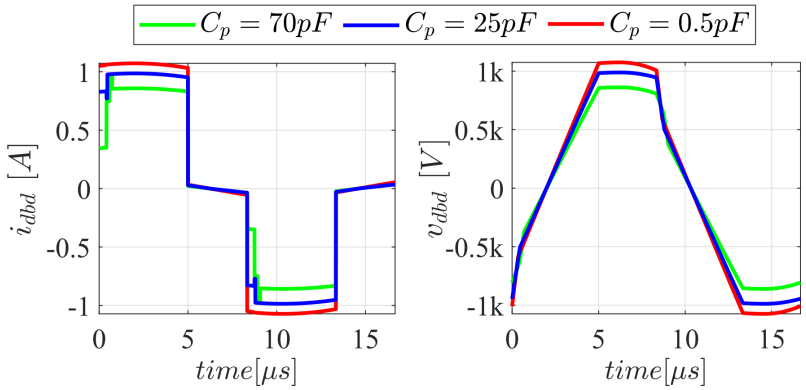

Figure 4.9: Impact of C_p in the DBD Waveforms. Example Conditions: $L_m = 1\ H$, $N = 10$, $C_d = 299\ pF$, $C_g = 119\ pF$, $V_{th} = 1740\ V$, $J = 1.2\ A$, $f_s = 60\ kHz$

4.4.1 Constant Current Source (CCS)

The CCS converts the input voltage, V_{in}, into a direct current, i_{DC}, which is delivered to the current inverter. Accordingly, the CCS has to drive a non-linear load with bidirectional voltages. With such characteristics in mind, a two-quadrant chopper converter connected to the inverter through an L filter is proposed. Figure 4.10 shows the CCS, including a schematic of the implemented current mode controller, which regulates the current amplitude. The current controller operates at a frequency ($f_{ch} = 1/T_{ch}$), higher than the frequency of the current inverter ($f_s = 1/T_s$). This section describes the CCS operation and presents the selection of chopper frequency, the computation of the minimum voltage required to attain a desired current, and the current ripple of the inductance L.

Let us start by examining the two-quadrant chopper operation. In this circuit, the two switches, M, are controlled simultaneously. When both M switches are ON, the chopper output voltage, v_{ch}, is directly connected to the input voltage, V_{in}. In this case, the diodes D are reverse biased, so they are in an open state. On the other hand, when M switches

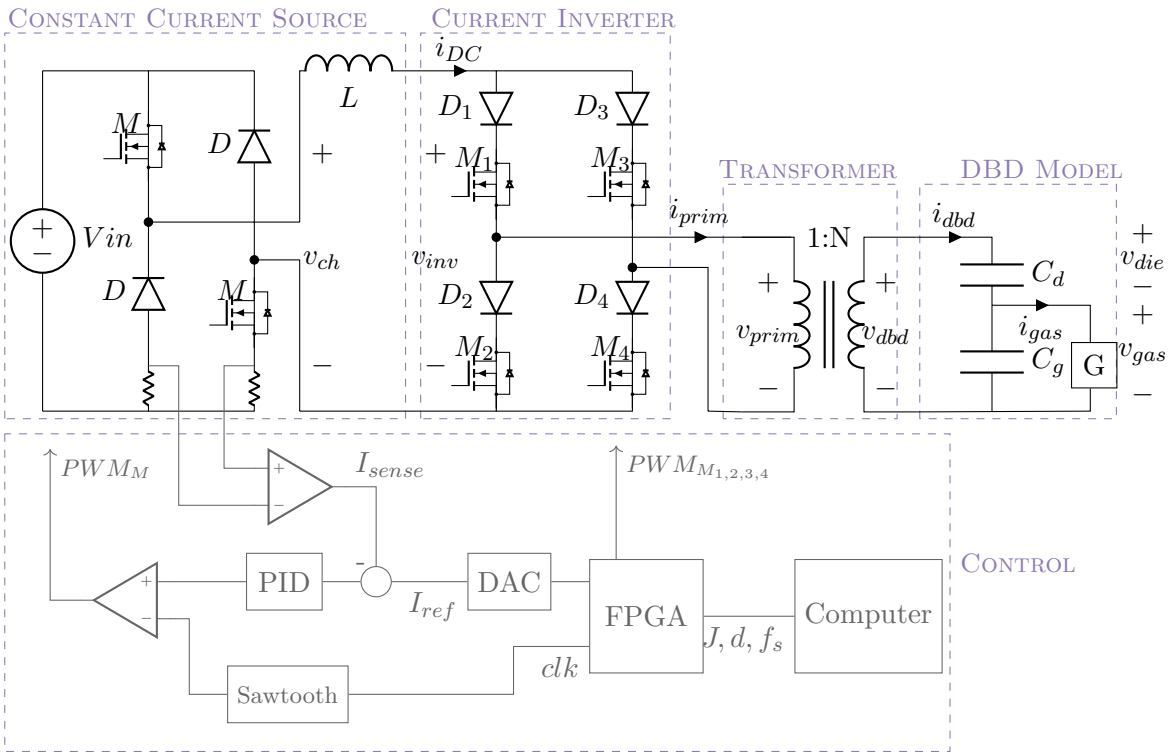

Figure 4.10: Square Current Source Topology with the average current-mode controller

are turned OFF, both diodes D starts conducting since the inductance L opposes sudden drops on its current. In consequence, when M switches are off, v_{ch} is connected to $-V_{in}$. It should be noted that the direction of the current i_{DC} is always positive since the diodes and MOSFETs only conduct in one direction.

On the other hand, the current inverter shapes the DC current, i_{DC}, into the square current pulses shown in Figure 4.1. For this purpose, the current inverter has four switching states, which produce a voltage in its input, v_{inv}, equals to:

$$v_{inv}(t) = \begin{cases} 0 & 0 \leq t < \dfrac{d'T_s}{2} & M_{1,2} \text{ ON}, \\ v_{prim} & \dfrac{d'T_s}{2} \leq t < \dfrac{T_s}{2} & M_{1,4} \text{ ON}, \\ 0 & \dfrac{T_s}{2} \leq t < \dfrac{T_s(d'+1)}{2} & M_{3,4} \text{ ON}, \\ -v_{prim} & \dfrac{T_s(d'+1)}{2} \leq t < T_s & M_{2,3} \text{ ON} \end{cases} \tag{4.12}$$

where v_{prim} is the DBD voltage reflected in the transformer primary winding, $d' = (1-d)$, d is the duty cycle of the square current pulses, and T_s is its period.

4.4.1.1 Chopper Operating Frequency

In order to have a better understanding of the CCS operation, Figure 4.11 presents the key waveforms of the converter working at two different chopper frequencies, f_{ch}. In Figure 4.11-a the frequency of the chopper is twice the frequency of the inverter, $f_{ch} = 2f_s$, whereas in Figure 4.11-b $f_{ch} = 2.5f_s$.

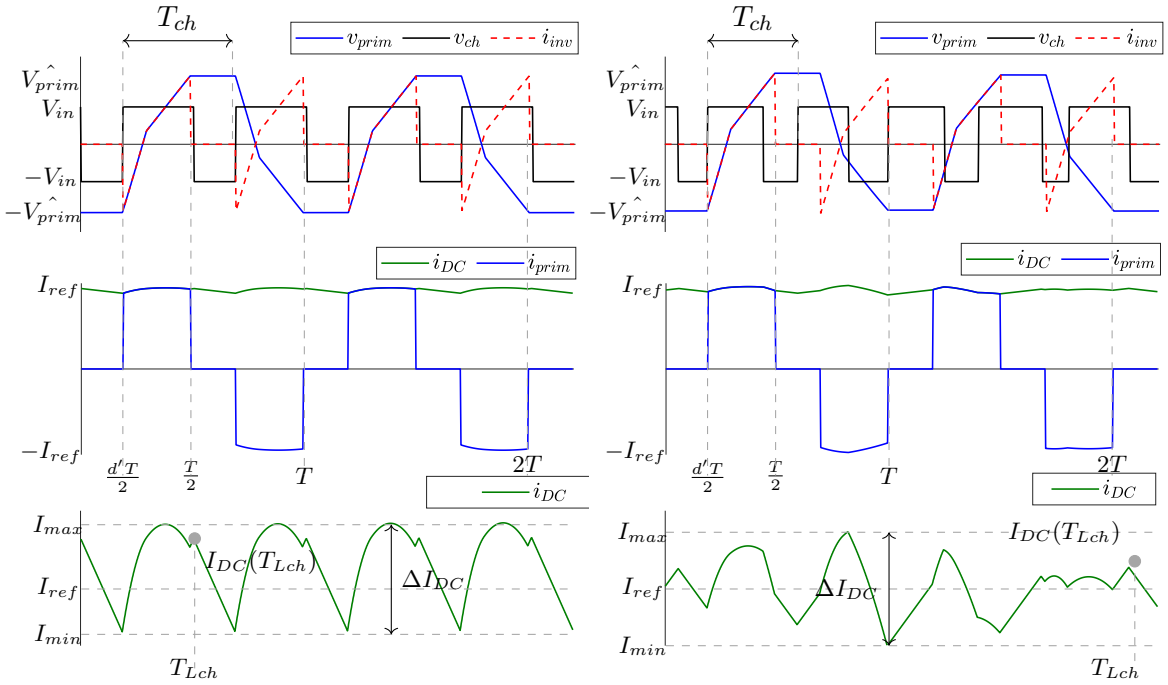

a) Example waveforms $f_{ch} = 2f_s$

b) Example waveforms $f_{ch} = 2.5f_s$

Figure 4.11: Constant Current Source Waveforms with average current-mode control

The inductance current, i_{DC}, can be found by integrating the voltage across the inductance, v_L.

$$v_L(t) = L\frac{i_L(t)}{dt} = v_{ch}(t) - v_{inv}(t) \tag{4.13}$$

Given that the frequency of both v_{ch} and v_{inv} are different, the resulting frequency of the v_L in steady state will determine the frequency of i_{DC}. On account of the fact that the fundamental frequency of a signal is the greatest common divisor (GCD) of all the involved frequencies, one can compute the frequency of i_{DC} as:

$$f_{L_{ch}} = GCD(2f_s, f_{ch}) \tag{4.14}$$

Accordingly, the current of the inductance, i_{DC}, can be sketched. The current begins at

some initial value $i_{DC}(0)$. When the voltage across the inductance, v_L, is positive, the current will increase; otherwise, the inductance current decreases. At some point, the desired average current, I_{ref} is achieved because of the average-current mode controller. As can be seen in Figure 4.11-b, the current waveform has a high frequency component due to the switching frequency of the chopper, and depending of the resulting frequency of v_L, the current waveform may have a lower frequency component at $f_{L_{ch}}$.

In the case of Figure 4.11-b, at steady state $f_{L_{ch}} = 0.5f_s$ (Equation 4.14). Given that $f_{L_{ch}}$ is lower than f_s, the amplitude of the DBD current pulses is not always the same, and an asymmetrical operation between the positive and negative pulses is observed. On the contrary, in the case presented in Figure 4.11-a, where $f_{ch} = 2f_s$, the resulting frequency is $f_{L_{ch}} = 2f_s$. Therefore, the current injected to the DBD in the positive pulse is completely symmetrical to the current injected in the negative one. Moreover, the converter steady-state operation can be easily analyzed, and the amplitude of all the current pulses will be the same.

As the inverter frequency, f_s, and duty cycle, d, are selected according to the desired DBD experimentation conditions, it is complex to estimate the converter steady-state waveforms when the chopper frequency is fixed. Nonetheless, by selecting the chopper frequency as a function of the inverter frequency, a predictable operation can be achieved. Accordingly, the chopper operating frequency is defined as $f_{ch} = 2f_s$.

4.4.1.2 Steady State Operation

For an steady state operation, the inductance volt-second balance must be achieved. It means that the net charge in the inductance over one period $T_{L_{ch}}$ has to be zero.

Integrating Equation 4.13 over $T_{L_{ch}}$ we obtain :

$$\begin{aligned} i_{DC}(T_{L_{ch}}) - i_{DC}(0) &= \frac{1}{L}\int_0^{T_{L_{ch}}} V_L(t)dt = \frac{T_{L_{ch}}}{L}\langle v_L\rangle_{T_{L_{ch}}} \\ &= \frac{T_{L_{ch}}}{L}\left(\langle v_{ch}\rangle_{T_{L_{ch}}} - \langle v_{inv}\rangle_{T_{L_{ch}}}\right) \end{aligned} \tag{4.15}$$

In steady-state, $i_{DC}(0) = i_{DC}(T_{L_{ch}})$, therefore, the average of v_L must be zero.

$$\langle v_L\rangle_{T_{L_{ch}}} = \frac{1}{T_{L_{ch}}}\int_0^{T_{L_{ch}}} v_L(t)dt = 0 \tag{4.16}$$

Assuming $f_{ch} = 2f_s$, we obtain that $T_{L_{ch}} = T_s/2$, and based on the ideal waveforms of the DBD presented in Figure 4.1, the average value of v_L can be calculated as:

$$\langle v_L\rangle_{T/2} = \frac{2JNT_sV_{in}d_{ch} - JNT_sV_{in} - JT_sV_{th}d + 4C_gV_{th}^2}{JT_s} = 0 \tag{4.17}$$

where d_{ch} is the duty cycle of the chopper, V_{in} is the input voltage, N is the transformer turns ration, J, d, and T_s are the parameters of the current pulses, and C_d, C_g, and V_{th} are the parameters of the DBD model. By solving Equation 4.17 for d_{ch}, we can find the duty cycle of the chopper at the steady-state.

$$d_{ch} = \frac{1}{2}\frac{J(NV_{in} + V_{th}d) * T_s - 4V_{th}^2 C_g}{JNT_s V_{in}} \tag{4.18}$$

Additionally, since the maximum value of d_{ch} is 1, we can find the minimum input voltage, V_{in}, that guarantees the current control of i_L. Hence, substitution of $d_{ch} = 1$ into Equation 4.18 yields

$$V_{inMIN} = \frac{V_{th}}{N}(d - \frac{4C_g V_{th}}{JT_s}) \tag{4.19}$$

The minimum V_{in} voltage depends on the conditions of the current pulses. Thus, V_{inMIN} has to be calculated for critical values of the J, d, and T_s range. However, examining Equation 4.19, one can see that it has an horizontal asymptote. Hence, if $V_{in} > V_{th}/N$ is ensured, the current of all the operating points will be controlled.

4.4.1.3 Current Ripple

To dimension the inductance L, the current ripple, Δi_{DC}, has to be calculated. Figure 4.12 presents the four possible cases identified for the current ripple calculation. In all cases the peak current is defined according to the following d_{ch} and V_{in} boundaries:

When d_{ch} is higher than d ($d_{ch} > d$), the cases A and B of Figure 4.12 can be attained. In the first case, the peak current is obtained before $dT_s/2$; therefore, the current current ripple can be calculated as:

$$\Delta i_{DCCaseA} = \frac{1}{L}\int_0^{t_{pk}} V_{in} - v_{inv}(t)dt \tag{4.20}$$

where t_{pk} is time at the peak current, computed when ($v_{inv}(t) = V_{in}$).

$$t_{pk} = \frac{(V_{in} - V_{br})C_d}{J} + T_{br} \tag{4.21}$$

Solving Equation 4.20:

$$\Delta i_{DCCaseA} = \frac{1}{32}\frac{16C_d^2\left(NV_{in} - V_{th}\right)^2 + C_d\left(8JNT_sV_{in}d - 8JT_sV_{th}d + 64C_gV_{th}^2\right) + J^2T_s^2d^2}{JLNC_d} \tag{4.22}$$

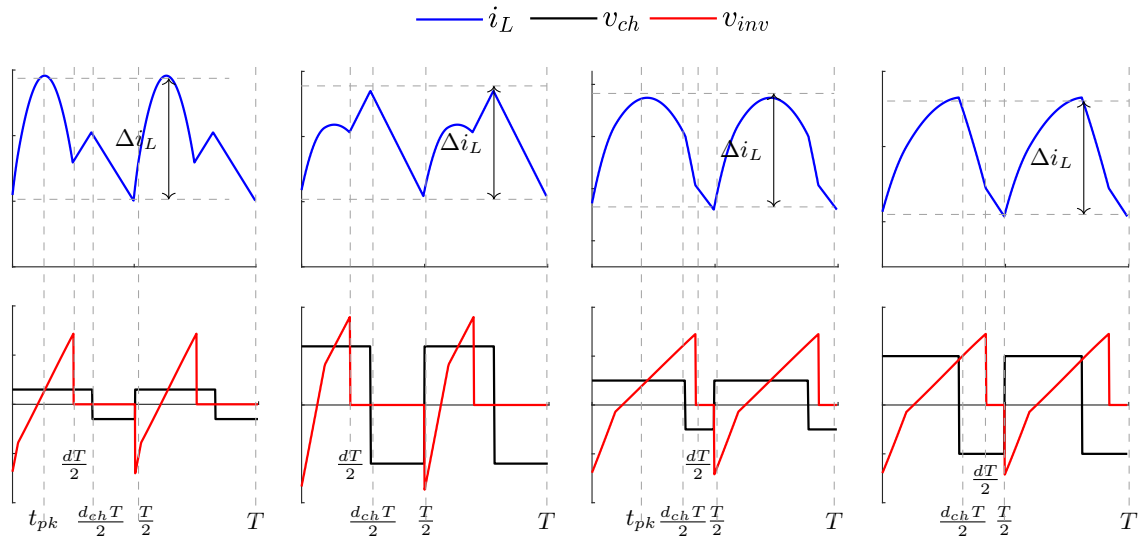

a) Case A: $d_{ch} > d$ $V_{in} < V_{inAB}$

b) Case B: $d_{ch} > d$ $V_{in} > V_{inAB}$

c) Case C: $d_{ch} < d$ $V_{in} < V_{inCD}$

d) Case D: $d_{ch} < d$ $V_{in} > V_{inCD}$

Figure 4.12: Current ripple cases

On the other hand, when the peak current is obtained after $dT_s/2$ (Case B), the current ripple is determined by:

$$\Delta i_{DCCaseB} = \frac{1}{L}\int_{\frac{d_{ch}T_s}{2}}^{\frac{T_s}{2}} V_{in}dt = \frac{V_{in}T_s(1-d_{ch})}{2L} \tag{4.23}$$

Combining Equations 4.22 and 4.23, and solving for V_{in}, we deduce the boundary input voltage, V_{inAB} between the cases A and B is:

$$V_{inAB} = \frac{1}{4}\frac{-\sqrt{J^2T_s^2\left(1-2d\right) - 8C_dV_{th}JT_s\left(d-1\right) - 32C_dC_gV_{th}^2} + 4C_dV_{th} - JT_s\left(d-1\right)}{NC_d} \tag{4.24}$$

In the same way, the current ripple for the cases where the $d_{ch} < d$ can be deduced (Cases C and D). The ripple of case C is the calculated exactly as Case A (Equations 4.20 and 4.22). However, for case D we obtain:

$$\Delta i_{DCCaseD} = \frac{1}{L}\int_{0}^{\frac{d_{ch}T_s}{2}} V_{in} - v_{inv}(t)dt \tag{4.25}$$

$$\Delta i_{DCCaseD} = \frac{1}{32}\frac{1}{JLN^3C_dV_{in}^2}\Big[8C_dJT_sN^3V_{in}^3 - {V_{th}}^2(dT_sJ - 4V_{th}C_g)^2 + \\ + 2N^2{V_{in}}^2(T_s^2J^2(d-1/2) + 4C_dT_sV_{th}J(-1+d) + 16{V_{th}}^2C_gC_d) + \\ + 2V_{th}NV_{in}(T_sJ(-1+d) - 4V_{th}C_d)(dT_sJ - 4V_{th}C_g)\Big] \tag{4.26}$$

Solving Equation 4.22 equals to 4.26 for V_{in}, the boundary input voltage between cases C and D is found.

$$V_{inCD} = \frac{\sqrt{{J^2T_s}^2(d-1)^2 + 8C_dV_{th}JT_s(d+1) + 16C_d{V_{th}}^2(C_d - 4C_g)} + 4V_{th}C_d - JT_s(d-1)}{8NC_d} \tag{4.27}$$

4.4.1.4 Controller Implementation

In order to implement the CCS controller, three requirements are established. First, the controller must allow a programmable switching frequency, since, as previously explained, it has to be twice the frequency of the current pulses. Additionally, it is desirable to have a stackable configuration. With this feature, several CCS can be connected in parallel to deliver a higher constant current. Moreover, as the stacked CCSs can be configured at the same frequency and interleaved phase shift, the current ripple can be decreased [3]. For this work, the interleaved configuration was not implemented. Nonetheless, it was a requirement for later uses of the converter. Finally, the controller must perform the average current-mode control for a large range of output currents.

According to such requirements, the integrated circuit TPS40180 was the chosen controller. The TPS40180 is usually employed for controlling stackable synchronous buck converters. It has two control loops for such purposes: the inner control loop regulates the peak inductor current, whereas the outer loop controls the buck output voltage. For the CCS converter, only one loop is required. In [3], a current source for DBD excimer lamps was implemented using the peak current-mode controller of TPS40180. However, the peak current-mode has a low noise immunity, as any noise spike can trigger the peak current detection and cause a false commutation. This problem is of particular importance for the application due to the high voltage and noisy environment.

On the contrary, the average current-mode controller regulates the state variable of interest directly by comparing it to the current set point. The noise immunity of the average current controller is higher than the peak current, and no compensation ramp is required. However, it is slower than the peak current-mode controller. Another difference between both modes is related to the current sensing. In the case of the peak current-mode, the current could be measured in any of the chopper legs since the inductance peak current is equal to the peak current of each leg. Conversely, the average current-mode requires the direct measurement of

the inductance current, which can be obtained directly on the inductance, or by the differential measure of both chopper legs current, as depicted in Figure 4.10.

4.4.2 Sizing of the converter components

To dimension the power supply, an experimental characterization of the DBD reactor was performed. The resulting values of the model parameters are: $C_d = 80\ pF$, $C_g = 125\ pF$, $V_{th} = 1400\ V$. Additionally, the following specifications for the converter are set up:

- Maximum CCS output current, $i_{DCmax} = 12\ A$
- Maximum CCS ripple, $\Delta i_{DC} = 0.05 i_{DC}$
- Frequency range for the current inverter $f_s = 50 - 200\ kHz$
- Power range $P_{dbd} = 0 - 500\ W$

The transformer design is a crucial step for DBD system. It adapts the reactor high voltage requirements to the converter, changes the range of the operating points which can explored, and introduces unwanted effects due to its parasitic elements. Concerning the range of the operating points, we can observe how the transformer turns ratio limits it. The higher the turns ratio, the lower the amplitude of the current pulses, $J = i_{DC}/N$. Whereas the lower the turns ratio, the higher the switches stress voltage $V_{prim} = V_{dbd}/N$. Accordingly, to maintain a wide range of current amplitudes and a safe operation of the converter, a suitable high voltage solution for the switching devices is required. In this way, lower turn ratios could be used, which is also preferable for the application since the transformer size and stray capacitance can be more easily minimized.

Silicon Carbide (SiC) power devices are a compelling solution for the application due to their high blocking voltage, high thermal capacity, and low switching losses. The typical breakdown voltage of SiC devices ranges from 600 V to 1.7 k V, and the amperage from 5A to 40A. After comparing several SiC MOSFET and diodes, the following devices are selected. The MOSFET C2M0080120D, fabricated by Wolfspeed/Cree, is a $1200\ V - 36\ A$ device, with a low on-resistance and low output capacitance ($R_{DS_{ON}} = 80\ m\Omega$, and $C_{oss} = 92\ pF$). The Schottky diode GC2X8MPS12, from GeneSiC, withstands $1200\ V - 30\ A$. Both the CCS and current inverter are implemented using these devices.

The initial characterization of the DBD reactor established the need for a peak voltage of around $10\ kV$ to produce the electric discharge. Based on the DBD requirements and chosen MOSFETs and diodes blocking capabilities, the transformer turns ratio, $N = 11$, was calculated with a security margin of 25%. As a result, the maximum amplitude of the DBD current pulses is $J = 1.09\ A$.

As was exposed before, the transformer design must reduce the parasitic capacitance and leakage inductance while maximizing the magnetizing inductance. Bonnin et al. presents a guide for DBD transformers design which minimize the parasitic capacitance for different winding arrangements [4]. Following their analysis, the optimum arrangement to reduce C_p is to use a single layer for the primary and secondary winding. It should be pointed out that the single-layer configuration results in a longer effective length and consequently a bigger transformer. Table 4.1 summarizes the assembly conditions of the transformer.

Characteristic	Description
Core	Material: 3C90
Primary Winding	Turns: 14 turns - Wire: Litz 81x39AWG
Secondary Winding	Turns: 154 turns - Wire: Litz 9x39 AWG
Isolation	Material: PLA, Depth: 3 mm

Table 4.1: Assembly conditions of the step-up transformer

The transformer was characterized in order to identify its model parameters. The frequency analyzer N4L PSM1700 was used to perform a frequency sweep from 100 Hz to 1.1 MHz in open and short circuit conditions. The obtained phase and amplitude impedance bode plots are illustrated in Figure 4.13. According to the resonance frequencies, the following values are deduced: $C_p = 17\ pF$, $L_m = 550\ \mu H$, and $L_{lk} = 3.4\ \mu H$.

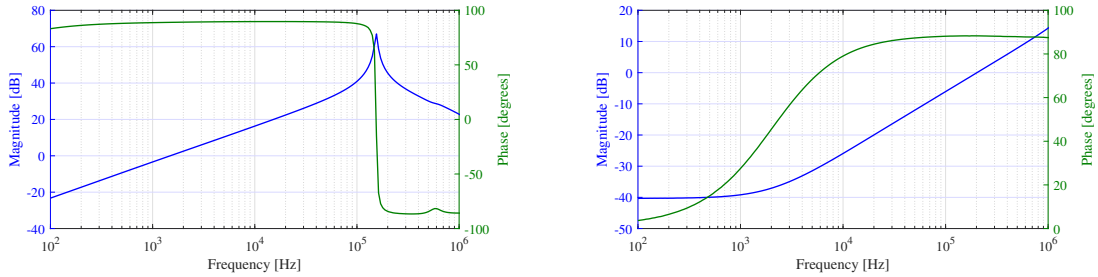

(a) Secondary winding open circuit (b) Secondary winding short circuit

Figure 4.13: Amplitude and Phase Bode Plots of step-up transformer

Finally, the filter inductance L was calculated to fulfill the current ripple requirements. The analysis of Section 4.4.1.3 was used for this calculation. The input voltage was fixed at $V_{in} = 200\ V$, which is higher than the minimum input voltage condition ($V_{in} > V_{th}/N$). The resulting value of L was 5 mH. Figure 4.14 shows the implemented power supply.

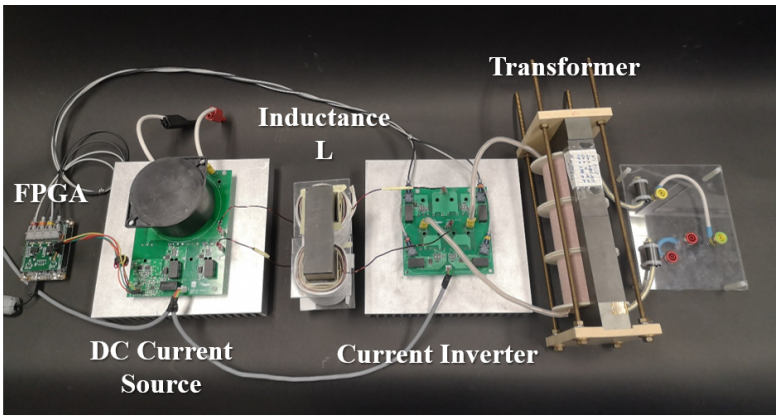

Figure 4.14: Implementation of the Square Current Source

4.5 Experimental Results

The experimental validation of the power supply was carried out for two different DBD loads: the NO_x treatment reactor and a DBD Excimer Lamp. Note that the DBD lamp is not related to the treatment of gases, which is the main focus of this research work. Nonetheless, it was used for testing the working principle of the converters and analysis methods. Moreover, as the DBD lamps have been subject to investigation of our research groups for several years, they were available for experimentation purposes since the early stages of the thesis.

4.5.1 DBD NOx reactor

The experimental waveforms of the NO_x treatment reactor working at four different operating conditions are shown in Figure 4.15 (red traces). The first two cases operate at a frequency of $f_s = 100\ kHz$, whereas the other two operate at $f_s = 200\ kHz$. In addition to the experiment waveforms, each plot presents the DBD waveforms obtained by ideal analysis (black traces), and the waveforms estimated considering the parasitic elements based on the iterative method proposed in Section 4.3.1 (blue traces).

The first remarkable difference between the experimental and estimated waveforms is a high-frequency oscillation in the DBD current. This oscillation is mainly caused by a resonance between the transformer leakage inductance, the equivalent DBD capacitance, and parasitic elements. Even though the estimated waveforms do not include the effects of the leakage inductance, it can be seen that the iterative method provides a good approximation of the DBD voltage, and Q-V plot.

Table 4.2 and 4.3 compares the estimation of the DBD power, P_{dbd}, and DBD peak voltage $\hat{V_{dbd}}$, using the ideal analysis and the iterative method. From Table 4.2, it can be observed that the DBD power is significantly underestimated with the ideal analysis at the low frequency cases ($f_s = 100\ kHz$). On the opposite side, at the high-frequency cases ($f_s = 200\ kHz$), the ideal analysis overestimates the power. This error in the calculation agrees with the effects of the magnetizing inductance and transformer stray capacitance. The lower the switching frequency, the closer it is to the resonance; therefore, the magnetizing current boosts the DBD current, and consequently, the DBD power and peak voltage increase. As the switching frequency increases, the magnetizing current decreases until its effects are neglected, which is the case of operating points at $f = 200\ kHz$. Here, the effects of the parasitic capacitance are dominant. Due to the current divider formed by the stray capacitance and the DBD equivalent capacitance, the DBD current decreases, so the power and peak voltage.

According to the data of Table 4.2, the average error of the power estimation with the ideal analysis is 21.3%, whereas the iterative method provided an average error of 3.8%. In like manner, the average error of the peak voltage estimation with the ideal analysis is 12.9%, and for the iterative method is 1%.

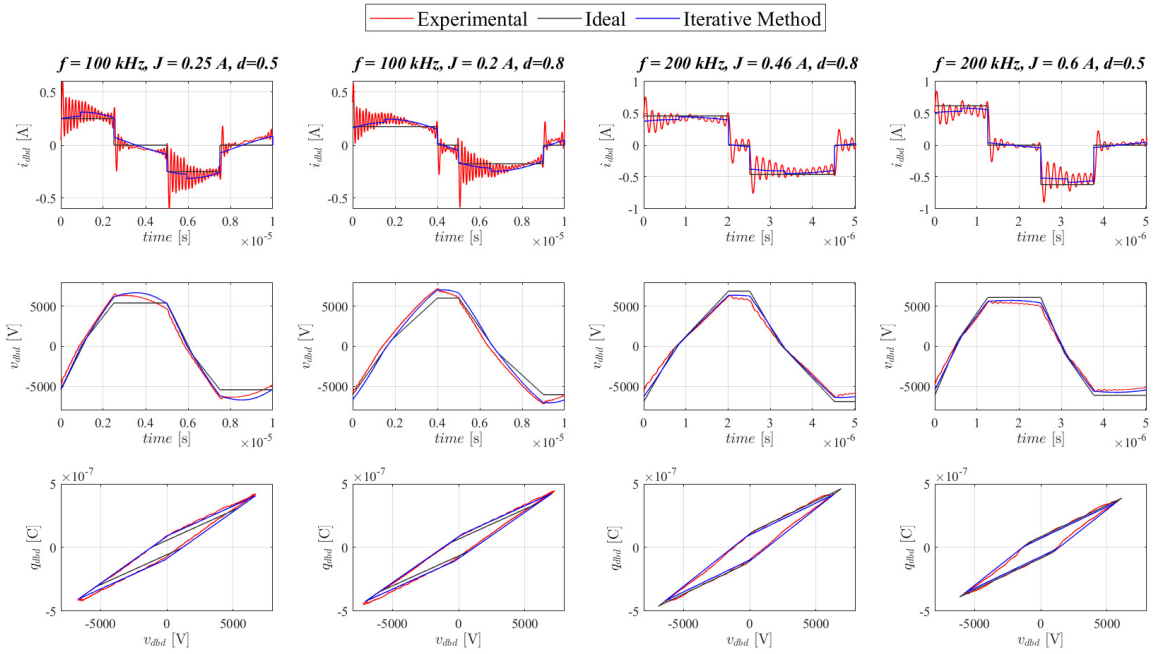

Figure 4.15: NO_x Reactor: DBD waveforms for different operating points.

Operating Point	P_{dbd} Exp.	P_{dbd} Ideal	P_{dbd} Iter. Method	Error P_{dbd} Ideal	Error P_{dbd} Iter. Method
$f = 100kHz, J = 0.25A, d = 0.5$	115 W	75 W	119 W	-34.6 %	3.6%
$f = 100kHz, J = 0.2A, d = 0.8$	122 W	91 W	126 W	-25.5%	2.9%
$f = 200kHz, J = 0.46A, d = 0.8$	272 W	306 W	260 W	12.4%	-4.6%
$f = 200kHz, J = 0.6A, d = 0.5$	209 W	236 W	201 W	12.9%	-4.2%

Table 4.2: NO_x Reactor: Power Estimation Comparison

Operating Point	$\hat{V_{dbd}}$ Exp.	$\hat{V_{dbd}}$ Ideal	$\hat{V_{dbd}}$ Iter. Method	Error $\hat{V_{dbd}}$ Ideal	Error $\hat{V_{dbd}}$ Iter. Method
$f = 100kHz, J = 0.25A, d = 0.5$	6718 V	5427 V	6705 V	-19.2%	-0.2%
$f = 100kHz, J = 0.2A, d = 0.8$	7274 V	6039 V	7067 V	-17.0%	-2.8%
$f = 200kHz, J = 0.46A, d = 0.8$	6336 V	6907 V	6387 V	9.0%	0.8%
$f = 200kHz, J = 0.6A, d = 0.5$	5745 V	6118 V	5746 V	6.5%	0.0%

Table 4.3: NO_x Reactor: Voltage Estimation Comparison

4.5.2 DBD Excimer lamp

UV production is a well-known application of the DBD technology. The DBD excimer lamps produce UV at a very selective wavelength, which depends on the gas composition. This

feature makes the excimer lamps attractive for germicidal processes and the treatment of some skin diseases. The geometry of the DBD lamps is similar to the NO_x treatment reactor. Both have a coaxial configuration made out of quartz with a similar setup of electrodes; however, the gas of the excimer lamps is enclosed by the dielectric walls at an specific pressure and gas mixture. Whereas in the NO_x reactor, there are two gas manifolds to allow the continuous gas flow.

Given that the UV radiation has shown to be related to the DBD current, the study of current-mode power supplies for excimer lamps have been intensely investigated by the research groups leading this project. Because of this, the excimer lamps were a departure point for the experimentation and validation of the power supply proposed. Additionally, based on the experimental validation of the DBD waveforms, some modifications to the excimer lamps electrical modeling were proposed. This section summarizes such results, but it is important to clarify that there are not related to the NO_x treatment application, so it will not be developed in detail.

The transformer used in the experimental setup with the excimer lamp has a turns ratio of $N = 10$, a magnetizing inductance of $L_m = 0.08\ H$, and a stray capacitance of $C_p = 16\ pF$. The DBD model parameters are: $C_d = 299\ pF$, $C_g = 119\ pF$, $V_{th} = 1740\ V$. Following the same methodology used with the NO_x reactor, an initial comparison between the experimental waveforms and the results of the ideal analysis and iterative method was performed. Figure 4.16 shows the results for one operating point working at a high frequency to avoid the magnetizing inductance effects. In this figure, it can be seen that the experimental DBD voltage decreases rapidly at the end of the current pulse. In contrast, the estimated waveforms, both ideal and iterative method, remain almost constant. Additionally, the experimental Q-V plot has an almond-like shape that differs from the ideal DBD parallelogram. Due to those differences, it was concluded that to accurately estimate the DBD waveforms and electrical parameters, it was necessary to modify the DBD electrical model.

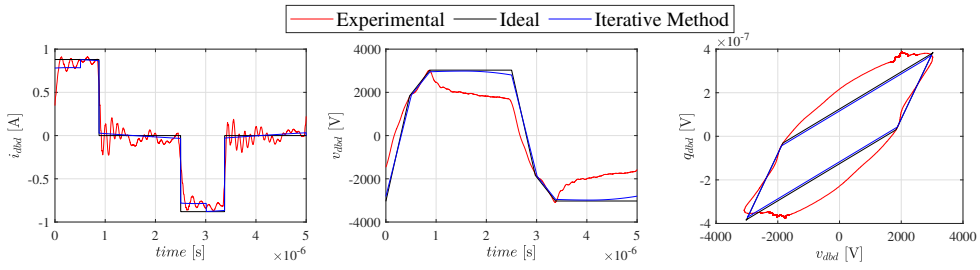

Figure 4.16: Excimer Lamp: DBD waveforms at $f_s = 200\ kHz$, $J = 0.8\ A$, $d = 0.35$

As can be observed in the experimental DBD voltage of Figure 4.16, the voltage drop tends to a negative exponential. This behavior suggested placing a resistor parallel to the gas conductance to simulate the voltage fall by discharging the gas capacitance. Figure 4.17 presents the DBD model including the parallel resistance. Note that during the discharge, the resistance, R_g, does not affect the DBD waveforms since the gas voltage remains constant at V_{th}. Therefore, during the discharge, the power consumed by R_g does not have any physical significance and can be neglected.

The modification of the electrical model was based on empirical experimentation. It means

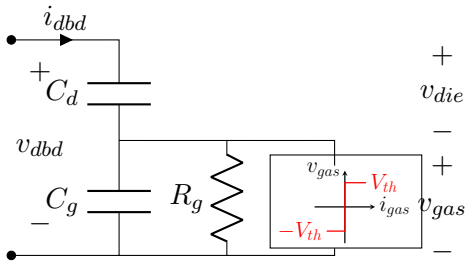

Figure 4.17: Improved DBD electrical model

that it was not the result of any physical analysis of the plasma behavior. Nonetheless, the improved model was compared to other DBD models, including the variable conductance model proposed by [5]. As explained in Section 3.2, the conductance equation proposed in [5] has three terms: the first term relates to the ionization process, the second relates to the recombination process after the gas breakdown, and the last term has a proportional coefficient between the gas current and conductance. Following their identification method, the recombination term is estimated based on the exponential decreasing behavior observed at the gas conductance after the discharge extinction, similar to the phenomenon electrically simulated through R_g. However, they are not the same coefficient.

In order to identify the improved model parameters, $[C_d, C_g, V_{th}, R_g]$, the Q-V plot was used to obtain an initial set of parameters based on the parallelogram (initial conditions). Then, a grey-box identification is performed. In the grey-box identification, the structure of the model (Figure 4.17) and one observable state (DBD voltage, v_{dbd}) are known. In this way, the problem seeks to find the best set of parameters to approximate the observable state. This can be formulated as an optimization problem which objective function minimizes the norm of the quadratic error between the experimental DBD voltage, v_{dbdEXP}, and the estimated voltage, v_{dbdEST}. The estimated DBD voltage is obtained solving the differential equations of the improved model (Equations 4.28-4.30), with the experimental current, i_{dbdEXP}, as input.

$$\begin{aligned} C_g \frac{dv_{gas}}{dt} + \frac{v_{gas}}{R_g} &= i_{dbd} \quad \text{, before breakdown} \\ v_{gas} &= \pm V_{th} \quad \text{, after breakdown} \end{aligned} \tag{4.28}$$

$$C_d \frac{dv_{die}}{dt} = i_{dbd} \tag{4.29}$$

$$v_{dbd} = v_{gas} + v_{die} \tag{4.30}$$

To solve this optimization problem, the minimization of the error with respect to the set parameters has to be done iteratively. The objective of each iteration is to find the disturbance to the parameters that reduces the objective function. The Levenberg-Marquardt gradient algorithm was used to find the DBD parameters [6]. After using the grey-box identification, the obtained parameters of the model are: $C_g = 248\ pF$, $C_d = 73\ pF$, $V_{th} = 1600\ V$, $R_g = 2900\ \Omega$.

On the other side, the analysis of the square current source with parasitic elements, using the improved model, can be performed with the same iterative method previously presented (Section 4.3.1). However, the gas voltage calculation, Equation 4.10, must be replaced by the Equation 4.28. Figure 4.18 shows the results of the estimation of three different operating waveforms using the ideal analysis, the iterative method with the classic model and the iterative method with the improved model. Additionally, Tables 4.4 and 4.5 compare the values of the experimental power and peak voltage estimated by the different methods.

As can be seen, there is a noticeable enhancement in the accuracy of the DBD waveforms and power estimation using the improved model. At high frequencies ($f_s = 200\ kHz$), the effects of the parasitic elements are weak, therefore, the differences between the ideal power and the experimental power are mostly given by the error of the DBD model. At this point, as well as at low frequencies, better results are obtained with the improved model.

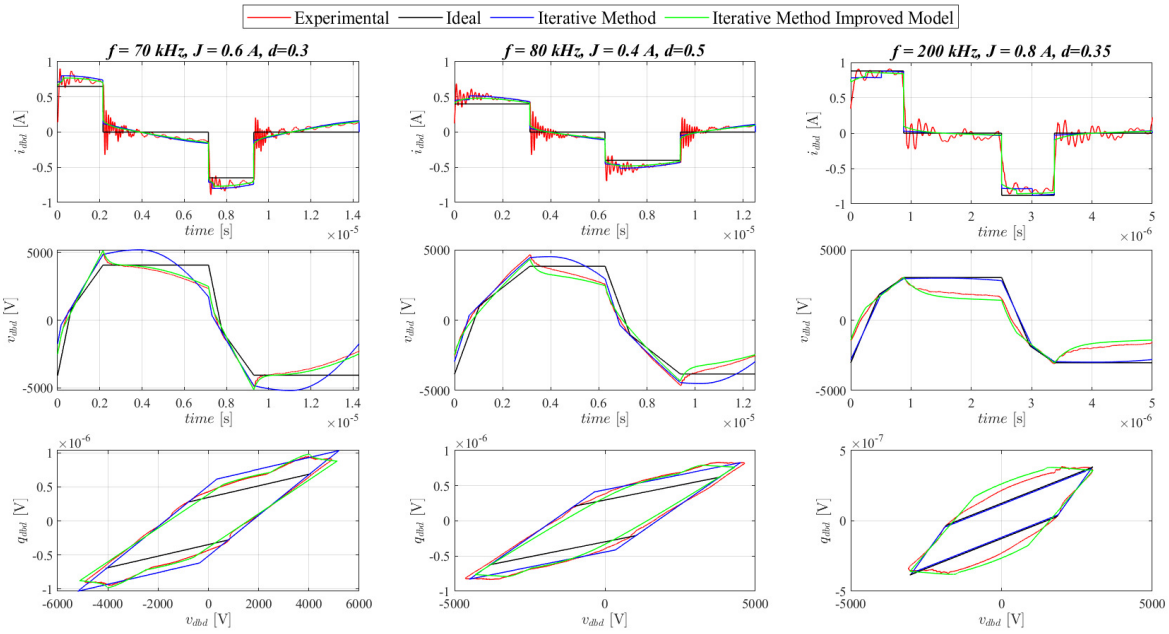

Figure 4.18: Excimer lamp: DBD waveforms for different operating points.

Operating Point	P_{dbd} Exp.	P_{dbd} Ideal	P_{dbd} Iter. Method	P_{dbd} Impro. Model	Error P_{dbd} Ideal	Error P_{dbd} Iter. Method	Error P_{dbd} Impro. Model
$f = 70kHz$, $J = 0.3A$, $d = 0.6$	357 W	238 W	400 W	360 W	-33.3%	12%	0.8%
$f = 80kHz$, $J = 0.4A$, $d = 0.5$	359 W	233 W	344 W	353 W	-35.1%	-4.2%	-1.7%
$f = 200kHz$, $J = 0.8A$, $d = 0.35$	374 W	248 W	227 W	376 W	-33.7%	-39.3%	0.5%

Table 4.4: Excimer lamp: Power Estimation Comparison

Operating Point	$\hat{V_{dbd}}$ Exp.	$\hat{V_{dbd}}$ Ideal	$\hat{V_{dbd}}$ Iter. Method	$\hat{V_{dbd}}$ Impro. Model	Error $\hat{V_{dbd}}$ Ideal	Error $\hat{V_{dbd}}$ Iter. Method	Error $\hat{V_{dbd}}$ Impro. Model
$f = 70kHz$, $J = 0.3A$, $d = 0.6$	4914 V	4070 V	5200 V	5133 V	-17.2%	5.8%	4.5%
$f = 80kHz$, $J = 0.4A$, $d = 0.5$	4647 V	3831 V	4514 V	4423 V	-17.6%	-2.9%	-4.8%
$f = 200kHz$, $J = 0.8A$, $d = 0.35$	3023 V	3028 V	2985 V	3042 V	0.2%	-1.3%	0.6%

Table 4.5: Excimer lamp: Voltage Estimation Comparison

4.6 Burst Operation Mode

In the previous analysis and validation of the square current source, the DBD was driven by continuous current pulses. The current amplitude, J, switching frequency, f_s, and pulse duration, T_{pulse}, are the three degrees of freedom used to control the DBD power. Henceforth, we will refer to that operation as the continuous mode. Another operation mode that will be investigated is the burst mode. In this mode, the pulsed current is alternatively turned on and off. Figure 4.19 sketches the DBD current waveform of the ideal burst operation. As can be seen, a train of current pulses is injected into the DBD; then, the pulses are interrupted during an idle time. This operation adds two new degrees of freedom into the DBD analysis: the number of pulses on (N_{on}) and the idle time, (T_{idle}). Additionally, the burst frequency is establish as: $f_{burst} = 1/(T_{on} + T_{idle})$.

Due to the burst modulation of the current pulses, the energy is only deposited in the discharge during the time period T_{on}. Accordingly, the average power for one complete burst

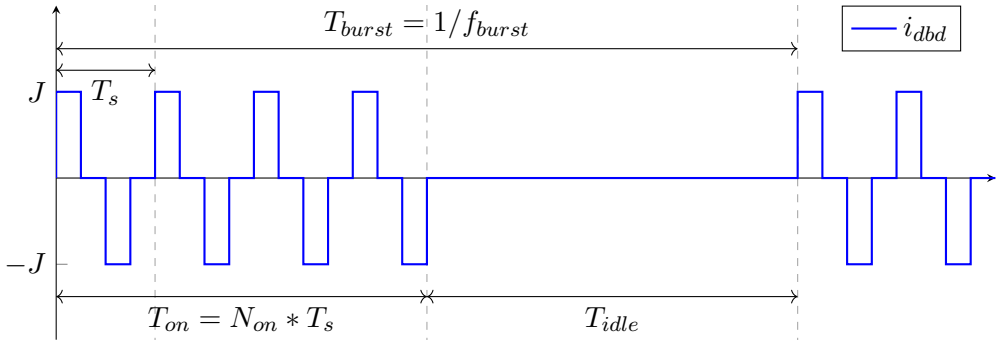

Figure 4.19: DBD Current Waveforms of Burst Operation

period $T_{on} + T_{idle}$, can be calculated as the sum up of the energy dissipated in each current pulse, ξ_n, divided by the burst period. The detailed electrical diagnostic of the operation will be presented in Section 5.4.3.

$$P_{burst} = \frac{1}{T_{burst}} \sum_{n=1}^{N_{on}} \xi_n \tag{4.31}$$

4.6.1 Implementation

The implementation of the burst mode is carried out using the same converter detailed in previous sections. Figure 4.20 shows the schematic of the current inverter connected to a non-ideal transformer model and the DBD load.

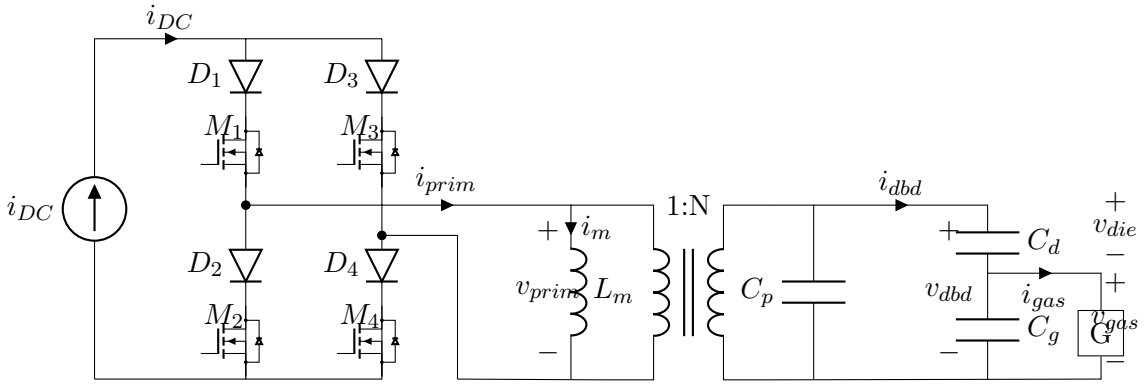

Figure 4.20: Current Inverter Schematic

During the idle time, the current inverter has to provide a closed path for the DC current. Figure 4.21 shows the simulated DBD waveforms considering the parasitic transformer elements and assuming one of the inverter legs closed during the idle time (M_1 and M_2 ON). As can be observed, even if the constant current source is short-circuited in the idle time, the magnetizing inductance current flows through the DBD since a parallel resonant circuit is formed (equivalent to Figure 4.4c). That produces a damped oscillation on the DBD

waveforms at a frequency equals to $w_{off} = \frac{1}{\sqrt{L_m C_{off}}}$.

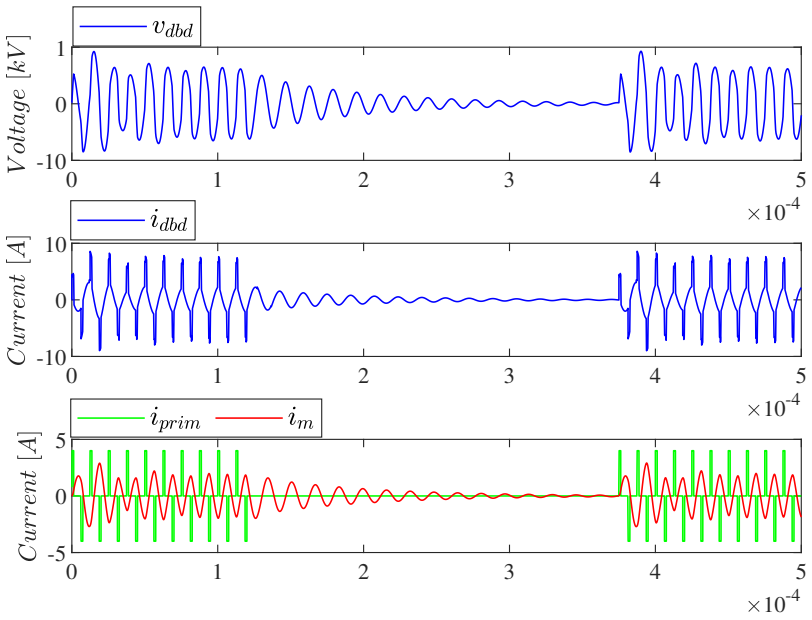

Figure 4.21: Simulation Waveforms of Burst Mode illustrating oscillations with $M1$ and M_2 ON during idle time.

Eventually, the oscillation fades out thanks to the parasitic resistive elements. Nonetheless, the oscillation is not desirable for the burst mode since it may produce additional discharges. Moreover, it is required to wait until the oscillation extinction to inject a new train of pulses. In order to prevent such oscillations, another approach is to turn on the switches M_1, M_2, and M_4 during the idle time. Figure 4.22 shows the simulated waveforms for two operating points using this approach.

As can be seen in both cases of Figure 4.22, there is a transition between the end of the current pulses and the zero voltage state. The transition starts when the last negative pulse finishes, t_1. At this time, the DBD voltage is close to its negative peak, therefore, when M_1, M_2, and M_4 are turned on, the voltage v_{prim} is negative, and the diode D_2 is reversed biased. In consequence, the constant current, i_{DC}, flows across M_1 and M_4, producing a positive current pulse (Interval A). In this interval, the DBD voltage suddenly starts rising, and once it crosses through zero, diode D_2 spontaneously conducts. At this point ($t = t_2$), if the current in diode D_4 is greater than zero, the primary winding of the transformer is short-circuited, keeping the DBD voltage and DBD current at zero (Interval C). This is the case depicted in Figure 4.22-a. The current of the diodes in interval C are:

$$i_{D1} = i_{DC} \tag{4.32}$$

$$i_{D2} = i_{DC} - i_m(t_2) \tag{4.33}$$

$$i_{D4} = i_m(t_2) \tag{4.34}$$

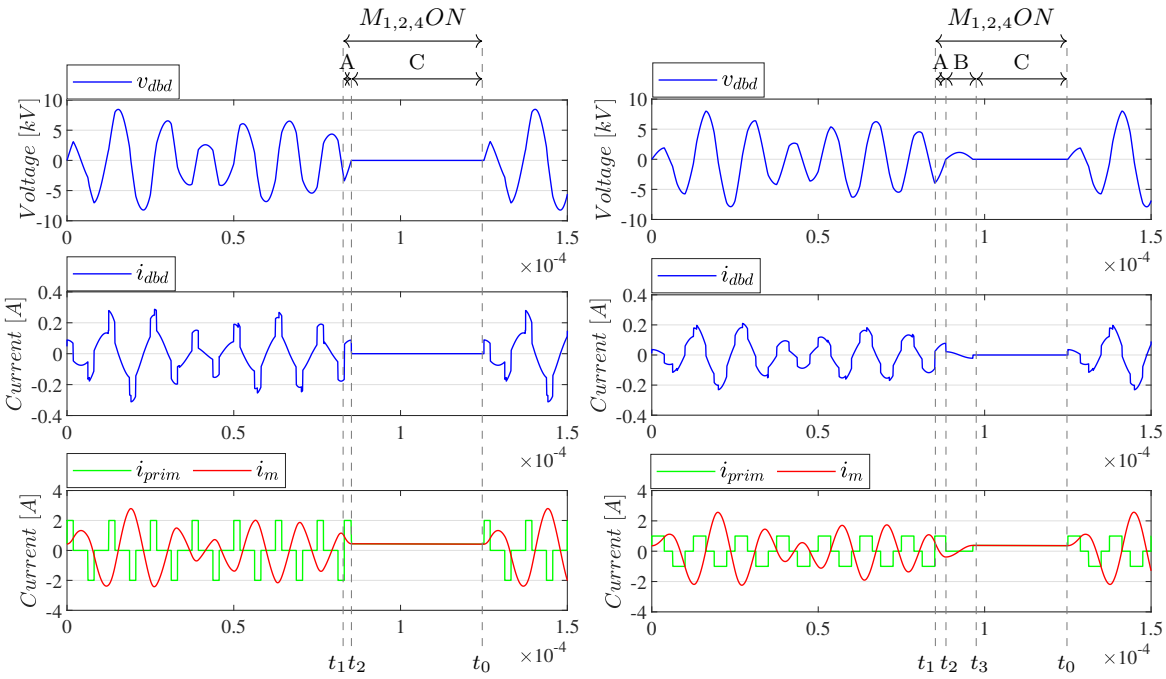

a) $f_s = 80kHz$, $J = 0.18A$, $d = 0.2$, $N_{on} = 7$, $T_{idle} = 50\mu s$

b) $f_s = 80kHz$, $J = 0.09A$, $d = 0.5$, $N_{on} = 7$, $T_{idle} = 50\mu s$

Figure 4.22: Simulation Waveforms of Burst Mode with M_1, M_2, and M_4 on during idle time.

However, if the current condition of $D4$ is not fulfilled ($i_m(t_2) < 0$), the diode $D4$ is turned off. This is the case depicted in Figure 4.22-b. As can be seen, during interval B, the constant current, i_{DC}, is derived through M_1 and M_2; therefore, only the magnetizing current flows through the DBD. At the time t_3, the DBD voltage crosses trough zero again, the diode conditions are re-evaluated, and the transformer primary winding is short-circuited.

In both of the described cases, the DBD voltage and current return to zero and are kept constant until the following train of pulses is injected (t_0). Note that when the current pulses start, the initial condition for the magnetizing inductance is $i_m(t_0) = i_m(t_2)$ for the case of Figure 4.22-a, and $i_m(t_0) = i_m(t_3)$ for the case of Figure 4.22-b. The initial condition of the DBD equivalent capacitance is $v_{Ceq}(t_0) = 0$. According to those conditions, the voltage and current waveforms exhibit a transient response at the first pulses. This transient causes differences in the energy injected by each of the first pulses. In fact, some of the current pulses may not obtain the gas breakdown, whereas some other pulses may produce a significantly higher amount of energy. The transient behavior will be further developed in the experimental diagnosis and analysis of the burst mode.

4.7 Conclusions

The analysis of the square current source, considering the effects of the parasitic capacitance and magnetizing inductance, is presented, and a numerical method is proposed for

finding the operating ratings and waveforms of the converter.

The square current source implementation is shown and used to validate the proposed method using two different DBD loads. It is demonstrated that the method accurately predicts the DBD electrical quantities under the presence of parasitic elements for the NO_x treatment reactor using a simple electric model. However, for the DBD excimer lamp, the need for a more complex model is raised. Therefore, an improved model is proposed and validated under different conditions. Finally, the implementation of the burst operation mode is introduced.

Bibliography

[1] D. Florez, R. Diez, H. Piquet, and A. K. Hay Harb, "Square-Shape Current-Mode Supply for Parametric Control of the DBD Excilamp Power," *IEEE Transactions on Industrial Electronics*, vol. 62, no. 3, pp. 1451–1460, 3 2015. doi: https://doi.org/10.1109/TIE.2014.2361601

[2] V. Rueda, A. Wiesner, R. Diez, and H. Piquet, "Power Estimation of a Current Supplied DBD Considering the Transformer Parasitic Elements," *IEEE Transactions on Industry Applications*, vol. 55, no. 6, pp. 6567–6575, 11 2019. doi: https://doi.org/10.1109/TIA.2019.2933519

[3] A. Wiesner, R. Diez, D. Florez, and H. Piquet, "System for experimental investigation of DBD excilamps in view of control and optimization of UV emission," *Mathematics and Computers in Simulation*, vol. 165, no. 40, pp. 92–106, 2019. doi: https://doi.org/10.1016/j.matcom.2019.02.021

[4] X. Bonnin, H. Piquet, R. Diez, and D. Florez, "Designing the high voltage transformer of power supplies for DBD: Windings arrangment to reduce the parasitic capacitive effects," in *2013 15th European Conference on Power Electronics and Applications (EPE)*. IEEE, 9 2013, pp. 1–9. doi: https://doi.org/10.1109/EPE.2013.6631928

[5] R. Díez, J.-P. Salanne, H. Piquet, S. Bhosle, and G. Zissis, "Predictive model of a DBD lamp for power supply design and method for the automatic identification of its parameters," *The European Physical Journal Applied Physics*, vol. 37, no. 3, pp. 307–313, 3 2007. doi: https://doi.org/10.1051/epjap:2007017

[6] J. J. Moré, "The Levenberg-Marquardt algorithm: Implementation and theory," in *Numerical Analysis. Lecture Notes in Mathematics, vol 630*. Springer Berlin Heidelberg, 1978, pp. 105–116. doi: https://doi.org/10.1007/BFb0067700

Chapter 5

Experimental Methods

Contents

5.1 Introduction

In order to investigate the impact of the current-mode power supplies on the NO_x treatment based on NTP, an experimentation prototype is developed. Such a prototype aims to standardize the $DeNO_x$ experiments and automate the results acquisition. In this chapter, a description of the entire experimental setup and methodology is exposed. The construction of the DBD reactor used for this dissertation is detailed, and the employed instruments and experimental procedure are introduced. Furthermore, the diagnostic methods of electrical waveforms, gas treatment, and discharge pictures are presented.

5.2 Experimental Setup

Figure 5.1 shows the schematic diagram of the experimental setup. It consists of a DBD reactor, a gas blending system, the power supply with its respective step-up transformer, the measurement instruments, and a control interface. In order to reproduce a gas composition similar to the diesel exhaust (Table 1.1), the feed-gas stream is composed of NO, N_2, and O_2. The gas mixture concentrations and the total flow rate are measured and regulated by

three Mass Flow Controllers (MFC) operated by the control interface. At the outlet of the MFCs, a mixing chamber blends and homogenizes the gas mixture before its injection into the plasma reactor.

The control interface is also connected to the gas analyzer and ozone meter, which measure the gaseous composition and temperature in the outlet stream. Furthermore, an infrared (IR) temperature sensor is pointed at the outer electrode, and a USB camera focuses the whole discharge area of the reactor.

As was previously said, a specially developed power supply is proposed in this thesis. The control interface drives the operating conditions of the power supply. In this manner, it can perform parametric sweeps of the different electric degrees of freedom. Finally, for the DBD electric diagnostic, an oscilloscope measuring the DBD voltage and current is used. The description of the experimental setup parts and instruments is presented below.

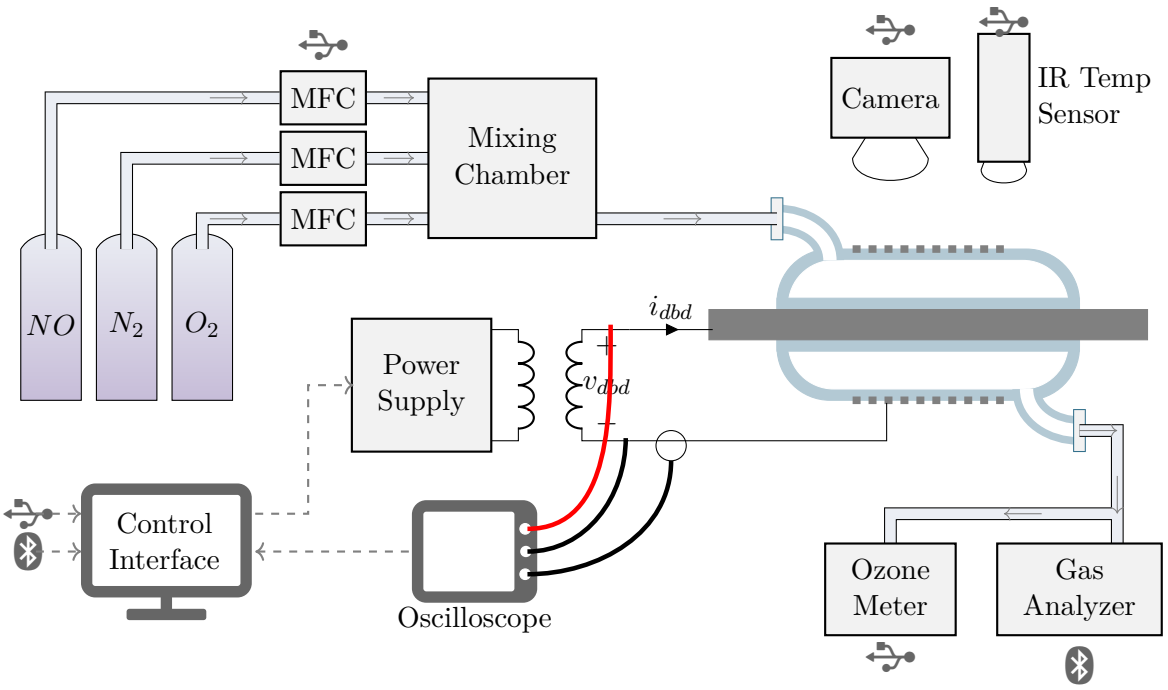

Figure 5.1: Experimentation Setup

5.2.1 DBD Reactor

To construct a DBD reactor suitable for the NO_x treatment application, the following specifications were established. These specifications are settled based on the literature review, and some preliminary experiences with plasma reactors.

- Circulation of possibly hot and corrosive gases. According to the application, the reactor must resist the high temperatures of the engine exhaust ($> 200\ ^\circ C$), and possible corrosive compounds of the gas.

- Visible electric discharge. Due to the experimental purpose of this reactor, it is desirable to observe the electric discharge. This allows us to diagnose the discharge and identify visual singularities that might be related to the treatment performance.
- Parasitic corona discharges. As a high voltage has to be applied between the electrodes, care must be taken to prevent the formation of parasitic corona discharges between the electrodes sharp edges and the air outside the reactor. Such discharges may derive a significant part of the injected energy, and reduce the treatment efficiency.
- Flexibility. The reactor must allow an easy assembly and disassembly.
- Security measures. The reactor design must guarantee perfect sealed operation and prevent the leakage of any dangerous gas. Moreover, due to the UV emission of the discharge, a UV protective barrier must be included.

Based on the specifications, a DBD reactor with a coaxial geometry was designed. Figure 5.2 depicts the lateral and cross-sectional views of the reactor, including its dimensions. The reactor is built upon two concentric quartz tubes sealed at the ends, with an inlet and outlet connector welded on each side. The use of transparent dielectric material, such as quartz, allows the visual assessment of the discharge. Moreover, the two dielectric barriers protect both electrodes from the reactive plasma species and the corrosive effects of the gas.

The inner electrode is a stainless steel foil with a thickness of 1 mm. The foil is rolled outside the reactor and then inserted into the inner dielectric tube. In this way, the foil unfurls inside the tube and takes its form; hence, one can assure that the inner electrode is in complete contact with the inner wall of the dielectric tube. On the other side, the outer electrode is a metallic mesh wrapped around the outer tube. As the endings of the metallic mesh have sharp edges, they may lead to the formation of parasitic corona discharges outside the plasma area. In order to prevent this problem, the mesh endings are covered by high-temperature silicone rubber.

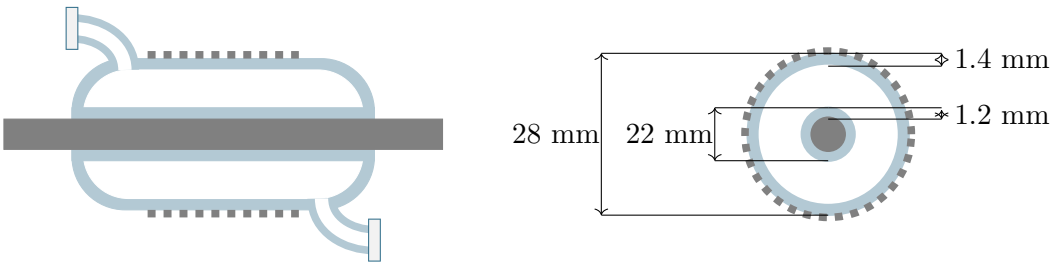

Figure 5.2: Reactor Dimensions

Figure 5.3 shows a picture of the reactor. The total length of the reactor, excluding manifolds, is 600 mm. Only a portion of this length is occupied by the outer electrodes. As can be seen, the reactor has three different metallic mesh sections to experiment with different discharge lengths. In the picture, the first section is being used while the other two sections are disconnected. The possible discharge lengths are 60 mm and 120 mm.

The whole reactor assembly is enclosed by a polycarbonate tube that filters the UV radiation and facilitates the discharge observation. The reactor rests on two perforated mounting

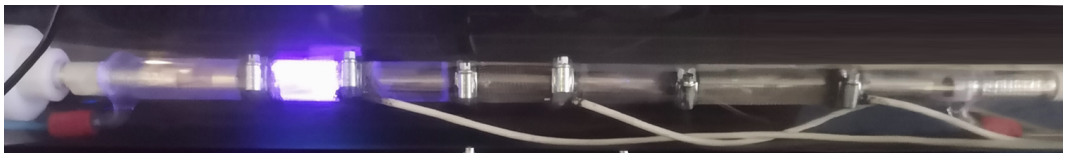

Figure 5.3: Picture of Reactor

supports, which center it inside the tube. Additionally, the air inside the tube is continuously flushed through two fans, one at each end. The airflow inside the polycarbonate tube refrigerates the reactor, prevents the accumulation of ozone, and in case of a leakage, flushes the toxic gases safely. Figure 5.4 shows the drawings of the mechanical mounting.

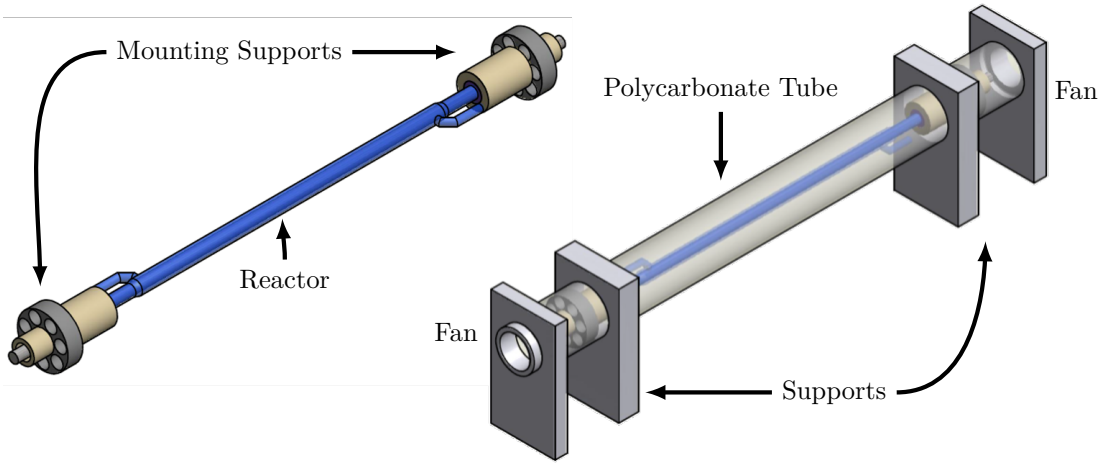

Figure 5.4: Reactor Mechanical Mounting

5.2.2 Gas Blending System

The simulated gas is derived from three gas bottles from Air Liquide at ambient temperature. The first one is an S01 bottle containing NO with a purity greater than 99.9 %. The second bottle is type L50 and contains N_2. And the last bottle is an L50 bottle of O_2. At the outlet of each bottle, there is a gas pressure regulator and a manual valve to enable the gas flow.

The flow rates of the gas streams are regulated by the following MFC from Bronkhorst (EL-Flow Prestige).

NO **MFC:** FG-201CV-ABD-11-V-AA-000, with a flow range of 0.2 to 10 mln/min

N_2 **MFC:** FG-201CV-ABD-22-V-AA-000, with a flow range of 0.3 to 15 ln/min

O_2 **MFC:** FG-201CV-ABD-22-V-AA-000, with a flow range of 30 to 1500 mln/min

Based on the flow range of the MFCs, Figure 5.5 presents by the shadowed area the

possible NO and O_2 concentrations as a function of the total gas flow, G. Note that the NO and O_2 concentration plots are limited at 4000 ppm and 25 Vol. %, respectively, since the gas analyzer cannot measure higher concentrations. Additionally, as the gas analysis requires a flow rate of at least 2 l/min, the minimum total flow is set at this value, and the maximum total flow is set according to the N_2 MFC range.

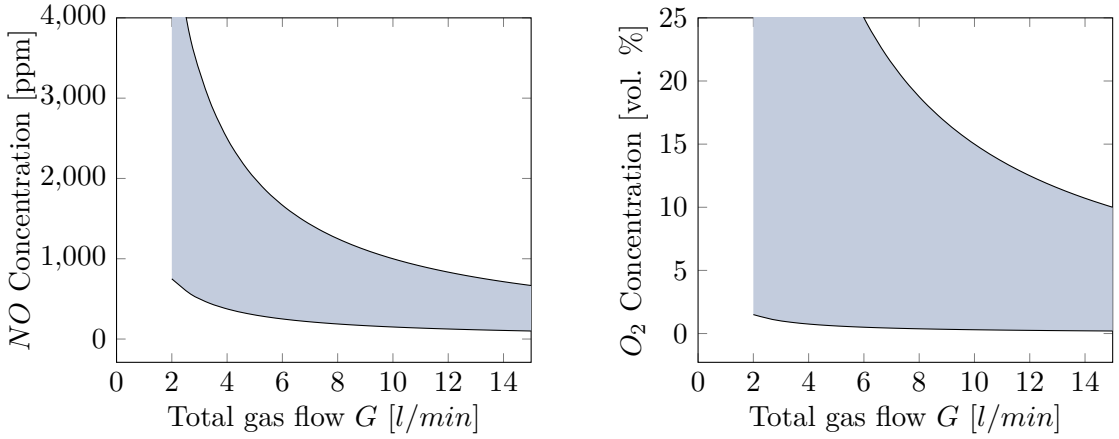

(a) NO concentration range (b) O_2 concentration range

Figure 5.5: Possible gas mixture concentrations

5.2.3 Gas Analyzers

Several technologies are available to measure the gas composition of the NO_x treatments. The Fourier Transform Infrared Spectroscopy (FTIR) provides a precise measurement of several compounds in diesel exhaust. This technique seeks to measure the IR light absorbed by the gas at each wavelength. Based on the obtained IR spectrum, one can determine the gas composition since each molecule absorbs the light at a different wavelength. Another technique is the Mass Spectroscopy (MS). In this technique, the gas is ionized, followed by the measurement of the mass-to-charge ratio of ions (m/Q). In this way, the mass spectrum of the gas can be analyzed. These two techniques can be used to perform real-time gas analysis, providing a complete characterization of the gaseous compounds. Nonetheless, they are complex techniques that require bulky and expensive equipment.

Another technique for the NO_x treatment analysis is based on electrochemical sensors. In contrast to the previous technologies, the electrochemical sensors do not characterize the entire gas, but only measure the concentration of a particular molecule. These are reliable and cheap devices that can operate accurately with a stationary gas composition. However, as some sensors have a slow response time, they are less accurate with dynamic gases (gas composition changing over time). The gas analyzer TESTO 350, with the electrochemical sensors of O_2, NO, and NO_2 is used for the $DeNO_x$ analysis.

As stated in Chapter 2, the ozone has a crucial role in the oxidation process of plasma-based treatments. Therefore, the gas analysis includes a 2B Technologies Model 106-M Ozone Monitor. This device measures the ozone concentration based on the technique of UV ab-

sorption.

5.2.4 Other Instruments

The electrical waveforms are measured and recorded by a 200 MHz digital oscilloscope (LeCroy HDO4024). The DBD current is acquired using a current probe (LeCroy AP015) with a bandwidth of 50 MHz. The DBD voltage is measured by two 20kV single-ended probes referenced to the ground (LeCroy PPE 20 kV). Each probe is connected to a DBD electrode; then, the DBD voltage is calculated as the voltage difference between the two voltage probes. To guarantee an accurate power estimation, the timing delay error between the voltage and current probes is eliminated by performing the probes deskew procedure. Furthermore, the measurements are taken with full-bandwidth and full vertical scale.

Images of the discharge are continuously obtained by the digital camera (Logitech C920). Additionally, an IR temperature sensor (OS211MT-MV) measures the temperature of the outer electrode. The sensor has a temperature range of 0 to 250 $^{\circ}C$, and a accuracy of 1 % of the reading.

5.2.5 Control Interface

The control interface drives all the instruments previously presented: MFCs, gas analyzers, oscilloscope, temperature sensor, camera, and power supply. Moreover, it centralizes the supervision of the experiment and records the results of different conditions to simplify the data analysis.

The interface has been developed in LabView with two main objectives in mind. First, the code structure seeks to be reusable and flexible, to quickly implement similar setups for other DBD applications of the research group. On this basis, an object-oriented programming approach is used. Each instrument of the setup is represented by a LabView *object*, with its *properties* or variables and its *methods* or functions. For instance, the MFC is an object with some configuration parameters (sampling time, and MFC flow range) and some methods (initialization, write flow rate, and read flow read). The instruments methods and properties depend on the functionality and communication protocol of the instrument but, overall, they all share a similar reusable structure. At the present time, the designed control interface has been adapted and is used for a plasma jet medical application, DBD excimer lamps, and the treatment of Particulate Matter.

The second and most important objective of the interface is to automate the experiments and collect the results in an easily accessible and reproducible manner. For such purposes, data is stored in a computer folder following a specific structure, and uploaded to a database to facilitate accessibility of the results. Table 5.1 presents the measurements acquired at each experiment.

Source	Type	Measurement
Oscilloscope	Array [.dat]	Array of the DBD Voltage and Current waveforms taken every 20 s.
Oscilloscope	.txt	Log of the oscilloscope measurements sampled every 1 s. (peak current, peak voltage, frequency, and electrical power)
MFCs	.txt	Log of measured gas flow rates sampled every 1 s.
Gas Analyzers	.txt	Log of the values of the gas analyzer and ozone monitor sampled every 1 s. NO, NO_2, NO_x, O_2, O_3, and gas stream temperature.
Camera	Array [.png]	Array of the discharge pictures taken every 20 s.
IR Sensor	.txt	Log of the outer electrode temperature, sampled every 1 s.
Experiment Configuration	.xml	Document with configuration of instruments and experiment.

Table 5.1: Measurements acquired by the interface

Figure 5.6 and 5.7 show the developed LabVIEW interface. It is composed of two tabs, in the first tab (configuration), all the instruments and experiment properties are established. Once all the parameters are set up, and the experiment runs, the second tab (supervision) shows the data acquisition and state of the experiments. Finally, Figure 5.8 shows a picture of the entire experimentation bench.

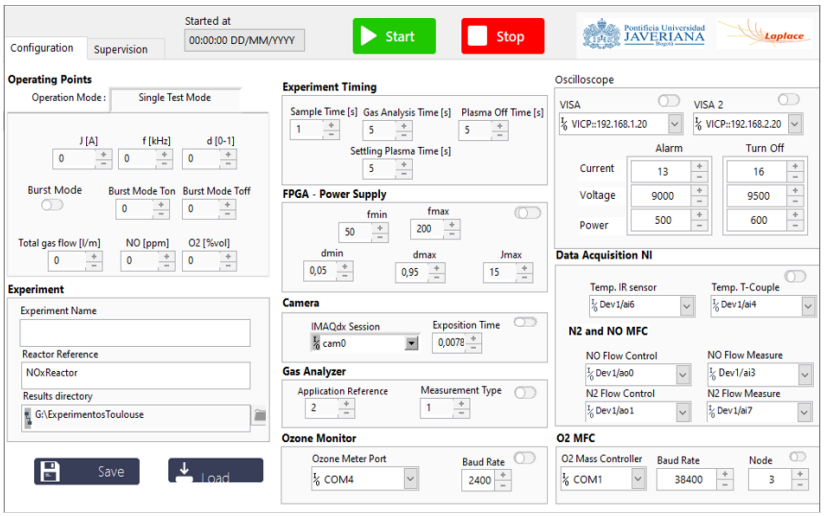

Figure 5.6: Control interface: Configuration Tab

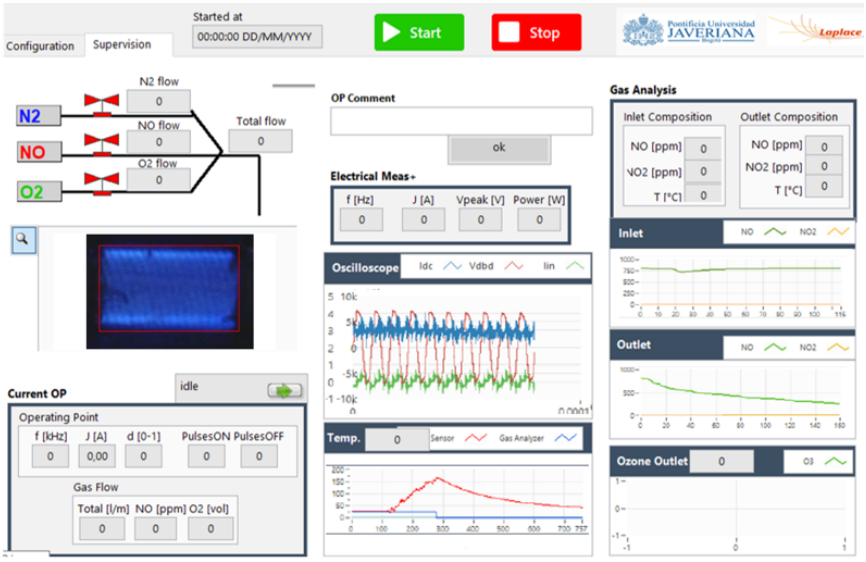

Figure 5.7: Control interface: Supervision Tab

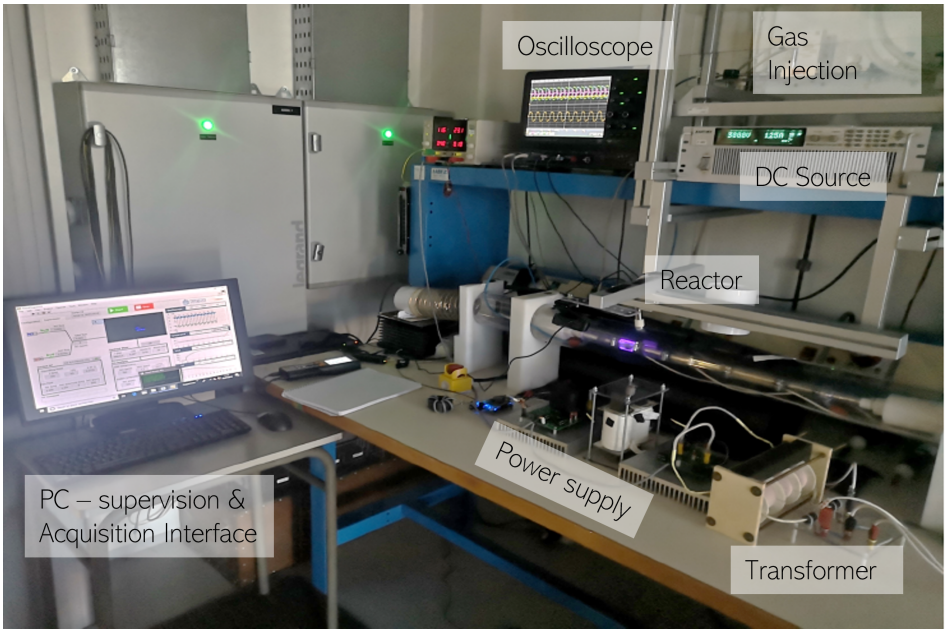

Figure 5.8: Picture Experimentation Bench

5.3 Experiments Procedure

For the sake of clarity in the terms used henceforth, the following definitions are introduced:

An *Operating Point (OP)* is defined as the set of experimental conditions, including the conditions of the power supply (J_{prim}, f_s, T_{pulse}, in the case of the burst mode N_{on}, T_{idle}),

and the conditions of the gas stream (total gas flow G, and NO and O_2 concentrations).

An *Experiment* is the execution of the procedure shown in Figure 5.9 for a given OP.

An *Experimental Study* is the group of experiments intended to study the effects of certain conditions on the treatment.

As depicted in the flowchart (Figure 5.9), the experiment is composed of three stages: before treatment, during treatment, and cool-down. At the time t_0, the experiment starts, the gas flow is activated, and the measurement of the gas composition before treatment is performed. During this stage, the gas flows through the reactor while the plasma remains off; therefore, the gas analyzers measure the gas composition before treatment at the reactor outlet.

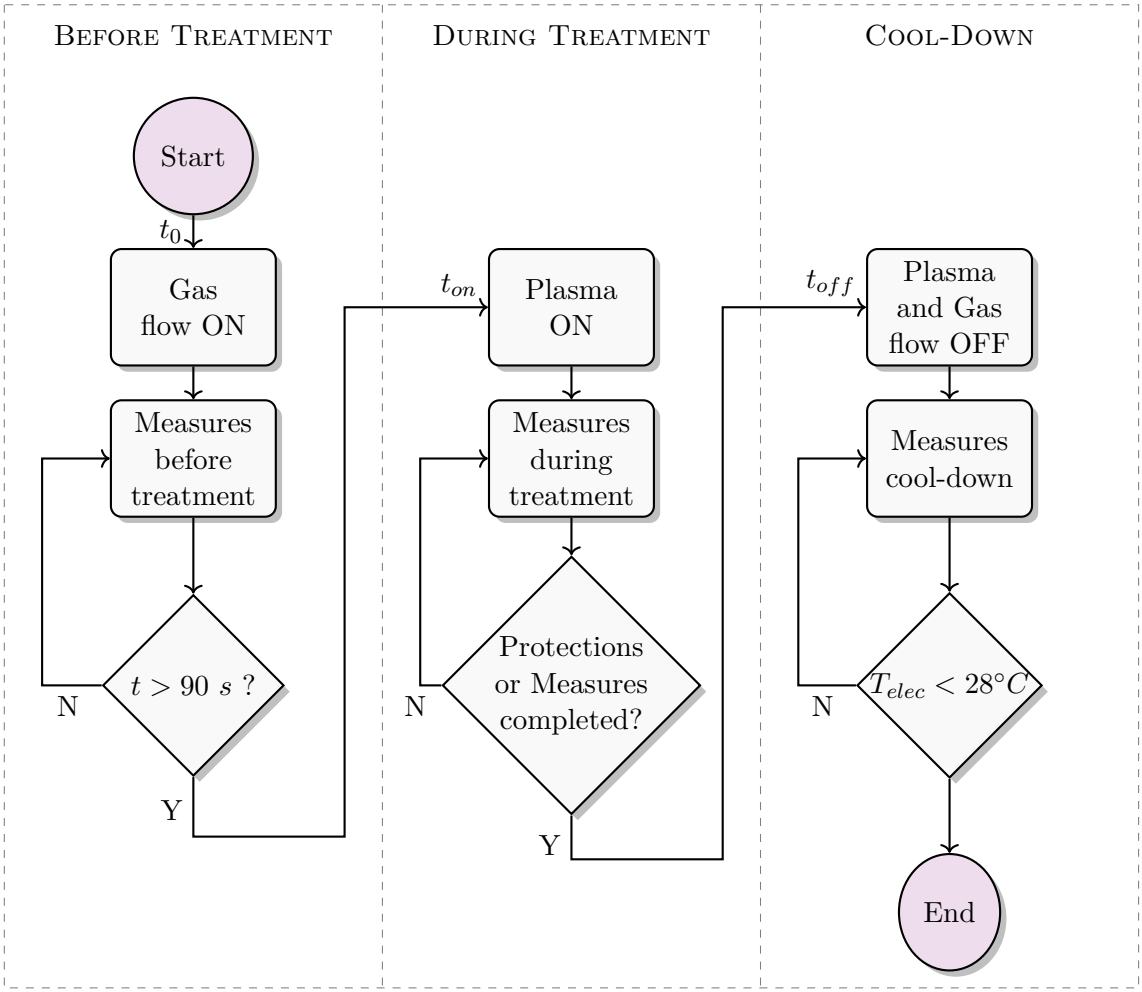

Figure 5.9: Experiment Flowchart

Then, at the time t_{on}, the plasma is ignited. During this stage, the system records the oscilloscope waveforms and reactor pictures every 20 seconds. The rest of the measurements are sampled every second. The treatment stage ends once the reactor reaches the thermal equilibrium, and the gas measurements are completed. However, the stage can be interrupted

when any of the system protections are activated. The protections include: the outer electrode exceeds 160 $°C$, or DBD peak voltage exceeds 10 kV.

After the treatment measurements have been taken, the plasma is turned off at the time t_{off}. At this moment, the gas flow is also inactivated, and the DBD is cooled down. To perform all the experiments under the same initial conditions, the duration of this stage depends on the outer electrode temperature. The cool-down finishes once the electrode temperature is lower than 28 $°C$.

Figure 5.10 shows an example of the data acquired at one experiment. In Figure 5.10-a some measurements of the stages *'before treatment'* and *'during treatment'* are shown. Once the plasma is ignited, the DBD power increases, and the effects of the treatment can be observed. Figure 5.10-b illustrates the temperature of the outer electrode for the three stages. In this particular experiment, the temperature arrives to 160 $°C$ rapidly, so it is stopped due to over-temperature. Then, almost 13 minutes are required to decrease the reactor temperature in order to start a new experiment. The long cool-down time slows down the experimentation process.

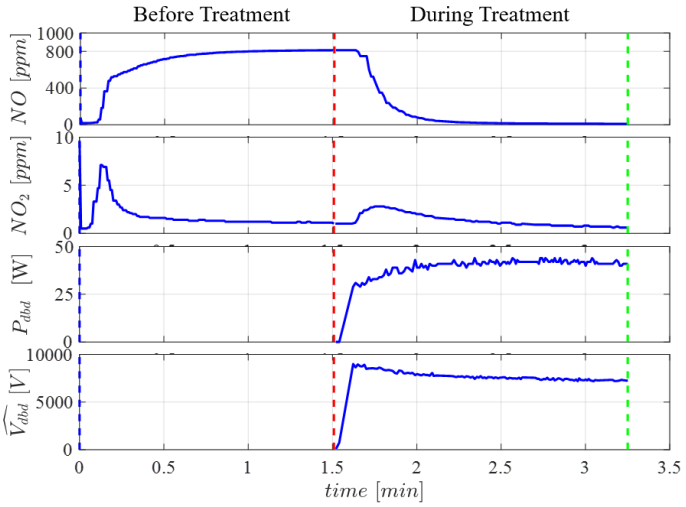

(a) Measurements

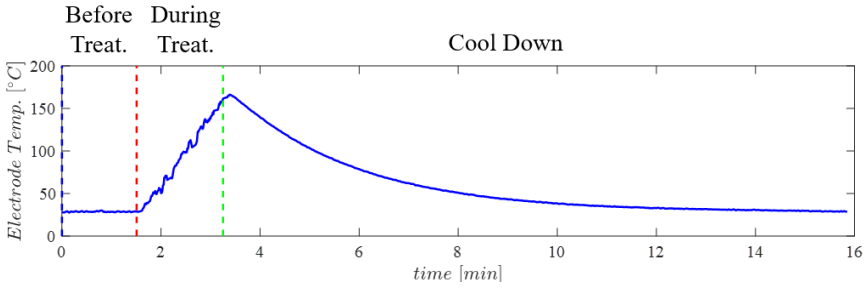

(b) Electrode Temperature

Figure 5.10: Example of Experimental data

5.4 Analysis Methods

Several plasma diagnostic techniques are employed to assess the performance of the DBD applications: the experimental chemical diagnostic of the plasma applications relies on the gas analysis methods. On the basis of the selected gas analyzers, some parameters are proposed in Section 5.4.1 to evaluate the treatment performances.

Optical diagnostic techniques are also commonly used for measuring some physical characteristics of the plasma. Optical imaging is a passive or non-invasive diagnostic technique that provides information about the plasma morphology and its spatial-temporal evolution [1]. With this techniques, the plasma is analyzed by taking pictures of the discharge. In this work, the discharge imaging is used to evaluate the morphology of the plasma using an image processing algorithm (Section 5.4.2).

Finally, the electric diagnostic is fundamental to characterize the plasma [2]. From the DBD voltage and current measurements, and based on the Q-V Lissajous plots [3]) essential properties of the discharge can be deduced (injected energy, power dissipated, electric model parameters,...). The methods proposed to obtain a complete electrical characterization of the DBD for different power supplies are presented in Section 5.4.3.

5.4.1 Chemical Diagnostic

To quantitatively evaluate the NO_x treatment under different conditions and with respect to the literature results, the following definitions are stated:

The NO and NO_x removal efficiencies are defined as:

$$\eta_{NO} = \frac{NO_i - NO_f}{NO_i} * 100[\%] \tag{5.1}$$

$$\eta_{NO_x} = \frac{NO_i - NO_{xf}}{NO_i} * 100[\%] \tag{5.2}$$

where NO_i is the NO concentration in ppm before treatment, NO_f is the concentration in ppm after treatment, and NO_{xf} is the concentration of $NO + NO_2$ after treatment.

The NO_2 selectivity is defined as the initial percentage of the NO part transformed into NO_2

$$Selectivity\ NO_2 = \frac{NO_{2f}}{NO_i} * 100[\%] \tag{5.3}$$

Furthermore, the Energy Density (ED) is defined as the relation between the discharge power and the gas flow rate:

$$ED = \frac{P * 60}{G}\ [J/l] \tag{5.4}$$

where P is the DBD average power $[W]$, and G is the total gas flow rate $[l/min]$. The ED express the total energy $[J]$ applied per unit volume of gas $[l]$.

Finally, the Energy Cost is defined as the energy required to remove one mole of NO

$$Energy\ Cost = \frac{ED * 22.4 * 10^6}{NO_i - NO_f}\ [MJ/mol] \tag{5.5}$$

All these quantities rely on the measurements of the gas analyzer Testo 350. Table 5.2 presents the specifications of the three sensors employed for the analysis (NO, NO_2, and O_2). According to the sensors documentation, using a stationary gas composition, the time taken to reach 90% of the full gas measurement, t_{90}, is 30 s and 40 s for the NO, and NO_2 sensors respectively. It means that a time longer than 40 s is required for obtaining a full measurement of the gas concentrations. Consequently, the sensors response time was evaluated using a stationary gas stream, without plasma, composed of NO = 800 ppm, $NO_2 = 0$ ppm, $O_2 = 0$ %, and $G = 3$ lpm. Figure 5.11 shows the NO and NO_2 measurements for seven repetitions of the experiment. As can be seen, all the NO measurements settle in approximately one minute; thus, for all the experiments in this work, the initial concentration of the gas is measured 1.5 minutes after the gas flow activation (NO_i, NO_{2i}, and O_{2i}).

Sensor	Measuring Range	Accuracy	Resolution	Reaction Time t_{90}
O_2	0 to 25 Vol. %	± 0.8 f.s.v	0.01 Vol. %	20 s
NO	0 to 4000 ppm	± 5% m.v. (100-1999 ppm) ± 10% m.v. (2000-4000 ppm) ± 5 ppm (0-99 ppm)	± 1 ppm	30 s
NO_2	0 to 500 ppm	± 5% m.v. (100-500 ppm) ± 5 ppm (0 - 99.9 ppm)	± 0.1 ppm	40 s
O_3	0 to 1000 ppm	± 2% m.v.	± 0.01 ppm	4 s

Table 5.2: Technical data of Testo sensors and Ozone Monitor. (f.s.v. full scale value, m.v. measured value)

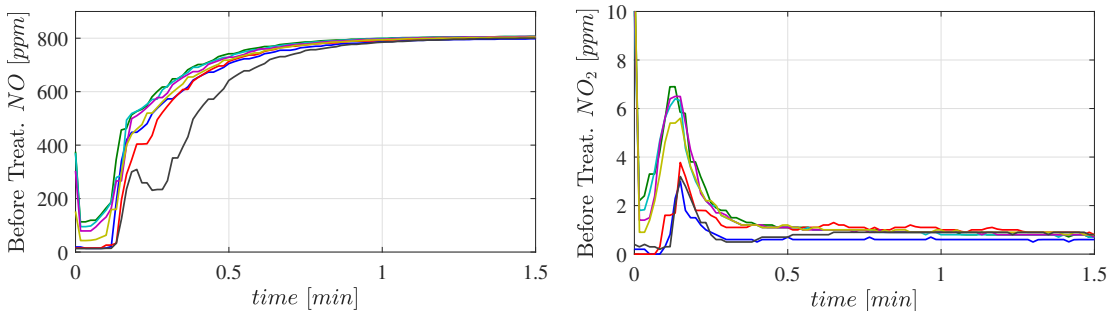

Figure 5.11: Measurements of the gas analyzer before treatment.

Following the same logic, during treatment, the gas measurements should be acquired at least one minute after the plasma has stabilized. However, this is not always possible since some experiments are interrupted when the electrode temperature exceeds 160 $°C$, because of the protection required to prevent the deterioration of the silicon rubber of outer electrodes endings. In those cases, the values acquired by the gas analyzer are not reliable. As the gas measurements are not settled yet, it is impossible to conclude about the treatment. In consequence, to obtain reliable gas measurements during treatment, the reactor temperature has to stabilize under 160 $°C$, and the gas measurements have to be acquired at least one minute after temperature settlement, (NO_f,NO_{2f}, and O_{2f}).

The uncertainties of the quantities here defined (η_{NO}, η_{NO_x}, and $SelectivityNO_2$) are calculated according to the accuracy of the measuring instrument (reported in Table 5.2). Such uncertainties will be plotted as error bars in the experimental results of the treatment (Chapter 6).

5.4.2 Image Processing Diagnostic

Different diagnostic methods have been proposed in the literature to study the impact of the discharge appearance in the DBD applications and to know the electrical conditions that lead to homogeneous discharges. These methods include Intensified Charge-Coupled Device (ICCD), optical emission spectrum, numerical simulations, and image processing. Given that the image processing method is effective, simple, and does not require expensive equipment, it is a good solution to analyze the discharges under different experimental conditions [4]. However, to distinguish between the filamentary and homogeneous discharge modes, high-speed imaging with exposure times shorter than the lifetime of a streamer ($\approx$ ten ns) is required. When longer exposure times are used, the filaments or streamers cannot be distinguished; nevertheless, the image processing can be used to analyze other discharge properties such as the area, uniformity and even detect filamentary patterns. Consequently, this work implements an image processing algorithm to study the uniformity and area of the discharges rather than the discharge mode (homogeneous or filamentary). Such analysis is based on the image gray-level histograms proposed in [4].

The discharge pictures are obtained by the digital camera (Logitech C920) with an exposure time of 1/128 s. The steps of the implemented image processing algorithm are:

1. The picture is converted into a gray-scale image.
2. The segmentation of the discharge area is performed.
3. The gray level histogram of the discharge area is analyzed.

To exemplify the working principle of the algorithm, Figure 5.12 shows the steps of three picture cases working with different electrical conditions but with the same gas conditions ($G = 3$ lpm, $NO = 800$ ppm, $O2 = 0$ %) and a similar power level $P_{dbd} \approx 36$ W . The image of Case A is taken using the square current pulses in continuous mode; Case B is obtained by square current pulses in burst mode; and Case C is obtained by the sinusoidal voltage source.

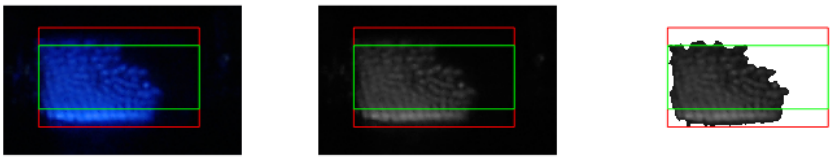

(a) Continuous Square Current:
$f_s = 80\ kHz$, $J = 3.2\ A$, $T_{pulse} = 1.562\ \mu s$ $P_{dbd} = 36.3\ W$

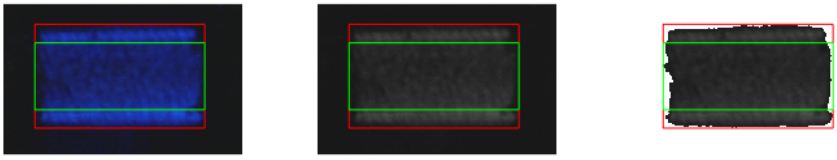

(b) Burst Mode Square Current:
$f_s = 80\ kHz$, $J = 3.0\ A$, $T_{pulse} = 1.562\ \mu s$, $N_{on} = 10$, $T_{idle} = 12.5\ \mu s$, $P_{dbd} = 38\ W$

(c) Sinusoidal Voltage:
$f = 10\ kHz$, $\hat{V_{dbd}} = 11\ kV$, $P_{dbd} = 36.6\ W$.

Figure 5.12: Image Processing

In the first step of the algorithm, the true-color image of (500x300) pixels is converted into a gray-scale image. Each element of the resulting matrix contains the gray level, ranging from 0 to 255. Due to the low intensity of case C, the gray level image looks dark, and it is hard to distinguish the discharge with the naked eye. However, the discharge is revealed in the segmentation step. In this step, the discharge area is segmented using a thresholding technique. It means that a gray-level value called "threshold value" is used as the delimiter between the background and the discharge area. All pixels with values less than the threshold value are considered background, and pixels with values greater than the threshold are considered the discharge area. In order to find the threshold value, Otsu's method is used [5]. This method chooses a threshold value that minimizes the variance of the thresholded background and discharge pixels. As evidenced in Figures 5.12-c, Otsu's method segments the discharge even at low-intensity uniform discharges.

As shown in all the cases of Figures 5.12, the upper and lower part of the discharge seems brighter than the central part. The coaxial geometry of the reactor causes this effect. In the central part of the discharge, the inner electrode creates a solid background. Whereas in the upper and lower parts, the gas gap and quartz barriers produce an optical effect that intensifies the discharge. Hence, to avoid biased results due to this effect, the statistical

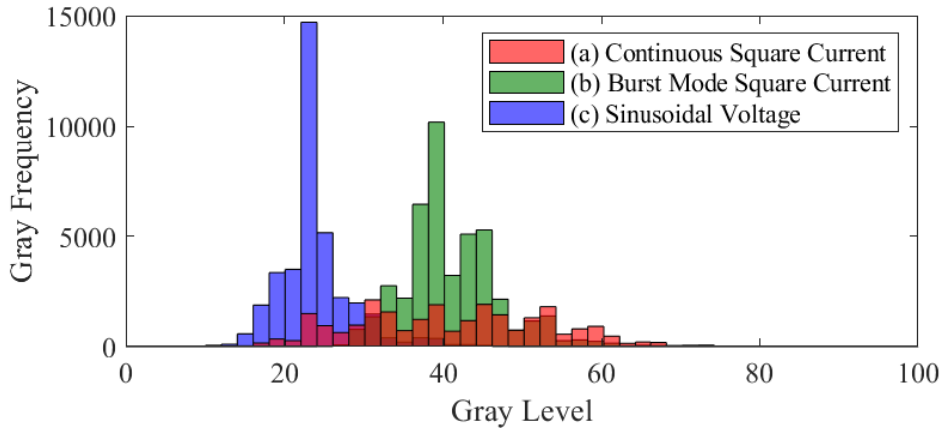

Figure 5.13: Gray Level Histograms

analysis of the discharge is performed only in the central part (area enclosed by the green rectangle).

The analysis of the discharge is based on the gray level histogram. Figure 5.13 shows the gray level histograms of the central part of the discharge for all the cases. The horizontal axis of the histogram presents the gray level value, and the vertical axis presents the gray frequency, calculated as the count of pixels for each level. Based on the histogram, statistical measurements are used to characterize the discharge. Below, the parameters of the analysis are explained:

- Discharge Area: It is the total number of pixels of the discharge multiplied by the pixel area. The segmentation process obtains the number of pixels, and the pixel area (0,15 mm * 0,15 mm) is deduced according to the dimensions of the reactor .
- Mean Gray Level (μ_{gray}): It is the mean of the gray-level value of the pixels in the central discharge area. This indicates the mean brightness of the discharge.
- Standard Deviation (SD): The SD measures the dispersion of the data from its mean value, and it is a crucial parameter to determine the discharge uniformity quantitatively. In an ideal uniform discharge, all the reactor pixels should have the same gray-level value; thus, the SD is zero in this case. In general, the lower the standard deviation, the data points tend to be closer to their mean, meaning a more uniform discharge.
- Coefficient of variation (CV):The CV, also known as the relative standard deviation, is defined as the ratio between the standard deviation and to the mean gray level, μ_{gray}. $CV = SD/\mu_{gray}$. This parameter provides a statistical comparison of the gray level histograms, even if the mean levels are drastically different from one picture to another. Thus, the CV allows the comparison of the discharge uniformity at different discharge brightness. As well as the SD, the lower the CV, the more uniform the discharge will be.

Table 5.3 presents the resulting parameters for the three cases of Figure 5.12. Considering

that all cases operate with a similar power level, several differences in the discharge appearance stand out. Concerning the discharge area, it can be seen that whereas in cases B and C, the discharge covers the whole area of the electrodes; in case A, a partial discharge occurs, covering only 48% of the visible area of the electrodes. Furthermore, the brightness of the discharge (μ_{gray}) of cases A and B (square current source) is significantly higher than case C (sinusoidal voltage).

Case	Area $[mm^2]$	μ_{gray}	SD	CV
(a) Continuous Square Current	709	41.45	11.98	0.29
(b) Burst Mode Square Current	1451	41.32	5.99	0.15
(c) Sinusoidal Voltage	1399	24.35	3.85	0.16

Table 5.3: Results of image processing

Based on the SD and CV value, it can be observed that the discharge obtained by the square current source in burst mode is more uniform than the continuous mode. Moreover, the SD of the sinusoidal voltage source is lower than the square current cases. Nonetheless, due to the big differences in the mean gray level μ_{gray}, the SD can not be directly used to compare the discharge uniformity. Instead, the CV value provides a more fair comparison. As the CV does not show a notable difference between the sinusoidal voltage and the burst mode square current, there is no significant difference in the uniformity of these two cases (B and C).

With these example images, some initial insights into the effect of the electrical conditions in the discharge appearance are observed. The following chapter investigates in depth the different supply methods and the effect of their parameters in the discharge using the image processing algorithm here exposed.

5.4.3 Electric Diagnostic

Three different electric supply methods are compared in this thesis: sinusoidal voltage source, square current source in continuous mode, and square current source in burst mode. The first two supply methods operate with a continuous imposition of their respective waveform, whereas, in the burst mode, there is a train of pulses followed by a zero voltage time. Regardless of the differences in the supply methods, the Q-V diagrams are essential for the parameters identification and characterization of the reactor; hence, the electric diagnostic is based on this tool. Below, the diagnostic for the waveforms in continuous mode is presented, followed by some additional analysis required for the burst mode.

5.4.3.1 Continuous Mode Diagnostic

Figure 5.14 shows an example of the electrical waveforms and Q-V Lissajous diagrams for the two power supplies in continuous operation: sinusoidal voltage source and square current source. These are the electrical waveforms corresponding to the example pictures presented in the previous section (Figure 5.12).

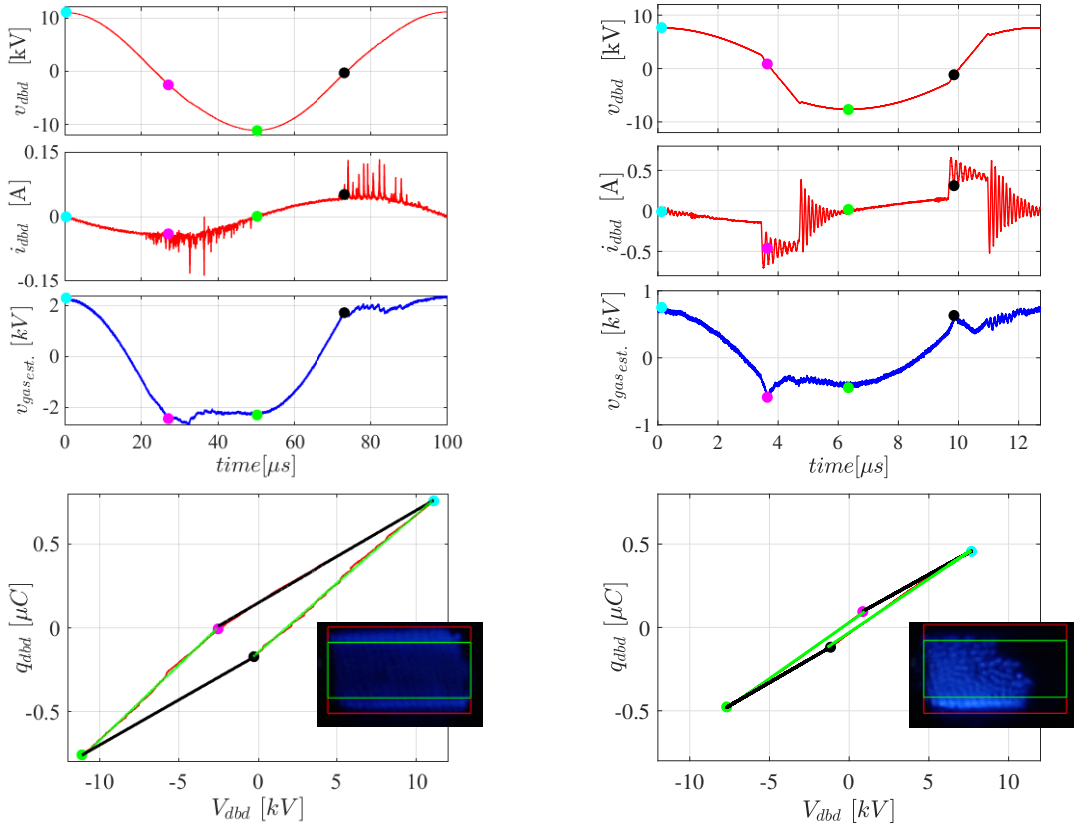

(a) Sinusoidal Voltage: $f = 10\ kHz$, $\hat{V_{dbd}} = 11\ kV$, $P_{dbd} = 36.6\ W$.

(b) Continuous Square Current: $f_s = 80\ kHz$, $J = 3.2\ A$, $T_{pulse} = 1.562\ \mu s$ $P_{dbd} = 36.3\ W$

Figure 5.14: Continuous Electric Diagnostics

In both cases, an entire period of the DBD waveforms is used to characterize the discharge, and the Q-V diagram is processed according to Manley's method to obtain the electric model parameters, discharge time, and delivered energy (Subchapter 3.2). We will refer to the identified values as the effective measurements $C_{eq_{Eff}}$, $C_{d_{Eff}}$, $C_{g_{Eff}}$, and $V_{th_{Eff}}$.

A Matlab script is employed to detect the corners of the parallelogram formed by the Q-V diagrams. Then, the slope of each segment is calculated based on a linear approximation. In Figure 5.14, the green lines of the Q-V plots correspond to the approximation of the segments when the discharge is ignited, and their slopes are equivalent to the dielectric capacitance $C_{d_{Eff}^{+,-}}$. The notation $C_{d_{Eff}^{+}}$, and $C_{d_{Eff}^{-}}$ refers to the value calculated with the positive and negative current direction. As the reactor has a coaxial geometry, the area of the outer electrode is bigger than the inner one. This asymmetry can cause differences for each current flow direction. On the other hand, the black lines correspond to the approximation during the off state of the discharge, and their slopes are related to the equivalent capacitance $C_{eq_{Eff}^{+,-}}$.

Moreover, from the Q-V diagram, the DBD voltage, v_{dbd}, at $q_{dbd} = 0$ is associated to V_{thEff}, and based on the values of C_{dEff} and $C_{eq_{Eff}}$, the gas capacitance, $C_{g_{Eff}}$, is deduced as:

$$\frac{1}{C_{g_{Eff}}{}^{+,-}} = \frac{1}{C_{eq}{}^{+,-}_{Eff}} - \frac{1}{C_{d}{}^{+,-}_{Eff}} \tag{5.6}$$

The average DBD power is calculated multiplying the instantaneous voltage and current and then averaging over a period:

$$\langle P_{dbd} \rangle_T = = \frac{1}{T} \int_0^T v_{dbd}(t) i_{dbd}(t) dt \tag{5.7}$$

Given that the area enclosed by the parallelogram is equivalent to the energy delivered to the discharge, the DBD average power can also be obtained as the parallelogram area multiplied by the frequency of the discharge cycle, $1/T$.

Furthermore, the voltage of the gas gap, v_{gas}, is estimated by Equation 5.8, where C_{dEff} is the value obtained from the parallelogram slopes. Figure 5.14 shows in blue the estimated waveform $v_{gas_{est.}}$. As can be seen, when the discharge is ignited, v_{gas} remains almost constant at V_{thEff}.

$$v_{gas}(t) = v_{dbd}(t) - \frac{1}{C_d} q_{dbd}(t) \tag{5.8}$$

Table 5.4 details the parameters calculated for both examples of Figure 5.14. Both cases have similar average power, but the energy delivered with the Square Current is lower as it works at a higher frequency. Concerning the identified DBD parameters, the estimated $C_{eq_{Eff}}$ values are similar in both cases and current directions (around 51 pF). Nonetheless, there are strong differences in the parameters identified when the discharge is ignited (C_{dEff}, V_{thEff}).

Case	$\hat{V_{dbd}}$ [kV]	P_{dbd} [W]	E_{dbd} [mJ]	$C_{eq}{}^{-}_{Eff}$ [pF]	$C_{eq}{}^{+}_{Eff}$ [pF]	$C_{d}{}^{-}_{Eff}$ [pF]	$C_{d}{}^{+}_{Eff}$ [pF]	V_{thEff} [V]
Sinusoidal Voltage	11.15	36.6	3.66	51.3	53.0	90.2	82.2	2380
Square Current	7.7	36.3	0.45	50.4	51.6	60.4	62.8	470

Table 5.4: Results of electric diagnostic

Electric model for Partial Discharging Area It is well known that the breakdown voltage, V_{th}, gas capacitance, C_g, and dielectric capacitance, C_d, are physical parameters de-

termined by the gas composition, pressure, dielectric material and geometry. However, it is commonly observed a variation in the identified parameters as a function of the electric conditions, even if the reactor geometry does not change [2]. This phenomenon in the model identification takes place when the voltage across the gas gap, v_{gas}, is not significantly higher than the breakdown voltage, V_{th} [6]. Consequently, the discharge occurs in a partial area of the available electrode surface. Such a behavior can be seen in the discharge picture of Figure 5.14-b. As the gas voltage increases, the discharge area extends until it fully covers the electrodes, and the values measured using Manley's diagram saturate at the theoretical ones. In that scenario, the classic DBD electric model completely represents the load. Nonetheless, for the partial surface discharging, a modified model is required. In consequence, an electric model where C_d, and C_g are split into the non-discharging area (α) and the discharging-area (β), for $\alpha + \beta = 1$ (model shown in Figure 5.15) have been proposed [7, 8].

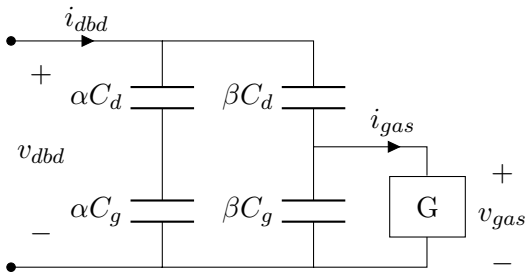

Figure 5.15: DBD Model proposed by [7] for partial discharging

It is important to mention that, as the non-discharging area is modeled as a parallel capacitance, it does not affect the energy and power estimation. In addition, the DBD equivalent capacitance remains at $C_{eq} = C_d C_g/(C_d + C_g)$. Contrary, the measured values of C_d, and V_{th}, referred to as C_{dEff} and V_{thEff}, will depend on the discharging area.

$$C_{dEff} = \alpha C_{eq} + \beta C_d \tag{5.9}$$

Solving the gas voltage for the partial discharging model, one obtain:

$$v_{gas}(t) = \Big(1 + \frac{\alpha}{\beta}\frac{C_{eq}}{C_d}\Big)v_{dbd}(t) - \frac{1}{\beta C_d}q_{dbd}(t) \tag{5.10}$$

Note that for $\beta = 1$, Equation 5.10 reduces to Equation 5.8. From Equation 5.10, V_{th} can be deduced as:

$$V_{th} = V_{thEff}\frac{1 - C_{eq}/C_d}{1 - C_{eq}/C_{dEff}} \tag{5.11}$$

Based on these simple relations between the measured values and the actual physical parameters, the discharge area can be determined and compared with the area obtained from the imaging processing algorithm. This will allow a better interpretation of the characterization

for the different supply methods in the following experimental results chapter.

5.4.3.2 Burst Mode Diagnostic

To properly diagnose the plasma generated by the Square Current Source in burst mode, some parameters must be redefined, and additional steps in the waveforms processing must be included. Figure 5.16 presents an example of the experimental DBD waveforms and their respective Q-V trajectory in the whole burst period. In this example, ten current pulses working at $f_s = 80\ kHz$, $T_{pulse} = 1.562\ \mu s$, and $J = 3\ A$, are delivered followed by a zero voltage idle time of $T_{idle} = 12.5\ \mu s$. As described in the implementation of the power supply (Subchapter 4.6), at the start of the current pulses, the initial conditions of the DBD capacitance and magnetizing inductance cause a transient in the waveforms. Consequently, the initial pulses behave differently, and the energy deposited into the discharge differs from pulse to pulse. Indeed, some pulses may not even produce the gas breakdown, whereas others may inject a high amount of energy. Such a strong variation in the waveforms will impact the treatment and has to be studied.

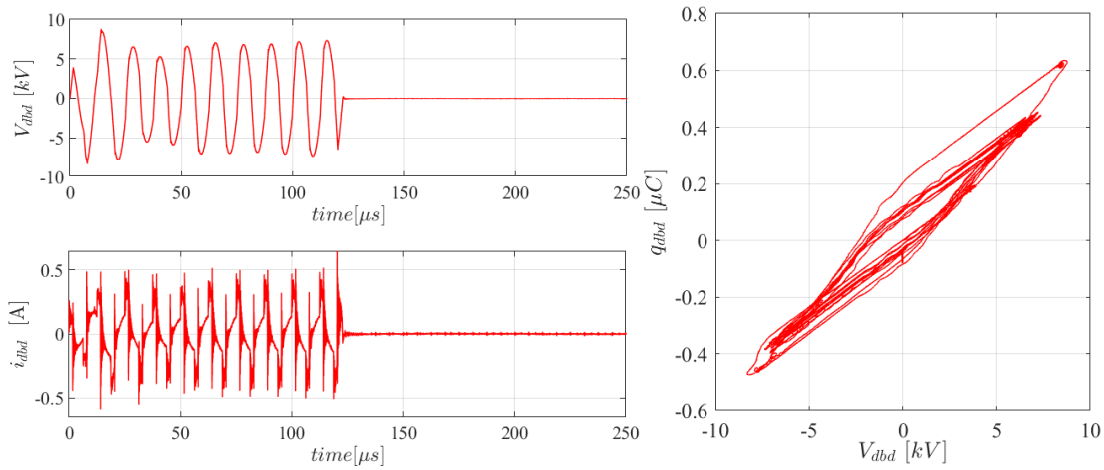

Figure 5.16: Electric Diagnostics in Burst Mode
$f_s = 80\ kHz$, $J = 3.0\ A$, $T_{pulse} = 1.562\ \mu s$, $N_{on} = 10$, $T_{idle} = 125\ \mu s$, $P_{dbd} = 38\ W$

In the first step of the burst diagnosis, an entire burst period is segmented to calculate some general parameters such as the positive and negative peak voltage, the burst frequency, $f_{burst} = 1/T_{burst}$, and the average power calculated in the burst period as:

$$\langle P_{dbd} \rangle_{burst} = = \frac{1}{T_{burst}} \int_0^{T_{burst}} v_{dbd}(t) i_{dbd}(t) dt \tag{5.12}$$

Then, each pulse is analyzed independently. When the DBD operates in a steady-state, the Q-V diagram over a discharge period forms a closed parallelogram, where each of the four segments is related to a state of the discharge. However, due to the transient state of the

burst mode, the initial pulses are not periodical, and their Q-V diagrams do not form closed parallelograms; hence, it is impossible to use the classic Manley method. As an alternative, we propose to analyze the Q-V trajectories by splitting the pulses using the DBD peak voltages as the time delimiter to define the periods which build the burst. Figure 5.17 shows the split pulses and trajectories. A different color represents each pulse, and to better visualize the differences between pulses, Figure 5.17 depicts the Q-V trajectory of the first four pulses individually and the six remaining pulses grouped.

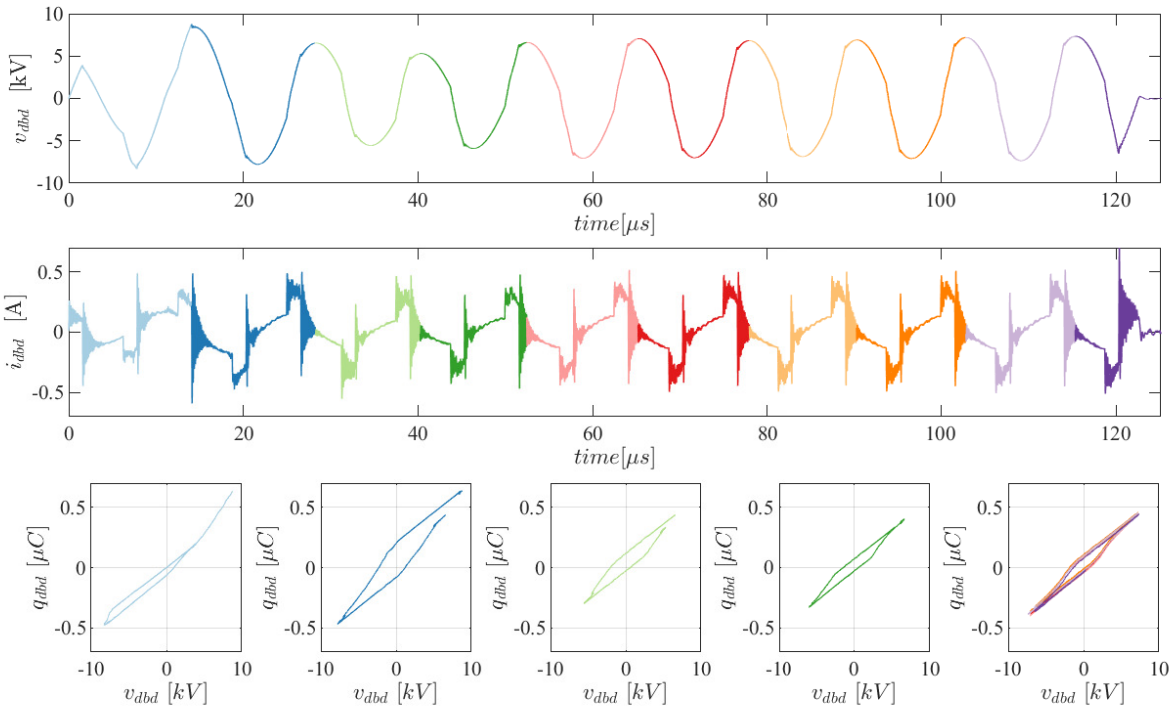

Figure 5.17: Electric Diagnostics in Burst Mode

As can be seen, using the peak voltage as time delimiter, all the Q-V trajectories have the four segments, even if the parallelogram is not closed. In this way, it is possible to estimate all the DBD capacitances using the segment slopes. Moreover, once the steady-state is achieved, the period of the pulses split using the peak voltage matches the period of the square current pulses T_s. However, as the initial trajectories are not closed, the area of the parallelogram can not be related to the energy; instead, the cumulative energy per current pulse is calculated as:

$$\xi_n = \int_{(n-1)T_s}^{nT_s} v_{dbd}(t) i_{dbd}(t) dt \tag{5.13}$$

As the energy is only deposited in the discharge during the train of pulses, the average power can also be calculated as the sum up of the energy delivered in each current pulse, ξ_n, divided by the total burst period.

$$\langle P_{dbd} \rangle_{burst} = \frac{1}{T_{burst}} \sum_{n=1}^{N_{on}} \xi_n \tag{5.14}$$

One of the most relevant observations of the burst mode is the fluctuations of the energy delivered per pulse. In this particular OP, the voltage of the first positive current pulse voltage is insufficient to ignite the discharge, and the following half-cycles generate the gas breakdown with different energies. Since it is complicated to describe the operation of each pulse for all the OPs, we introduce into the diagnosis the ratio between the discharge energy per pulse to the total energy of the burst period. On this basis, the percentage of the total energy delivered per pulse can be more easily interpreted. This analysis is inspired by [9], where slight differences in burst pulses are studied. Figure 5.18-a shows the energy delivered per pulse and Figure 5.18-b depicts the percentage of energy in a grouped bar diagram. As can be seen, in this example OP, the second pulse has the highest energy among all the pulses; after the fifth pulse, they get closer to the steady-state, and all behave similarly, with equivalent energy consumption. The energy distribution will have significant changes with the operating conditions, as shown in the following chapter.

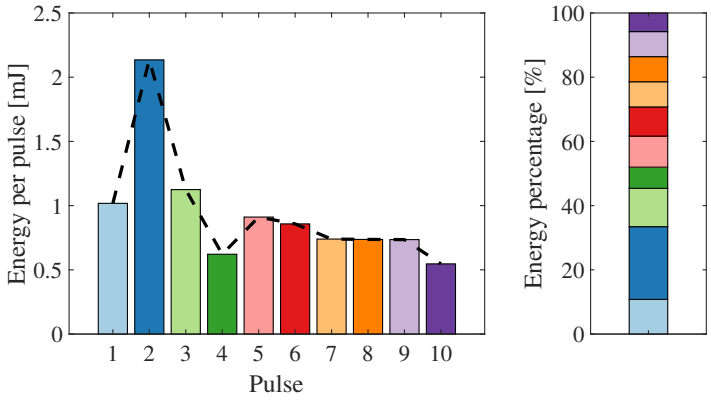

Figure 5.18: Energy delivered per pulse in Burst Mode

5.5 Conclusions

An experimental bench for NO_x treatment has been implemented. This system is intended to be a tool for finding the effects of the power supplies on the NO_x treatment. The instruments, set-up, and experimental protocol are introduced, and based on the measurements acquired at each experiment, a methodology for the data analysis is proposed. The data analysis of the treatment is split into chemical, optical and electric diagnostic. Some experiments are presented to exemplify the diagnostic methods that will be employed in experimental results analysis.

Bibliography

[1] P. Bruggeman and R. Brandenburg, "Atmospheric pressure discharge filaments and microplasmas: physics, chemistry and diagnostics," *Journal of Physics D: Applied Physics*, vol. 46, no. 46, p. 464001, 11 2013. doi: https://doi.org/10.1088/0022-3727/46/46/464001

[2] F. Peeters and T. Butterworth, "Electrical Diagnostics of Dielectric Barrier Discharges," *Atmospheric Pressure Plasma - from Diagnostics to Applications*, no. November 2018, 2019. doi: https://doi.org/10.5772/intechopen.80433

[3] T. C. Manley, "The Electric Characteristics of the Ozonator Discharge," *Transactions of The Electrochemical Society*, vol. 84, no. 1, p. 83, 1943. doi: https://doi.org/10.1149/1.3071556

[4] Y. Wu, Q. Ye, X. Li, and D. Tan, "Classification of dielectric barrier discharges using digital image processing technology," *IEEE Transactions on Plasma Science*, vol. 40, no. 5 PART 2, pp. 1371–1379, 2012. doi: https://doi.org/10.1109/TPS.2012.2187802

[5] N. Otsu, "A Threshold Selection Method from Gray-Level Histograms," *IEEE Transactions on Systems, Man, and Cybernetics*, vol. 9, no. 1, pp. 62–66, 1 1979. doi: https://doi.org/10.1109/TSMC.1979.4310076

[6] F. Peeters, "The Electrical Dynamics of Dielectric Barrier Discharges," Ph.D. dissertation, Technische Universiteit Eindhoven, 2015.

[7] F. J. J. Peeters and M. C. M. van de Sanden, "The influence of partial surface discharging on the electrical characterization of DBDs," *Plasma Sources Science and Technology*, vol. 24, no. 1, p. 015016, 12 2014. doi: https://doi.org/10.1088/0963-0252/24/1/015016

[8] A. Belinger, N. Naudé, and N. Gherardi, "Transition from diffuse to self-organized discharge in a high frequency dielectric barrier discharge," *The European Physical Journal Applied Physics*, vol. 79, no. 1, p. 10802, 7 2017. doi: https://doi.org/10.1051/epjap/2017160487

[9] Y. Zhang, L. Wei, X. Liang, and M. Šimek, "Ozone Production in Coaxial DBD Using an Amplitude-Modulated AC Power Supply in Air," *Ozone: Science & Engineering*, vol. 41, no. 5, pp. 437–447, 9 2019. doi: https://doi.org/10.1080/01919512.2019.1565986

Part III

Results

Chapter 6

Experimental Results

Contents

6.1 Introduction

Based on the methods and methodology proposed to analyze the $DeNO_x$ treatment, this chapter presents the experimental results of the power supplies under study: Sinusoidal voltage source, Square current source in continuous mode, and Square current source in burst mode. Initially, the Sinusoidal Voltage Source results are presented to have a comparison baseline, since this can be considered as the most traditional supply method. Then, the Square current Source is investigated in both of its operation modes. In the continuous mode, the frequency of the pulses, f_s, injected current, J_{prim}, and pulse duration, T_{pulse}, are the parameters controlling the DBD power. However, due to some experimental limitations of the continuous mode, the results are not robust enough to conclude about the effects of the pulse parameters in $DeNO_x$ treatment. The limitations are related to two aspects that will be detailed: the plasma stabilization and evolution of the discharge over time.

On the other hand, more robust results are attained with the burst operation. Section 6.4 presents the burst mode outcomes. At first, the plasma stabilization, evolution of the discharge, and the experiments variability are evaluated and compared with the continuous mode. Then, the impact of the HF pulses, burst and gas parameters are studied. The three analysis methods described in Section 5.4 are used to determine the optimum supply conditions: electrical waveforms analysis, treatment results, and discharge appearance.

6.2 Sinusoidal Voltage Source

The sinusoidal voltage source is a traditional power supply employed in the experimentation of DBD systems. For the $DeNO_x$ treatment, several experiments using this supply method are reported [1–5]. Such results serve as a starting point for identifying the performances achieved by voltage sources (previously presented in state of the art). Nonetheless, given that the reactor design and gas conditions are not standard among the literature results, some experiments using the proposed experimentation bench supplied by a sinusoidal voltage source are carried out. The objective of this set of experiments is to establish a baseline for the assessment of the current-mode power supplies. In order to evaluate the impact of the sinusoidal voltage on the $DeNO_x$ treatment, the electrical, optical, and chemical diagnostic methods previously exposed are employed.

6.2.1 Electric Diagnostic

The sinusoidal voltage is produced using a low voltage signal generator (Agilent 33210) connected to an audio amplifier (Crest Audio - CA 18) that feeds a step-up transformer (Montoux S= 600 VA, 60 V/9 kV). The DBD reactor is placed in the output of the step-up transformer (Figure 6.1). According to the transformer and audio amplifier limitations, the peak voltage can vary from 0 kV to 12 kV, and the frequency from 2 kHz to 15 kHz. All the experiments performed with the sinusoidal voltage source have a fixed gas composition: $NO = 800$ ppm, $O_2 = 0$ %, and $G = 3$ lpm.

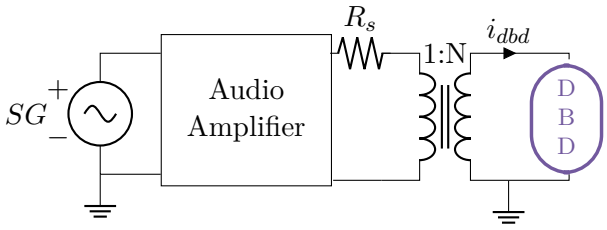

Figure 6.1: Sinusoidal Voltage Source Setup

In this setup, the DBD power consumption can be controlled by both of the sinusoidal supply parameters (peak voltage and frequency). This is clearly seen in Manley's Formula [6], in which the DBD power is deduced as a function of the voltage frequency, f, amplitude ($\hat{V_{dbd}}$), and DBD model parameters (C_g,C_d, V_{th}). Some of the voltage and current waveforms obtained at different supply conditions are shown in Figure 6.2.

$$P_{dbd} = 4 f V_{th} C_d (\hat{V_{dbd}} - \frac{V_{th} C_g}{C_{eq}}) \tag{6.1}$$

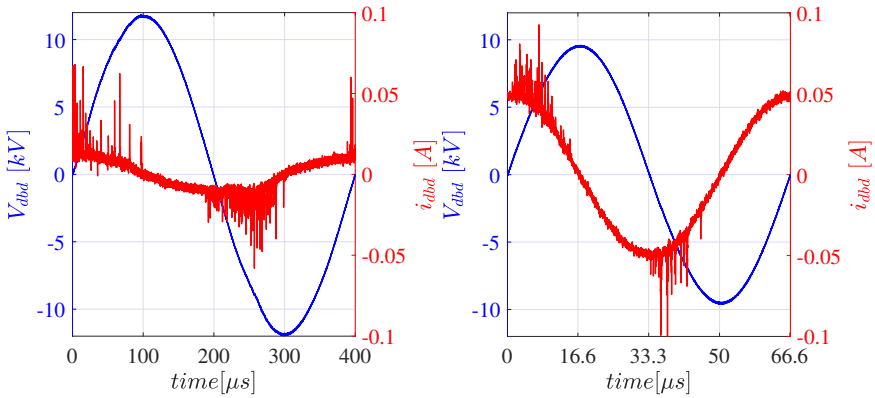

(a) $f = 2.5\ kHz$, $V_{dbd} = 12\ kV$ (b) $f = 15\ kHz$, $V_{dbd} = 9.5\ kV$

Figure 6.2: Waveforms of sinusoidal voltage source working at $\langle P_{dbd} \rangle_T \approx 10\ W$

Figure 6.3 shows the relation between the experimental peak voltage and DBD power at different frequencies. For each frequency, the minimum peak voltage is the experimental voltage demanded to produce the discharge. Once the plasma appears, the power increases with the peak voltage and frequency. Note that because of the voltage limitation of the setup, the DBD power range achieved at each frequency is not the same. The lower the frequency, the higher the DBD peak voltage demanded to attain a desired power.

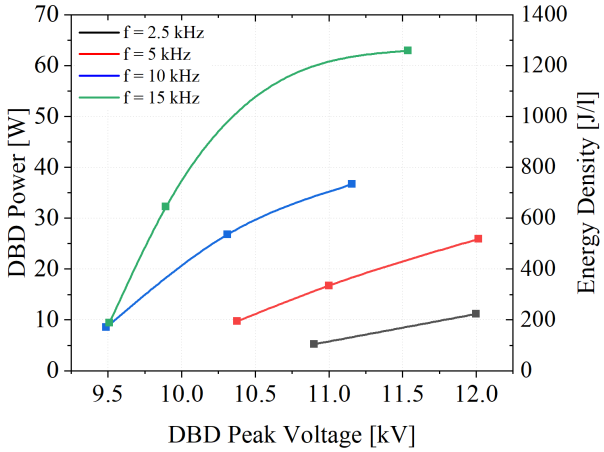

Figure 6.3: Peak voltage vs Power for sinusoidal voltage source

The electrical characterization of the reactor is performed by means of the Q-V trajectories. Figure 6.5 presents the Q-V plots for the OPs working at $f = 15\ kHz$. Each of the parallelograms are processed as discussed in Subchapter 5.4.3 to obtain the set of the electrical DBD parameters ($C_{eq_{Eff}}$, C_{dEff}, V_{thEff}). Remember that the notation, X_{Eff}, is used to

specify the effective measurement of the DBD parameters. Given that the discharge area of some OPs may not cover the entire electrode's surface, the measured DBD parameters vary with the discharge area, thus differ from the theoretical model parameters (C_d, C_g, V_{th}).

The results of the parameters identification are shown in Figure 6.4. As seen in Figure 6.4-a, the identified equivalent capacitance of the reactor, $C_{eq_{Eff}}$, does not change with any of the sinusoidal parameters (the value remains constant at $51 \pm 0.56\ pF$). The stable value of $C_{eq_{Eff}}$ is also observed in Figure 6.5, where the upper and lower segments of all the trajectories have the same slope.

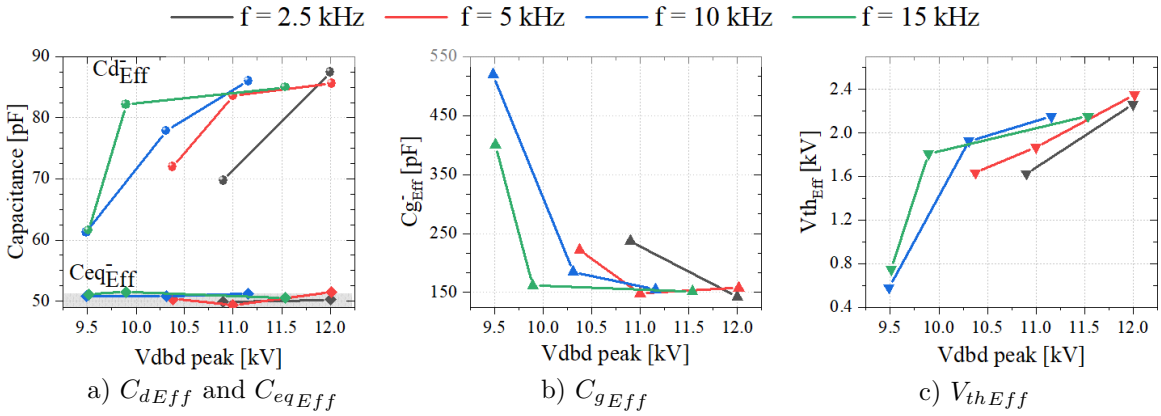

a) C_{dEff} and $C_{eq_{Eff}}$ b) $C_{g_{Eff}}$ c) $V_{th\,Eff}$

Figure 6.4: DBD electrical model parameter obtained from the Sinusoidal Voltage Supply OPs.

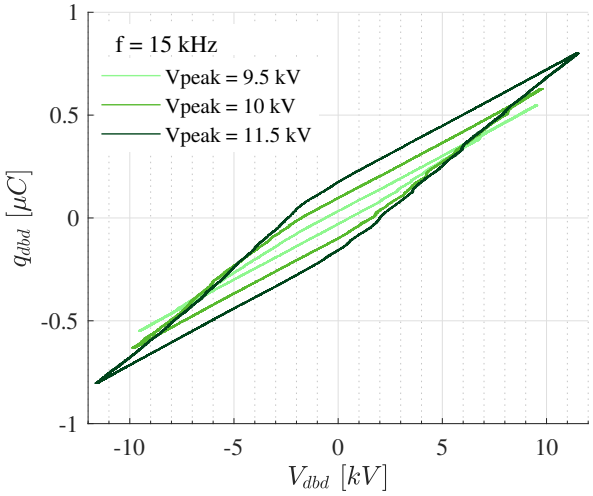

Figure 6.5: Q-V Trajectories of Sinusoidal Voltage Source

On the opposite, the measured dielectric capacitance C_{dEff}, gas capacitance $C_{g_{Eff}}$, and breakdown voltage $V_{th\,Eff}$ have strong variations. As mentioned, such variations are caused by discharges covering only a portion of the electrodes, which may occur when the DBD voltage

is not significantly higher than the breakdown voltage. As the DBD voltage increases, the area covered by the discharge grows until it fully covers the electrodes. At this point, the measured values C_{dEff}, $C_{g_{Eff}}$, and V_{thEff} saturate. In this set of experiments, it can be seen that C_{dEff} increases with the peak voltage and tends to 87 pF. In the same way, $C_{g_{Eff}}$ decreases tending to 150 pF, and V_{thEff} tends to 2350 V. As the discharge of the high voltage OPs covers most of the electrode's surface, one can assume that the maximum measured parameters approximate to the full discharge area values C_d, C_g, and V_{th}.

Based on the electrical model obtained characterizing the reactor at each operating point, the theoretical DBD power is calculated using Equation 6.1 with the effective measurements (C_{dEff}, $C_{g_{Eff}}$, V_{thEff}). The comparison between the experimental and calculated power is exhibited in Table 6.1. The average error of all the experiments is 12%.

f [kHz]	$\hat{V_{dbd}}$ [kV]	$C_{d_{Eff}}^{-}$ [pF]	$C_{g_{Eff}}^{+}$ [pF]	V_{thEff} [V]	P_{dbd} Exp. [W]	P_{dbd} Theo. [W]	Relative Error [%]
2.5	10.74	69.7	237.1	1627	5.2	4.1	22%
2.5	11.81	87.5	142.7	2262	11.1	11.6	4%
5	10.38	72.0	221.9	1634	9.7	8.7	10%
5	10.90	83.6	147.9	1866	16.7	17.9	7%
5	12.02	92.0	139.6	2554	25.9	26.3	1%
10	9.49	60.9	548.8	579	6.2	5.2	15%
10	10.31	81.6	167.0	1929	26.8	27.9	4%
10	11.16	90.1	142.8	2169	36.6	43.4	18%
15	9.59	60.6	400.9	745	9.4	10.6	13%
15	9.89	82.2	161.6	1807	32.2	40.4	25%
15	11.54	88.2	142.5	2154	62.9	67.3	7%

Table 6.1: DBD electrical modeling and power estimation

Additionally, the effective measurements of the DBD parameters presented in Table 6.1, can be used to estimate the discharge area (β) by means of the Equation 6.2, introduced by the partial discharging area model (Section 5.4.3.1)

$$C_{dEff} = (1 - \beta)C_{eq} + \beta C_d \tag{6.2}$$

where, C_{dEff} is the effective measurement at each OP, and C_{eq} and C_d are the DBD parameters when the discharge fully cover the reactor surface (approximately $C_{eq} = 51$ pF, and $C_d = 87$ pF). This analysis is used above to compare the estimation of the discharge area with the image processing results.

6.2.2 Optical Diagnostic

The first step of the image processing algorithm is the segmentation of the discharge. This step results in the discharge area measured in mm^2, which can be related to the parameter β of the electric model for partial area discharges. Figure 6.6 presents the discharge area obtained by the image processing algorithm for each OP (represented by the diamond symbols), and shows the differences with the discharge area calculated by the electrical parameters identification of Equation 6.2 (presented as error bars).

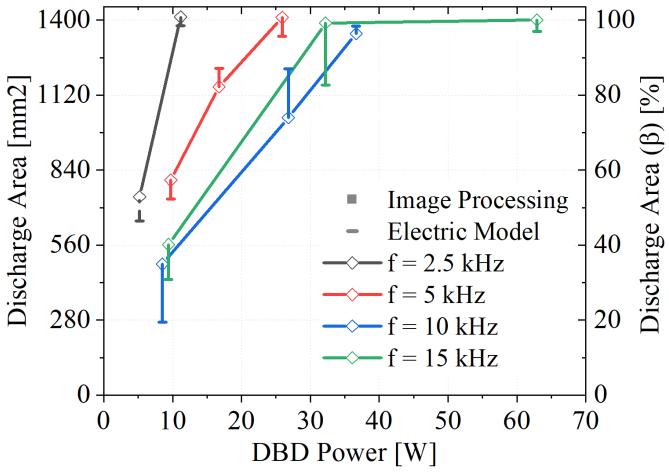

Figure 6.6: Discharge area calculated with Image processing vs characterization of the partial discharging electric model

It should be mentioned that both methods have some pitfalls. For the image processing algorithm, as the reactor has a cylindrical geometry, and the picture is only taken in the frontal face of the reactor, the area of the hidden face is unknown and assumed symmetrical to the frontal face. Additionally, as the picture is taken using a camera with low exposure times, the discharge filaments can not be distinguished individually. Therefore, exposure time is a source of error in the area estimation. On the other side, the area calculated by the electrical characterization relies on the model identification at each OP and the model values when the discharge covers the whole reactor area. In this case, we assumed the maximum C_d value identified in Table 6.1 as the full discharge capacitance and employed Equation 5.9 to solve β. However, a better estimation of the full discharge parameters might require increasing further the peak voltage, which was no longer possible with the current sinusoidal voltage setup.

Notwithstanding the pitfalls of both methods for estimating the discharge area, an average difference of 13% between them is obtained, and similar trends are observed. From Figure 6.6, it can be seen that at low frequencies, the power required to cover the whole reactor area is lower than at higher frequencies. For instance, at $f = 2.5\ kHz$, the discharge covers the entire area at $10\ W$. Whereas at similar power levels and higher frequencies, the discharge covers less than 60 % of the available area. This result is explained by the fact that the

lower the frequency, the higher the DBD voltage demanded to produce the required power. In consequence, the gas breakdown conditions is more easily attained at low frequencies, thus the discharge area is larger [7].

Finally, Figure 6.7 presents the mean gray level results (related to the discharge brightness) and the standard deviation, SD, and coefficient of variation, CV, parameters (associated with the discharge uniformity).

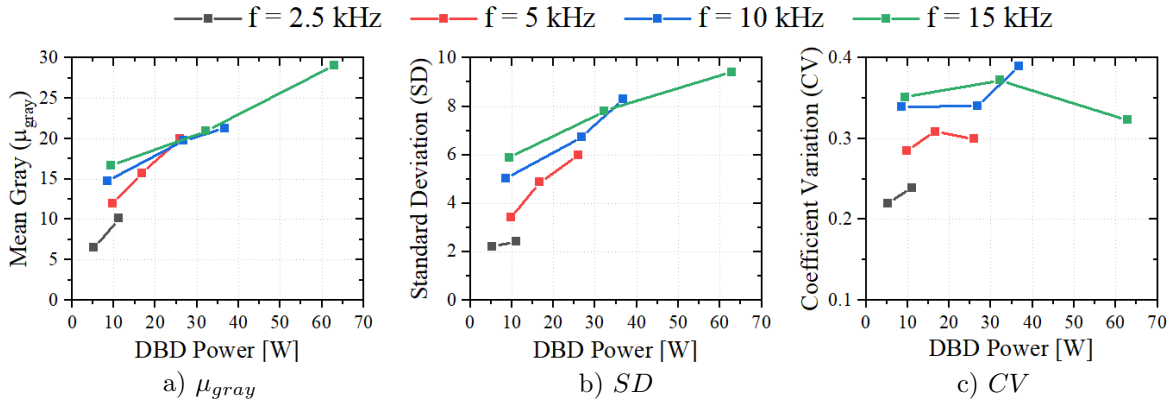

a) μ_{gray} b) SD c) CV

Figure 6.7: Results image processing for sinusoidal voltage source

As expected, the higher the power, the more bright is the discharge. Furthermore, by analyzing the results of the discharge uniformity, an effect of the voltage frequency is observed. The lower CV values are obtained at the lowest frequency (f = 2.5 kHz), which means that the discharge is more uniform in those cases. As the frequency increases, the CV values increase, suggesting a relation between the frequency and the discharge uniformity.

6.2.3 Thermal and Chemical Results

The thermal behavior of the reactor has proven to be an important parameter for identifying the plasma stabilization, and therefore, to obtain stable measurement of the gas composition. Figure 6.8 shows the temperature of the outer electrode of the DBD as a function of the power. In all the experiments, the temperature stabilized below 160 $°C$, which guarantees proper gas analysis.

Concerning the chemical diagnostic, Figure 6.9-a reveals that the NO_x removal efficiency increases with the power. As the range of the power swept at each frequency is not the same due to the voltage setup limitations, the impact of the frequency on the treatment can not be thoroughly examined. Nevertheless, to have a baseline for comparing the efficiency of the voltage source with the proposed current sources, a reference around $\eta NO_x = 90\%$ will be used. For $f = 10\ kHz$, $\eta NO_x = 91 \pm 5\%$ is obtained at $\langle P_{dbd} \rangle_T = 36.5\ W$, equivalent to an energy density equals to $ED = 730\ J/l$. Note that this is not the maximum efficiency achieved by the sinusoidal voltage source. In fact, if the power continues to increase, the efficiency increments. The maximum efficiency of this set of experiments was obtained at $f = 15\ kHz$ $\langle P_{dbd} \rangle_T = 63\ W$, $\eta NO_x = 97 \pm 5\%$.

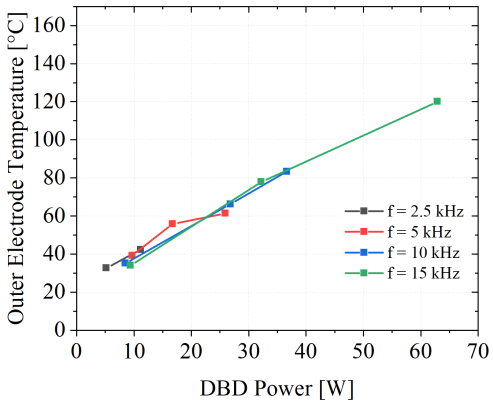

Figure 6.8: Outer electrode temperature vs electric power for Sinusoidal Voltage Source

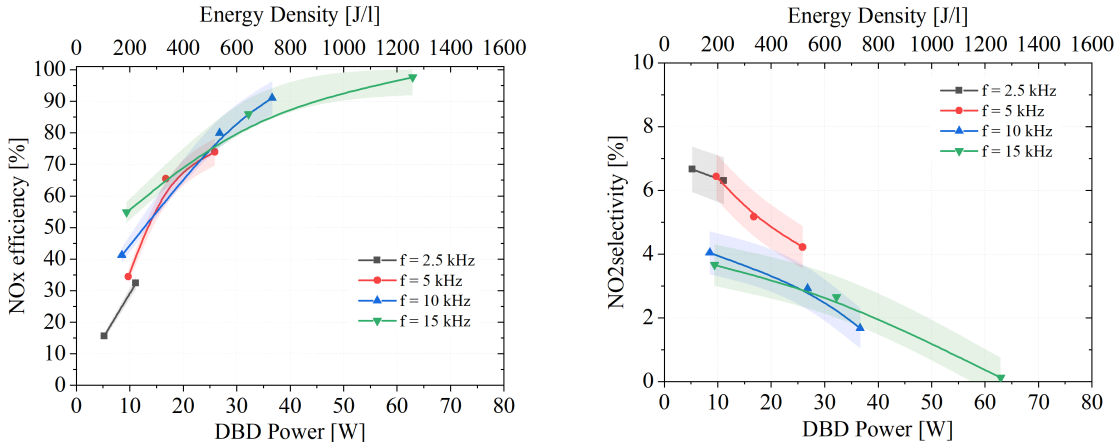

(a) $DeNO_x$ Efficiency (b) NO_2 Selectivity

Figure 6.9: Treatment performances of Sinusoidal Voltage Source

As shown in Figure 6.9-b, the portion of NO that oxidizes into NO_2 is higher at low power levels. Indeed, the production of NO_2 affects the total $DeNO_x$ efficiency. When the power is high enough, both the NO and NO_2 can be fully removed. From there, a first sight of the promising results of the $DeNO_x$ treatment are distinguished, and the opportunity to optimize the power required to get a complete NO_x removal is checked.

6.3 Square Current Source in Continuous Mode

The Square Current Source was conceived to deliver current pulses in the range of $f_s = 50 - 200\ kHz$, with a current amplitude up to 12 A in the primary side of the transformer and a maximum DBD peak voltage of 10 kV. The power supply schematic and analysis is presented in Subchapter 4.4. As was mentioned in the introduction, the continuous mode exhibits two limitations that are detailed above: the plasma stabilization at high temperature,

and the evolution of the discharge over time.

To exhibit the behavior and limitations of this supply mode, a set of experiments operating at $f_s = 80\ kHz$, and $T_{pulse} = 1.25\mu s$ are used. A sweep on the current amplitude J_{prim} is performed to control the DBD power. The lowest J_{prim} value is the minimum current required to produce the discharge ignition. For this study, J_{prim} is varied from $4.1 - 6.2\ A$, equivalent to a power variation of $\langle P_{dbd} \rangle_{T_s} = 19 - 142\ W$. The gas conditions are set at $G = 3\ lpm$, $NO = 800\ ppm$, and $O_2 = 0\ \%$. Two of the experimental electrical waveforms working at different power levels are shown in Figure 6.10.

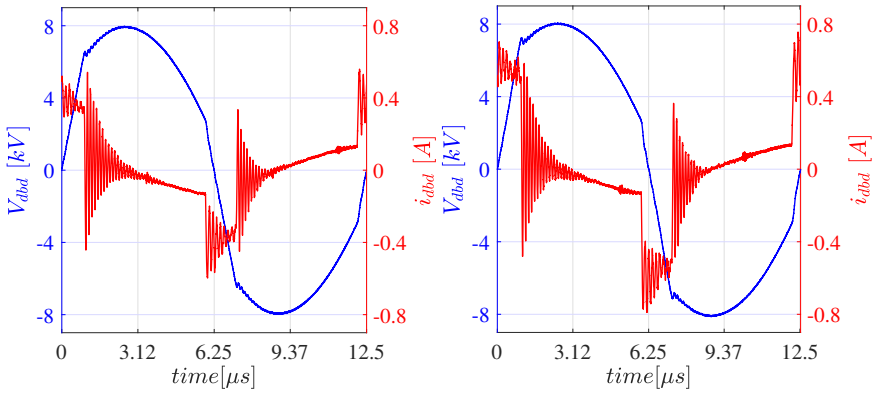

(a) $J_{prim} = 4.1\ A, P = 19\ W$ (b) $J_{prim} = 6.2\ A, P = 142\ W$

Figure 6.10: Waveforms in of Square Current Source in Continuous Mode. $f_s = 80\ kHz$, $T_{pulse} = 1.25\mu s$

6.3.1 Thermal and Chemical Results

Let us start by examining the thermal behavior of the reactor during treatment for this set of experiments. Figure 6.11 shows the temperature of the outer electrode recorded every 1 s after the discharge ignition for each OP. Remember that the experiments are interrupted when the electrode temperature exceeds $160°C$, protection required to prevent the deterioration of the silicon rubber of outer electrodes extremes, and prevent parasitic corona discharges. As can be seen, all the experiments start with the same initial temperature (26 $°C$). When the plasma is ignited, the reactor temperature starts rising. As expected, the higher the DBD power, the faster the temperature increases. At high power levels, the temperature increases so rapidly, that in less than two minutes the over-temperature protection is triggered. Only the first experiment ($J_{prim} = 4.1\ A, \langle P_{dbd} \rangle_{T_s} = 19\ W$) attained a stable thermal operation at a temperature slightly below 160 $°C$.

The fact that the over-temperature protection is triggered even at the low power levels is one of the most relevant limitations of the experimentation in continuous mode. In comparison with the thermal results of the Sinusoidal Voltage Source (Figure 6.8), there is a significant increase of the temperature, and therefore, in the amount of energy lost in the form of heat. With the sinusoidal voltage source, at $\langle P_{dbd} \rangle_T \approx 20W$, the electrode temperature stabilizes around 60 $°C$. In contrast, at a similar power level, the temperature of the experiment

($J_{prim} = 4.1\ A, \langle P_{dbd} \rangle_{T_s} = 19\ W$) is close to 160 $°C$.

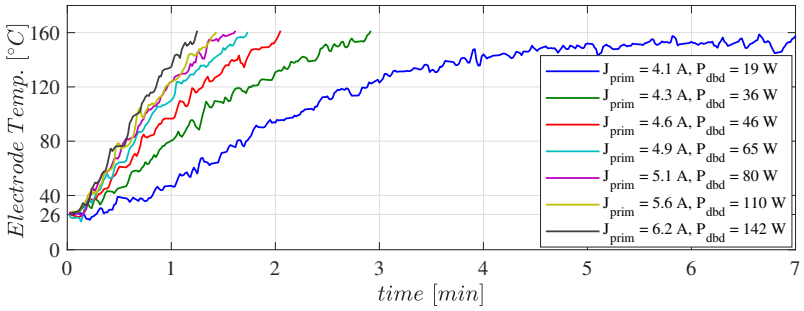

Figure 6.11: Variation of the temperature of the outer electrode during treatment. OPs working at : Continuous mode, $f = 80\ kHz$, $T_{pulse} = 1.25\mu s$

Several attempts to use the parameters of the current pulses to regulate the temperature were unsuccessful. Within the frequency, pulse duration, and current ranges of the power supply, no significant improvement in the thermal behavior of the reactor was observed. Only very few experiments obtained a steady thermal operation, close to 160 $°C$.

As most of the OPs do not reach the plasma steady-state before the over-temperature protection, the gas analyzer measurements are not settled; thus, the treatment analysis is not viable. This is clearly seen in Figure 6.12. Unfortunately, due to the thermal restriction, it is not possible to investigate the optimum supply condition using the continuous injection of current pulses with the proposed experimental setup. To further investigate this operating mode, the thermal resistance of the reactor, which is currently limited by the insulating silicon rubber, has to be improved, or the reactor has to be successfully cooled down. Nonetheless, as will be exposed in the optical diagnostic, the thermal and chemical results are not the only limitation of this operating mode. The evolution of the discharge over time poses additional problems.

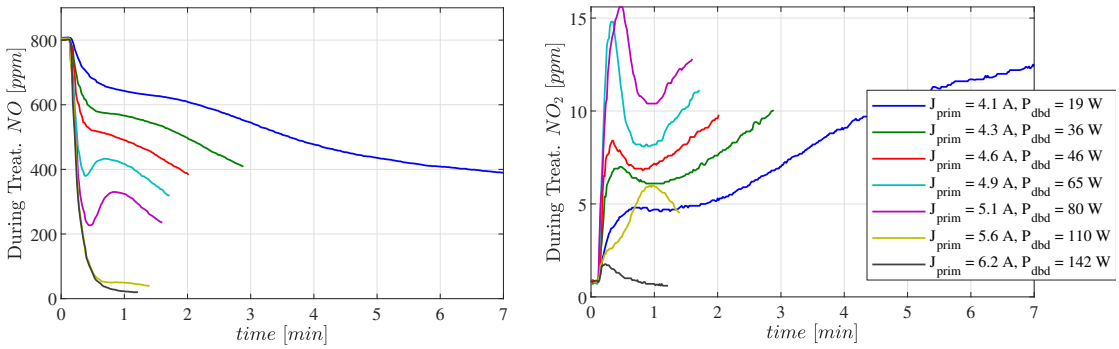

Figure 6.12: Measurements of the gas analyzer during treatment. OPs working at : Continuous mode, $f = 80\ kHz$, $T_{pulse} = 1.25\mu s$

6.3.2 Optical diagnostic

The second stage in studying the continuous mode limitations and behavior is related to the evolution of the discharge appearance. This study is based on the discharge pictures taken every 20 seconds after the discharge ignition for each OP. Figure 6.13 presents the discharge pictures of the experiments; as the execution time of the experiments is limited by the thermal protection, the high power experiments have less pictures than the low power experiments. Each row depicts the evolution over time of the discharge for a given experiment. The red boxes represent the total reactor area. Based on the pictures, three characteristics of the discharge are distinguished: the initial location, the effect of the gas flow, and the discharge area.

Several conditions of the reactor influence the discharge location. In an ideal reactor, the gas gap distance is perfectly spaced, thus, the breakdown voltage is constant across the entire reactor surface. However, the dielectric wall imperfections may shorten the gas gap distance in specific points, facilitating the discharge condition there. Additionally, remaining excited species inside the reactor can also promote the discharge in certain areas. Figure 6.13 reveals that, immediately after the ignition, the discharge prefers to appear in the lower part of the reactor, probably because of imperfections in the reactor setup. As time passes, the discharge location changes, and it seems to be pushed in the gas flow direction. As explained in [8], this may be caused by the excited species that are progressively pushed by the gas flow toward the reactor exit. This evolution is more clearly seen in the low power cases, where the discharge area does not cover the whole electrode surface. Concerning this last characteristic, it is visible how the discharge area increases with the power until it fills the entire reactor.

The discharge location, area, and evolution over time have a critical impact on the gas treatment. When the discharge only covers the bottom part of the reactor, a portion of gas flows through it without touching the plasma region. As a consequence, treatment efficiency is not optimal. As time passes and the discharge is pushed, it tends to distribute radially in the reactor exit. Notwithstanding that the treatment performance should improve, it is not convenient to have a long transient time with bad performances. Furthermore, the discharge does not always appear in the lower part of the reactor. Sometimes, after many consecutive high power experiments or other random conditions that are not fully understood, the discharge locates in a different position, and the entire transient changes.

The pitfalls related to the settling time of the discharge area and location can be solved using high enough power levels to cover the whole electrode surface immediately after the first ignition. However, due to the over-temperature experimental restriction and the objective of minimizing the $DeNOx$ energy consumption, this is not a satisfactory solution for the investigation.

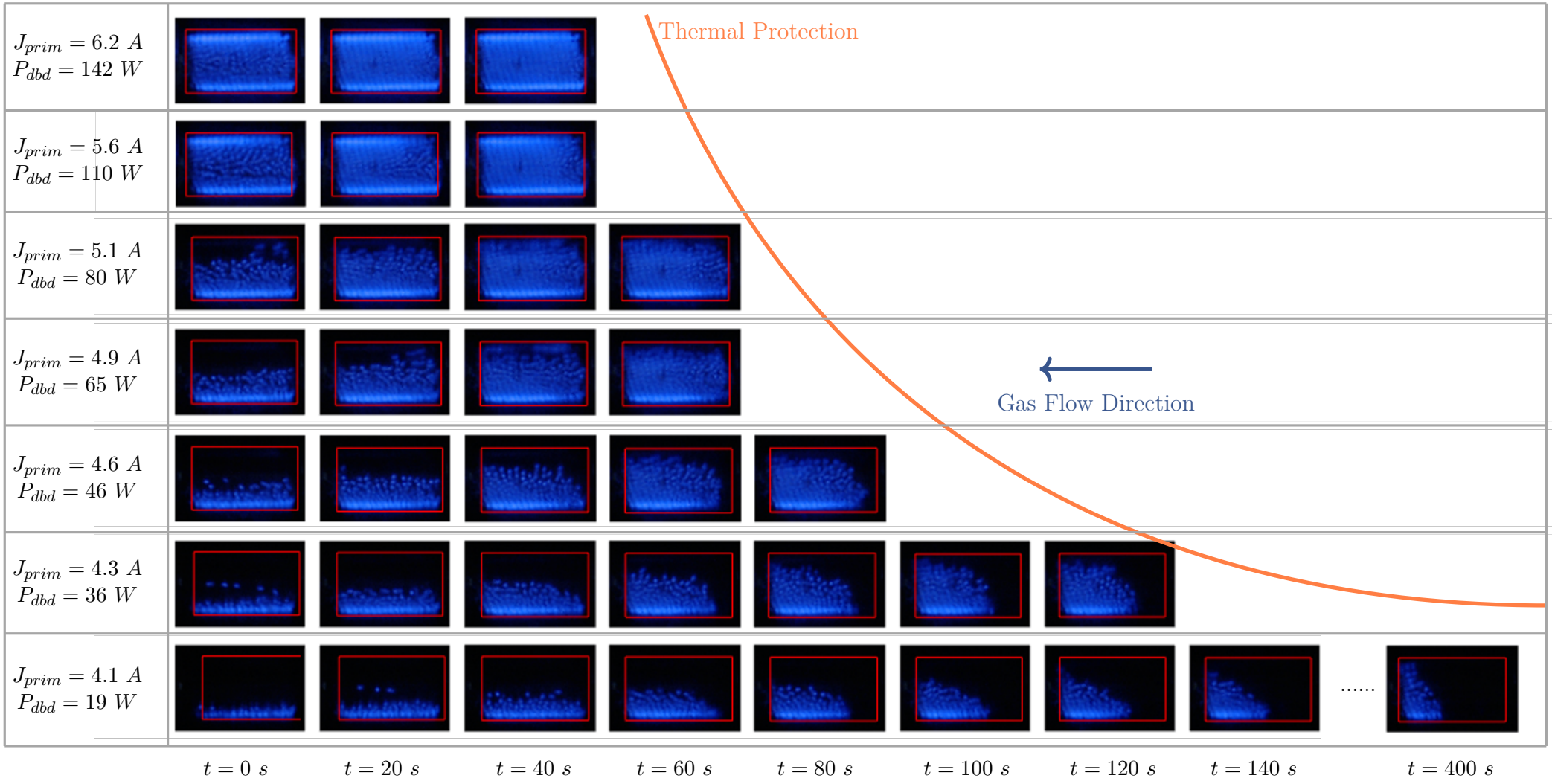

Figure 6.13: Evolution of the discharge during treatment. OPs working at : Continuous mode, $f_s = 80\ kHz$, $T_{pulse} = 1.25\mu s$

6.4 Square Current Source in Burst Mode

In the attempt to improve the stabilization and thermal behavior of the NO_x reactor, an alternative operating supply mode is investigated. The burst mode, also referenced in some publications as amplitude modulation, has been successfully used to enhance different DBD applications, including ozone production [9], and UV excimer lamps [10]. In this mode, the supply waveforms are alternatively turned ON and OFF at a frequency lower than the frequency of the pulses. The implementation of the burst mode was introduced in Chapter 4. Figure 6.14 depicts the experimental DBD waveforms of one OP to recall its operation and parameters.

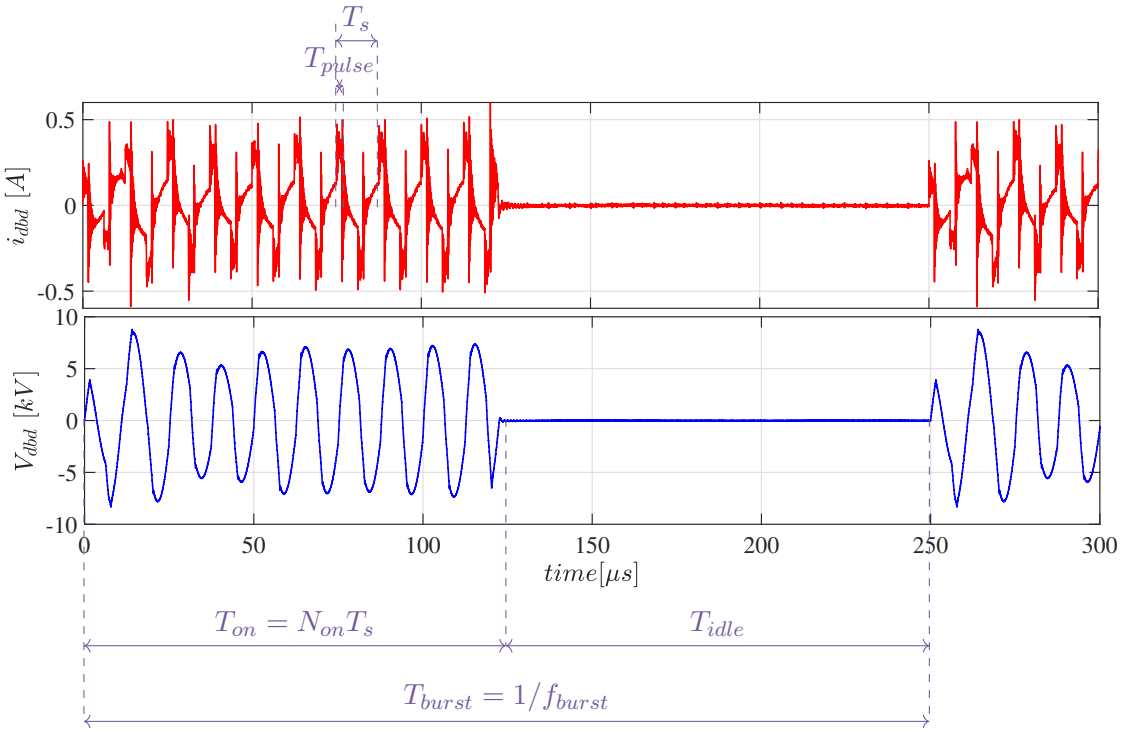

Figure 6.14: Experimental waveforms in burst mode. Example at $f_s = 80\ kHz$, $T_{pulse} = 1.25\ \mu s$ $J_{prim} = 6.1\ A, N_{on} = 10, T_{idle} = 125\ \mu s$

Employing the burst approach, the energy injected into the DBD is controlled by the train of pulses while the DBD average power is modulated at the burst frequency. This implies that the amount of energy injected per pulse can be increased without having an average power limitation. In this way, we expect to inject sufficient energy into the reactor to perform the treatment at a lower average DBD power than with the continuous mode. Hopefully, this will result in an efficient treatment at lower temperatures, allowing us to perform the parametric study of the pulses and burst parameters. Furthermore, some authors have reported that including relaxation times between discharges can contribute to a more uniform distribution of the discharge along the area of the electrodes [10], which is related to the second problem faced by the continuous mode.

Accordingly, both limiting aspects of the continuous mode (temperature rise, and surface of the reactor covered by the discharge) are evaluated and compared with the burst mode. Then, a repeatability analysis of the experiment is presented, and finally, the parametric study on the impact of the electrical parameters and gas composition is thoroughly developed.

It is important to remind the reader that the average power in the burst mode, is calculated by multiplying the instantaneous voltage and current and then averaging over a complete burst period:

$$\langle P_{dbd} \rangle_{burst} = \frac{1}{T_{burst}} \int_0^{T_{burst}} v_{dbd}(t) i_{dbd}(t) dt \tag{6.3}$$

whereas, in the continuous mode (both sinusoidal and square current source), the instantaneous power is averaged over the HF pulses period.

6.4.1 General Comparison with Continuous Mode

Before investigating the impact of the burst parameters, this section aims to exhibit some of the improvements of burst mode compared to the continuous mode. Accordingly, following the same analytic approach, the electrode temperature, gas measurements, and discharge pictures are evaluated. For such analysis, a set of experiments working at $f_s = 80\ kHz$, $T_{pulse} = 1.25\mu s$, with a sweep of J_{prim} to control the DBD power is used (same conditions than the continuous mode analysis); but, the burst parameters are included and fixed at $N_{on} = 10$, and $T_{idle} = 125\mu s$.

The thermal behavior of the reactor is one of the major improvements of the burst operation. Figure 6.15 illustrates the evolution of the temperature of the outer electrode for different power levels in burst mode (continuous traces), and plots as a reference the OP in continuous mode which obtained a stable temperature under $160°C$ (dashed trace). At first sight, it can be seen that all the burst experiments attain a stable temperature below the 160 $°C$ restriction in less than 3.5 minutes. Moreover, comparing the experiment that achieved a stable thermal operation using the continuous mode ($\langle P_{dbd} \rangle_T = 19\ W$, $Temp. \approx 160°C$) with an experiment at a similar power level using the burst mode ($\langle P_{dbd} \rangle_{burst} = 23\ W$, $Temp. = 70°C$), a tremendous diminution of the temperature stands out.

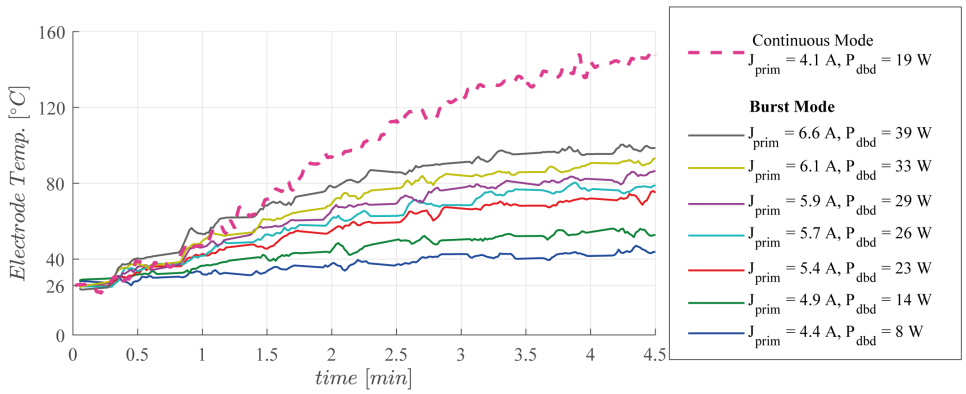

Figure 6.15: Variation of the temperature of the outer electrode during treatment. OPs working at : Burst mode, $f_s = 80\ kHz$, $T_{pulse} = 1.25\mu s$, $N_{on} = 10$, $T_{idle} = 125\mu s$

On the other hand, the reactor's pictures evidence an effect in the spatial distribution of the discharge. Figure 6.16 displays the discharge evolution for some of the burst experiments presented above (first three rows), which can be compared to the stable OP in continuous mode (last row).

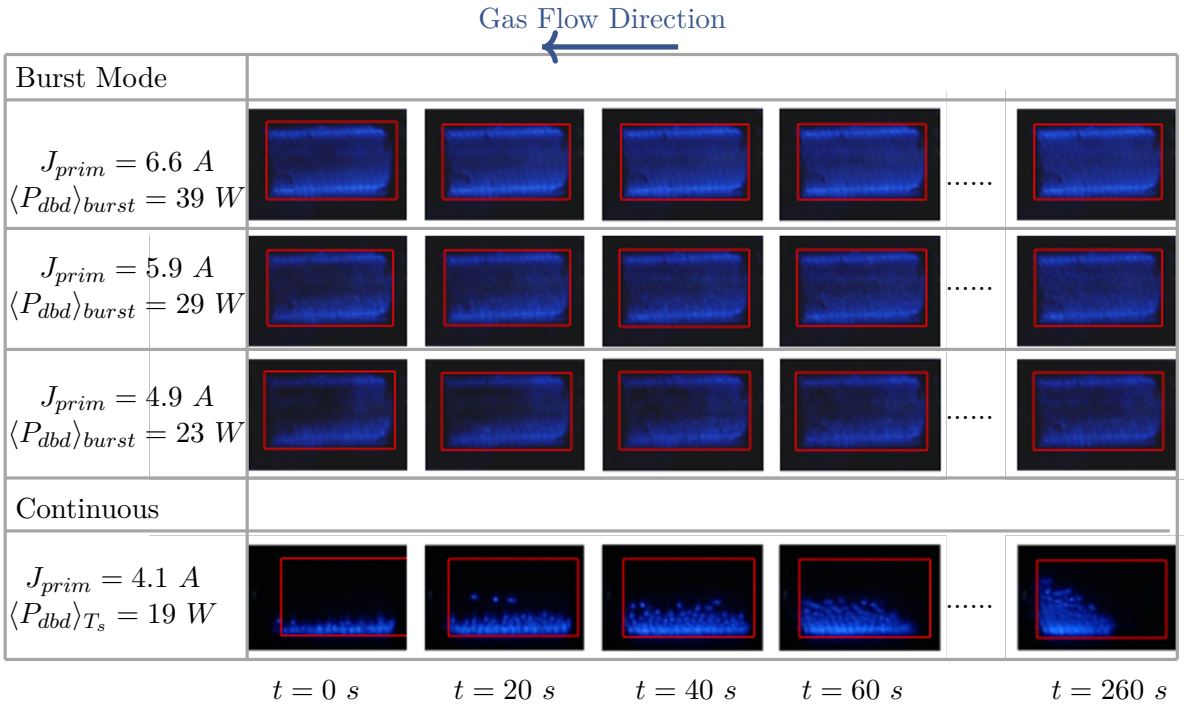

Figure 6.16: Evolution of the discharge during treatment. OPs working at : Burst mode, $f_s = 80\ kHz$, $T_{pulse} = 1.25\mu s$, $N_{on} = 10$, $T_{idle} = 125\mu s$

Based on the discharge pictures, we can note four differences between modes:

- The discharge is more uniformly distributed. Whereas in continuous mode, at $\langle P_{dbd} \rangle_T = 19\ W$, only 23% of the electrodes area is covered by the discharge, in the burst mode, the discharge fully covers the reactor at an equivalent power.
- There are no transversal non-discharging areas at any moment, which means that unlike the continuous mode, the gas always crosses the plasma region.
- The discharge is not "pushed" in the direction of the gas flow with the burst mode.
- The distribution of discharge produces less intense images at equivalent power levels. That might be related to a lower power density and the reduction of the reactor temperature.

The advantageous burst mode conditions are also reflected in the gas analyzer measurements (Figure 6.17). Both of the NO and NO_2 measurements during treatment show a stable concentration value that allows us to proceed with the treatment analysis.

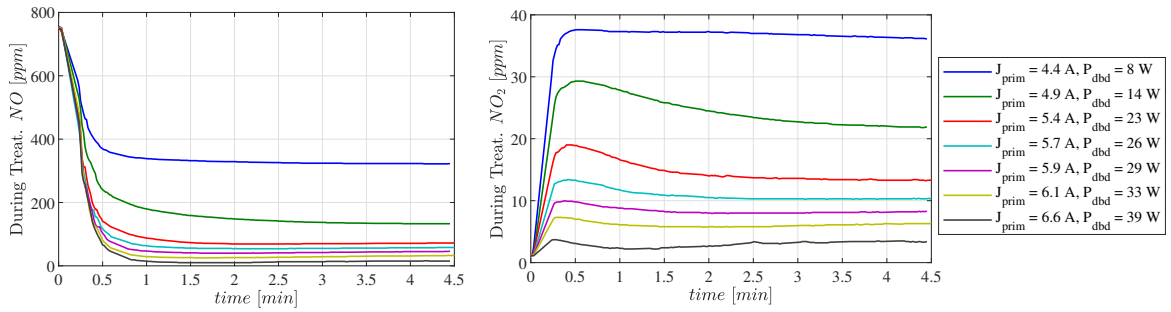

Figure 6.17: Measurements of the gas analyzer during treatment. OPs working at : Burst mode, $f = 80\ kHz$, $d = 0.1$, $N_{on} = 10$, $N_{off} = 10$

6.4.2 Experiments Variability

Ideally, each of the experiments should be repeated several times to draw accurate conclusions and remove random errors inherent in the experimentation. Unfortunately, our proposed experimentation setup has an average execution time per experiment of 18 minutes, including the reactor cool-down. Due to such a long duration, and the large amount of OPs to explore, only some experiments are repeated and used to evaluate the variability of the measurements.

Table 6.2 shows the results of four different OPs repeated at least three times. All the repetitions are randomly executed during various experimentation days. The key parameters resulting from the electrical, chemical, and optical diagnostic are presented to estimate the variability of both the experiment and methods employed in the analysis.

A) $f_s = 80\ kHz$, $J_{prim} = 1.2\ A$, $T_{pulse} = 3.12\mu s$, $N_{on} = 10$, $T_{idle} = 125\mu s$

	Electric Diagnostic			Chemical and Thermal			Optical Diagnostic		
Rep.	J_{prim} [A]	P_{dbd} [W]	$\widehat{V_{dbd}}$ [V]	ηNO_x [%]	Selec. NO_2 [%]	$Temp$ [$^\circ C$]	Area [%]	μ_{gray}	CV
1	1.23	23.5	9088	92.2	1.03	73	98	35.61	0.170
2	1.26	25.4	9186	95.5	0.75	75	100	36.79	0.173
3	1.25	26.6	9112	97.1	0.60	86	93	37.16	0.180
4	1.23	21.6	9075	91.7	1.24	72	94	36.38	0.178
Avg	1.24	24.28	9115.19	94.12	0.90	76.45	96.31	36.49	0.18
Std	0.013	1.906	42.855	2.236	0.248	5.914	2.908	0.578	0.004
	1.06%	7.85%	0.47%	1.29%	27.44% *	7.74%	3.02%	1.58%	2.26%

B) $f_s = 80\ kHz$, $J_{prim} = 1.7\ A$, $T_{pulse} = 3.12\mu s$, $N_{on} = 10$, $T_{idle} = 125\mu s$

	Electric Diagnostic			Chemical and Thermal			Optical Diagnostic		
Rep.	J_{prim} [A]	P_{dbd} [W]	$\widehat{V_{dbd}}$ [V]	ηNO_x [%]	Selec. NO_2 [%]	$Temp$ [$^\circ C$]	Area [%]	μ_{gray}	CV
1	1.68	53.7	10260	100	0.05	134	97	55.17	0.128
2	1.69	54.5	10249	99.6	0.06	131	98	51.98	0.121
3	1.76	59.0	10218	99.2	0.07	140	96	53.92	0.124
Avg	1.71	55.7	10242	99.8	0.06	135	97	53.69	0.124
Std	0.033	2.3	18	0.5	0.01	3.9	1.0	1.31	0.0026
	1.92%	4.2%	0.2%	0.6%	16.9%*	2.9%	1.0%	2.4%	2.1%

C) $f_s = 160\ kHz$, $J_{prim} = 4.2\ A$, $T_{pulse} = 1.56\mu s$, $N_{on} = 10$, $T_{idle} = 62.5\mu s$

	Electric Diagnostic			Chemical and Thermal			Optical Diagnostic		
Rep.	J_{prim} [A]	P_{dbd} [W]	$\widehat{V_{dbd}}$ [V]	ηNO_x [%]	Selec. NO_2 [%]	$Temp$ [$^\circ C$]	Area [%]	μ_{gray}	CV
1	4.26	16.9	6581	83.7	2.28	48	74	35.44	0.202
2	4.25	16.0	6470	80.1	2.76	52	76	32.82	0.190
3	4.33	17.8	6753	87.5	1.66	46	60	36.95	0.214
Avg	4.28	16.9	6601	83.8	2.23	48	70	35.07	0.202
Std	0.035	0.7	117	3.0	0.45	2.4	6.9	1.71	0.010
	0.81%	4.2%	1.8%	3.6%	20.2%*	4.9%	9.9%	4.9%	4.9%

D) $f_s = 160\ kHz$, $J_{prim} = 5\ A$, $T_{pulse} = 1.56\mu s$, $N_{on} = 10$, $T_{idle} = 62.5\mu s$

	Electric Diagnostic			Chemical and Thermal			Optical Diagnostic		
Rep.	J_{prim} [A]	P_{dbd} [W]	$\widehat{V_{dbd}}$ [V]	ηNO_x [%]	Selec. NO_2 [%]	$Temp$ [$^\circ C$]	Area [%]	μ_{gray}	CV
1	4.98	68.1	6976	97.3	0.31	153	98	63.42	0.163
2	4.99	74.0	6926	94.8	0.72	154	97	63.66	0.149
3	4.93	64.5	6942	96.7	0.39	146	98	61.40	0.167
Avg	4.97	68.8	6948	96.3	0.47	151	98	62.83	0.159
Std	0.028	3.9	21	1.1	0.18	3.6	0.4	1.01	0.0077
	0.57%	5.7%	0.3%	1.1%	37.5%*	2.4%	0.4%	1.6%	4.8%

* Variation in agreement with NO_2 sensor uncertainty (± 5ppm)

Table 6.2: Experiments Variability for different conditions

From the electric parameters of the four OPs, good repeatability is observed in the current delivered by the DC current source (J_{prim}), and DBD peak voltage (V_{dbd}) with a variation of less than 2% for both parameters. Similarly, the estimated $\langle P_{dbd} \rangle_{burst}$, calculated as the average of the instantaneous power over a full burst period, obtained a variation below 8%. Concerning the optical diagnostic, a good agreement in the discharge pictures and image processing methods is observed. The mean gray level (μ_{gray}) and coefficient CV obtained a variation under 5%. A higher variation, but still acceptable (below 10%), is obtained by estimating the discharge area.

Finally, the chemical and thermal results show a good agreement in the temperature below 8% and $DeNO_x$ efficiency below 5%. On the contrary, very high variations in the NO_2 Selectivity are seen. Such a variation of up to 38% is caused by the high uncertainty of the gas analyzer measurements of NO_2. According to the sensor specifications, for NO_2 measurements under 100 ppm, an uncertainty of $\pm 5 ppm$ is stipulated. This absolute uncertainty is more critical at low NO_2 concentrations, as observed in these experiments. Given that the rest of experiments are only executed once, and the gas analysis showed a relevant variation, the theoretical uncertainty of the $DeNO_x$ efficiency and NO_2 selectivity will be plotted as error bars of each OP. The rest of the electrical and optical quantities have proven to have a good degree of agreement.

6.5 Parametric Study of the System parameters

Three main studies are carried out in order to understand the DeNOx treatment performances of the proposed experimentation setup: study on the burst parameters (T_{idle}, N_{on}), study on the HF pulses (f_s, T_{pulse}, J_{prim}), and study on the gas conditions (G, NO, O_2). For each study, the electrical, optical, and chemical diagnostics are completely evaluated. Nevertheless, only the results showing significant effects in each study are discussed in this chapter; the rest of the results can be consulted in Appendix A.

At first, the effect of the burst parameters are investigated (T_{idle}, N_{on}). For this initial study, the gas composition, frequency, and duration of the HF pulses are kept constant. The current intensity of the HF pulses is configured at three different values; for each level, T_{idle} is swept to control the DBD average power $\langle P_{dbd} \rangle_{burst}$, and to analyze its effect on the treatment. Afterward, the process is repeated using N_{on} to control the DBD power. From the results of the T_{idle}, and N_{on} effects, the optimum values of these parameters are obtained and used to continue with the subsequent two parametric studies.

In the second study, the effects of the HF pulses are analyzed; particularly, the duration of the current pulses, T_{pulse}, is investigated. Some authors have reported that short current pulses of high intensity can contribute to DBD applications such as excimer lamps [11, 12]. Hence, there is a particular motivation for studying the effect of the HF pulse duration. To do so, the gas and burst conditions are kept constant at the optimum values of T_{idle}, and N_{on} previously found; moreover, the frequency of the pulses f_s is fixed, and several pulses duration are tested. For these experiments, the current amplitude is used to control the DBD power at each T_{pulse}. The procedure is repeated at two switching frequencies to validate the findings.

Some conclusions about the impact of HF parameters on the treatment are presented, and a set of HF pulses conditions is selected.

Finally, the last study aims to analyze the treatment capabilities when the gas conditions change. The parameters selected by the two previous studies are fixed, and the current intensity J_{prim} is used to control the DBD power. The impact on the treatment of the gas flow rate G, and the NO, and O_2 concentrations are addressed.

6.5.1 Study on the impact of the Burst Mode Parameter

Theoretically, the DBD average power in a burst period can be expressed as the total energy injected by the burst pulses, ξ_{burst}, divided by the burst period, where $T_{burst} = T_{idle} + N_{on}T_{pulse}$.

$$\langle P_{dbd} \rangle_{burst} = \frac{1}{T_{idle} + N_{on}T_{pulse}} \sum_{n=1}^{N_{on}} \xi_n \tag{6.4}$$

$$\xi_{burst} = \sum_{n=1}^{N_{on}} \xi_n \tag{6.5}$$

Accordingly, the DBD power can be controlled either by the energy injected by the HF pulses, ξ_n, or by the burst parameters (N_{on} and T_{idle}). This experimental study intends to analyze the effect of T_{idle} and N_{on} when the gas conditions and the frequency and pulse duration of the HF pulses are maintained constant. The gas conditions are $NO = 800\ ppm$, $O_2 = 0\ \%$, $G = 3\ lpm$, and the frequency and duration of the HF pulses are fixed at $f_s = 160\ kHz$, $T_{pulse} = 1.56\mu s$. The current amplitude, J_{prim}, is adjusted at three levels to be able to analyze the effect of the burst parameters considering different amounts of energy injected by the HF pulses. The experimental results of each parameter is presented as follows.

6.5.1.1 Effect of zero-voltage idle time, T_{idle}

When the conditions of the HF current pulses remain constant, no matter the duration of the zero voltage time, T_{idle}, the total amount of energy delivered to the discharge in a burst period, ξ_{burst}, is the same; however, because of power modulation at the burst frequency, the average DBD power, $\langle P_{dbd} \rangle_{burst}$, decreases with T_{idle} (Equation 6.4). To be able to compare the behavior of the treatment at different zero-voltage times duration, T_{idle}, but with equivalent power levels, the energy delivered by the train of ten pulses is adjusted by means of J_{prim}. Accordingly, three levels of J_{prim} are used $[4.6,\ 5.0,\ 5.4]\ A$. For each value of J_{prim}, the DBD power is controlled in the range of $10 - 70\ W$ through a T_{idle} sweep. Two of the electric waveforms at similar power are shown in Figure 6.18.

Electric Diagnostic In this set of experiments, the power is gradually decreased by means of the raised zero voltage T_{idle} time. Figure 6.19-a shows the DBD power as a function of T_{idle}.

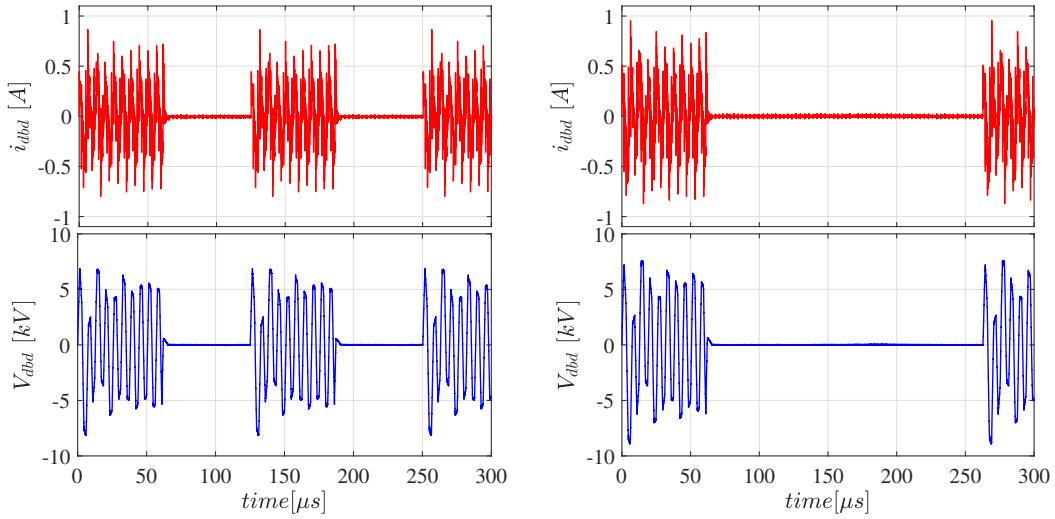

a) $J_{prim} = 4.6\ A, T_{idle} = 62.5\ \mu s, P_{dbd} = 34.1\ W$ b) $J_{prim} = 5.4\ A, T_{idle} = 200\ \mu s, P_{dbd} = 33.4\ W$

Figure 6.18: DBD waveforms at similar power working at $f_s = 160\ kHz$, $T_{pulse} = 1.56\mu s$, $N_{on} = 10$

In the right axis, the corresponding Energy Density is calculated based on the total gas flow rate ($G = 3\ lpm$). The graph shows that T_{idle} effectively controls the power. As expected, the experiments at high currents ($J_{prim} = 5.4\ A$) require longer idle times to obtain the same power than the lower current experiments. In order to remind the reader this relation, a notation of ($J_{prim} = 5.4\ A$, $T_{idle} \uparrow$), and ($J_{prim} = 4.6\ A, T_{idle} \downarrow$) is included. $J_{prim} = 5\ A$ is used as an intermediate reference.

Given that in these experiments the current level is the only condition varied between traces, all the experiments at a given current should deliver the same energy, ξ_{burst}, and produce the same peak voltage. Figure 6.19-b presents the obtained DBD peak-to-peak voltage. A variation of less than 2% was obtained in the voltage for each current sweep, consistent with the variability study.

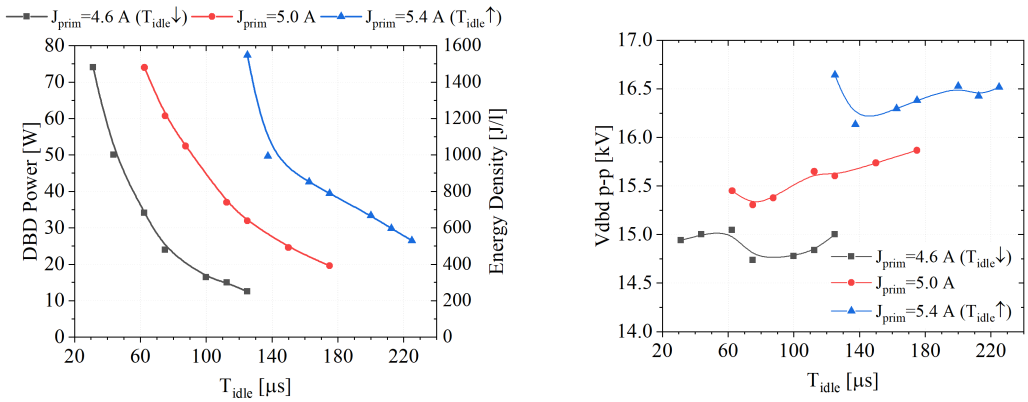

(a) DBD power controlled by T_{idle} (b) DBD peak-peak voltage

Figure 6.19: Effect of T_{idle} in electric quantities

The second step in the electric diagnostic concerns the characterization of the DBD electrical model. Figure 6.20 shows the effective measurements of electrical model considering partial discharging areas (C_{dEff}, C_{gEff}, and V_{thEff}). These values are obtained using the Q-V plot of the first discharge in the train of pulses. As can be seen, the OPs working at ($J_{prim} = 4.6\ A, T_{idle} \downarrow$), have a greater variations in the identified capacitances; C_{dEff} increases with the power, and C_{gEff} decreases. This phenomenon provides a clue about a possible discharge covering only a portion of the electrodes area, which is confirmed below with the optical diagnostic. Less variation in the capacitances is observed at high currents ($T_{idle} \uparrow$). Furthermore, C_d seems to increase with the current level. More ambiguous results are observed in the identification of the breakdown voltage.

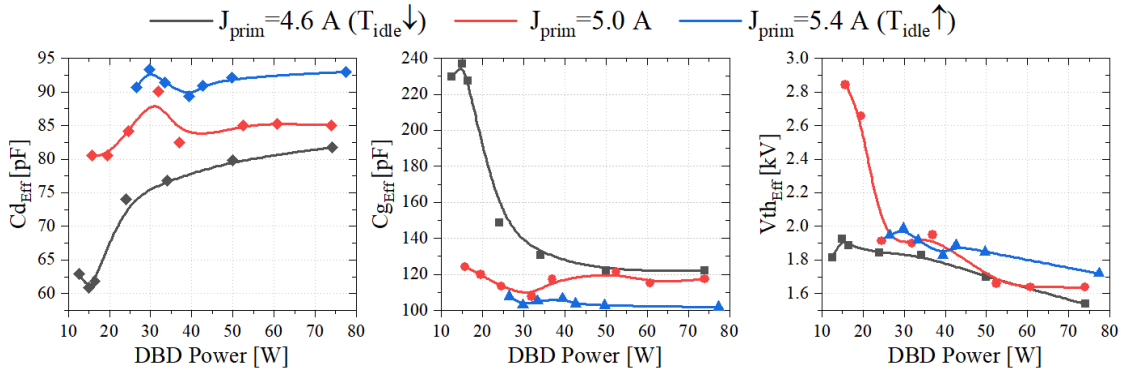

(a) C_{dEff} (b) C_{gEff} (c) V_{thEff}

Figure 6.20: Effect of T_{idle} in DBD characterization results

Optical Diagnostic The discharge pictures in the steady-state of all the experiments are processed using the proposed algorithm. The resulting discharge area, mean gray level, and coefficient of variation are presented in Figure 6.21. The first remark of the optical diagnostic is in agreement with the findings of the DBD model characterization; for $J_{prim} = 4.6\ A$

($T_{idle}\downarrow$), the discharge covers only a portion of the area of the electrodes. This yields to the variation of the identified capacitances.

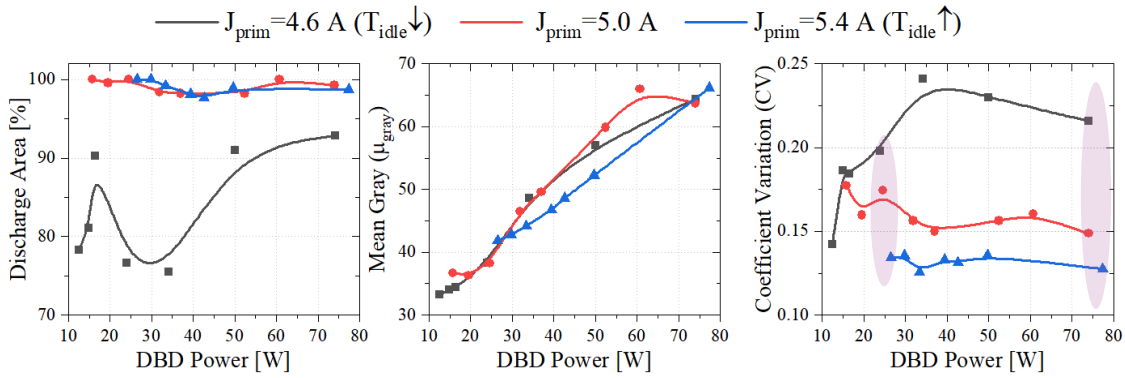

a) Discharge Area b) μ_{gray} c) CV

Figure 6.21: Effect of T_{idle} in discharge appearance

On the other hand, for $J_{prim} = 5.4\ A$ and $J_{prim} = 5.0\ A$, the segmentation of the discharge leads to full coverage of the electrodes in the same power range. Nonetheless, there are some differences in the electric model characterization for these two sets of experiments (Figure 6.20), implying different discharge areas. As the micro-discharges can not be individually distinguished in the images due to the exposure time limitations of the camera, there is an expected error in the area estimation. Therefore, the uniformity of the discharge is evaluated to complement the analysis.

As can be seen in Figure 6.21-c, the results of the CV parameter also exhibit a relevant impact of T_{idle} in the discharge uniformity. The higher the zero-voltage idle time, $J_{prim} = 5.4\ A$ ($T_{idle}\uparrow$), the lower the coefficient; thus, the more uniform is the discharge. This can explain the variation in the electric model characterization between $J_{prim} = 5.4\ A$ and $J_{prim} = 5.0\ A$, since a more uniform discharge indicates a better distribution of micro-discharges, thus a larger discharge area. To evidence the changes in the discharge appearance, Figure 6.22 provides the discharge images of the OPs circled in Figure 6.21 (equivalents to $\langle P_{dbd}\rangle_{burst} \approx 25\ W$, and $\langle P_{dbd}\rangle_{burst} \approx 75\ W$)

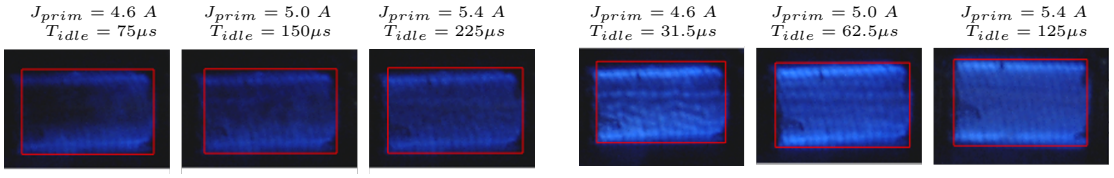

(a) $\langle P_{dbd}\rangle_{burst} \approx 25\ W$ (b) $\langle P_{dbd}\rangle_{burst} \approx 75\ W$

Figure 6.22: Effect of T_{idle} in discharge appearance

As was encountered in the experimentation with continuous high-frequency pulses, the micro-discharges tend to re-ignite at the same locations, probably because of remaining excited species in the gas and the memory charges accumulated by preceding discharges [10, 13].

The zero voltage idle time between groups of pulses allows the recombination of those excited species and decreases the in-homogeneous accumulation of charges on the dielectrics, contributing to a better spatial distribution of the discharge as has been observed in this experimental study.

Chemical Results Concerning the treatment performances, in Figure 6.23 the removal efficiency and NO_2 selectivity is evaluated. From these results, it is observed that the removal efficiency increases until it levels off around $\eta NO_x = 97 \pm 5\%$. The highest amount of NO_2 is produced at low power levels, and declines with the power. The shadowed area around the data represents the theoretical uncertainty of the gas analyzer measurements. Due to the similarity in the treatment results, and considering the uncertainty of the three set of experiments is intersected, it is complicated to conclude about the effects of T_{idle} in DeNOx efficiency, within the considered experimentation range. Furthermore, no significant effect of T_{idle} in the temperature is observed (Figure 6.24).

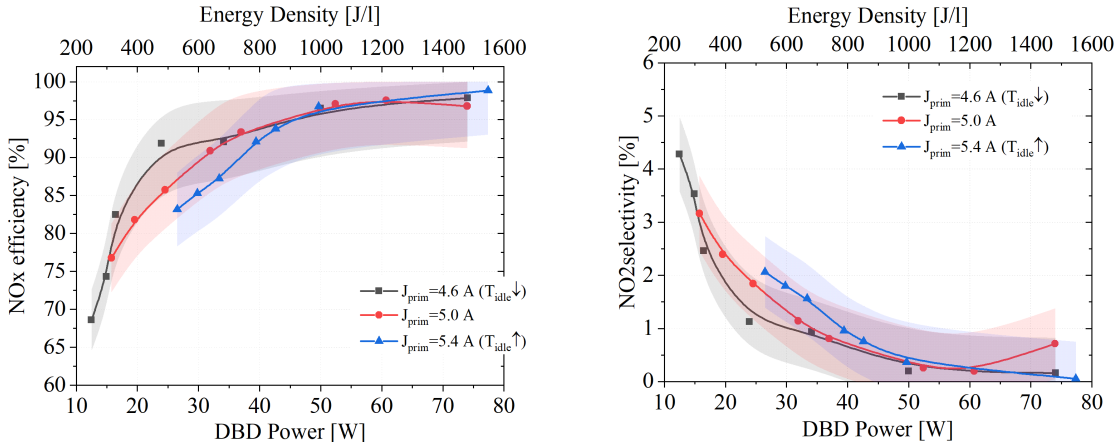

(a) $DeNO_x$ Efficiency (b) NO_2 Selectivity

Figure 6.23: Effect of T_{idle} Treatment performances

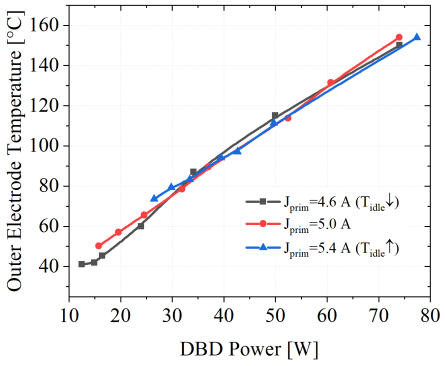

Figure 6.24: Effect of T_{idle} in outer electrode temperature

Conclusion In order to have a better visualization on the effect of T_{idle} in the treatment, the experiments within the study working at similar power levels ($\langle P_{dbd}\rangle_{burst} \approx 25, 33, 50$, and $75\ W$ are grouped in Figure 6.25-a. Here, the $DeNO_x$ efficiency is plotted against T_{idle} for each power level. As observed in Figure 6.23, the higher the power, the higher the removal efficiency. If the power is high enough, the idle time does not impact the efficiency, since it is already close to the maximum. However, at low power levels there is a moderate drop in the efficiency with the increase of T_{idle}. For example, at $\langle P_{dbd}\rangle_{burst} \approx 25\ W$, the efficiency drops from $92 \pm 5\%$ to $83 \pm 5\%$, with a change in T_{idle} from 75 to 225 μs.

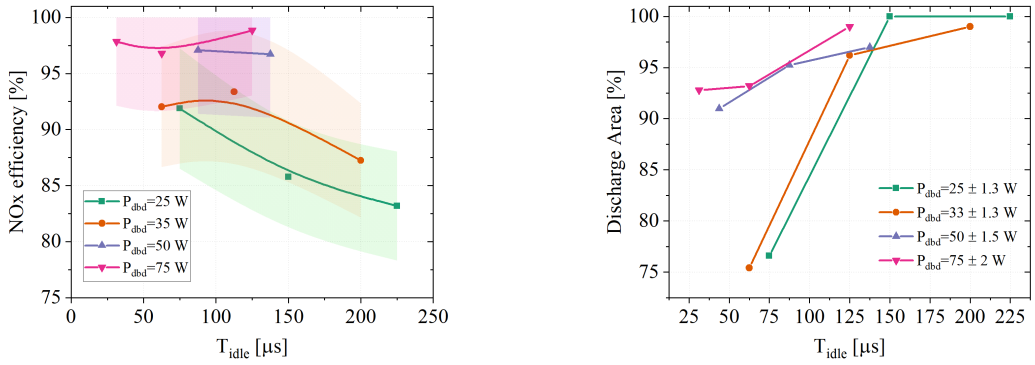

(a) T_{idle} vs the NO_x efficiency (b) T_{idle} vs the discharge area

Figure 6.25: Summary of the treatment performances for T_{idle} study

If only the treatment efficiency is considered to select the optimum T_{idle}, one may decide to use short idle times to prevent the detected efficiency drop. However, another important factor to consider is the discharge distribution over the electrode area. The optical diagnostic evidence that T_{idle} promotes the uniform distribution of the discharge in the area of the electrode, an important feature to ensure a reproducible performance and increase the region of contact between the plasma and the gas. Figure 6.25-b summarizes the effect of T_{idle} in the discharge area for the previous OPs grouped by the power level. For all the power levels, the discharge area increases with T_{idle}. To select the ideal idle time, a compromise between discharge area and efficiency is required. Accordingly, T_{idle} is selected at 125 μs, since at this value, the discharge area of all the OPs is higher than 95% (even at low power levels), and the efficiency drop is not significant.

6.5.1.2 Effect of number of pulses, N_{on}

The second step studying the degrees of freedom offered by the burst mode seeks to determine the effect of the number of current pulses delivered to the DBD, N_{on}. To do so, the parameters of the high frequency pulses are maintained constant at $f_s = 160\ kHz$, $T_{pulse} = 1.56\ \mu s$, while N_{on} is gradually increased. Additionally, the total burst period is fixed at $T_{burst} = 125\ \mu s$. In this way, the burst power increases with N_{on}, at a constant burst frequency $f_{burst} = 8\ kHz$. One should notice that T_{idle} varies with N_{on} as $T_{idle} =$

$T_{burst} - N_{on}T_s$.

Similar to the previous experimental study, three levels of $J_{prim} = [4.5,\ 4.7,\ 4.9]\ A$ are employed. For each current level, the power is controlled by N_{on}. Figure 6.26 displays two of the OPs of the experimental study that obtained a similar power when injecting a different number of current pulses (N_{on}).

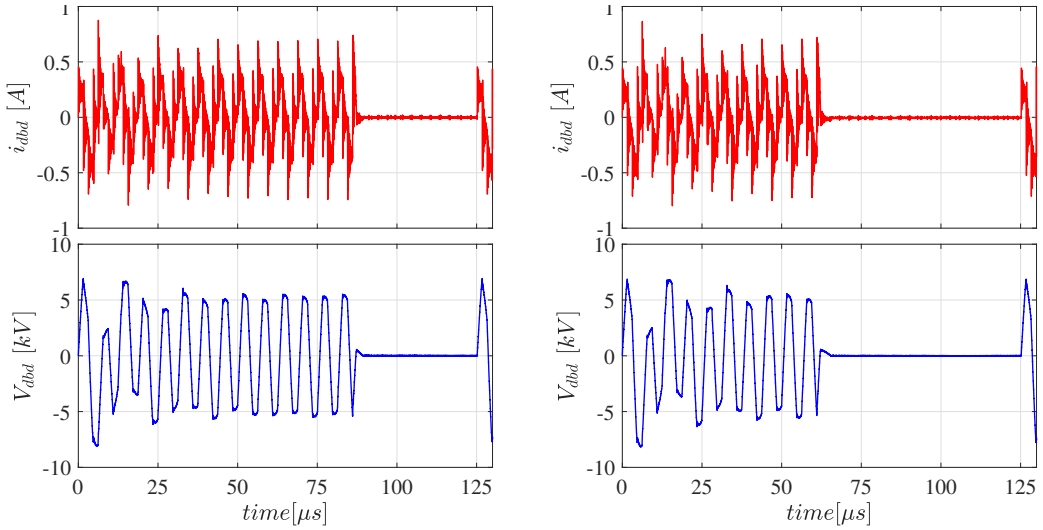

a) $J_{prim} = 4.5\ A, N_{on} = 14, \langle P_{dbd}\rangle_{burst} = 46.5\ W$ b) $J_{prim} = 4.9\ A, N_{on} = 10, \langle P_{dbd}\rangle_{burst} = 45\ W$

Figure 6.26: DBD waveforms at similar power working at $f_s = 160\ kHz$, $T_{pulse} = 1.56\mu s$, $f_{burst} = 8\ kHz$

Minimum number of N_{on} pulses Due to the transient response of the system operated in burst mode, the amplitude of the initial DBD current and voltage pulses are not constant, especially at the beginning of the burst. Such response mostly depends on the initial conditions of the current in the transformer magnetizing inductance. As was explained in Subchapter 4.6, at the beginning of the train of pulses, the initial condition of the magnetizing inductance current is equal to the inductance current at the end of the last current pulse (before the zero-voltage idle time). Therefore, given that this experimental study intends to vary the number of pulses injected to the DBD, it is of special interest to guarantee that a steady-state is achieved before the last current pulse. Otherwise, the transient response will change from experiment to experiment and corrupt the analysis of the experimental results.

To clearly describe the limitation of the N_{on} experimental study caused by such transient response, Figure 6.27 presents the simulation results of the power supply with ideal switching devices and using the transformer and DBD electrical models (PSIM). For the simulations, all power supply parameters are fixed, and different values of N_{on} are simulated. Two characteristics stand out from the simulations. First, when the train of pulses is interrupted before the steady-state, the transient pulses change. This can be seen in the zoomed region of Figure 6.27; for $N_{on} = 2$ and $N_{on} = 6$, the waveforms of the first pulses are clearly different when compared with the cases where $N_{on} \geq 10$. Second, the switching transition between

the last pulse and the zero voltage idle time also changes (differences highlighted by arrows of Figure 6.27). For $N_{on} = 2$ and $N_{on} = 6$, the transition to the zero-voltage is longer, seen as a positive half-sinus; whereas at $N_{on} \geq 10$ the transition is faster. Both characteristics are undesirable for this experimental study since the objective is to isolate effects of N_{on}, and maintain the burst conditions. Accordingly, based on the experimental and simulation results, the minimum number of pulses injected to the DBD is selected at $N_{on} = 10$.

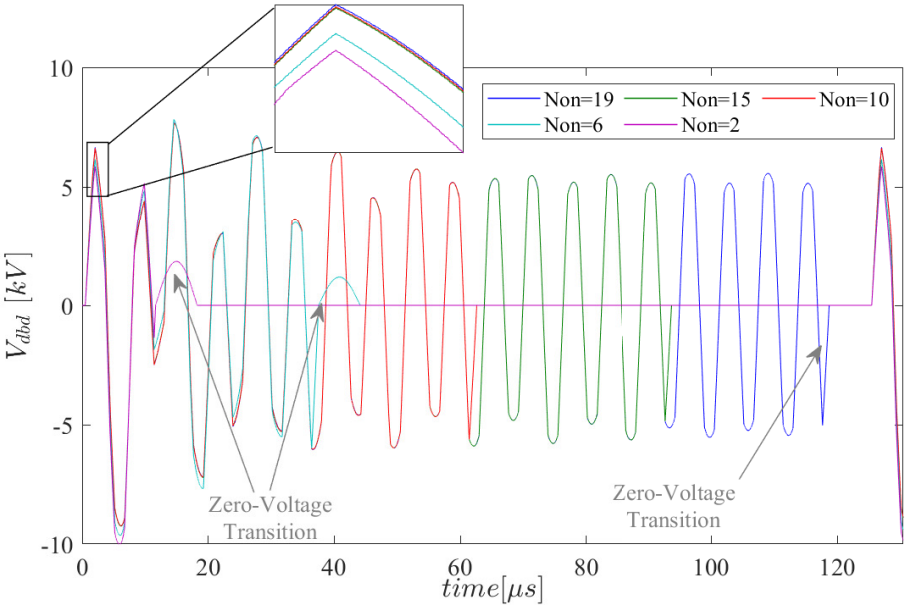

Figure 6.27: Simulations to describe the effect of N_{on} in the transient response working at $f_s = 160\ kHz$, $T_{pulse} = 1.56\mu s$, $J_{prim} = 4.5\ A$, $f_{burst} = 8\ kHz$

Electric Diagnostic: With this minimum value of N_{on}, Figure 6.28 presents the experimental DBD power as a function of the number of pulses for three current levels. The upper horizontal axis shows T_{idle} calculated as $T_{burst} - N_{on}T_s$. From the graphic, a consistent increment of the power with N_{on} is observed; moreover, it can be seen that the experiments at the lowest current $J_{prim} = 4.5\ A$ require the injection of more current pulses to attain the same power than the OPs at higher currents. Accordingly, a notation $J_{prim} = 4.5\ A\ (N_{on} \uparrow)$, and $J_{prim} = 4.9\ A, (N_{on} \downarrow)$ is employed.

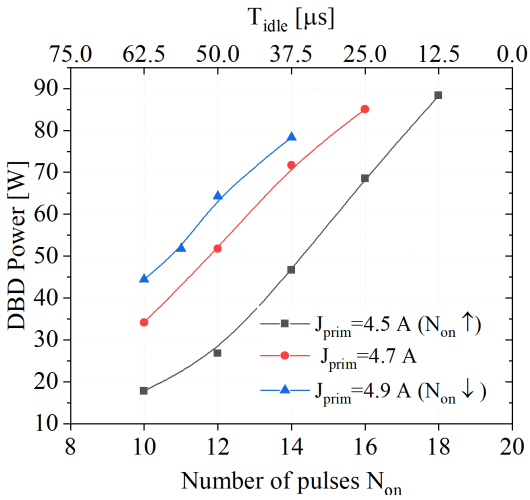

Figure 6.28: Effect of N_{on} in DBD power

Considering that this experimental study evaluates the impact of controlling the power by means of N_{on}, while the burst frequency is kept constant, a non-negligible effect is the diminution of the zero voltage idle time as N_{on} increases, approaching the burst operation to the continuous mode. Therefore, some of the T_{idle} effects described in the previous study can also take place in these experiments. For instance, in the characterization of the DBD electrical model (Figure 6.29), a wider variation of the identified capacitances is observed for the OPs working at $J_{prim} = 4.5\ A$ (N_{on} ↑). As the notation indicates, these are the OPs with higher number of pulses N_{on}, thus, shorter idle time. In the previous section, it was proved that the discharge has an inferior distribution and uniformity at short T_{idle}, producing a variation in the identification of the DBD capacitances and image processing results. Although N_{on} cannot be ruled out from the impact in the parameters identification, these outcomes are in agreement with the T_{idle} trends and ratify its effects.

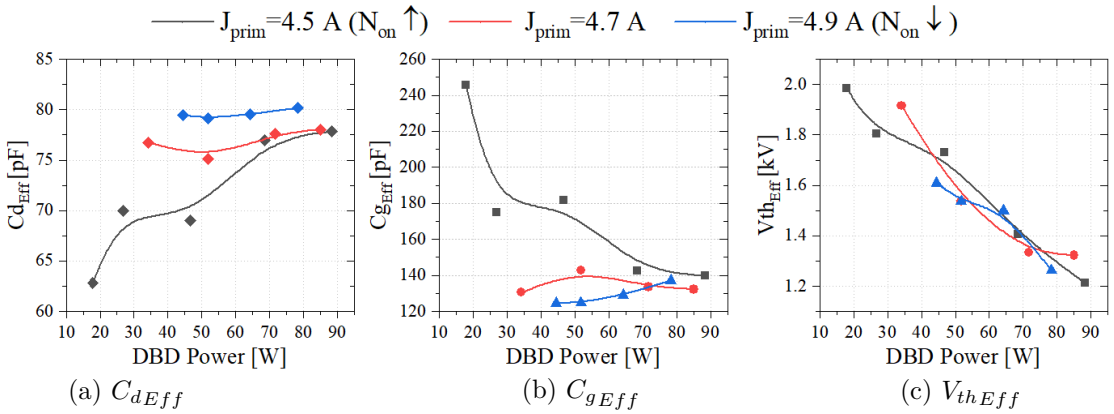

(a) C_{dEff} (b) C_{gEff} (c) V_{thEff}

Figure 6.29: Effect of N_{on} in DBD characterization results

Optical Diagnostic Based on the image processing results, it is observed that for a fixed burst frequency, the OPs injecting a large number of pulses (N_{on} ↑) produce a discharge that covers less area than the OPs at similar power but with fewer current pulses. This can be seen in Figure 6.30-a, where the OPs working at $J_{prim} = 4.5\ A$ (N_{on} ↑) have lower percentages of the discharge area in comparison to the OPs working at $J_{prim} = 4.9\ A$ (N_{on} ↓) where the discharge area is close to 100%. Again, the phenomenon can be associated with the reduction of the zero voltage idle time as N_{on} increases. The results of the discharge brightness and uniformity show a less explicit impact of N_{on}.

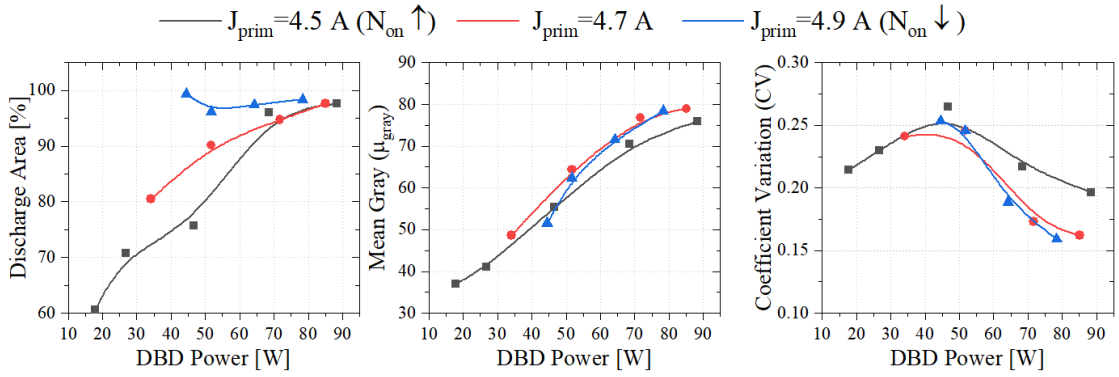

a) Discharge Area b) μ_{gray} c) CV

Figure 6.30: Effect of N_{on} in discharge appearance

Chemical Results As mentioned, the increment of the number of pulses injected to the DBD while f_{burst} is kept constant implies an operation approaching the continuous mode, bringing back some of the limitations encountered by such operating mode. Figure 6.31 provides the temperature of the outer electrode for all the OPs. As can be seen, some of the high power experiments attain a temperature higher than $160°C$; thus, the experiments are interrupted before getting reliable gas measurements. Figure 6.32 exhibits the treatment results of the experiments that obtained a stable temperature under $160°C$. As the power range of the remaining valid experiments is not the same for the three sweeps, it is difficult to compare the results properly. Nonetheless, it is observed that in the power range of $40-60\ W$, the highest removal efficiency is $\eta NO_x = 94.5 \pm 5\%$, and the lowest NO_2 selectivity is 6%. Additionally, if we focus on the OPs working at $J_{prim} = 4.9\ A$, it can be seen that the increments in the power by means of N_{on} does not have a major effect improving the removal efficiency nor reducing the amount of generated NO_2.

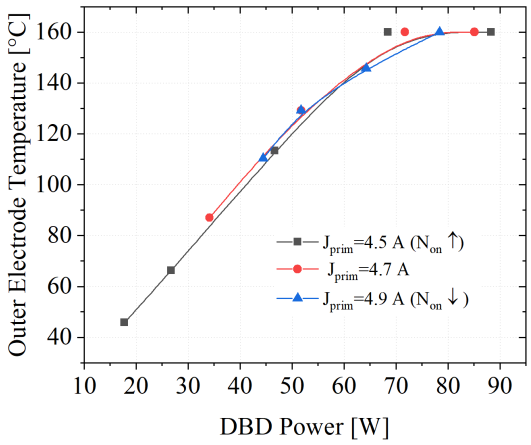

Figure 6.31: Effect of N_{on} in the reactor temperature

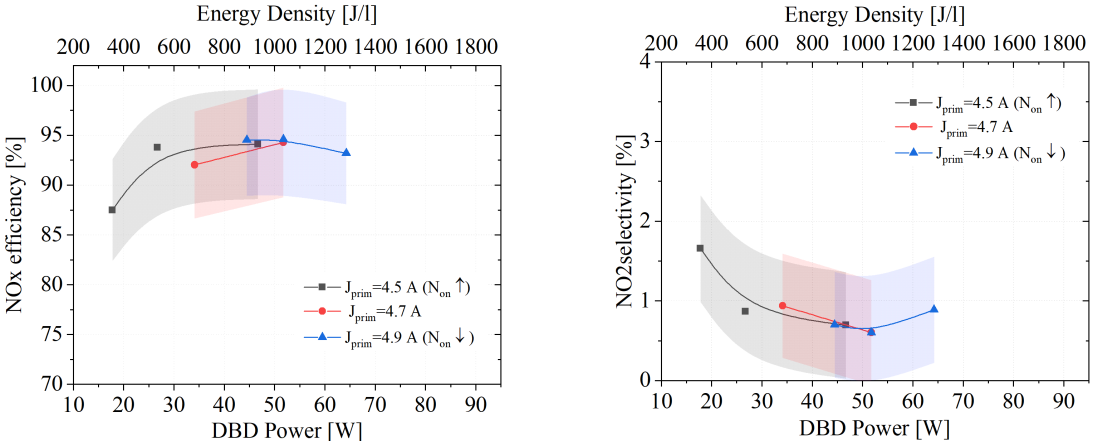

(a) $DeNO_x$ Efficiency (b) NO_2 Selectivity

Figure 6.32: Treatment performances at $f_{burst} = 8kHz$

Comparison at different Burst Frequency To further analyze the effect of N_{on}, and to conclude whether the injection pulses contribute or not to the treatment performances, a second stage studying the impact of N_{on} is proposed. The objective of this stage is to compare the results previously presented (OPs working at $f_{burst} = 8\ kHz$) with a new set of OPs at a lower burst frequency. Accordingly, the HF parameters are fixed at $f_s = 160\ kHz$, $T_{pulse} = 1.56\ \mu s$, and $J_prim = 4.9\ A$, and the two burst frequencies are selected at $f_{burst} = 8\ kHz$ and $f_{burst} = 4\ kHz$, equivalent to $T_{burst} = 125\ \mu s$ and $T_{burst} = 250\ \mu s$ respectively.

As the DBD average power is inversely proportional to the burst frequency, f_{burst} (Equation 6.6) and the parameter of the HF pulses are fixed in this experimental study; the DBD average power is directly controlled by N_{on}. This implies that more energy, hence more pulses, must be injected at low frequencies to obtain a given power. Figure 6.33 shows the waveforms

of two OPs with similar power, where the relation stands out.

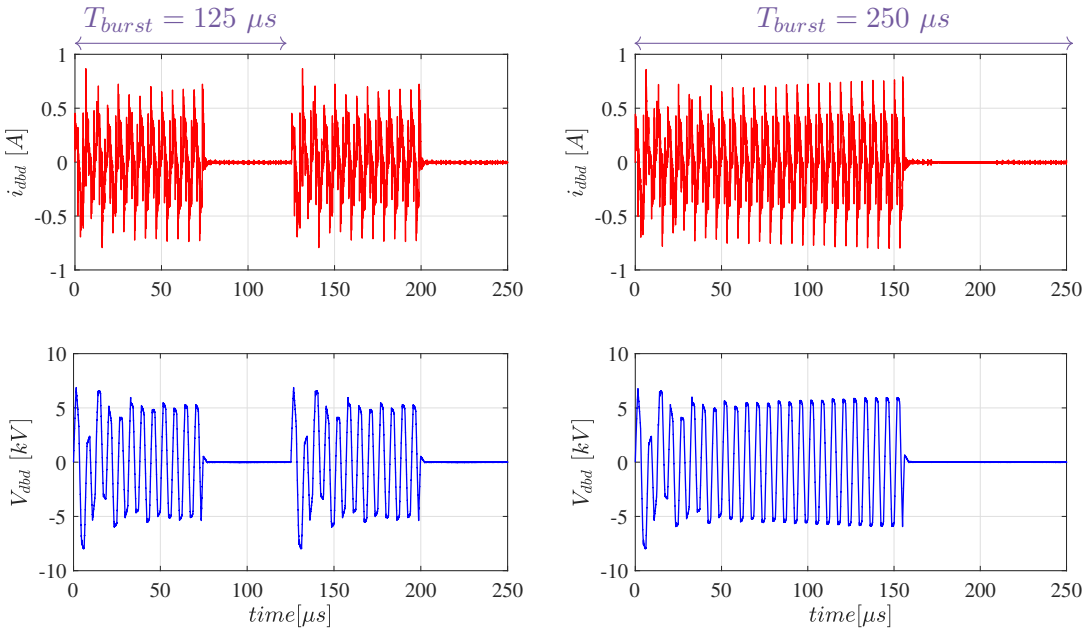

a) $f_{burst} = 8\ kHz, N_{on} = 11, \langle P_{dbd}\rangle_{burst} = 51.5\ W$ b) $f_{burst} = 4\ kHz, N_{on} = 28, \langle P_{dbd}\rangle_{burst} = 49.5\ W$

Figure 6.33: DBD waveforms at similar power working at $f_s = 160\ kHz$, $T_{pulse} = 1.56\mu s$, $J_{prim} = 4.9\ A$

$$\langle P_{dbd}\rangle_{burst} = f_{burst} \sum_{n=1}^{N_{on}} \xi_n \tag{6.6}$$

In Figure 6.34-a, the DBD power versus the number of pulses for the OPs sweep at both burst frequencies is presented. Note that the maximum number of pulses that can be injected at $f_{burst} = 8\ kHz$ is $N_{on} = 19$, whereas at $f_{burst} = 4\ kHz$ is $N_{on} = 39$. As observed, N_on controls the DBD power at both burst frequencies. Furthermore, Figure 6.34-b shows the temperature of the DBD outer electrode for the experiments; remarkably, the OPs at $f_{burst} = 4\ kHz$ obtained a significantly lower temperature with respect to those working at $f_{burst} = 8\ kHz$.

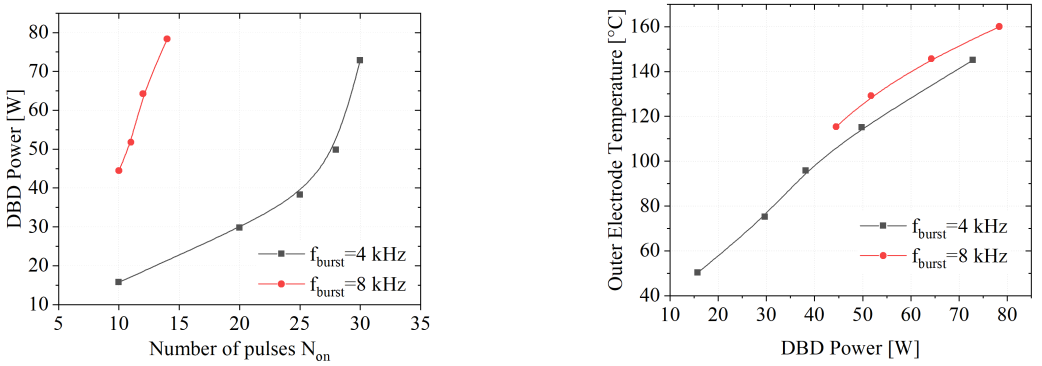

(a) DBD power (b) Outer electrode temperature

Figure 6.34: Effect of N_{on} in the power and temperature at a constant burst frequency

At first sight, a diminution of the temperature of almost $10°C$ might seem favorable for the application; but, a closer inspection in the treatment performances indicates that it is not the case in this experimental study. Figure 6.35 compares $DeNO_x$ performances revealing surprising results:

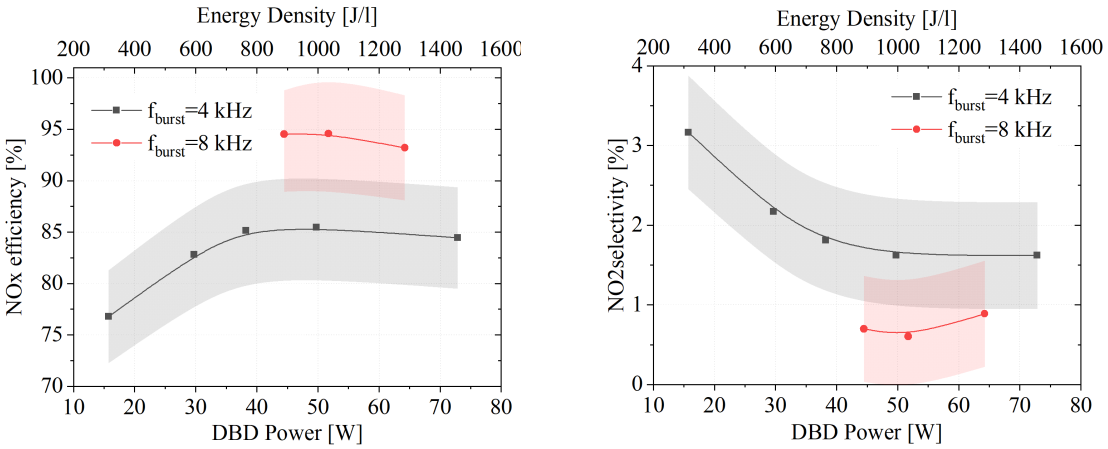

(a) $DeNO_x$ Efficiency (b) NO_2 Selectivity

Figure 6.35: Effect of N_{on} in the treatment performances at a constant burst frequency

- It is observed that the OPs working at $f_{burst} = 4\ kHz$ (injecting more current pulses) exhibit a lower removal efficiency and produce more NO_2 than the OPs at $f_{burst} = 8\ kHz$.
- The removal efficiency curve at $f_{burst} = 4\ kHz$ rapidly saturates at $\eta NO_x = 85 \pm 5\%$, suggesting that controlling the power through N_{on} at low burst frequencies is not adequate for the treatment.

- Even the experiments working at $f_{burst} = 8\ kHz$ seems to have a limited efficiency ($\eta NO_x = 94.5 \pm 5\%$), which is slightly lower than the capabilities evidenced in the experimental study of T_{idle}, where by controlling the power through T_{idle}, the efficiency $\eta NO_x > 97 \pm 5\%$ after 50 W is obtained.

Given that these findings are obtained under a particular burst operation characterized by strong transients, the results should be treated with considerable caution. Thus, it is necessary to contemplate the possible consequences of the transient response. As the initial pulses may provide a higher DBD voltage and inject more energy than those in steady-state, the latter may generate weaker discharges causing no significant contribution to the NO_x reduction. Figure 6.36-b shows the accumulative energy deposited into the discharge per pulse in the five experiments working at ($f_{burst} = 4\ kHz$), and details in Figure 6.36-a the energy injected by each current pulse in one of the experiments ($\langle P_{dbd} \rangle_{burst} = 50\ W$). As can be observed, the energy of the first HF period ($\xi_1 = 1.84\ mJ$) is higher than those in steady-state ($\xi_{28} = 0.27\ mJ$); almost seven times higher. Such a difference provides a possible explanation of the poor treatment results when the power is controlled by means of N_{on}. Furthermore, the results also point out the importance of improving the power supply to reduce the transient and deliver pulses of the same magnitudes. Although it is not part of this thesis, those improvements are proposed as future work to be able to eliminate the transient effects and effectively analyze the impact of N_{on}.

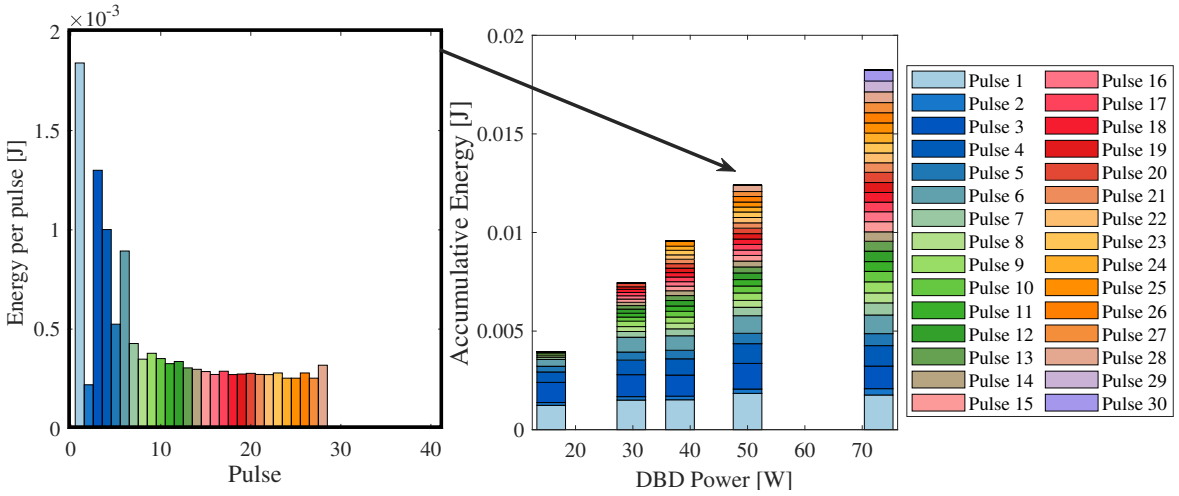

a) Energy per pulse of OP at $N_{on} = 28, \langle P_{dbd} \rangle_{burst} = 49.5\ W$

b) Accumulative energy of all OPs at $f_{burst} = 4\ kHz$

Figure 6.36: Energy analysis of OPs at $f_s = 160\ kHz$, $T_{pulse} = 1.56\mu s$, $J_{prim} = 4.9\ A$, $f_{burst} = 4\ kHz$

Conclusion Summarizing the results of the burst parameters:

Due to the limited $DeNO_x$ efficiency exhibited by controlling the DBD power by means of N_{on}, and due to the experimental limitations of the power supply to inject the same energy into the discharge per current pulse, the best condition for our particular experimentation setup is to fix the number of pulses N_{on} at ten. This value is equivalent to the minimum number of pulses which guarantees the steady-state before the zero voltage time.

Moreover, based on the T_{idle} findings, to obtain uniform discharges fully spread on the area of the electrodes, the idle time, T_{idle}, is required. However, as it may compromise the treatment efficiency, based on the experimentation results, $T_{idle} = 125\mu s$, is selected.

6.5.2 Study on the impact of the HF pulses Parameters

The three degrees of freedom of the HF pulses: switching frequency, f_s, pulse duration, T_{pulse}, and current amplitude, J_{prim}, can be employed to control the energy delivered in the burst period, thus the DBD average power, $\langle P_{dbd} \rangle_{burst}$. In order to evaluate the impact of the HF parameters in the $DeNO_x$ treatment, the gas conditions are maintained at $NO = 800\ ppm$, $O_2 = 0\ \%$, $G = 3\ lpm$, and the burst parameters are fixed at the previously selected values, $N_{on} = 10$ and $T_{idle} = 125\ \mu s$.

For this study, two values of the pulses frequency, ($f_s = 80\ kHz$ and $f_s = 160\ kHz$), and three pulses duration for each frequency are tested. At $f_s = 80\ kHz$, the pulses duration under study are $T_{pulse} = [625\ ns,\ 3.13\mu s\ 6.25\mu s]$, equivalent to a HF duty cycle of $d = [0.1,\ 0.5,\ 1]$. Additionally, at $f_s = 160\ kHz$, the same pulses duration are examined, equivalent to duty cycles of $d = [0.2,\ 0.5,\ 1]$. The current amplitude, J_{prim}, is used to vary the power in a range of $\langle P_{dbd} \rangle_{burst} = 10 - 60\ W$ for each set of frequency and pulse duration.

In Figures 6.38 and 6.37, the DBD waveforms of some of the OPs working close to $\langle P_{dbd} \rangle_{burst} \approx 30\ W$ are presented.

As expected, the transient response of the pulses changes with the HF conditions. Particularly, in Figure 6.37 it can be observed that in the OPs at $f_s = 80\ kHz$, the voltage amplitude of the first pulse is the lowest among the ten pulses, whereas, in Figure 6.38 at $f_s = 160\ kHz$, the second pulse has the lowest amplitude. This means that there are crucial differences in the energy distribution of the experiments.

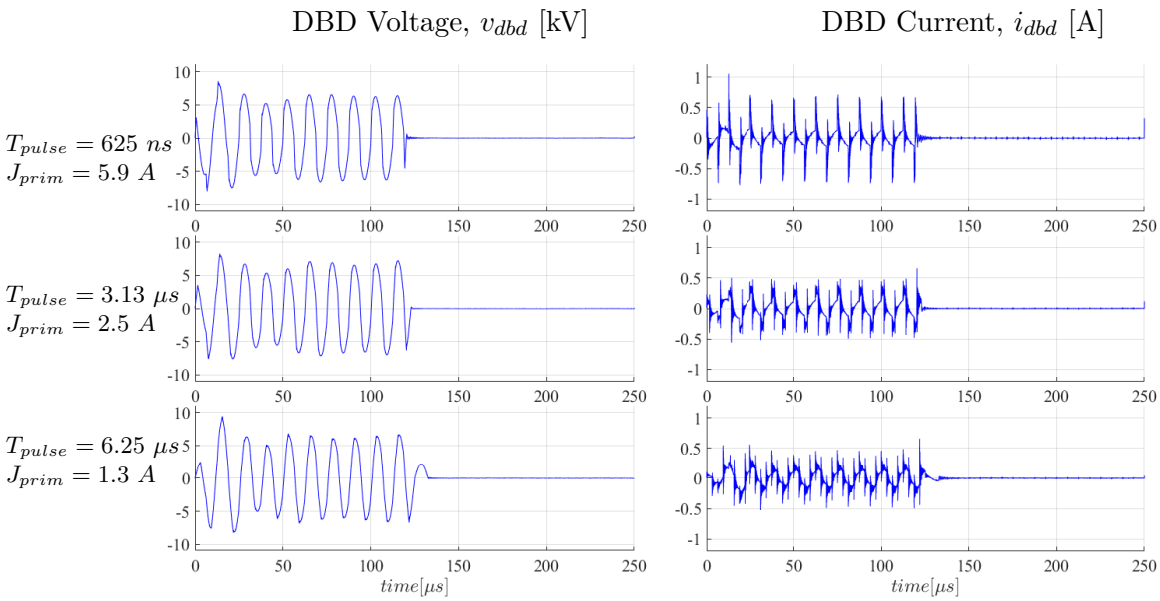

Figure 6.37: DBD waveforms of OPs at $\langle P_{dbd} \rangle_{burst} \approx 30\ W$, $f_s = 80\ kHz$

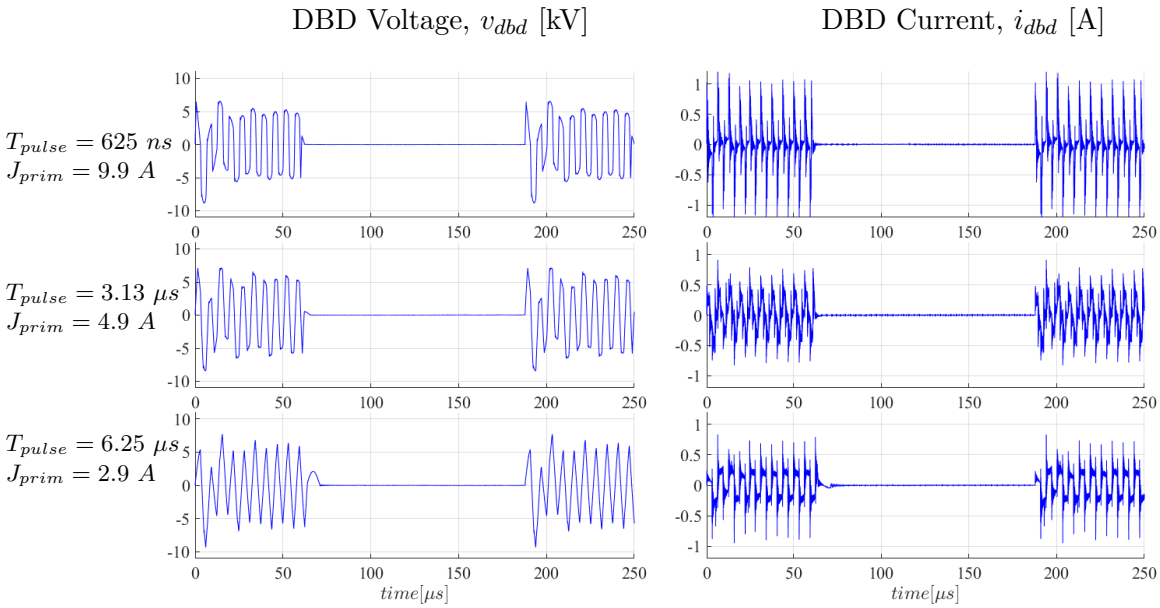

Figure 6.38: DBD waveforms of OPs at $\langle P_{dbd} \rangle_{burst} \approx 30\ W$, $f_s = 160\ kHz$

To further analyze the experiment's energy distribution, Figure 6.39 shows the ratio of the energy of each pulse to the total burst energy for the experiments operating close to $\langle P_{dbd} \rangle_{burst} \approx 30\ W$. Here, a substantial impact of the HF pulses on the transient response, hence, on the energy distribution, is evidenced. The major differences in the energy distri-

bution are noted by comparing the energy of the initial four pulses at different switching frequencies (Figure 6.39-a versus Figure 6.39-b). Much softer differences in the energy distribution are observed when comparing the results at a fixed frequency but different pulse duration, T_{pulse} . For instance, at $f_s = 160kHz$, the energy distribution of the OPs is almost the same despite the changes in the pulse duration.

We are aware that the evaluation of the parameters(f_s, T_{pulse}, J_{prim}) implies as a side effect changes in transient response. Nevertheless, the impact of pulse duration T_{pulse}, is evaluated below since the literature suggest that this parameter can enhance some DBD applications [14–16].

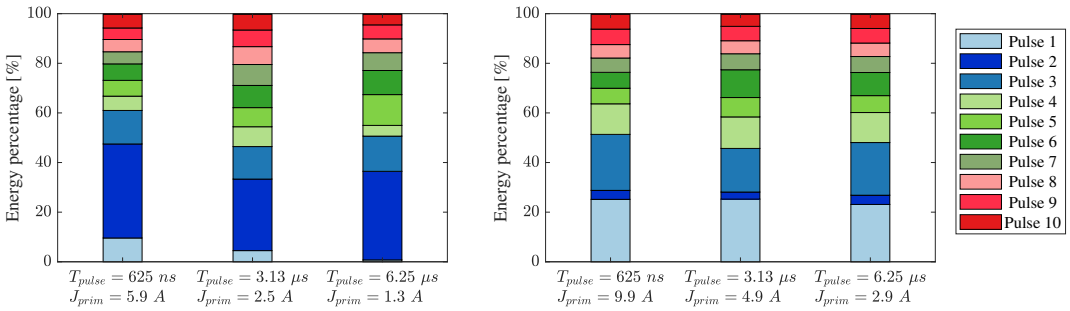

(a) OPs at $f_s = 80\ kHz$ (b) OPs at $f_s = 160\ kHz$

Figure 6.39: Ratio of energy for each pulse to the total energy at different HF pulses conditions

6.5.2.1 Effect of the pulse duration, T_{pulse}

The evaluation of the duration of the HF pulses is performed using the set of experiments working at $f_{sw} = 80\ kHz$. For each pulse duration, T_{pulse}, a sweep of the current amplitude is used to control the DBD power in the range of $\langle P_{dbd} \rangle_{burst} = 10 - 60\ W$. Figure 6.40 shows how the power is effectively controlled at the four different pulses duration by means of J_{prim}. The OPs with shorter pulses require higher current, than those with longer pulses. With this set of experiments, a wide range of the current source capabilities is explored.

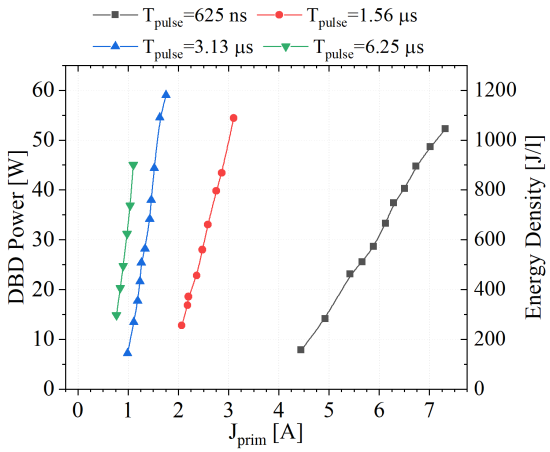

Figure 6.40: DBD power controlled by HF pulses at $f_s = 80\ kHz$

Electric and Optical Diagnostic In general, the electrical and optical diagnostic of the T_{pulse} experimental study show no remarkable effects on the discharge appearance of DBD modeling. As can be seen in Figure 6.41 and Figure 6.42 all the analyzed quantities behave similarly no matter the duration of the pulse duration.

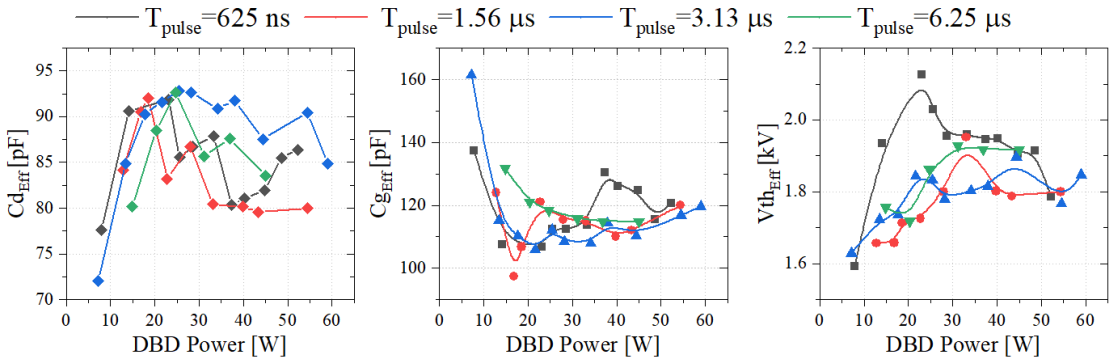

(a) C_{dEff} (b) C_{gEff} (c) V_{thEff}

Figure 6.41: Effect of T_{pulse} in DBD characterization results at $f_s = 80\ kHz$

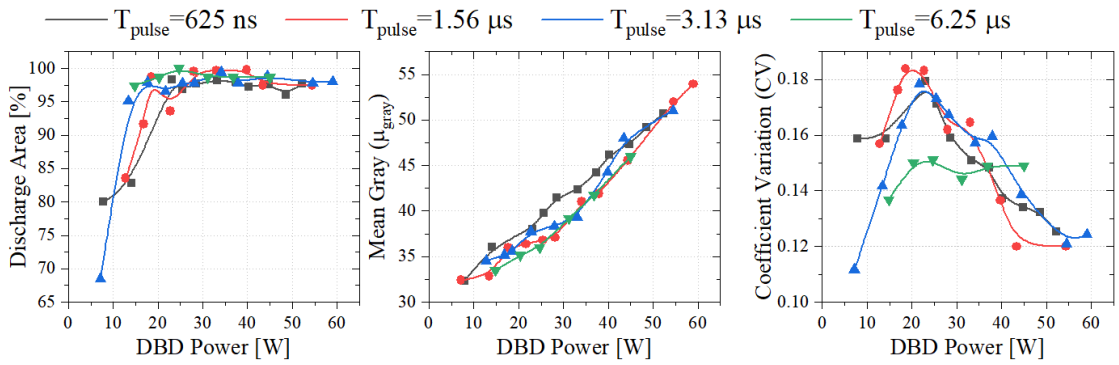

a) Discharge Area b) μ_{gray} c) CV

Figure 6.42: Effect of T_{pulse} in discharge appearance at $f_s = 80\ kHz$

Chemical Results Align with the optical and electrical results, no effects in the treatment performances are detected concerning T_{pulse}. Figure 6.43 displays the treatment results; as can be seen, the removal efficiency and NO_2 selectivity are very close in all the T_{pulse} curves. Furthermore, as the uncertainty of the measurements, represented by the shadowed area, overlap between curves, it is impossible to conclude about possible effects of the pulse duration. The same conclusion was obtained by analyzing the OPs working at $f_s = 160\ kHz$ (Appendix A)

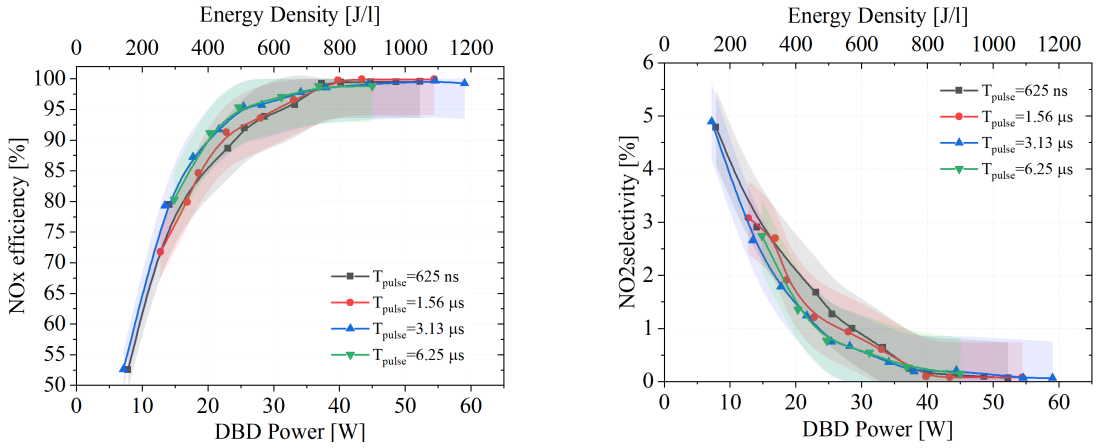

(a) $DeNO_x$ Efficiency (b) NO_2 Selectivity

Figure 6.43: Treatment performances for study of T_pulse at $f_s = 80\ kHz$

Conclusion Contrary to what was previously thought about possible treatment improvements by employing current pulses of short duration and high amplitude, no significant effects in the treatment nor in any of the discharge characteristics is observed. In fact, as similar results are obtained at $f_s = 80\ kHz$, and, $f_s = 160\ kHz$, it is concluded that the dominant effect of the HF pulses conditions in the treatment is related to the change in the DBD average

power, but not directly by the parameters.

Accordingly, to complete the study of the system parameters, the HF pulses parameters are selected at $f_s = 80\ kHz$, and $T_{pulse} = 3.13\mu s$, equivalent to $d = 0.5$. For these values, with $T_{idle} = 125\mu s$ and $N_{on} = 10$, at J_{prim} around 1.42 A, the removal NOx efficiency crosses, $97 \pm 5\%$ at $\langle P_{dbd} \rangle_{burst} = 34\ W$ (Figure 6.43).

These HF values are defined to operate the power supply in a secure range since both the switching losses and the conduction losses are reduced due to the low switching frequency and low J_{prim} operation.

6.5.3 Study on the impact of the gas composition

The diesel exhaust is mainly composed of N_2 and O_2. Although both components influence the $DeNO_x$ reactions, the initial experiments were carried out using a simple N_2/NO gas mixture, with a fixed gas flow rate at 3 lpm and a NO concentration of 800 ppm. This section evaluates the treatment capabilities when the gas flow rate, G, and NO concentration increase. Besides, the O_2 is gradually introduced in the mixture to observe its effects. For this study, we will only focus on chemical diagnostic.

Furthermore, in this study the electric conditions selected in the previous studies are employed ($f = 80\ kHz$, $T_{pulse} = 3.125\ \mu s$, $N_{on} = 10$, and $T_{idle} = 125\mu s$). Four levels of $J_{prim} = [1.2, 1.45, 1.7, 1.9]\ A$, are used to control the DBD power in the range of $\langle P_{dbd} \rangle_{burst} = 22 - 70\ W$.

6.5.3.1 Effect of the total gas flow, G

The performance of the $DeNO_X$ treatment has proven to be related to the energy applied per liter of gas (Energy Density, ED) and the time the gas spends inside the discharge (residence time, τ_{res}). Both parameters are functions of the total gas flow, G; thus, it is expected to obtain substantial variations in the $DeNO_X$ performance when G changes. For this study, three gas flow rates are compared $G = 3, 5, 8\ lpm$, corresponding to the following gas residence times $\tau_{res} = 2.37, 1.42, = 0.89\ ms$ respectively.

When the gas flow rate increases, less energy is applied per liter of gas, and the gas molecules spend less time in contact with the plasma, which reduces the probability of interaction between the pollutants and the plasma radicals [17]. Therefore, both of the treatment indicators, $DeNOx$ efficiency, and NO_2 selectivity, are impacted by the gas flow rate as shown in Figure 6.44. Although the power supply restrictions do not allow us to obtained the same ED range for the three gas flow rates, lower efficiencies are obtained at high flow rates. This is more clearly seen in Figure 6.45-a, where some OPs that obtained similar EDs are compared. In these OPs, even if the same energy density is applied, the treatment efficiency varies, most likely because of the differences in the residence time (τ_{res}). Furthermore, it is observed that the outer electrode temperature reduces with G, which implies that the heat is being removed faster (Figure 6.45-b).

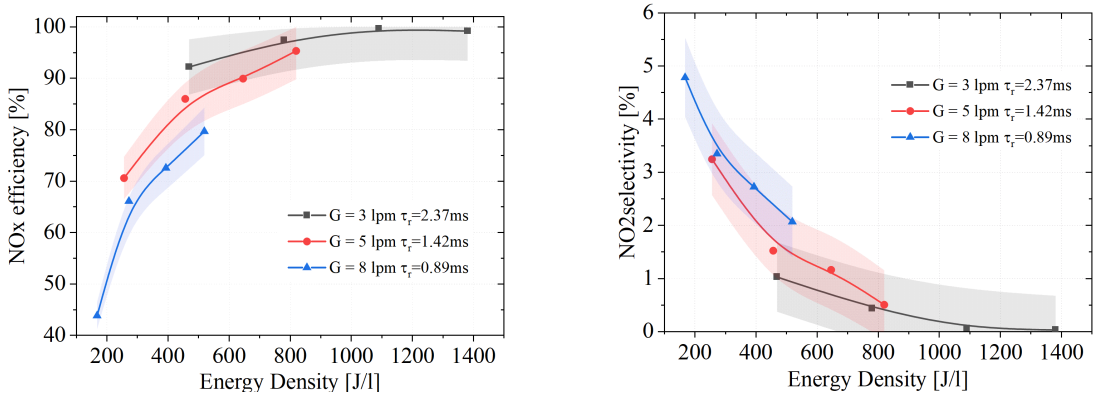

(a) $DeNO_x$ Efficiency (b) NO_2 Selectivity

Figure 6.44: Effect of gas flow rate in the treatment performances

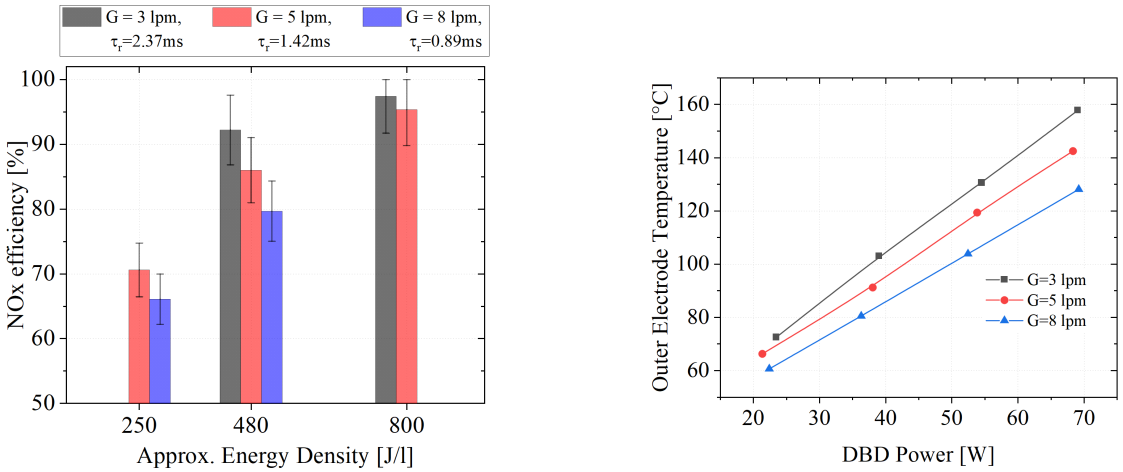

(a) Effect of G and τ_{res} in the NO_x efficiency (b) Effect of G in outer electrode temperature

Figure 6.45: Effect of gas flow rate in the treatment and temperature

6.5.3.2 Effect of the NO concentration

The typical NO concentration in diesel engines is 800 ppm. All the experiments previously presented use such value to simulate the exhaust gas. However, in this experimental study, the initial NO concentration is increased to $NO = 2000$ ppm and $NO = 3000$ ppm to evaluate its impact on the treatment. Similar to the previous study, the DBD power is controlled by four levels of J_{prim}, keeping the rest of electric and gas conditions constant.

Figure 6.46 illustrates how the removal efficiency decreases with the increase of the NO concentration, and how more NO_2 is produced at high NO concentrations. For each NO

concentration, it is observed that the $DeNO_x$ efficiency increases with the power. At $NO = 800\ ppm$, removal efficiencies above 93 % are obtained at a $\langle P_{dbd} \rangle_{burst}$ equals to 25.5 W (equivalent to $ED = 510\ J/l$). A similar removal efficiency is achieved at $NO = 2000\ ppm$, with a significant higher power $\langle P_{dbd} \rangle_{burst} = 58.7\ W$ ($ED = 1174\ J/l$).

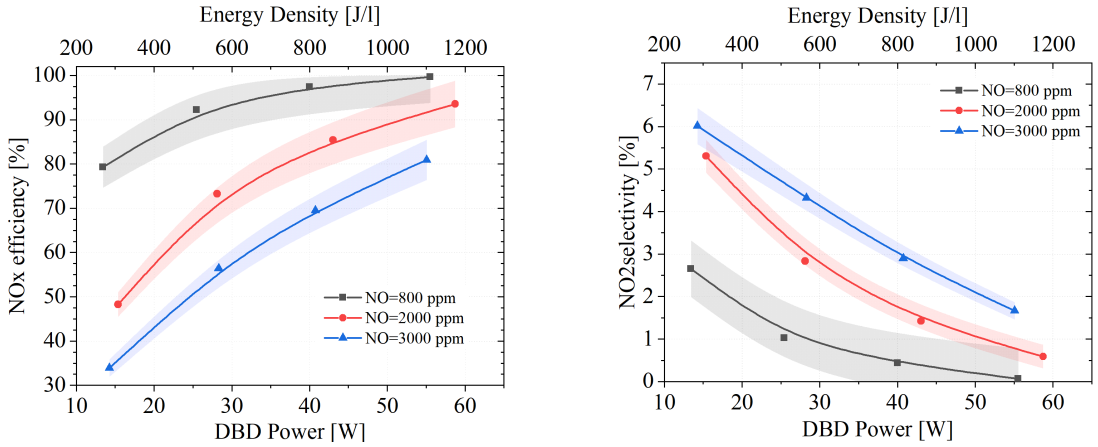

(a) $DeNO_x$ Efficiency (b) NO_2 Selectivity

Figure 6.46: Effect of the initial NO in the treatment performances

6.5.3.3 Effect of the initial O_2 concentration

Without the presence of O_2, the NO removal is mostly caused by denitrification pathways [18, 19]. As explained in Section 2.4, when the O_2 is included in the mixture, the oxidation of the NO, into NO_2, or further N_xO_y oxidation states, obstructs the full NO removal. In order to analyze such effects, the experimental study of the O_2 concentration includes three levels of oxygen, $O_2 = 0,\ 1,\ 5$ %, and a sweep of the current J_{prim} to control the average power. In this section, besides the proposed diagnostic methods, the optical spectroscopy of the radiated light is analyzed for each oxygen level.

The most important effect of the O_2 is the significant diminution of the treatment efficiency once it is included in the gas stream. Figure 6.47 present the treatment performances. It can be seen that the NO_x removal efficiency decreases with the initial O_2 concentration, whereas the production of NO_2 is promoted. The efficiency variation can also be seen in Figure 6.47-c, where the $DeNO_x$ efficiency is plotted against the oxygen level at three different DBD power levels.

For, at $\langle P_{dbd} \rangle_{burst} \approx 40\ W$, the efficiency of the treatment without O_2 is higher than 95%. However, when the O_2 concentration increases to 5%, the removal efficiency decreases to less than 40%. Different studies have been conducted about the impact of oxygen in the treatment. In such studies, it has been concluded that the oxygen reactive species slow and constrain the NO removal process [20, 21]. Indeed, as the interactions of O_2 and N_2 could produce NO and NO_2, if the O_2 is raised beyond a critical concentration, the removal efficiency can get

negative.

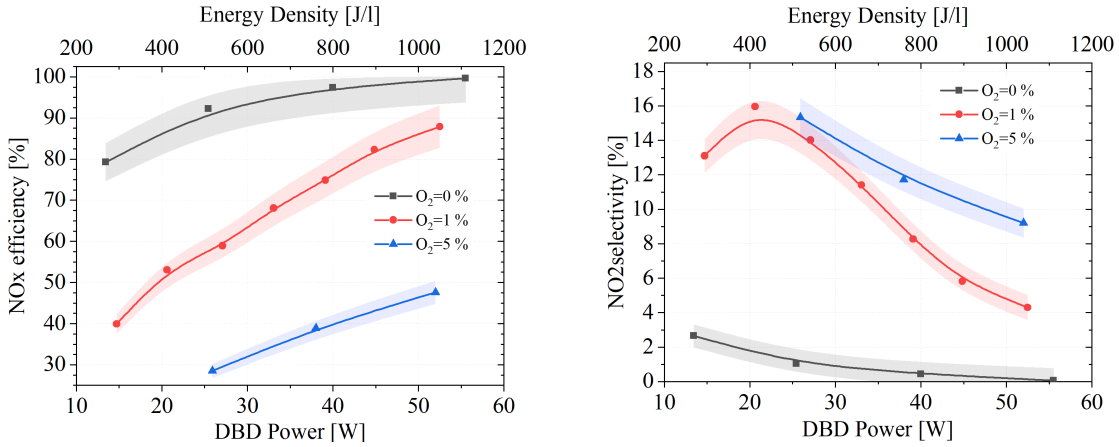

(a) $DeNO_x$ Efficiency (b) NO_2 Selectivity

Figure 6.47: Effect of the O_2 concentration in the treatment performances

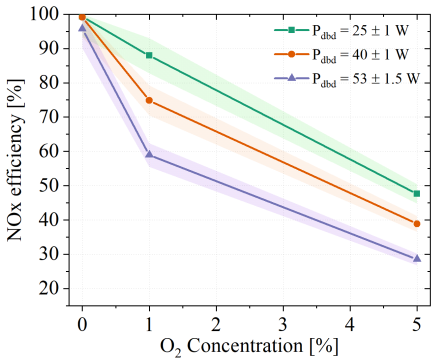

(a) O_2 effect on $DeNO_x$ efficiency

In order to better elucidate the $DeNO_x$ process in the presence of the oxygen, the spectrum of the UV light emitted by the discharge for the OPs working at $\langle P_{dbd} \rangle_{burst} \approx 40W$ is analyzed. The top plot of Figure 6.48 shows the spectrum for a gas mixture composed only by N_2, ($NO = 0$ ppm, and $O_2 = 0$ %). This spectrum serves as a reference of the N_2 emission bands; intense peaks appear between 300 and 400 nm, in agreement with the N_2 emission (Secondary Positive System) [22, 23], with a dominant head at 337 nm. Another set of emission bands (First Positive System) is expected in the visual-near infrared (600 to 900 nm); however, it is out of the range of the employed spectrometer.

In the bottom plot of Figure 6.48, the spectrum for a fixed NO concentration of $NO =$ 800 ppm and different oxygen levels are compared. From the red trace (corresponding to $NO = 800$ ppm, and $O_2 = 0$ %), it can be seen that once the NO is included in the gas mixture, additional peaks between 200 and 300 nm appear. These emissions are attributed

to the transition of NO molecules from an excited state to the ground state (NO_γ bands) [23], and they can be related to the effect of the plasma producing excited NO molecules. It is also seen that when O_2 is added to the mixture, the amplitude of all the bands is reduced. However, there is a more drastic drop in the amplitude of the NO_γ bands. At $O_2 = 5\%$ (green trace), the NO_γ bands are almost unnoticed, conforming to the low $DeNO_x$ efficiency in the presence of oxygen.

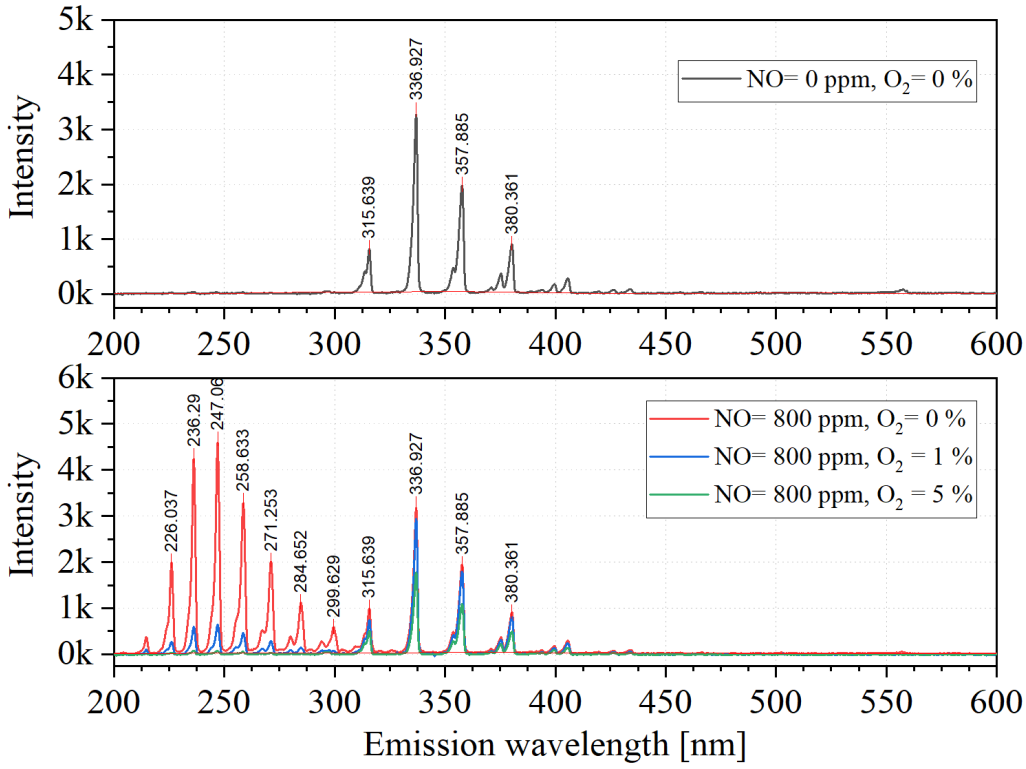

Figure 6.48: UV-spectrum of the light emitted by the discharge working at $\langle P_{dbd} \rangle_{burst} \approx 45W$, for different initial concentrations of oxygen ($O_2 = 0\%, 1\%, 5\%$)

The changes in the light emitted by the discharge in the presence of O_2 are also visible from the discharge pictures. In Figure 6.49 it can be seen that the discharge gets darker at high O2 concentrations.

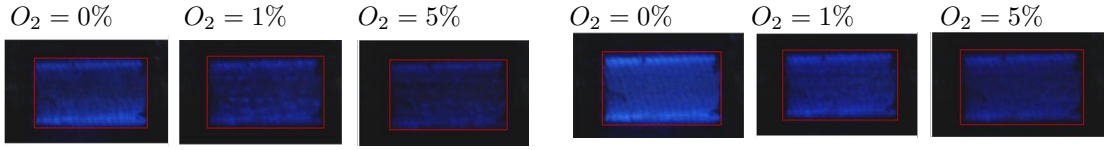

(a) $P_{dbd} \approx 27\ W$ (b) $P_{dbd} \approx 40\ W$

Figure 6.49: Effect of the initial O_2 in discharge pictures

6.6 Conclusions

The methodology proposed in Chapter 5 has been applied to three different power supplies: sinusoidal voltage source, square current source in continuous mode, and square current source in Burst mode.

Based on the results of the traditional sinusoidal voltage source, a baseline for treatment performances was established at $\eta NO_x = 91 \pm 5\%$ at $\langle P_{dbd} \rangle_T = 36.5\ W$. This power supply has been used as a reference point for the treatment capabilities.

Unfortunately, the square current source in continuous mode exhibits important experimentation limitations related to the thermal behavior of the reactor and the stabilization of the discharge. Therefore, it was not possible to evaluate its performance. Nonetheless, the burst mode, proposed as an alternative operation of the square current source, shows significant improvements in the thermal behavior and stabilization of the discharge with respect to the continuous mode, allowing the parametric study of the electrical parameters.

The burst parameters have the strongest impact among the power supply parameters. The distribution of the discharge in the electrodes is positively impacted by T_{idle}. On the other hand, the number of pulses injected into the discharge, N_{on}, limits the treatment efficiency due to a non-homogeneous injection of energy. The transient operation of the current pulses produces low intensities discharge in the steady-state, which do not significantly contribute to the treatment. Surprisingly, no relevant effects of the HF pulses parameters are observed in the tested OPs.

For a fixed gas composition ($G = 3\ lpm$, $NO = 0\ ppm$, and $O_2 = 0\ \%$), the best treatment results are obtained at $T_{idle} = 125\mu s$, $N_{on} = 10$, $f_s = 80\ kHz$, $T_{pulse} = 3.12\mu s$, and $J_{prim} = 1.42\ A$. For this OP, $\eta NO_x = 97 \pm 5\%$ at $\langle P_{dbd} \rangle_{burst} = 34\ W$ and $ED = 680 J/l$ is obtained. This results is 6% higher than the removal efficiency of the sinusoidal voltage source using the same reactor, and it is in a similar ED range of some publications with similar reactors and gas conditions [1, 24, 25]. Further details of such publications were summarized in Table 2.2.

Finally, it is reported that an increment in the gas flow rate, G, or NO concentration decreases the treatment performances. Besides, the addition of O_2 into the gas mixture drastically reduces the NO_x removal and even promotes the formation of NO_2. To further improve the removal efficiency in the presence of oxygen, it is necessary to include catalysts stages and include reducing agents.

Bibliography

[1] T. Wang, B. M. Sun, H. P. Xiao, J. Y. Zeng, E. P. Duan, J. Xin, and C. Li, "Effect of reactor structure in DBD for nonthermal plasma processing of NO in N2 at ambient temperature," *Plasma Chemistry and Plasma Processing*, vol. 32, no. 6, pp. 1189–1201, 2012. doi: https://doi.org/10.1007/s11090-012-9399-3

[2] C. R. McLarnon and B. M. Penetrante, "Effect of Reactor Design on the Plasma Treatment of NOx," in *International Fall Fuels and Lubricants Meeting and Exposition*. SAE International, 10 1998. doi: https://doi.org/10.4271/982434

[3] T. Q. Vinh, S. Watanabe, T. Furuhata, and M. Arai, "Fundamental study of NO x removal from diesel exhaust gas by dielectric barrier discharge reactor," *Journal of Mechanical Science and Technology*, vol. 26, no. 6, pp. 1921–1928, 2012. doi: https://doi.org/10.1007/s12206-012-0402-y

[4] T. Yamamoto, M. Okubo, K. Hayakawa, and K. Kitaura, "Towards ideal NO x control technology using a plasma-chemical hybrid process," *IEEE Transactions on Industry Applications*, vol. 37, no. 5, pp. 1492–1498, 2001. doi: https://doi.org/10.1109/28.952526

[5] V. Ravi, Y. S. Mok, B. S. Rajanikanth, and H.-c. Kang, "Studies on Nitrogen Oxides Removal Using Plasma Assisted Catalytic Reactor," *Plasma Science and Technology*, vol. 5, no. 6, pp. 2057–2062, 12 2003. doi: https://doi.org/10.1088/1009-0630/5/6/007

[6] T. C. Manley, "The Electric Characteristics of the Ozonator Discharge," *Transactions of The Electrochemical Society*, vol. 84, no. 1, p. 83, 1943. doi: https://doi.org/10.1149/1.3071556

[7] F. Peeters, "The Electrical Dynamics of Dielectric Barrier Discharges," Ph.D. dissertation, Technische Universiteit Eindhoven, 2015.

[8] A. Belinger, N. Naudé, and N. Gherardi, "Transition from diffuse to self-organized discharge in a high frequency dielectric barrier discharge," *The European Physical Journal Applied Physics*, vol. 79, no. 1, p. 10802, 7 2017. doi: https://doi.org/10.1051/epjap/2017160487

[9] Y. Zhang, L. Wei, X. Liang, and M. Šimek, "Ozone Production in Coaxial DBD Using an Amplitude-Modulated AC Power Supply in Air," *Ozone: Science & Engineering*, vol. 41, no. 5, pp. 437–447, 9 2019. doi: https://doi.org/10.1080/01919512.2019.1565986

[10] S. Beleznai, G. Mihajlik, I. Maros, L. Balzs, and P. Richter, "High frequency excitation waveform for efficient operation of a xenon excimer dielectric barrier discharge lamp," *Journal of Physics D: Applied Physics*, vol. 43, no. 1, 2010. doi: https://doi.org/10.1088/0022-3727/43/1/015203

[11] A. A. El-deib, "Modeling of and Driver Design for a Dielectric Barrier Discharge Lamp," Ph.D. dissertation, University of Toronto, 2010. [Online]. Available: http://hdl.handle.net/1807/24745

[12] D. M. Flórez Rubio, "Power Supplies for the Study and Efficient use of DBD Excimer UV Lamps," Ph.D. dissertation, Institut National Polytechnique de Toulouse and Pontificia Universidad Javeriana, 2014.

[13] S. Liu and M. Neiger, "Electrical modelling of homogeneous dielectric barrier discharges under an arbitrary excitation voltage," *Journal of Physics D: Applied Physics*, vol. 36, no. 24, pp. 3144–3150, 12 2003. doi: https://doi.org/10.1088/0022-3727/36/24/009

[14] T. Namihira, S. Tsukamoto, D. Wang, S. Katsuki, R. Hackam, H. Akiyama, Y. Uchida, and M. Koike, "Improvement of NOX removal efficiency using short-width pulsed power," *IEEE Transactions on Plasma Science*, vol. 28, no. 2, pp. 434–442, 2000. doi: https://doi.org/10.1109/27.848102

[15] R. J. Carman and R. P. Mildren, "Computer modelling of a short-pulse excited dielectric barrier discharge xenon excimer lamp (172 nm)," *Journal of Physics D: Applied Physics*, vol. 36, no. 1, pp. 19–33, 2003. doi: https://doi.org/10.1088/0022-3727/36/1/304

[16] X. Bonnin, J. Brandelero, N. Videau, H. Piquet, and T. Meynard, "A high voltage high frequency resonant inverter for supplying DBD devices with short discharge current pulses," *IEEE Transactions on Power Electronics*, vol. 29, no. 8, pp. 4261–4269, 2014. doi: https://doi.org/10.1109/TPEL.2013.2295525

[17] J. Vinogradov, B. Rivin, and E. Sher, "NOx reduction from compression ignition engines with DC corona discharge—An experimental study," *Energy*, vol. 32, no. 3, pp. 174–186, 3 2007. doi: https://doi.org/10.1016/j.energy.2006.04.011

[18] A. C. Gentile and M. J. Kushner, "Reaction chemistry and optimization of plasma remediation of N xOy from gas streams," *Journal of Applied Physics*, vol. 78, no. 3, pp. 2074–2085, 1995. doi: https://doi.org/10.1063/1.360185

[19] B. S. Rajanikanth, A. D. Srinivasan, and V. Ravi, "Discharge plasma treatment for NOx reduction from diesel engine exhaust: A laboratory investigation," *IEEE Transactions on Dielectrics and Electrical Insulation*, vol. 12, no. 1, pp. 72–79, 2005. doi: https://doi.org/10.1109/TDEI.2005.1394017

[20] Z. Wang, H. Kuang, J. Zhang, L. Chu, and Y. Ji, "Nitrogen oxide removal by non-thermal plasma for marine diesel engines," *RSC Advances*, vol. 9, no. 10, pp. 5402–5416, 2019. doi: https://doi.org/10.1039/c8ra09217f

[21] L. Yang, K. Lian, X. Zhang, Y. Li, C. Q. Jia, B. Zhao, and X. Ma, "Nitric oxide removal from flue gas using dielectric barrier discharge coupled with negative pulse corona," *Chemical Engineering Research and Design*, vol. 143, pp. 170–179, 2019. doi: https://doi.org/10.1016/j.cherd.2019.01.003

[22] M. Yousfi, N. Merbahi, J. P., O. Eichwald, A. Ricard, J. Gardou, O. Ducasse, and M. Benhenni, "Non Thermal Plasma Sources of Production of Active Species for Biomedical Uses: Analyses, Optimization and Prospect," *Biomedical Engineering - Frontiers and Challenges*, 2011. doi: https://doi.org/10.5772/19129

[23] A. Abahazem, N. Merbahi, H. Guedah, and M. Yousfi, "Electric and Spectroscopic Studies of Pulsed Corona Discharges in Nitrogen at Atmospheric Pressure," *Journal of Analytical Sciences, Methods and Instrumentation*, vol. 07, no. 03, pp. 57–74, 2017. doi: https://doi.org/10.4236/jasmi.2017.73006

[24] S. J. Anaghizi, P. Talebizadeh, H. Rahimzadeh, and H. Ghomi, "The Configuration Effects of Electrode on the Performance of Dielectric Barrier Discharge Reactor for NOx

Removal," *IEEE Transactions on Plasma Science*, vol. 43, no. 6, pp. 1944–1953, 2015. doi: https://doi.org/10.1109/TPS.2015.2422779

[25] M. Arai, M. Saito, and S. Yoshinaga, "Effect of oxygen on NOX removal in corona discharge field: NOX behavior without a reducing agent," *Combustion Science and Technology*, vol. 176, no. 10, pp. 1653–1665, 2004. doi: https://doi.org/10.1080/00102200490487535

Part IV

Conclusions

General Conclusions

This last part summarizes the research carried out to study the interaction between current-mode power supplies and the NO_x treatment based on DBDs, it draws some conclusions from the results of previous chapters, and discuss some thoughts and open issues for future developments.

As stated at the beginning of this document, the objective of this thesis is to identify the conditions of the current-mode power supplies that improve the $DeNO_x$ treatment based on DBD. The motivation, challenges, and potential problems of the $DeNO_x$ treatment are firstly exposed (Chapter 1 and 2). This included a survey on plasma-based treatment technologies, particularly on the $DeNO_x$ results of DBD reactors, revealing a research gap in investigating DBD current-mode power supplies. Following this opportunity, the two main supply methods (current and voltage imposition), along with several DBD power supplies [1, 2, 2], are compared (Chapter 3), and a Square Current Source is chosen for experimentation purposes.

A common problem faced by the experimentation of plasma-based systems is related to procedural and human errors. Small variations in the setup can alter the results. Reproducible experimentation demands full-time supervision and attention to detail to guarantee the same experimentation conditions. With the proposed automated experimentation setup, those issues are avoided, and more reliable, reproducible, and organized data is obtained [3].

The detailed analysis of the Square Current Source play a crucial role in the design of the converter and in understanding the treatment results [2, 4–6]. As the parasitic elements of the system alter the operation of the power supply, a numerical method is proposed and validated for estimating the DBD waveforms considering the stray transformer capacitance and magnetizing inductance . This tool is helpful to understand the effect on the DBD waveform of each parasitic element. Accordingly, the transformer design should maximize the magnetizing inductance while the stray capacitance is minimized to produce ideal square current pulses. As it is very challenging to design HV transformers following those two requirements, the parasitic elements must be considered in the analysis of the treatment results.

Particularly, in the burst mode, the parasitic elements cause a strong transient response in each burst. Hence, it is impossible to separate the burst parameters effect from the transient effects. When analyzing the impact of the number of pulses injected by the burst, N_{on}, it is observed that the initial pulses of the transient deliver more energy than those in steady-state. Accordingly, the steady-state pulses do not significantly contribute to the treatment performance, and the $DeNO_x$ efficiency tends to saturate at low values of the pulses number, without significant improvement when a long train of pulses is injected. It is still unknown whether a long train of pulses of the same magnitude (without transient) can promote or not the $DeNO_x$ treatment. As future work, some enhancements in the power supply to reduce the transient are suggested.

The analysis of the experimental data employing the electrical, optical, and treatment diagnostics reveal some interesting effects of the power supply degrees of freedom and some

correlation between the results of the diagnostic techniques. The electrical characterization of the DBD based on the Q-V Manley diagram is employed to measure the DBD electrical parameters. Due to the variation of the identified DBD parameters when the discharge does not cover the entire electrodes surface, a partial discharging area model is introduced. Based on this model, the effective measured DBD parameter (C_{dEff}, $C_{g_{Eff}}$, V_{thEff}) can be related with the full-area discharge parameters (C_d, C_g, V_{th}) to estimate the area covered by the discharge. In the same way, based on the proposed image processing algorithm, the segmentation of the images is used to segment the discharge area and analyze its uniformity. The discharge area obtained by the image processing is validated with the one deduced from the partial discharging area electrical model. In all the experimental studies, both diagnostic methods show similar results. Further improvements in the image processing algorithm are suggested. For instance, the top and bottom part of the reactor pictures are not considered in the statistical analysis, with proper algorithms the discharge could be also segmented in those regions.

The discharge area is an important characteristic for an optimal operation of the $DeNOx$ reactor. A full discharge area guarantees that the whole gas flows through the plasma region, increasing the probability of interaction between the pollutants and the plasma. An undesirable operation is obtained by the Square Current Source operated in continuous mode; in this case, the discharge concentrates in a small region. The only way to increase the discharge area is by incrementing the DBD power, leading to high reactor temperatures. A significant improvement in the discharge distribution is obtained by introducing the burst operation. In the experimental study of the burst parameter, T_{idle}, it is observed that it promotes the uniform distribution of the discharges in the area of the electrodes. Additionally, as T_{idle} decreases, the operation gets closer to the continuous mode where the discharge concentrates in a smaller region.

Based on the parametric study of the square current source operated in burst mode, the maximum treatment efficiency of $\eta NO_x = 97\%$ at $P_{dbd} = 34\ W$, $ED = 680\ J/l$ is obtained with in following OP: $T_{idle} = 125\mu s$, $N_{on} = 10$, $f_s = 80\ kHz$, $T_{pulse} = 3.12\mu s$, and $J_{prim} = 1.42\ A$, $G = 3\ lpm$, $NO = 0\ ppm$, and $O_2 = 0\ \%$. This efficiency is 6% higher than the one obtained by the sinusoidal voltage source using the same reactor and gas conditions at a similar power level. These results show a promising improvement of the current sources that can be further explored by expanding number of OPs investigated by this setup, or by increasing the power supply capabilities to expand the range of the OPs parameters. For instance, in the experimental study of the HF parameters (f_s, T_{pulse}), no significant effects of any parameter were detected; some effects might stand out with a wider range of frequency or duration of the pulses. Finally, in order to market the technology, the treatment efficiency has to be improved in the presence of O_2. The experimental study of the O_2 concentration shows a significant diminution of the treatment efficiency when O_2 is added in the mixture. Additives or catalytic stages might be required to obtain full removal in real engines applications. Additionally, some other gaseous components such as CO_2 and H_2, can be added to the gas mixture to better reproduce the diesel exhaust composition.

Bibliography

[1] V. Rueda, A. Diop, R. Diez, and H. Piquet, "Series Resonant Inverter Efficiency Improvement with Valley Switching for Dielectric Barrier Discharges," *Proceedings of the International Conference on Power Electronics and Drive Systems*, vol. 2019-July, no. July, 2019. doi: https://doi.org/10.1109/PEDS44367.2019.8998891

[2] H. Piquet, R. Diez, and V. Rueda, "Power supplies dedicated to the efficient control of the excimer lamps power," in *XIV International Conference on Pulsed Lasers and Laser Applications*, A. V. Klimkin, V. F. Tarasenko, and M. V. Trigub, Eds. SPIE, 12 2019, p. 17. doi: https://doi.org/10.1117/12.2547460

[3] A. Ivankov, T. Capela, V. Rueda, E. Bru, H. Piquet, D. Schitz, D. Florez, and R. Diez, "Experimental Study of a Nonthermal DBD-Driven Plasma Jet System Using Different Supply Methods," *Plasma*, vol. 5, no. 1, pp. 75–97, 2 2022. doi: https://doi.org/10.3390/plasma5010007

[4] V. Rueda, A. Wiesner, R. Diez, and H. Piquet, "Enhancement of the DBD power for current-mode converters using the step-up transformer elements," *2018 IEEE Industry Applications Society Annual Meeting, IAS 2018*, pp. 1–8, 2018. doi: https://doi.org/10.1109/IAS.2018.8544496

[5] V. Rueda, R. Diez, and H. Piquet, "Optimum transformer turns ratio for the power supply of dielectric barrier discharge lamps," *IET Power Electronics*, vol. 11, no. 1, pp. 62–67, 2018. doi: https://doi.org/10.1049/iet-pel.2016.0497

[6] V. Rueda, A. Wiesner, R. Diez, and H. Piquet, "Power Estimation of a Current Supplied DBD Considering the Transformer Parasitic Elements," *IEEE Transactions on Industry Applications*, vol. 55, no. 6, pp. 6567–6575, 11 2019. doi: https://doi.org/10.1109/TIA.2019.2933519

Appendix A

Supplementary Experimental Results

In this appendix, some of the results from the experimental studies that were not presented in Chapter 6 are shown.

A.1 Study of Gas conditions

A.1.1 Effect of the total gas flow, G

Figure A.1 shows the DBD power and DBD peak-peak voltage of the OPs working at $f_s = 80kHz$, $Tpulse = 3.125\mu s$, $Non = 10$, $T_{idle} = 125\mu s$ and $G = 3, 5, 8lpm$. Within this power range, a linear increment of the DBD power with J_{prim} can be observed for all the gas flow rates. Additionally, at each current level, there is a small variation in the DBD power of around ±2W between G = 3lpm and G = 8lpm. As illustrated in Figure 6.42-b, the produced DBD voltage is also impacted by G; the highest peak voltages are produced at a high flow rate G = 8lpm. Such differences may be the effect of changes in the DBD electrical parameters due to G. Figure A.2 shows the estimated DBD model parameters. As can be observed, the dielectric and gas capacitances present slight changes between flow rates, with a variation of less than ±4% around the average value. Nonetheless, a consistent increment in gas the breakdown, Vth, with G is observed. The highest breakdown voltage is measured at high gas flow rates; this may explain the variation of the DBD peak voltage when the same DBD current is applied

As displayed in Figure A.3, for this set of electric conditions, the gas flow rate has no significant impact on the discharge area. In all the experiments, the area is higher than 97%. In the same manner, the coefficient CV for the three gas flow rates behaves similarly; CV decreases with the increase in Pdbd, which means that the discharge is less uniform at low power levels. Moreover, some differences in the brightness of the discharge are observed. The estimated mean gray level is lower at low gas flow rates; in other words, the discharge appears darker

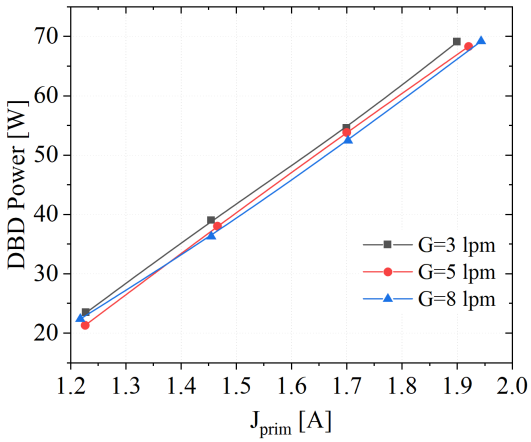

Figure A.1: DBD power controlled by J_{prim} for the gas flow rate G analysis

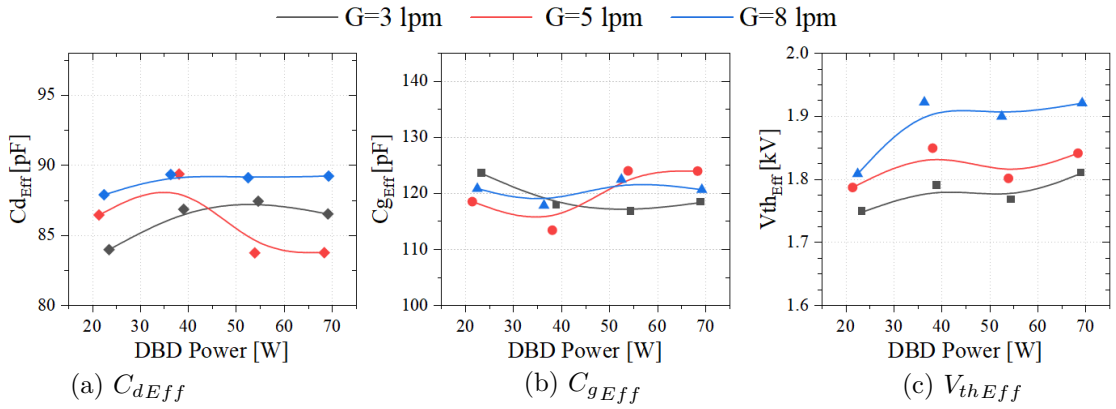

(a) C_{dEff} (b) C_{gEff} (c) V_{thEff}

Figure A.2: Effect of gas flow rate G in DBD characterization results

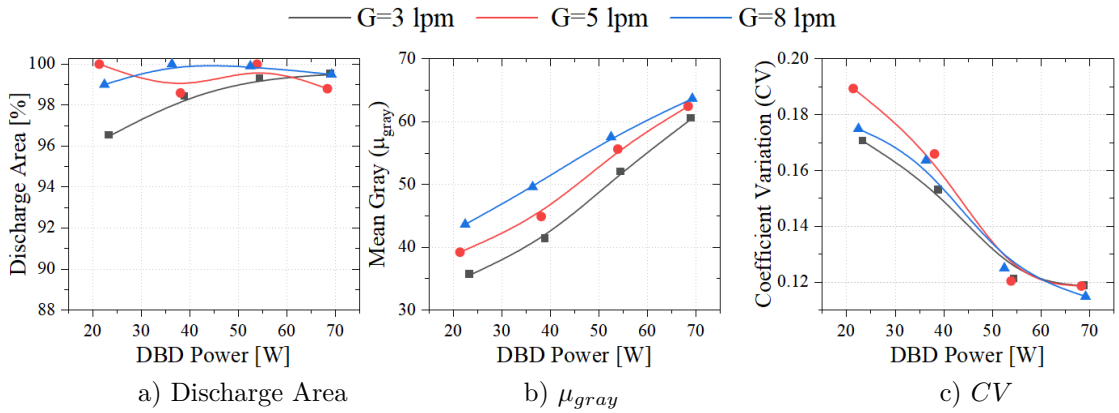

a) Discharge Area b) μ_{gray} c) CV

Figure A.3: Effect of gas flow rate G in discharge appearance

A.1.2 Effect of NO concentration

Under the following conditions: $f_s = 80kHz$, $T_{pulse} = 3.125\mu s$, $N_{on} = 10$, $T_{idle} = 125\mu s$ and $NO = 800, 2000, 3000ppm$, the changes in the DBD power and peak voltage are evaluated at different NO concentrations. No significant impact is observed (Figure A.4). On the other hand, the variation in the initial amount of NO produces changes in the electrical model identification. From Figure A.5, it can be seen that the estimated dielectric capacitance, Cd, of the OPs at high NO concentration varies with the power, whereas for OPs at NO = 800 ppm is steadier. Those variations are also seen in the gas capacitance Cg. For DBD powers above 20 W , the gas breakdown voltage of all the measurements remained in a range of $1.7 \pm 0.5kV$.

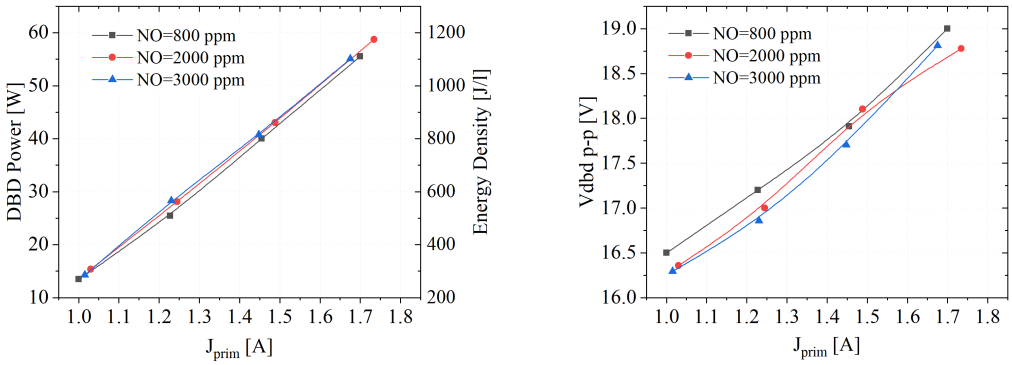

(a) DBD power controlled by J_{prim} (b) DBD peak-peak voltage

Figure A.4: Effect of NO concentration in electric quantities

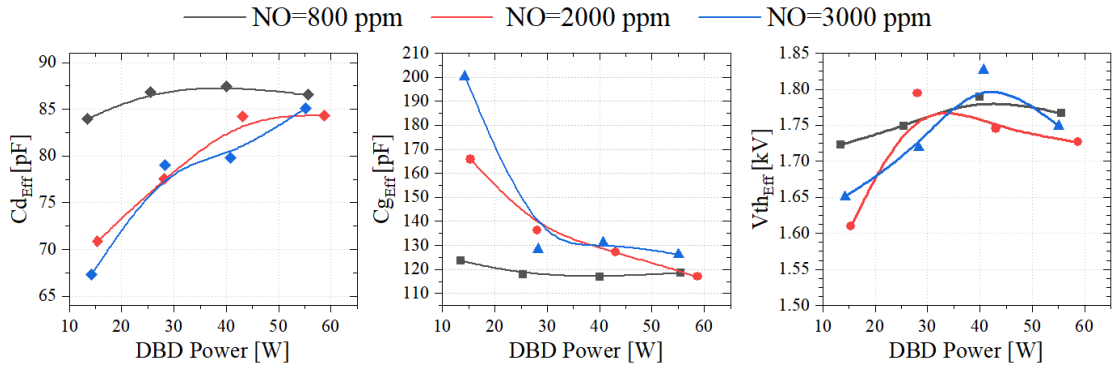

(a) C_{dEff} (b) C_{gEff} (c) V_{thEff}

Figure A.5: Effect of the initial NO concentration in DBD characterization results

In the optical diagnostic, it is observed that the OPs with the lower NO concentration attain discharges more widely distributed in the electrodes area (Figure A.6-a), less brighter (Figure A.6-b), and more uniform (Figure A.6-c)

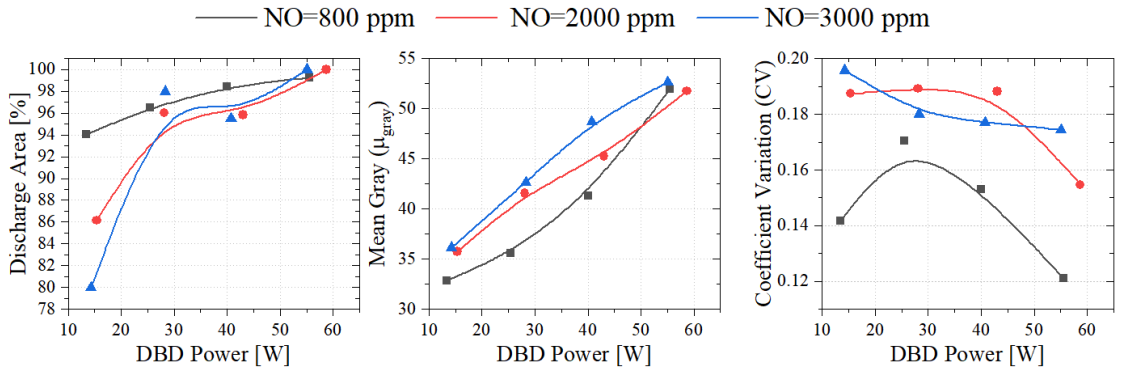

a) Discharge Area b) μ_{gray} c) CV

Figure A.6: Effect of the initial NO in discharge appearance

A.1.3 Effect of O_2 concentration

Under the following conditions: $f_s = 80kHz$, $Tpulse = 3.125\mu s$, $Non = 10$, $T_{idle} = 125\mu s$ and $O2 = 0, 1, 5\%$, the changes in the DBD power and peak voltage are evaluated at different O_2 concentrations. Similar to the effects of the NO concentration in the electrical quantities, no major variation in the DBD power and voltage are obtained when only the O2 concentration varies (Figure A.7). Moreover, the estimated capacitances, Cd and Cg, follow the same behavior that has been already described, where the estimated Cd increases with the power,and accordingly, Cg, decreases (Figure A.8).

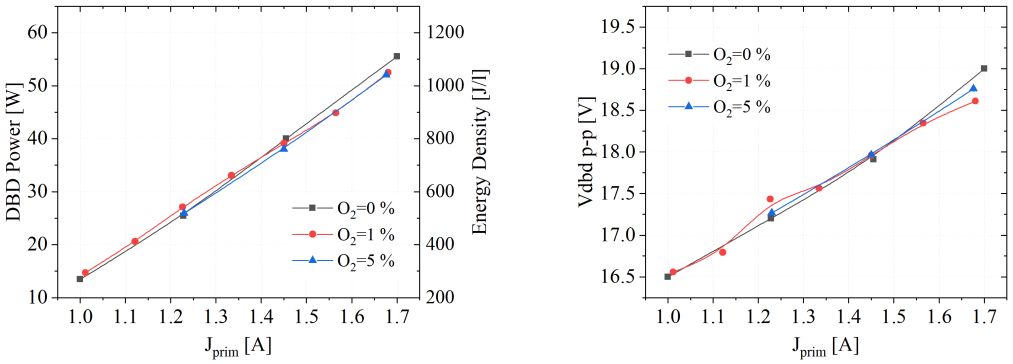

(a) DBD power controlled by J_{prim} (b) DBD peak-peak voltage

Figure A.7: Effect of O_2 concentration in electric quantities

Concerning the discharge appearance, examined in Figure A.9, for all the O2 levels the discharge is well established in the area of the electrodes, covering more than 94% of the total area. Additionally, it can be seen that the discharge gets darker at high O2 concentrations. The same trends were qualitatively observed the pictures of Figure 6.49.

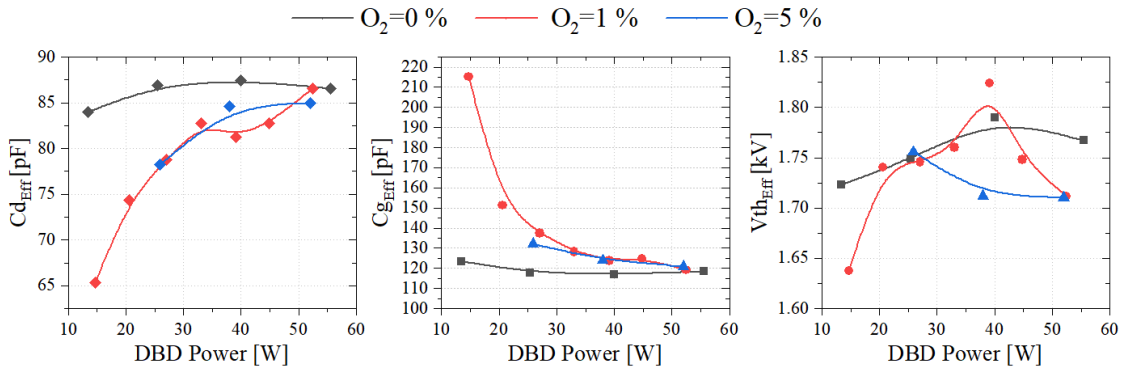

(a) C_{dEff} (b) C_{gEff} (c) V_{thEff}

Figure A.8: Effect of the initial O_2 concentration in DBD characterization results

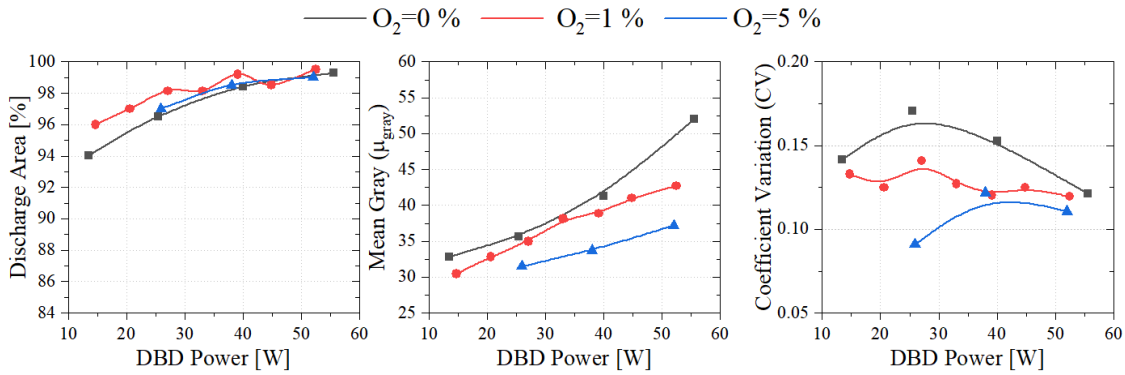

a) Discharge Area b) μ_{gray} c) CV

Figure A.9: Effect of the initial O_2 concentration in discharge appearance

A.2 Study of the HF pulse Parameters

A.2.1 Effect of T_{pulse} at $f_s = 80\ kHz$

No effect of the pulse duration on the reactor temperature was observed.

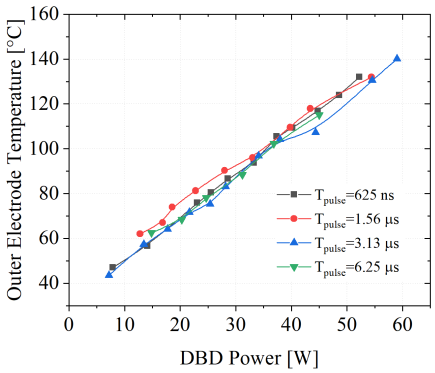

Figure A.10: Effect of T_{pulse} in outer electrode temperature